AFOSR-TR- 89-0282

(2)

BIFURCATING JETS AT HIGH REYNOLDS NUMBERS

By

D. E. Parekh, A. Leonard and W. C. Reynolds

Prepared with the support of the
Air Force Office of Scientific Research
under Contracts
AF-F49620-84-K-0005 and AF-F49620-86-K-0020

Report No. TF-35

Thermosciences Division
Department of Mechanical Engineering
Stanford University
Stanford, California 94305

December 1988

UNCLASSIFIED
SECURITY CLASSIFICATION OF THIS PAGE

AD-A205 218

REPORT DOCUMENTATION PAGE

1a REPORT SECURITY CLASSIFICATION Unclassified	1b RESTRICTIVE MARKINGS
2a SECURITY CLASSIFICATION AUTHORITY	3 DISTRIBUTION/AVAILABILITY OF REPORT Approved for public release.
2b DECLASSIFICATION/DOWNGRADING SCHEDULE	Distribution is unlimited.
4 PERFORMING ORGANIZATION REPORT NUMBER(S) TF-35	5 MONITORING ORGANIZATION REPORT NUMBER(S) AFOSR-TR- 89-0282
6a NAME OF PERFORMING ORGANIZATION Stanford Unviersity — 6b OFFICE SYMBOL (If applicable)	7a NAME OF MONITORING ORGANIZATION AFOSR
6c ADDRESS (City, State, and ZIP Code) Stanford, CA 94305	7b ADDRESS (City, State, and ZIP Code) Building 410 Bolling Air Force Base, DC 20332-6448
8a NAME OF FUNDING/SPONSORING ORGANIZATION AFOSR/NA — 8b OFFICE SYMBOL (If applicable) NA	9 PROCUREMENT INSTRUMENT IDENTIFICATION NUMBER F 4962-86-K0020
8c ADDRESS (City, State, and ZIP Code) Building 410 Bolling Air Force Base, DC 20332-6448	10 SOURCE OF FUNDING NUMBERS PROGRAM ELEMENT NO. 61103D — PROJECT NO 3484 — TASK NO A1 — WORK UNIT ACCESSION NO

11 TITLE (Include Security Classification)
Bifurcating Jets at High Reynolds Numbers

12 PERSONAL AUTHOR(S)
D. E. Parekh, A. Leonard and W. C. Reynolds

13a TYPE OF REPORT Technical	13b TIME COVERED FROM 7 Dec TO 88	14 DATE OF REPORT (Year, Month, Day) 1988, December 7	15 PAGE COUNT 276

16 SUPPLEMENTARY NOTATION

17 COSATI CODES		
FIELD	GROUP	SUB-GROUP

18 SUBJECT TERMS (Continue on reverse if necessary and identify by block number)
Flow control, jet mixing, turbulent jets, vortex simulations

19 ABSTRACT (Continue on reverse if necessary and identify by block number)
The combination of axial and helical excitation has been used to control the spreading rate of turbulent jets at Reynolds numbers up to 100,000. This report presents analysis of the basic flow using vortex dynamics and experiments. The mechanisms of the processes are explained and the levels of excitation necessary to produce the enhancements.

20 DISTRIBUTION/AVAILABILITY OF ABSTRACT ☒ UNCLASSIFIED/UNLIMITED ☐ SAME AS RPT. ☐ DTIC USERS	21 ABSTRACT SECURITY CLASSIFICATION Unclassified
22a NAME OF RESPONSIBLE INDIVIDUAL James M. McMichael	22b TELEPHONE (Include Area Code) (202) 767-4936 — 22c OFFICE SYMBOL AFOSR/NA

DD FORM 1473, 84 MAR — 83 APR edition may be used until exhausted. All other editions are obsolete.

SECURITY CLASSIFICATION OF THIS PAGE
UNCLASSIFIED

BIFURCATING JETS
AT HIGH REYNOLDS NUMBERS

by

D. E. Parekh
A. Leonard
W. C. Reynolds

Prepared with the support of the
Air Force Office of Scientific Research
under Contracts
AF-F49620-84-K-0005 & AF-F49620-86-K-0020

Report No. TF-35

Thermosciences Division
Department of Mechanical Engineering
Stanford University
Stanford, California 94305

December 1988

ACKNOWLEDGMENTS

The authors gratefully acknowledge the contributions of their colleagues at Stanford University and the NASA Ames Research Center. At Stanford University, Prof. M. G. Mungal provided invaluable advice in the planning and evaluation of the experimental work. Mr. P. Juvet made most of the hot-wire measurements presented in this report and, along with Messrs. C. R. Koch and A. Eaton, assisted in setting up and performing several of the experiments. Dr. M. J. Lee shared numerous insights regarding his work on bifurcating and blooming jets. At Ames Research Center, Dr. P. Spalart and Mr. K. Shariff contributed through many stimulating discussions.

Financial support was provided by the Air Force Office of Scientific Research under grants AF-F49620-84-K-0005 and AF-F49620-86-K-0020. The NASA Ames Research Center provided the computer time for this research. These contributions are also gratefully acknowledged.

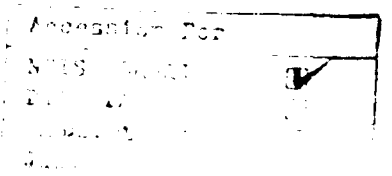

A-1

ABSTRACT

There is much current interest in the use of controlled excitations to manage various types of flows. This work focuses on the use of dual-mode forcing to alter dramatically the structure of round turbulent jets. Properly-combined axial and helical excitations can cause a round jet to split into two distinct jets. This Y-shaped jet, known as a *bifurcating jet*, exhibits spreading angles as high as 80 degrees. Vortex rings are formed at the jet exit and propagate along the two branches of the jet.

A vortex-filament code was developed for simulating the large-scale features of bifurcating jets. The motion and interaction of the vortex structures in this flow are tracked in a three-dimensional, Lagrangian coordinate system. This simulation showed that inviscid vortex interactions cause the dramatic changes in jet development and that spreading angle increases with axial Strouhal number.

The experimental apparatus consists of an acoustically-excited, 2-cm-diameter air jet. The jet evolution is documented by flow visualization at velocities up to 75 m/s, Reynolds numbers up to 100,000, and Mach numbers up to 0.22. Instantaneous and phase-averaged cross-sections of the jet reveal the effects of forcing amplitude on the structure and spreading angle of axially-excited, helically-excited, and bifurcating jets. The primary conclusions of this experiment are that dual-mode acoustic excitation can produce bifurcation in air jets at high Reynolds numbers and that the jet spreading angle increases with both excitation amplitudes, Additionally, the excitation amplitude required to produce bifurcation increases with Reynolds number, but the corresponding excitation Strouhal number is invariant.

TABLE OF CONTENTS

LIST OF TABLES

LIST OF FIGURES

NOMENCLATURE

Roman Symbols

A_a, A_h	axial and helical excitation amplitude
D	diameter of nozzle or of cylindrical vortex sheet
E	anemometer bridge voltage
$E(m)$	complete elliptic integral of the second kind
E_0	King's law parameter
f	frequency
f_a, f_h	axial and helical excitation frequencies
f_n	natural frequency of shear layer
f_v	vortex-passage frequency
F	spatially-averaged, nondimensional, axial momentum flux or number of light pulses per exposure
h	size of subinterval
$I(\bar{\eta})$	intermediate integral
k	King's law parameter
$K(m)$	complete elliptic integral of the first kind
l	measured distance between vortical structures
m, m_1	arguments of elliptic integrals
n	node index or King's law exponent
p'	rms acoustic perturbation
$\bar{p}$	nondimensional pressure perturbation, $p'/(\frac{1}{2}\rho U^2)$
p_{ref}	reference pressure, 2×10^{-5} Pa
Q_i^j	partial integral over intervals i to j
r	radial coordinate
$\mathbf{r}(\xi)$	three-dimensional space curve
R	radius of vortex ring or of cylindrical vortex sheet
$\mathcal{R}_f$	ratio of axial to helical frequency
$\mathcal{R}_s$	ring-spacing ratio

Re	Reynolds number, UD/ν
s	distance between adjacent vortex rings
SPL	sound pressure level
St_D	Strouhal number, fD/U
St_a, St_h	axial and helical Strouhal numbers
St_θ	Strouhal number, $f\theta/U$
t	time
T	temperature
$T(\bar{\mu}, \bar{\eta})$	Teri integral
$\mathbf{u}$	instantaneous-velocity vector
u'	rms fluctuation of axial velocity
u_c	convection velocity
u_r	radial component of velocity
u_s	self-induced velocity
u_z	streamwise component of velocity
U	time-averaged axial velocity
$\mathbf{x}$	three-dimensional space coordinate
z	streamwise coordinate

Greek Symbols

α	parameter of Biot-Savart integral
β	bifurcation angle
γ	circulation per unit length
$\tilde{\gamma}$	time average of γ
Γ	circulation of vortex filament
δ	nozzle displacement or core parameter
δ_ω	vorticity thickness of shear layer
Δ	magnitude of core asymmetry
δt	time step of simulation
Δt	time interval between creation of filaments

θ	momentum thickness or azimuthal coordinate
ν	kinematic viscosity
ξ	vortex-filament parameter
ρ	density
σ	nominal core radius
ψ	azimuthal angle
ω	vorticity vector

Chapter 1

INTRODUCTION

Much current interest in the field of fluid mechanics relates to the use of controlled excitations to manage various types of flows. This work focus on the use of dual-mode, dual-frequency, acoustic forcing to alter dramatically the structure of round, turbulent, air jets. Dual-mode refers to the combination of axial and helical perturbations. Dual-frequency denotes that these two different types of perturbations are single frequency excitations of differing frequency.

Properly-combined axial and helical excitations can cause a round jet to split into two distinct jets. This Y-shaped jet, known as a *bifurcating jet*, exhibits spreading angles as high as 80°. Vortex rings are formed at the jet exit and propagate along the two branches of the jet. This study is a combined computational and experimental investigation of bifurcating jets at high Reynolds numbers. The aim of this effort is to understand the mechanism causing bifurcation and to document visually the response of the bifurcating jet to variations in several flow and excitation parameters.

1.1 Background

The sensitivity of jets to sound has fascinated researchers for many decades. In the middle of the 19th century, Leconte (1858) and Tyndall (1867) demonstrated this sensitivity in jets with and without combustion. Early in this century, Brown (1935) demonstrated that laminar jets develop vortex structures and increase in spreading angle in response to acoustic excitation at various critical frequencies.

Understanding the nature of a jet's response to sound and other perturbations is a key to knowing how to use controlled excitations to transform a jet from its natural state to some desired state. Due to the Kelvin-Helmholtz instability, the shear layer of a jet naturally rolls up into distinct vortex rings in a somewhat random

manner. These structures are directly related to a jet's growth, and their formation is very sensitive to perturbations over a wide range of frequencies.

There is a tremendous amount of information in the literature about the structure, evolution, and control of turbulent shear layers. For an extensive overview, the reader should consult the reviews by Cantwell (1981) and Ho & Huerre (1984). The works cited in the following pages are those which, to our knowledge, relate most closely to the present study.

1.1.1 Role and evolution of large structures

The current interest in the role of organized structures in turbulent shear flows was sparked primarily by the works of Crow and Champagne (1971), Brown and Roshko (1974), and Winant and Browand (1974). Crow and Champagne (1971) found that the structure of round turbulent jets at a Reynolds number, based on diameter, around 10^4 includes large-scale vortex 'puffs'. Brown and Roshko (1974) showed that 'large coherent structures' are the dominant feature of mixing layers even over a wide range of density ratios. As a result of their study of planar mixing layers, Winant and Browand (1974) proposed the pairing of large-scale vortex structures as the mechanism of mixing layer growth at moderate Reynolds numbers. The term 'pairing' refers to the coalescence of two vortices into a single, larger structure.

Zaman and Hussain (1980) proposed that the pairing of structures in axisymmetric shear layers can be classified in terms of a shear layer mode and a jet column mode. The 'shear layer mode' refers to the pairing of the small vortices initially formed by the shear layer. The spacing of these vortices is of the order of the shear layer thickness. The 'jet column mode' refers to the pairing of the large vortices formed from the smaller ones. The typical spacing between these larger structures is of the order of the jet diameter. They found that pairing in the shear layer mode is most likely to occur if one excites the shear layer at a Strouhal number, based on initial momentum thickness, of 0.012. Pairing in the jet column mode is most likely to occur at a Strouhal number, based on diameter, of 0.85.

Other researchers have also shown that the vortex formation and pairing processes can be controlled by axial excitation. Bouchard and Reynolds (1981) used axial perturbations to control jet growth by enhancing or suppressing vortex pairing. Ho and Huang (1982) caused several vortices to coalesce into one larger structure by forcing a planar mixing layer at a subharmonic of its most-amplified frequency. The number of vortices involved in a 'collective interaction' corresponds to the subharmonic chosen. Ho and Huang found that high excitation levels ($u'/U \simeq 2\%$) are typically required to cause a collective interaction. At low excitation levels, only vortex pairings occur. At very high levels, the mixing layer forms a large vortex directly, bypassing the stage of vortex pairings or collective interactions. Arbey & Williams (1984) demonstrated control of the generation of harmonics and subharmonics in a jet by controlling the phase between the fundamental and the harmonically-related signal.

In a flow-visualization study of a round jet, Hussain and Clark (1981) showed that the typical view of axisymmetric mixing layer growth by orderly vortex pairings is not accurate at very high Reynolds numbers ($Re = 360{,}000$). Instead, they observed that "most of the time the mixing layer is in a state of disorganization, consisting of relatively smaller scale, random and diffuse turbulent motions." They found that the large scale structures did not evolve from complete pairings of smaller structures. Typically, only segments of vortical structures would combine ('fractional pairing'), or one structure would engulf only part of another structure ('partial pairing'). However, axial forcing can produce a stable, orderly arrangement of vortex structures (Lepicovsky *et al.* 1986). Lepicovsky *et al.* studied the effects of axial forcing on heated (temperatures up to 800°K) and unheated jets in the ranges of $350{,}000 \leq Re \leq 1{,}300{,}000$ and $0.3 \leq M \leq 0.8$.

By altering the orientation or shape of the large-scale structures in a jet, one can modify the jet's spreading and entrainment. In their work with inclined and stepped nozzles, Wlezien and Kibens (1984) found that the jet shear layer growth is enhanced in some azimuthal planes but suppressed in others. Ho and Gutmark

(1987) found that the entrainment ratio of a small-aspect-ratio elliptic jet is several times higher than that of the corresponding circular jet.

1.1.2 Preferred modes of axisymmetric shear layers

While the interaction of vortex structures is a strongly nonlinear process, linear stability theory can fairly accurately model many features of the initial development of the mixing layer (Michalke & Hermann 1982, Ho & Huerre 1984, Gaster *et al.* 1985, Samet & Petersen 1987, and Monkewitz 1988). These features include amplification of disturbances, pairing events, and the effects of velocity ratio.

The shear layer amplifies disturbances over a broad frequency range. The frequency corresponding to the peak of the amplification curve is typically called the natural or most-amplified frequency. In planar and axisymmetric mixing layers with a hyperbolic-tangent velocity profile and a velocity ratio of unity, the Strouhal number ($f\theta/U$) of the initially most-amplified disturbance is 0.017 (Ho & Huerre 1984 and Michalke 1972). In axisymmetric shear layers, this Strouhal number increases as the velocity ratio decreases and as one moves downstream from the jet exit (Michalke & Hermann 1982). The velocity ratio of a mixing layer is typically defined as $(U_1-U_2)/(U_1+U_2)$, where U_1 and U_2 are the velocities of the two streams and $U_1 \geq U_2$. The corresponding momentum thickness, θ, of the axisymmetric shear layer is defined by

$$\theta = \int_0^\infty \left(\frac{U(r)-U_2}{U_1-U_2}\right)\left(1-\frac{U(r)-U_2}{U_1-U_2}\right)\,dr. \qquad 1.1$$

Both axisymmetric and helical disturbances are amplified in circular jets (Chan 1977). The amplification of axisymmetric disturbances is stronger in the near field, but the first-order helical distrubances are more strongly amplified in the far field (Michalke & Hermann 1982 and Tso & Hussain 1987). Michalke & Hermann (1982) also showed that according to stability theory the amplification of helical disturbances in the near field will be greater than that of axisymmetric ones if the disturbance frequency is much less than the natural frequency.

In their study of excited circular jets with thin boundary layers, Crow and Champagne (1971) found that the Strouhal number (fD/U) of the *axisymmetric*

disturbance that can sustain the greatest total amplification is 0.3. They referred to this disturbance as the 'preferred mode' of the jet. This concept of a preferred mode implies the existence of a global instability in jet flows and should not be confused with the initial shear layer instability discussed earlier. The preferred mode also corresponds to the dominant large-scale, axisymmetric structures in unperturbed jets. Hussain and Zaman (1981) found that the shape and orientation of these structures are essentially the same whether the boundary layer is laminar or turbulent but that the characteristics of these structures depend on Reynolds number.

The existence of a preferred mode has been confirmed by many researchers, but there has been no agreement on the corresponding Strouhal number. Gutmark and Ho (1983) found a variation from 0.24 to 0.64 in the works they surveyed. They attributed this scatter to initial conditions. Initial conditions are important when no controlled excitations are used since the initial conditions affect the formation of the small vortex structures which subsequently combine to form the large structures associated with the preferred mode.

Recently, Petersen and Samet (1987) have shown that the preferred mode can be understood in terms of local instability concepts. They demonstrate that the naturally-occurring shear layer instabilities scale with the local momentum thickness and that the preferred mode corresponds to the local shear layer instability near the end of the potential core. They attribute the apparent existence of a preferred mode to the fact that beyond the potential core region helical disturbances are more strongly amplified than are axisymmetric ones.

1.1.3 Characteristics of bifurcating and blooming jets

The work that laid the foundation for the current study is the work of Lee & Reynolds (1982, 1985a, & 1985b). They discovered that dual-mode, dual-frequency forcing can produce a bifurcating jet (Fig. 1.1). The bifurcating jet occurs when the ratio, $\mathcal{R}_f$, of the axial to the helical frequency is exactly two. When $\mathcal{R}_f$ is non-integer between 1.6 and 3.2, the jet explodes into a shower of vortex rings (Fig. 1.2). Since this jet reminded them of flowers blooming, they named it the *blooming jet*.

The work of Lee & Reynolds involved mechanically-excited water jets in the Reynolds number range of 2,800 to 10,000. A diaphragm on the piston driving the flow provided a large amplitude axial excitation ($u'/U = 17\%$). The helical excitation was achieved by moving the tip of the nozzle in a circular orbit about the nominal jet centerline. The peak-to-peak displacement amplitude of the nozzle's tip was 4% of the jet diameter.

Lee & Reynolds (1985b) showed that bifurcating jets only occur within a range of Strouhal numbers (0.35–0.7). Over most of that range, the angle formed by the two branches of the jet increases with Strouhal number (Fig. 1.3). They also found that the mean velocity profile of a bifurcating jet has two peaks corresponding to the jet's two branches (Fig. 1.4). These two peaks remain separate and distinct up to 35 diameters from the jet exit. Their chemical reaction experiments demonstrated that the bifurcating jet, along with blooming jets, exhibits enhanced mixing relative to the natural jet.

This review has presented some of the past and present findings regarding the role of large scale structures in shear flows, the existence of instability modes in axisymmetric shear layers, and the characteristics of bifurcating and blooming jets. The rest of this chapter summarizes the objectives, approach, and results of the current work.

1.2 Objectives

Many important technological devices rely on jet flows to accomplish their purpose. Thus, the better we understand the fundamental physical processes in jet flows, the better we can design these devices. If we can dramatically alter the development and characteristics of these flows, we can move beyond making small improvements in devices to developing new generations of such devices.

The present work is part of several related but separate research projects aimed at furthering our understanding of how to control jet flows. The work of Bouchard and Reynolds (1982) focused on the effects of various types of axial forcing on the

growth and mixing in an axisymmetric shear layer. Lee and Reynolds (1985b) built on that work to demonstrate the effects of dual-mode forcing on the structure, mixing, and momentum of round turbulent jets. The present work extends the discoveries of Lee and Reynolds to high Reynolds numbers, considers the effects of various flow parameters, and develops a model for the instability mechanism in bifurcating jets. New studies recently initiated by Koch, Powell, and Reynolds and by Juvet and Reynolds will apply closed-loop control to jet flow manipulation and will explore new forcing and measurement techniques applicable to complex jet flows.

The present work had the following specific objectives:

1. To develop an understanding of the mechanisms causing bifurcation and blooming.
2. To develop a vortex-method code for simulating excited jet flows.
3. To produce bifurcating air jets at high Reynolds numbers by acoustic excitation.
4. To study the effects of Reynolds number, Strouhal number, and the amplitude and phase of the excitation signals on the large-scale characteristics of bifurcating jets.

1.3 Overview

The dominant presence and related arrangement of vortex structures in both the bifurcating and blooming jets suggest that the same mechanisms govern both bifurcating and blooming jets. While the blooming jet might prove to be the most useful in potential applications of dual-mode forcing, the bifurcating jet provides a better test case for studying the effects of various flow and excitation parameters. Unlike the blooming jet, the bifurcating jet occurs at only one value of $\mathcal{R}_f$. This simplifies our choice of this parameter. Additionally, since the bifurcating jet spreads in only one plane, it is more amenable to laser-sheet visualization.

The current study of bifurcating jets involves both computational and experimental research. The computational work focuses primarily on understanding

the governing mechanism and on determining the dependence of jet spreading on Strouhal number variations. The experimental work demonstrates the effectiveness of dual-mode acoustic forcing in generating bifurcating jets and considers the effects of Reynolds number, Strouhal number, and excitation amplitude and phase. Portions of the computational and experimental results have been reported by Parekh *et al.* (1983 & 1987), Leonard *et al.* (1985), and Parekh & Reynolds (1988).

The computational work includes developing a jet simulation program, carrying out a parametric study of bifurcating jets, and refining the numerical method. The fundamental algorithm of this code is based on the discrete-vortex method of Leonard (1980). Unlike typical finite-difference schemes, vortex methods are grid free and Lagrangian in nature. They focus on calculating the evolution of a given vorticity field. The velocity field is not calculated directly but is derived from the computed vorticity field. Our program is written in Fortran and executed on a Cray X-MP supercomputer. The refinements of this program consist of both improvements in the physical model and in the numerical method.

Since many potential applications of bifurcating jets could involve gas jets at higher Reynolds numbers, one of the first steps of the current experimental research was demonstration of the concept of dual-mode forcing in moderate-Reynolds-number air jets. A low-speed air jet apparatus using acoustic excitation was designed and built. The initial results with this apparatus included jets at Reynolds numbers of 10,000 and 20,000 which correspond to exit velocities of 7 and 14 m/s. The required excitation frequencies range from 80 to 400 Hz.

The next step in this experimental work was the design and fabrication of a high-speed air jet apparatus. Jets at Reynolds numbers up to 100,000 and Mach numbers, M, up to 0.22 were studied in this facility. The corresponding exit velocities and excitation frequencies range up to 75 m/s and 2000 Hz, respectively. A different acoustic excitation system was developed to provide the required high levels of acoustic power at these higher frequencies.

The experimental methods used included flow visualization, hot-wire anemometry, and condenser-microphone measurements. Since most of the questions of interest concern global features of the jet structure, flow visualization was the primary technique used. Additionally, flow visualization provides information that could not be obtained by velocity measurements. With flow visualization one can see the details and structure of the entire flow field in one instant of time. In some cases a picture is worth a thousand probes! The velocity and acoustic measurements provide information about the jet exit conditions and the amplitude and phase of the excitation.

1.4 Summary of Results

A combined numerical and experimental study of the effects of excitation frequency, amplitude, and phase on the development of moderate and high Reynolds numbers jets is described in the following chapters. Some of the primary conclusions of this work are

1. Dual-mode acoustic excitation can produce bifurcating jets in air at Reynolds numbers up to 100,000 and Mach numbers up to 0.22.
2. The bifurcation phenomenon can be modeled as an inviscid, vortex-interaction process. The axial excitation generates rings. The helical excitation displaces them. The array of vortex rings produced by the combination of these two excitations is unstable as a result of the rings' mutually induced motions.
3. Bifurcation occurs only within a range of Strouhal numbers. Within that range, the spreading angle increases with Strouhal number. The numerical simulations predict that range to be 0.30–0.42. However, the experiments show that the upper limit should be around 0.65.
4. The spreading angle increases with both excitation amplitudes. The results suggest that bifurcation does not occur below certain levels and that jet spreading does not continue to increase beyond certain limits. The bounds of this amplitude range could not be clearly defined.

Other conclusions along with recommendations for related research are presented in Chapter 7.

Chapter 2
NUMERICAL METHOD

The computational portion of this research was carried out concurrently with the last stages of the experimental work of Lee and Reynolds and was continued beyond the time of conclusion of their work. This timing provided a beneficial opportunity to enhance each project by joint sharing of insights and results. The work of Lee and Reynolds suggested that since vortex structures are such a dominant feature of bifurcating jets, the computations might be able to successfully simulate the large scale evolution of the jet by calculating the evolution of the vortex structures. Additionally, the calculations demonstrated the effects of some key parameters on the jet evolution. These effects were subsequently investigated experimentally. The results of the experiments of Lee and Reynolds and those of the computations provided valuable guidance in the planning of the high-Reynolds-number experiments described in later chapters.

The objective of the computational work was not to calculate a detailed velocity field for comparison with experiment. Rather, the objective was to determine the mechanism causing bifurcation and to estimate the effect of various parameters on the structure of the jet. Thus, a code was written and developed based on the discrete-vortex method, and this code was used to study the effects of excitation frequency and amplitude on the spreading of the bifurcating jet.

The discrete-vortex method is ideal for studying this type of flow as specified by the objectives noted above. Instead of a grid, the computational structure is the vortex elements of the flow. The basic approach taken here involves an analytical function to describe the source flow and discrete, computational vortex elements to represent the vortex rings formed at the jet exit. The flow is assumed to be inviscid and constant in density.

2.1 Discrete-vortex method

There are many different schemes that could be classified as discrete-vortex methods. The main similarities among them are that they discretize the vorticity field, calculate the evolution of the discrete vortex elements, and track the motion of these elements in a Lagrangian reference frame. One can derive an equation for the velocity field as a function of the vorticity field. The velocity field associated with a vortex element is often referred to as the "induced" velocity field. The motion of each vortex element is determined by the induced velocity due to itself and the other vortex elements. It is this mutual induction process that is the heart of the vortex method.

Since vortex methods typically assume an inviscid, constant-density fluid, they are ideal for handling high Reynolds number flows in which the vorticity is confined to small regions. By the theorems of Kelvin and Helmholtz, these assumptions require that the vortex elements move just as fluid elements (see Batchelor 1967). Thus, one can track the motion of fluid particles by simply tracking the motion of the discrete vortices. To mark the motion of fluid particles that are not in the vorticity containing regions of the flow, one can introduce passive particles in the simulation and track their motion.

Though vortex methods have not had the benefit of all the attention that finite-difference methods receive, many excellent researchers have succeeded in developing vortex methods into a useful numerical method for solving certain classes of complex fluid flows. For information on their work and on vortex methods in general, the reader should consult the excellent review articles by Saffman & Baker (1979) and by Leonard (1980 & 1985). A recent example of the application of vortex methods to a complex flow is the simulation of the three-dimensional evolution of a plane mixing layer by Ashurst & Meiburg (1988). They found that the streamwise vortical structures originate in the braid region between the larger spanwise structures of the mixing layer and that the initial evolution of these structures can be explained in terms of inviscid vortex dynamics.

The equation that defines the velocity induced by a vortex element is known as the Biot-Savart law for the velocity field. From the definition of vorticity,

$$\boldsymbol{\omega} \equiv \nabla \times \mathbf{u}, \tag{2.1}$$

and the constant-density continuity equation,

$$\nabla \cdot \mathbf{u} = 0, \tag{2.2}$$

one finds that

$$\nabla^2 \mathbf{u} = -\nabla \times \boldsymbol{\omega}. \tag{2.3}$$

Using the infinite medium Green's function for Eqn. 2.3, one obtains the Biot-Savart integral:

$$\mathbf{u}(\mathbf{x},t) = -\frac{1}{4\pi} \int \frac{(\mathbf{x}-\mathbf{x}') \times \boldsymbol{\omega}(\mathbf{x}',t)}{|\mathbf{x}-\mathbf{x}'|^3} \, d\mathbf{x}' + \nabla\phi, \tag{2.4}$$

where ϕ is the velocity potential that satisfies the inviscid boundary condition,

$$\mathbf{u} \cdot \mathbf{n}|_{surface} = 0. \tag{2.5}$$

Vector quantities are denoted by **bold face** type.

If the vortex element is a circular line filament of infinitesimal thickness, two difficulties arise. First, a logarithmic singularity in the induced velocity field exists along the filament. Second, due to self-induced motion, the filament propagates at infinite speed. To handle these difficulties, vortex methods typically use filaments whose vorticity is smoothed out within a finite core. This makes physical sense as well since vorticity is not concentrated on a line but spread out within a tube. True line vortices can only be approached in superfluids.

Numerically, each vortex filament is represented by a three-dimensional, periodic space curve, $\mathbf{r}_i(\xi,t)$, where i =1, 2, 3, ..., M (number of vortex elements), and ξ is a material coordinate on the curve. When a space curve is defined in terms of discrete points (or nodes) on the curve, one can choose ξ to be a discrete variable such as node number.

The use of discrete vortex filaments with finite cores leads to the following modified Biot-Savart integral which expresses the velocity, $\mathbf{u}$, induced at a point, $\mathbf{r}$, by all the vortex filaments in the flow:

$$\mathbf{u}(\mathbf{r}) = -\sum_j \frac{\Gamma_j}{4\pi} \int_{\mathbf{r}_j} \frac{[\mathbf{r} - \mathbf{r}_j(\xi',t)] \times \frac{\partial \mathbf{r}_j}{\partial \xi'}(\xi',t)}{[|\mathbf{r} - \mathbf{r}_j(\xi',t)|^2 + \alpha {\sigma_j}^2]^{3/2}} \, d\xi', \qquad 2.6$$

where Γ_j is the circulation of vortex filament $\mathbf{r}_j$, σ_j is the filament's core radius, and α is a free parameter. To calculate the motion of a point on a vortex filament, one uses the following similar equation:

$$\frac{\partial \mathbf{r}_i}{\partial t}(\xi,t) = -\sum_j \frac{\Gamma_j}{4\pi} \int_{\mathbf{r}_j} \frac{[\mathbf{r}(\xi,t) - \mathbf{r}_j(\xi',t)] \times \frac{\partial \mathbf{r}_j}{\partial \xi'}(\xi',t)}{[|\mathbf{r}(\xi,t) - \mathbf{r}_j(\xi',t)|^2 + \alpha({\sigma_i}^2 + {\sigma_j}^2)/2]^{3/2}} \, d\xi'. \qquad 2.7$$

Several different approaches to spreading the vorticity within the core have been reported in the literature. Each approach leads to a different form of the Biot-Savart integral. The approach that leads to Eqns. 2.6 and 2.7 is the Rosenhead-Moore approximation as described by Leonard (1980).

By choosing $\alpha = 0.413$, the self-induced velocity of a perfectly-circular ring filament equals that of a vortex ring with a Gaussian distribution of vorticity for $\sigma/R \ll 1$ (Leonard 1980). The nominal core radius, σ, is uniform along each filament. For an inviscid flow, the dynamics of the core is defined by

$$\frac{d}{dt}({\sigma_i}^2 L_i) = 0, \qquad 2.8$$

where $L_i(t)$ is the instantaneous length of filament i. This corresponds to a conservation of volume and results in the magnitude of the vorticity increasing when the vortex filament is stretched. Core dynamics and the parameter α are also discussed by Leonard (1980 & 1985).

2.2 Vortex filaments

The vortex filaments used in this simulation are three-dimensional rings. One way of representing a ring is by a set of straight segments connected end to end with a set of nodes corresponding to the points where two segments are connected. This approach permits one to simulate a ring that changes shape as well as size and position. The velocity induced by a multi-segment filament is determined by summing the contributions of each segment. The total induced velocity field is given by the sum of the velocities induced by all the filaments in the flow field.

Since the segments defining each filament are straight segments, one can integrate Eqn. 2.6 exactly to obtain an explicit expression for the velocity induced by any segment. The velocity induced at a point by the vortex vector defined by $\mathbf{r}_j(n+1,t) - \mathbf{r}_j(n,t)$ is given by

$$\mathbf{u}(\mathbf{r}) = -\frac{\Gamma_j}{4\pi}\left[\frac{(1-p)}{\sqrt{(1-p)^2+\lambda^2}} + \frac{p}{q}\right]\frac{[(\mathbf{r}-\mathbf{r}_j(n,t))\times\mathbf{e}]}{\lambda^2|\mathbf{e}|^3}, \qquad 2.9$$

where n is the node number of the tail of the vector and

$$\mathbf{e} \equiv \mathbf{r}_j(n+1,t) - \mathbf{r}_j(n,t), \qquad 2.10a$$

$$p \equiv \frac{\mathbf{e}\cdot(\mathbf{r}-\mathbf{r}_j(n,t))}{|\mathbf{e}|^2}, \qquad 2.10b$$

$$q \equiv \sqrt{\frac{|\mathbf{r}-\mathbf{r}_j(n,t)|^2 + \alpha{\sigma_j}^2}{|\mathbf{e}|^2}}, \qquad 2.10c$$

$$\lambda^2 \equiv q^2 - p^2. \qquad 2.10d$$

Thus, the velocity induced by all the vortex filaments is

$$\mathbf{u}(\mathbf{r}) = -\sum_j \frac{\Gamma_j}{4\pi}\sum_n\left[\left(\frac{(1-p)}{\sqrt{(1-p)^2+\lambda^2}} + \frac{p}{q}\right)\frac{[(\mathbf{r}-\mathbf{r}_j(n,t))\times\mathbf{e}]}{\lambda^2|\mathbf{e}|^3}\right]. \qquad 2.11$$

Another way to represent a ring is by a single circular filament that can change in size but not shape. This type of filament is useful in simulations of axisymmetric flows. Since the filament is assumed to remain circular, it can be specified in terms of its radius and streamwise position. By integrating Eqn. 2.6 along a circle of radius, R, one can obtain the exact velocity field of a circular filament with a finite core. This induced velocity is given by the following equations for the radial and streamwise components, u_r and u_z:

$$u_r(\bar{r},\bar{z}) = \frac{(\Gamma/R)\bar{z}}{2\pi\bar{r}\sqrt{\bar{\nu}+2\bar{r}}}\left[\frac{1}{(1-\bar{\eta})}E(1-m_1) - K(1-m_1)\right], \qquad 2.12a$$

and

$$u_z(\bar{r},\bar{z}) = \frac{(\Gamma/R)}{\pi\bar{\nu}^{3/2}\sqrt{1+\bar{\eta}}}\left[\frac{(1-\frac{\bar{\nu}}{2})}{(1-\bar{\eta})}E(1-m_1) + \frac{\bar{\nu}}{2}K(1-m_1)\right], \qquad 2.12b$$

where

$$\bar{r} \equiv \frac{r}{R}, \qquad 2.13a$$

$$\bar{z} \equiv \frac{z}{R}, \qquad 2.13b$$

$$\bar{\sigma} \equiv \frac{\sigma}{R}, \qquad 2.13c$$

$$\bar{\nu} \equiv 1 + \bar{r}^2 + \bar{z}^2 + \alpha\bar{\sigma}^2, \qquad 2.13d$$

$$\bar{\eta} \equiv \frac{2\bar{r}}{\bar{\nu}}, \qquad 2.13e$$

$$m_1 = 1 - \frac{(1-\bar{\eta})}{(1+\bar{\eta})}, \qquad 2.13f$$

and $E(m)$ and $K(m)$ are complete elliptic integrals of the first and second kind, respectively. For definitions of $E(m)$ and $K(m)$, see Eqn. A.7.

The exact solution for a circular filament, Eqn. 2.12, provides a useful means of checking the accuracy of the multi-segment representation of filaments, Eqn. 2.11. When computing u_r by Eqn. 2.12a, one encounters a numerical singularity at $\bar{r} = 0$. This difficulty can be handled by treating that case as an exception and using the exact solution, $u_r(0,\bar{z}) = 0$. The details of the derivations of Eqns. 2.9 and 2.12, along with polynomial approximations of $E(m)$ and $K(m)$, are given in Appendix A.

2.3 Jet velocity function

The simulation of a jet flow is incomplete without some means to account for the jet source flow. The filaments only represent the vortex structures formed by shear layer instabilities. However, by applying the Biot-Savart integral, Eqn. 2.6, to a semi-infinite, cylindrical vortex sheet of finite thickness (Fig. 2.1), one can derive an explicit function to define the mean jet flow. This function is referred to as the "jet velocity function" and takes the following form:

$$u_r(\bar{r},\bar{z}) = \frac{\gamma}{2\pi\sqrt{\bar{\nu}}} I(\bar{\eta}), \tag{2.14a}$$

and

$$u_z(\bar{r},\bar{z}) = \frac{\gamma}{2\pi\bar{\rho}}\left\{\frac{\pi}{2}\left[\frac{(2-\bar{\rho})}{\sqrt{1-\bar{\mu}^2}}+\bar{\rho}\right] - \frac{\bar{z}}{\sqrt{\bar{\nu}}}\left[\frac{2}{\sqrt{1+\bar{\eta}}}K(1-m_1)+(\bar{\mu}-\bar{r})\,T(\bar{\mu},\bar{\eta})\right]\right\}, \tag{2.14b}$$

where

$$\bar{\rho} \equiv 1+\bar{r}^2+\alpha\bar{\sigma}^2, \tag{2.15a}$$

$$\bar{\mu} \equiv \frac{2\bar{r}}{\bar{\rho}}, \tag{2.15b}$$

$$I(\bar{\eta}) \equiv \int_0^{\pi} \frac{\cos\theta}{\sqrt{1-\bar{\eta}\cos\theta}}\,d\theta, \tag{2.15c}$$

$$T(\bar{\mu},\bar{\eta}) \equiv \int_0^{\pi} \frac{\cos\theta}{(1-\bar{\mu}\cos\theta)\sqrt{1-\bar{\eta}\cos\theta}}\,d\theta. \tag{2.15d}$$

The variables $\bar{r}$, $\bar{z}$, $\bar{\sigma}$, $\bar{\nu}$, $\bar{\eta}$, and m_1 were previously defined in Eqn. 2.13. The parameter γ is the circulation per unit length of the cylindrical vortex sheet. The details of the derivation of Eqn. 2.14 are presented in Appendix A.

The expression for the jet velocity function contains two definite integrals, $I(\bar{\eta})$ and $T(\bar{\mu},\bar{\eta})$. It is shown in Appendix A that the definite integral $I(\bar{\eta})$ can be expressed as elliptic integrals as follows:

$$I(\bar{\eta}) = \frac{2}{\bar{\eta}\sqrt{1+\bar{\eta}}}[K(1-m_1)-(1+\bar{\eta})\,E(1-m_1)]. \tag{2.16}$$

This expression contains a numerical singularity at $\eta = 0$. This difficulty can be handled by replacing $I(\bar{\eta})$ by $T(0, \bar{\eta})$ for $\bar{\eta} \ll 1$. The integral $T(\bar{\mu}, \bar{\eta})$, however, must be evaluated numerically.

An adaptive integration scheme based on the fourth-order Newton-Cotes method was developed especially for evaluating $T(\bar{\mu}, \bar{\eta})$. The adaptive scheme makes use of two facts concerning the integrand. First, when $\bar{\mu}$ and $\bar{\eta} \to 0$, the integrand becomes antisymmetric about $\pi/2$, and $T(\bar{\mu}, \bar{\eta}) \to 0$. Second, as $\bar{\mu}$ or $\bar{\eta} \to 1$, the integrand approaches infinity for $\theta \ll 1$. Thus, the integration scheme distributes subintervals symmetrically about $\pi/2$, and the size of the subintervals become smaller and smaller near the limits of integration as $\bar{\mu}$ or $\bar{\eta} \to 1$. By distributing the subintervals in this way, one calculates exactly zero when $\bar{\mu}$ and $\bar{\eta} = 0$, and the computation cost is kept low while maintaining a specified accuracy even when $\bar{\mu}$ or $\bar{\eta} \to 1$.

The fourth-order Newton-Cotes method assumes that the interval of integration is divided into sets of four equally-sized subintervals. The partial integral Q over one set of subintervals is found from the following equation:

$$Q_i^{i+4} = \frac{h_i}{45}[14f_i + 64f_{i+1} + 24f_{i+2} + 64f_{i+3} + 14f_{i+4}], \qquad 2.17$$

where h_i is the size of the subintervals and f_i is the value of the integrand at θ_i.

To make the method adaptive, the size of the subintervals are chosen according to the following relations:

$$h_i = \begin{cases} 2^0 h_0, & \text{for } i = 0, 1, 2, \ldots, 7; \\ 2^1 h_0, & \text{for } i = 8, 9, 10, 11; \\ 2^2 h_0, & \text{for } i = 12, 13, 14, 15; \\ \vdots, & \text{for } i \geq 16. \end{cases} \qquad 2.18$$

while $\theta_i < \pi/2$. The size of the remaining subintervals are specified by requiring all the subintervals to be symmetric about $\theta = \pi/2$. The size of the smallest subinterval, h_0, is chosen to be

$$h_0 = \frac{\pi}{2^k}, \qquad 2.19$$

where $k = [\text{integer part of } (3 + 6\bar{\mu} + 3\bar{\eta})]$. This adaptive procedure for choosing the size and number of subintervals is simple to implement and keeps the relative

total error of the integration below 0.001% as long as $\bar{\sigma} > 0.01$. One can show that $T(\bar{\mu}, \bar{\eta})$ is bounded for all values of $\bar{\mu}$ and $\bar{\eta}$ if and only if $\bar{\sigma} > 0$ since $0 \leq \bar{\eta} \leq \bar{\mu} < 1$ only for $\bar{\sigma} > 0$.

The semi-infinite sheet of vorticity extends from $-\infty$ to the origin (Fig. 2.1). Its axis defines the jet centerline, and the end of the sheet defines the jet exit. The helical excitation used in the experiments of Lee and

Reynolds (1985b) is modeled by rotating the axis of the vortex cylinder about the nominal jet centerline. The displacement, A_h, of the jet centerline from the nominal centerline corresponds to the amplitude of excitation, and $\bar{A}_h \equiv A_h/R$. The rotation frequency is given by:

$$f_h = \frac{f_a}{\mathcal{R}_f}, \tag{2.20}$$

where

$$f_a = St_a \frac{\gamma}{D}, \tag{2.21}$$

The frequency f_a is the rate at which filaments are generated at the origin.

The interaction of the vortex sheet with the filaments is assumed to be such that the sheet influences the motion of the filaments but the filaments do not influence the sheet. The velocities induced by each filament and by the jet function are superimposed to determine the trajectory of each filament. The sheet, however, is constrained to remain cylindrical and is not moved by the filaments since the cylindrical sheet corresponds to a mean flow whose centerline is determined solely by the position of a physical nozzle.

2.4 Algorithm

The numerical algorithm is a straightforward implementation of the concepts discussed in the previous sections. A schematic of this algorithm is given in Fig. 2.2. The excitation and time integration parameters are initialized, and the first filament is created at the origin. Subsequent filaments are created as specified by the Strouhal number.

The circulation of each filament is identical and is determined from circulation conservation constraints. Assuming the thickness of the cylindrical sheet to be much smaller than its radius, the vorticity flux (per unit of circumference) within the sheet through any plane perpendicular to the jet's axis is given by $U^2/2$. By the assumption of a perfect fluid, the vorticity convected from the cylindrical sheet must equal the vorticity convected by the discrete filaments. This conservation relation can be expressed in terms of Γ and γ as

$$\frac{\Gamma}{\Delta t} = \frac{\gamma^2}{2}, \tag{2.22}$$

where Γ is the circulation of each ring filament, γ is the circulation per unit length of the cylindrical vortex sheet, and Δt is the time between generation of ring filaments. By Eqns. 2.21 and 2.22, one obtains

$$\gamma = St_a \frac{\Gamma}{R}. \tag{2.23}$$

At each time step the velocity at each node due to the combined effects of the jet function and the vortex segments is calculated at the beginning and in the middle of the time step. The velocities are computed from Eqns. 2.9 and 2.14. These velocities are used by the second-order, Runge-Kutta method to determine the solution at the next time step as follows

$$\mathbf{x}^\star = \mathbf{x}^j + \frac{\delta t}{2}\mathbf{u}^j, \tag{2.24a}$$

$$\mathbf{x}^{j+1} = \mathbf{x}^j + \delta t\, \mathbf{u}^\star, \tag{2.24b}$$

where $\mathbf{x}^j$ and $\mathbf{u}^j$ denote a node's position and velocity at time t_j, and δt is the time increment between time steps and is typically an order of magnitude smaller than Δt. The new position of the cylindrical vortex sheet is determined on the basis of the excitation amplitude and frequency and the time step.

To keep the algorithm simple and to eliminate the unknown effects of various numerical refinements, the initial calculations constrained the vortex cores to remain constant in time and did not incorporate any nodal redistribution. When filaments

are far apart, their interaction is essentially independent of σ though their self-induced velocity is not. The effect of varying σ to satisfy Eqn. 2.8 is studied in the multi-filament shear layer discussed in Sec. 2.5.1.

A program implementing this algorithm was written in Fortran for execution on the Cray X-MP. By properly structuring the iterative loops in the code, the vectorization capabilities of the Cray are enabled. A complete listing of this code, named BIJET, is given in Appendix B. Because of the nature of the mutual induction process, the cost of the simulation is proportional to the square of the number of segments.

2.5 Refinements

Several refinements to the numerical scheme described in the earlier sections were developed and tested. These refinements were motivated by the desire to understand the discrepancies between experimental results and the computational results described in the next section. Additionally, these refinements improve the method in general and give indications of the errors resulting from various assumptions regarding the vortex filaments.

Three areas of refinement are described in this section. First, instead of simply creating ring filaments to represent discrete vortex rings, the formation of the vortex rings is simulated by discretizing the shear layer. Second, non-uniformities in vorticity distribution within a filament are considered by using multiple filaments to represent each physical vortex ring. Finally, a numerical scheme based on cubic splines rather than linear segments is developed to improve the accuracy and decrease the cost of the computation.

Each of these refinements was developed and tested as independent problems. In most cases the algorithms and results were brought to the point where they could be implemented in the jet simulation code. However, these refinements were not so implemented because the initial numerical work was adequate to answer most of the key questions regarding the instability mechanism in bifurcating jets and because

the objectives of this project dictated that a complementary experiment at high Reynolds numbers also be planned and executed.

2.5.1 Multi-filament shear layer

The axisymmetric shear layer issuing from a round jet is a continuous distribution of vorticity. The instability of the shear layer amplifies even very small perturbations such that vorticity concentrates in discrete physical vortex rings. Axial forcing can control this ring formation process. The numerical scheme previously described approximates this process by periodically introducing a numerical ring filament at the jet origin. However, since the formation process is not modeled, the initial size and location of a ring filament and the size of its core can only be loosely approximated. To enhance our understanding of the effects of axial and helical forcing on a ring's formation, the scheme was modified to simulate shear layer dynamics.

To model the evolution of a shear layer with a vortex method, one must use many closely-spaced filaments. When the computational filaments are used to represent discrete portions of the shear layer rather than discrete vortex rings, the effect of the axial excitation can no longer be assumed. The numerical scheme must include some means of simulating the axial forcing. This is achieved by pulsing the mean flow by sinusoidally varying γ, such that

$$\gamma(t) = [1 + \bar{A}_a \cos(2\pi f_a t)]\tilde{\gamma}, \qquad 2.25$$

where $\tilde{\gamma}$ is the time-averaged circulation and $\bar{A}_a$ is the perturbation amplitude. Correspondingly, the filaments also vary in circulation.

Three different ways of specifying the circulation, Γ_i, of each filament are used. All of these methods are based on the circulation matching principle of Eqn. 2.22. The first method, referred to as *quadrature matching*, uses the value of γ at the instant filament i is generated to calculate Γ_i. Thus,

$$\Gamma_i = [1 + \bar{A}_a \cos(2\pi f_a t_i)]^2 \Delta t \frac{\tilde{\gamma}^2}{2}, \qquad 2.26$$

where t_i is the time when filament i is generated and Δt is the reciprocal of the filament formation frequency. This method approximates $\int_{t_i}^{t_{i+1}} \gamma(t)\, dt$ by simple quadrature.

The second method, *integral matching*, evaluates the integral exactly over the time interval associated with the filament creation, such that

$$\Gamma_i = \left\{ \left(1 + \frac{A_a^2}{2}\right) \Delta t + \frac{A_a}{\pi f_a}[\sin(2\pi f_a t_{i+1}) - \sin(2\pi f_a t_i)] + \frac{A_a^2}{8\pi f_a}[\sin(4\pi f_a t_{i+1}) - \sin(4\pi f_a t_i)] \right\} \frac{\tilde{\gamma}^2}{2}. \tag{2.27}$$

The third method, *growth matching*, is identical to the second method in determining Γ_i but differs in the temporal assignment of that value. The first two methods assign circulation Γ_i to filament i at the instant of its creation. The third method initially assigns zero circulation and increases the circulation by equal increments over successive time steps. Filament i attains its final value of circulation when filament $i + 1$ is created.

When simulating axisymmetric shear layers, the speed and accuracy of the method can be significantly improved. Instead of using filaments made up of numerous segments, one can use circular filaments. The exact solution for the velocity field induced by these filaments can be solved analytically and was presented earlier in Sec. 2.2. With the circular filaments one only has to keep track of their radius and streamwise location. The code AXLAYER, listed in Appendix B, is an implementation of this idea. When modeling a helically-excited shear layer, however, one can no longer use these circular filaments since the filaments must be allowed to deform in three dimensions.

The significance of changes in core size due to vortex stretching was also considered in the simulations of an axisymmetric jet. In one case the core sizes remained constant in time. In the other case they varied in time according to Eqn. 2.8. These changes in core sizes due to vortex stretching do not occur in two-dimensional flows.

2.5.2 Multi-filament vortex ring

It is not clear how a vortex ring forms when the shear layer is perturbed helically. One might expect that the initial ring formation results in azimuthal variations in the size of the vortex core. However, those asymmetries might be quickly smoothed out by azimuthal flow within the vortex. This smoothing process has been proposed by Moore and Saffman (1972).

If one were to use only a single filament with a spatial variation in core size, linear impulse would not be conserved. Therefore, to model a vortex ring with a spatially varying core size, one must modify Eqn. 2.6 to allow for flow within a filament or use multiple filaments. In this work, multiple filaments having azimuthally uniform cores are combined. The relative orientations of these filaments define the shape and core characteristics of the vortex ring.

This multiple-filament approach was used to simulate the evolution of non-uniform-core vortices. In one case, the evolution of a pair of rings initially positioned side by side is considered. In the other case, a pair of eccentric rings are studied. This configuration is similar to the arrangement of adjacent rings in the near-field region of a bifurcating jet.

2.5.3 Spline approximation

When representing a single arbitrary vortex filament by a set of linear segments, one makes several approximations. The linear segments can only approximately represent the shape of the filament. Additionally, by using linear segments, one makes an error in calculating the local induction of the filament. Local induction refers to the velocity induced at a point on a filament as a result of the filament's curvature near that point. From Eqn. 2.9, it is evident that every pair of adjacent linear segments induces no velocity on the node between them. Errors in representing the shape of the filament and in estimating the local induction decrease as the number of segments becomes large.

These approximations are improved by using a periodic cubic spline instead of linear segments. A set of points on the filament defines the spline. Assuming unity

intervals, one obtains the system of equations

$$\frac{1}{6}[\mathbf{f}''_{i-1} + 4\mathbf{f}''_i + \mathbf{f}''_{i+1}] = \mathbf{x}_{i-1} - 2\mathbf{x}_i + \mathbf{x}_{i+1}, \qquad 2.28$$

where $\mathbf{x}_i$ denotes the spatial position of node i, $\mathbf{f}''_i$ is the second derivative with respect to the parameter ξ of the spline function, and i =1, 2, ..., N (number of nodes per filament). The spline in turn defines the local derivative $\partial \mathbf{r}_j / \partial \xi'$ in Eqn. 2.6 to be $\mathbf{f}'$ where $\mathbf{f}'$ is given by

$$\mathbf{f}'_i = \mathbf{x}_{i+1} - \mathbf{x}_i - \frac{1}{6}[\mathbf{f}''_{i+1} + 2\mathbf{f}''_i]. \qquad 2.29$$

This estimate of the local derivative is used with the trapezoid rule to solve Eqn. 2.6.

The implementation of this method is both straight forward and convenient. The technique of LDU decomposition can be used to solve Eqn. 2.28, and if N remains constant, the factorization needs to be performed only once. The method's convenience becomes apparent when solving Eqn. 2.6 for a system of filaments. Since the trapezoid rule is used, Eqn. 2.6 can be simplified to a single summation over all the nodes. This simplifies the bookkeeping since one does not need to keep track of neighboring nodes as in the multi-segment scheme (see Eqn. 2.9).

For the same number of nodes, the spline approach does a better job of approximating the shape of an arbitrary filament than does the multi-segment scheme. The spline method also includes the effect of the local induction rather than neglecting it. The tradeoff is that the velocity induced by the spline must be calculated by quadrature, whereas the induced velocity of linear segments is specified exactly by Eqn. 2.9. This tradeoff is not a penalty since quadrature is computationally cheaper than evaluating Eqn. 2.9. An example of the spline approach is provided by the code SIVSPLINE, which calculates the self-induced velocity of a ring filament. This code is included with the other program listings in Appendix B.

Chapter 3

NUMERICAL RESULTS

The computational portion of this work involved development of a new discrete-vortex code, simulations of vortex interactions and bifurcating jets, and refinements of the numerical scheme. The principles underlying this code were presented in the previous chapter. Validation tests were performed to test the accuracy of different portions of the program, and the results of these tests are given in Section 3.1. To test the code as a whole, some simple vortex interactions were simulated. These interactions, described in Section 3.2, involved vortex pairing, collision, and separation, and discrete axisymmetric shear layers.

The main results of the computational work are detailed in the remainder of this chapter. Section 3.2 considers the momentum of a finite train of rings in an attempt to estimate ring spacing and bifurcation angle in bifurcating jets. Section 3.4 presents the simulation of the bifurcating jet at different excitation amplitudes and frequencies. The other sections all deal with refinements to the basic numerical approach and method. In Section 3.5, an axially-excited shear layer is modeled with discrete vortex rings. In Section 3.6, multiple computational filaments are used to represent vortex rings with non-uniform cores. Finally, Section 3.7 demonstrates the significant improvements of the spline-based scheme over the standard linear-interpolation approach.

All the simulations in this study were performed on the computer facilities at NASA Ames Research Center. The code was developed on a VAX 11/780, and the simulations were carried out on the Cray X-MP. Various graphics packages were used to provide plots, slides, and movies of the results.

3.1 Validation of code

Since the entire program consists of entirely new code, some basic validation tests were performed prior to simulating jet flows. These tests consisted of comparisons

between computed and theoretical vortex ring velocity fields. These comparisons provide a check of the code's main part, the subroutine that calculates induced velocities. Additional tests concerned numerical parameters. Different numbers of nodes were used to represent each vortex filament, and different time intervals were considered.

Unlike a point vortex, a vortex ring has a self-induced velocity. This velocity depends on the ratio of the core radius, σ, to the ring radius, R, and on the vorticity distribution within the core. For $\sigma/R \ll 1$, the self-induced velocity, u_s, of a filament with a finite, constant-vorticity core is (Lamb 1932)

$$u_s = \frac{\Gamma}{4\pi R}\left[\ln\left(\frac{8R}{\sigma}\right) - \frac{1}{4}\right]. \qquad 3.1$$

For a ring with a Gaussian distribution of vorticity, the corresponding expression is (Saffman 1970)

$$u_s = \frac{\Gamma}{4\pi R}\left[\ln\left(\frac{8R}{\sigma}\right) - 0.558\right]. \qquad 3.2$$

One can also evaluate the ring speed by evaluating Eqn. 2.12 at $(\bar{r}, \bar{z}) = (1, 0)$. The constant α in this expression is set to 0.413 to match the ring speed of a Gaussian ring as specified by Eqn. 3.2. For $\sigma/R \ll 1$, Eqns. 2.12 and 3.2 predict ring speeds that are identical to three significant figures. The advantage of using Eqn. 2.12 is that the actual vorticity distribution within the core is identical to the computational filaments composed of multiple segments.

Figure 3.1 compares the self-induced velocity of a ring filament having varying number of linear segments with the theoretical self-induced velocity of a circular filament. Since adjacent nodes define a segment on the periodic filament, the number of nodes and segments are identical. The calculated self-induced velocity asymptotically approaches the theoretical velocity as the number of segments is increased. Ideally, one would use a very large number of segments for the sake of accuracy. However, because the cost of the calculation goes like the square of the number of segments, a compromise must be made. For the bifurcating jet simulations, 32 nodes define each ring filament. With 32 nodes, the calculated self-induced velocity is 21.5% lower than the theoretical value.

Another test to determine an adequate number of nodes is to compare the velocity fields of a multi-segment ring with that of a circular filament. The velocity field of the circular filament is given by Eqn. 2.12 and is presented in Fig. 3.2. The velocity field of the multi-segment ring is very similar. The velocity field within and around the filament core of a circular filament is presented in Fig. 3.3. The fluid within the core appears to be in almost solid-body rotation. The velocity at the core's center corresponds to the self-induced ring velocity. The peak velocity essentially defines the edge of the core. From this plot it is evident that the core parameter $\bar{\sigma}$ provides only a nominal value of the core radius. In this case $\bar{\sigma} = 0.1$ while the actual core radius is 0.04.

Along with the calculation of filament velocities, the velocity field of the jet function was also tested. A cylindrical vortex sheet of infinite length and infinitesimal thickness has uniform axial velocity within the sheet and zero velocity outside the sheet. Thus, one would expect the semi-infinite sheet depicted in Fig. 2.1 to have similar characteristics for $z \ll 0$. The velocity profiles in Fig. 3.4 substantiate this expectation. Since the semi-infinite sheet has finite thickness, 2σ, there is also a velocity gradient within the sheet (Fig. 3.5). In Fig. 3.5, the nominal radius of the cylindrical sheet equals 1.

The flow from a semi-infinite cylindrical vortex sheet (Fig. 3.6) is similar to that of an inviscid jet issuing from a hole in a wall. However, because of the finite thickness of the sheet, there is some flow through the "wall" defined by $\bar{z} = 0$ and $\bar{r} > 1$. The amount of flow through the wall decreases as the sheet thickness is decreased. The velocity fields of vortex sheets of differing thicknesses are essentially identical except in the region of $\bar{z} = 0$ and $\bar{r} = 1$ (Fig. 3.7). If the vortex sheet were defined to have zero thickness, there would be zero through-flow, but there would also be a singularity at $\bar{z} = 0$ and $\bar{r} = 1$.

3.2 Simulation of simple vortex interactions

The previous section described checks of different components and parameters of the code. The simple vortex interactions considered in this section provide a

check of the code as a whole. All but the last case involve the interaction of only two vortex rings. The simulation of these interactions are documented in the 16 mm, computer-generated film entitled "The Propagation and Interaction of Inviscid Vortex Rings." Copies of this film are also available on VHS video tape.

In axisymmetric shear flows, vortex rings are often observed to combine to form larger rings through a pairing process. One ring accelerates into the ring immediately downstream from it and passes through it prior to merging with it. As the rings near each other, the downstream ring increases in radius and slows down while the upstream one decreases in radius and moves faster. In certain cases of two impulsively started rings, the rings pass through each other a few times prior to combining (Oshima & Kuwahara 1984). This is often referred to as leapfrogging.

This leapfrogging process is the first vortex interaction simulated. Two identical, concentric rings with thin cores are initially positioned one radius apart and then allowed to propagate and interact. The rings leapfrog through each other indefinitely, and their relative motion is exactly periodic.

The second test case involves two identical, concentric rings colliding with each other. As they near each other, their velocities decrease. When they are very close, they slow down tremendously while rapidly expanding in size. These features are similar to those observed in the experiments of Oshima (1978). One could also relate this simulation to a ring impinging on a wall. In this case the two rings would represent the physical ring and its image.

The third case focuses on two identical, concentric rings that move away from each other. This could represent a vortex ring moving away from a wall. The rings initially shrink in size. Eventually, they move far enough apart that their mutually induced velocities are small. At that point their propagation is essentially due only to their self-induced velocities.

Finally, an unforced, axisymmetric shear layer is modeled by discrete vortex filaments. Filaments are created periodically at the origin of the system such that they are initially close to each other. The nominal core radius, $\bar{\sigma}$, is 0.1. No regular nor random perturbations are introduced, and the jet function is not used. The

growth and development of this discrete shear layer is presented in Fig. 3.8. The small circular marker shows the origin of the system. Several diameters downstream from the origin, the filaments bunch together to form, large, distinct structures. This case provided a guide for choosing an adequately small time step. When the time step is too large, a numerical instability results in the azimuthal variations seen on certain rings in Fig. 3.9. These wiggles are completely removed by simply reducing the time step, $\delta\bar{t}$, from 0.1 to 0.025, where $\delta\bar{t} = \delta t\,\Gamma/R^2$. The value of $\delta\bar{t}$ used in the bifurcating jet simulations (Sec. 3.4) was typically less than 0.006.

3.3 Analysis of a finite train of rings

In this section the velocity field of a finite train of coaxial, equally-spaced vortex rings is considered in an attempt to gain insights related to the ring spacing and bifurcation angle of bifurcating jets. The positions of the rings are fixed in time, and all the analyses focus on the ring in the middle of the train of rings. The primary parameter, $\bar{s}$, in this analysis is the distance between rings normalized by the radius of the rings. The rings are represented by circular filaments whose velocity fields are specified by Eqn. 2.12. The average flow quantities are obtained by trapezoid-rule integration over the region, $-\bar{s}/2 \leq \bar{z} \leq \bar{s}/2$.

The streamwise velocity induced by all the rings on the central ring is defined as the convection velocity $\bar{u}_c$, where $\bar{u}_c = u_c R/\Gamma$. From the definition of St,

$$St = \frac{(u_c/s)(2R)}{(\Gamma/s)}, \tag{3.3}$$

which can be simplified to

$$St = 2\bar{u}_c. \tag{3.4}$$

The dependence of $\bar{u}_c$ on $\bar{s}$ for three different values of $\bar{\sigma}$ is plotted in Fig. 3.10. The number of vortex rings, N_v, used in this calculation is 41. For $\bar{s} \gg 1$, $\bar{u}_c$ asymptotically approaches the self-induced velocity of a single ring.

One can use calculations of $\bar{u}_c$ to estimate the relative spacing of rings in the bifurcating jet. In a bifurcating jet, the vortex passing frequency, f_j of the large

rings upstream of the bifurcation region is twice the frequency, f_b, of the rings on the jet's two branches. Thus, the ratio, $\mathcal{R}_s$, of the distance between rings can be estimated as follows:

$$\mathcal{R}_s \equiv \frac{\bar{s}_b}{\bar{s}_j} = 2\frac{\bar{u}_{c_b}}{\bar{u}_{c_j}}. \qquad 3.5$$

For a given $\bar{s}_j$, this equation must be solved iteratively to determine the correct value of $\bar{s}_b$. For $\bar{s}_j = 2.0$, $\mathcal{R}_s$ decreases from 1.71 to 1.60 as $\bar{\sigma}$ increases from 0.10 to 0.50. For $\bar{\sigma} = 0.1$, $\mathcal{R}_s$ increases from 1.64 to 1.78 as $\bar{s}_j$ increases from 1.60 to 2.40, and for $\bar{\sigma} = 0.3$, $\mathcal{R}_s$ increases from 1.57 to 1.71 as $\bar{s}_j$ increases from 1.60 to 2.40. Thus, for a wide range of $\bar{s}_j$ and $\bar{\sigma}$, $\mathcal{R}_s$ falls in the narrow range of 1.6 to 1.7. This important result will be discussed further in Section 6.5.

The effect of the number of rings and the ring spacing on the instantaneous and mean velocity profiles is presented in Figs. 3.11 and 3.12. The shapes of the profiles are similar, but the velocity magnitudes are lower by a few percent for $N_v = 5$ compared to those for $N_v = 41$. For a given value of N_v, the velocity profiles are essentially self-similar when plotted in terms of us/Γ.

If one assumes that the branches of the bifurcating jet behave as two independent jets whose momentum fluxes approximately equal those of a finite train of rings with the same ring spacing, one can attempt to obtain a bifurcation angle from a momentum balance. The axial momentum flux of a single branch is given by $< \int\int \rho u_b^2 \, dA > \cos(\beta/2)$, where ρ is the fluid's density, u_b is the velocity along the branch, $\beta/2$ is the angle between the jet's centerline and the axis of the branch, and $< >$ denotes a spatial average in the direction of the branch axis. For a constant-density bifurcating jet, the resulting equation for the bifurcation angle, β, is

$$\beta = 2\cos^{-1}\left(\frac{< \int\int u_j^2 \, dA >}{2 < \int\int u_b^2 \, dA >}\right), \qquad 3.6$$

where u_j is the axial velocity of the jet upstream of the bifurcation region. The calculated axial momentum flux, F, corresponding to different values of $\bar{s}$ and $\bar{\sigma}$ are presented in Fig. 3.13, where $F = < \int\int u^2 \, dA > /\Gamma^2$ and u is the velocity component

parallel to the axis of the train of rings. Using the jet exit conditions and Eqn. 2.23 and ignoring the increase in momentum flux due to axial forcing, one obtains

$$< \int\int u_j^2 \, dA >= \pi St^2 \Gamma^2. \tag{3.7}$$

By Eqns. 3.4, 3.6, and 3.7,

$$\beta = 2\cos^{-1}\left(\frac{2\pi \bar{u}_c^2(\bar{\sigma}, \bar{s}_j)}{F(\bar{\sigma}, \bar{s}_b)}\right). \tag{3.8}$$

For all values of $\bar{\sigma}$ and $\bar{s}_j$ considered, the argument of $\cos^{-1}$ in Eqn. 3.8 is greater than unity. This is true even if the numerator in Eqn. 3.8 is replaced by $F(\bar{\sigma}, \bar{s}_j)$. Thus, while the analysis presented in this section can provide a useful estimate of relative ring spacings in a bifurcating jet, it is inadequate to provide any insight regarding the bifurcation angle. In spite of this inadequacy, the momentum analysis has been included here for the sake of completeness and as additional justification for the more complex approach presented in the next section.

3.4 Simulation of bifurcating jet

The bifurcating jet simulations examine the effects of physical parameters as well as modifications of the numerical model. The physical parameters are the axial Strouhal number, St_a, and the helical excitation amplitude, $\bar{A}_h$. To consider the effects of the cylindrical vortex sheet, some simulations are run without the sheet. Additionally, both helical and flapping excitations are considered. The helical excitation is achieved by moving the cylindrical sheet in a circular orbit of radius A_h about the nominal centerline of the jet. The flapping excitation is achieved by moving the sheet sinusoidally back and forth along a line passing through the nominal jet center. The half-length of that line is also referred to as A_h.

The code BIJET, listed in Appendix B, was used to simulate the bifurcating jet. This code includes the jet function to model the source flow and discrete vortex filaments to represent the vortex rings. Each vortex filament is composed

of 32 piecewise-linear segments of vorticity. The nominal core radius, $\bar{\sigma}$, of each ring is 0.1. This value was chosen based on an order-of-magnitude estimate of the core sizes of the physical vortex rings. Variations of core size in the range of 0.03-0.10 have little or no effect on the spreading angle of the bifurcating jet. The nominal thickness of the cylindrical vortex sheet is 0.2 times the ring radius. The non-dimensional time step, $\delta\bar{t}$, is typically less than 0.006. Unless otherwise specified, the cylindrical sheet is included, and a helical mode of excitation is used. To simulate the bifurcating jet, the excitation frequency ratio, $\mathcal{R}_f$, is exactly two in all cases. Twenty different cases were simulated, and the parameters corresponding to these cases are tabulated in Appendix C.

The initial positions of the filaments are staggered to correspond to the excitation. One might wonder whether the staggering is sufficient to produce a bifurcating train of rings, or whether the source flow is required. Figure 3.14 compares two simulations in which one has no source flow. Both vortex trains exhibit a bifurcation pattern, but the one with the source flow has a bifurcation angle of 27° in contrast to an angle of 16° for the other case. The ***bifurcation angle*** is determined by measuring the angle between the centerlines of the two trains of rings. Each of the cases noted in Table C.1 include the source flow.

It is important to note that the relative phase of the axial excitation is more important than the exact type of transverse forcing. Whether the transverse forcing employs a helical or flapping motion, the bifurcating jet is produced. However, the relative phase between filament generation and helical excitation determines the diametrical plane in which the jet bifurcates. If a flapping excitation is adopted and if each new filament is generated when the cylindrical sheet has no displacement, the jet behaves essentially as a natural jet.

Unlike the physical flow, large levels of excitation are required to produce bifurcating jets in the simulation. Figure 3.15 compares two jets at the same Strouhal number ($St_1 = 0.3$) and at different excitation levels ($A_h = 0.1$ and 0.5). At $A_h = 0.1$, the rings are eccentric, but the jet does not bifurcate at all. The tangle of vortex filaments is due to the interaction of two eccentric rings. At $A_h = 0.5$, the

jet splits into two distinct jets. A similar comparison at $St_a = 0.35$ and $A_h = 0.3$ and 0.5 is given in Fig. 3.16. The jet at $A_h = 0.3$ is presented one axial excitation period later than the jet at $A_h = 0.5$. The jets appear very similar, and both exhibit a bifurcation angle of 34°. The displacement of newly-created filaments from the jet's nominal center, marked by the small sphere, indicates the difference in A_h. Apparently, one can not increase the bifurcation angle by increasing A_h beyond 0.3 when $St_a = 0.35$.

The jet response to different Strouhal numbers ($0.25 \leq St_a \leq 0.50$) and the same excitation amplitude ($A_h = 0.5$) was also considered. Figure 3.17 shows the evolution of a bifurcating jet at $St_a = 0.3$ over several excitation periods. Similar results are presented for $St_a = 0.40$ in Fig. 3.18. End views of these two cases are shown in Fig. 3.19. The results in Figs. 3.17–3.19 demonstrate that the simulation captures the bifurcating jet's dominant features, the formation of two distinct jets and the asymmetric spreading pattern. The simulations also predict an increase of the bifurcation angle with St_a. The maximum bifurcation angle is obtained at $St_a = 0.42$ (Fig. 3.20). The difference between the evolution of the rings farthest downstream and the development of those upstream is due to the fact that the first rings generated have no rings downstream of them to affect their trajectories. This start-up condition was also seen in the experiments of Lee & Reynolds (1985b).

Figure 3.21 presents the jet bifurcation angle as a function of Strouhal number. The dashed lines in Fig. 3.21 denote a range in which bifurcating jets occur. At Strouhal numbers below this range, the jets appear as slightly perturbed round jets. Above this range the jets exhibit spreading angles larger than those of natural jets, but they do not have two distinct branches as the bifurcating jets within the specified range. Within this range the bifurcation angle rises sharply with St_a. The implications of this behavior are examined in the comparison with experiments in Sec. 6.5 and in the discussion of mechanisms in Sec. 6.6.

The cause for this dependence of bifurcation angle on St_a can be understood by considering the temporal onset of bifurcation at different St_a (Fig. 3.22). The Strouhal number determines the spacing of the ring filaments. The filaments are

relatively far apart at $St_a = 0.3$. At $St_a = 0.42$, the filaments are so close that they barely avoid colliding with each other as they separate along different trajectories. At $St_a = 0.43$, the rings are too close to each other to be able to escape getting entangled with each other, and thus the jet does not bifurcate.

The remaining sections of this chapter present the results of various refinements to the numerical model and method. Although each refinement was tested on some simple problems, these refinements have not yet been incorporated in the bifurcating jet code.

3.5 Roll-up of excited shear layer

The axial excitation in the bifurcating jet simulation presented in the previous section is modeled by periodically creating ring filaments at the jet exit. This model is based on the fact that sinusoidally forcing an axisymmetric shear layer will produce regularly-spaced vortex rings. However, the actual formation of vortex rings is not instantaneous, and this simple model has no means to account for the effects of the axial and helical excitations on the formation process. The simulations described in this section allow us to examine the effect of axial forcing on the initial roll-up of an axisymmetric shear layer into discrete vortex rings.

In the simulations described here, the shear layer is discretized into a single-layer of closely-spaced circular filaments. The filaments are generated at the jet exit at regular intervals. As many as twenty filaments are generated per axial excitation period. The axial excitation is modeled by sinusoidally varying the circulation per unit length, γ, of the cylindrical vortex sheet. This corresponds to periodically varying the mean flow. The bunching up of circular filaments into a distinct group corresponds to the formation of a discrete vortex ring.

The objective of this particular simulation was not only to consider the effect of axial forcing on ring formation but also to investigate different approaches to matching the vorticity flux of the jet function to that of the filaments. The three approaches (quadrature, integral, and growth matching) described in Sec. 2.5.1 have

been implemented, and their corresponding results are compared in this section. In addition, the influence of the source flow generated by the jet function and the importance of using image filaments are also considered.

Effect of source flow. The simulated initial roll-up of the unforced axisymmetric shear layer is shown with and without the source flow in Fig. 3.23. The circular marker shows the center of the jet exit. Note that the source flow causes the initial trajectory of the filaments to be parallel to the jet axis, whereas without the source flow the jet initially contracts. Hence, one could think of the source flow as a means of satisfying the Kutta condition at the jet exit. It is important to realize that the value of γ was not chosen to produce this parallel flow but was determined simply on the basis of a vorticity conservation constraint, Eqn. 2.22.

General effect of forcing. The initial evolution of an unforced axisymmetric shear layer is compared with that of a forced layer in Fig. 3.24. The symbols denote the positions of the filaments' cores. In the unforced case, the shear layer has rolled up into a single large vortex structure composed of many filaments. In the excited case, the filaments are grouped into two distinct groups. The existence of two groups corresponds to the two periods of forcing that have been completed by this point in the simulation. In these and the following cases, the filaments are initially generated one core radius, σ, downstream of the jet exit. Since the flow is assumed to remain axisymmetric, only the radial and streamwise position of each filament's core is necessary to describe the position of the entire filament.

Effect of vorticity-matching schemes. Since in the forced case γ varies in time, the vortex filaments do not have the same circulation, Γ_i. Three different methods for calculating Γ_i were described in Sec. 2.5.1. The evolution of the axially-excited shear layer as calculated by each method is presented in Fig. 3.25. Image filaments are included, and the core sizes of all filaments are constant. In each case the shear layer forms discrete bunches of vortex filaments as a result of the forcing. These bunches correspond to the vortex structures seen in physical flows. The methods differ noticeably in their prediction of the trajectories of the filaments. However, the initial necking down of the jet and the positions of the centroids of the groups

of filaments are very similar. Doubling the number of filaments created during each excitation period produces no significant change in the initial necking down of the jet nor in the locations of the vorticity centroids (Fig. 3.26).

Comparing Figs. 3.24b and 3.25a, one can see that the presence of image filaments increases the initial necking down of the jet. This large initial contraction of jet width (Fig. 3.25) is also seen in experiments with strong axial-forcing (Lee & Reynolds 1985b). Nevertheless, it is not clear that it is better to include image filaments since their inclusion would violate the Kutta condition in the unforced case.

Pairing of vortex rings. To check whether the simulation can capture the pairing of vortex rings, the evolution of the axially-forced jet is presented at the end of two, three, and four excitation periods in Fig. 3.27. One group of filaments is formed each excitation period. For example, at the end of two excitation periods, two groups are seen in Fig. 3.27a. However, the number of groups present at the end of each period depends on whether a pairing event has taken place. Pairing reduces the number of groups by one. Thus, existence of only two groups at the end of three excitation periods indicates that two groups have combined into one. Pairing also doubles the distance between filament groups. This increase in length scale corresponds to the subharmonic of the forcing frequency and is seen in Fig. 3.27c.

Effect of forcing amplitude. The effect of excitation amplitudes of 5% and 20% are compared in Fig. 3.28. In each case the growth matching scheme is used and the time corresponds to the end of two excitation periods. Forcing at $\bar{A}_h = 5\%$ only produces one distinct group of filaments in contrast to the two groups produced at $\bar{A}_h = 20\%$ (see also Fig. 3.27a). Thus, forcing at $\bar{A}_h = 5\%$ is not sufficient to control the formation of vortices from the shear layer. However, experiments in the planar mixing layer show that forcing levels even below 1% are adequate to exercise control over the vortex formation frequency (Ho & Huang 1982). This discrepancy between computations and experiments suggests that the multi-filament simulation underestimates the amplification of perturbations in the shear layer.

Effect of temporal, core-size variations. In all the simulations previously described, the core size of each filament is constant. However, in an inviscid flow the core size should vary with the filament radius as specified in Eqn. 2.8. The effect of keeping the core size constant is not too significant in the bifurcating jet simulation since the filaments are far apart. In the shear layer simulations, however, temporal variations in core size could be important. Figure 3.29 compares the pathlines of the first filament in the forced-layer simulations for the two cases of fixed and temporally-varying core size. The divergence of the two trajectories is 6.5% of the jet radius at the end of one excitation period. While one might expect that this difference in the trajectory of a single filament would increase with time, it is not clear whether the global features of the flow would also exhibit significant differences after a long time.

3.6 Rings with non-uniform cores

Mechanism of formation. Helical as well as axial perturbations affect the evolution of a round jet. Thinking in terms of the discrete-filament model of the shear layer, one could imagine that a helical perturbation could produce a ring with azimuthal variations in core size. Figures 3.30 and 3.31 show different views of a helically-excited jet at different phases of the excitation. The small circular marker shows the nominal center of the jet. If axial forcing with $f_a/f_h = 2$ were included, the filaments shown would form two vortex rings with non-uniform cores.

Interaction of non-uniform rings. To investigate the interaction of a pair of rings with azimuthal core variations, simulations were made with pairs of rings, each composed of nine filaments. Each filament has a constant core radius, $\bar{\sigma}$, equal to 0.1. Eight filaments are equally distributed about one central filament such that their distance, δ, from the central filament varies linearly according to the following relation:

$$\delta(\psi) = \begin{cases} \delta_0 + \frac{\psi}{\pi}\Delta, & \text{if } 0 \le \psi < \pi; \\ \delta_0 + (2 - \frac{\psi}{\pi})\Delta, & \text{if } \pi \le \psi < 2\pi, \end{cases} \qquad 3.9$$

where ψ is the azimuthal position in radians on the central filament and Δ is the magnitude of the core variation.

The first simulation involves two rings side by side (Fig. 3.32). In case (a), the fattest sections of the rings are adjacent to each other, but in case (b), the thinnest sections are closest. In both cases, $\delta_0/R = 0.1$ and $\Delta/R = 0.2$. As time progresses, the core variations are smoothed out and then reverse in orientation. The spiral shape of the filaments indicates the presence of azimuthal flow within the rings.

The second simulation involves the interaction of two eccentric rings with uniform and non-uniform cores (Fig. 3.33). The initial positions of these rings approximate the relative positions of two adjacent rings upstream of the bifurcation region in a bifurcating jet. If the largest sections of the rings are initially closest to each other, the tilting of the rings does not appear to increase over that in the case of uniform cores. However, if the smallest sections are initially nearest to each other, the tilting effect is significantly enhanced over that for the uniform rings.

These results suggest that azimuthal variations of core size could affect the angle at which a bifurcating jet spreads. The fact that these core variations were not included in the bifurcating jet simulation of Sec. 3.4 might partially explain why the computations required larger excitation amplitudes and did not predict spreading angles as large as those seen in experiments (compare Figs. 1.3 and 3.21). Whether the core variations would be smoothed out (see Fig. 3.22) before they could affect ring interactions in the bifurcating jet is not known. A jet simulation that models the formation of the vortex rings and uses multiple filaments to represent each ring would be required to answer this question.

3.7 Improvement by spline approximation

The refinements presented in the previous two sections concerned the use of filaments to model the jet. The refinement discussed here is an improvement in the numerical description of the filaments. Instead of using piece-wise linear segments to represent a filament, a periodic, cubic spline is used. To compare the accuracy of

these two representations, their predictions of ring speed are compared with theory. Figure 3.34 shows the convergence of the calculated ring speed as a function of number of nodes for both filament representations. The spline scheme achieves the same accuracy as the linear scheme with just half the number of nodes.

Not only is the spline scheme more accurate, it also has several practical advantages over the linear scheme. First, the spline scheme enables the programmer to construct much longer vectors in the time-intensive, iterative portions of the code. The longest vector with the linear scheme is the number of nodes per filament, but with the spline scheme it is the total number of nodes in the simulation. This is an advantage since supercomputers generally operate more efficiently with long vectors. The ideal vector length depends on the memory architecture of the particular computer. Second, the spline scheme allows one to perform nodal redistribution more accurately and efficiently.

Third and most importantly, the spline scheme is almost an order of magnitude faster than the linear scheme. Since the cost of these calculations are proportional to the square of the number of nodes and since the spline scheme requires half the number of nodes for the same accuracy, the spline scheme is faster by a factor of four. Since the number of operation counts for the spline scheme is half that of the linear scheme, speed increases by an additional factor of two. These two factors correspond to an eight-fold increase in speed. The additional cost savings due to longer vectors will differ with the type of computer.

One could consider the spline scheme to be an improvement on the basis of a purely physical argument. Depicting a vortex filament as a collection of connected linear segments results in non-physical cusps at each node. But with the spline scheme, one can specify the numerical filament to be smooth as is the physical filament. Thus, the spline representation corresponds to a more physically-realistic structure.

3.8 Summary

This chapter has presented the results of vortex-filament simulations of simple ring interactions and bifurcating jets and of refinements of the numerical model and method. The most significant results pertain to the bifurcating jet. The simulations demonstrate that the bifurcation of round jets is the consequence of the mutual induction of eccentric rings and that the bifurcation angle increases with Strouhal number. Another important result is that the numerical representation of a filament by a periodic, cubic spline rather than by multiple straight segments provides an order of magnitude decrease in computational cost for a given accuracy.

There are two major discrepancies between this simulation of the bifurcating jet and the experiment of Lee & Reynolds (1985b). First, to achieve large spreading angles, the simulation requires a helical excitation amplitude about ten times larger than that of the experiment. Second, the maximum bifurcation angle of the simulation was around 50° (at $St_a = 0.42$) compared to 80° (at $St_a = 0.6$) for the experiment. These discrepancies can be attributed to the simulation's coarse spatial resolution, underestimate of self-induced velocity, and inability to model the initial amplification of disturbances in the shear layer.

Chapter 4

EXPERIMENTAL APPARATUS AND APPROACH

The objective of the experimental portion of this research is to test the concept of bifurcation at high Reynolds numbers and to study the effects of various excitation parameters. Previous experimental work (Lee & Reynolds 1985b) and the computational results described in the previous chapter demonstrate that dual-mode excitation can cause a round jet to bifurcate into two distinct jets. Those results also point to an inviscid vortex interaction process as the primary mechanism causing bifurcation. Thus, one would expect to be able to apply the concept successfully to jets at Reynolds numbers higher than those of the previous experiment.

However, the implementation of dual-mode forcing in high speed gaseous jets does pose several previously unresolved questions. What is the best way to introduce the dual-mode excitation at the high forcing frequencies required by high Re flows? Will the low amplification rates associated with forcing at frequencies much lower than the shear layer's initially most-amplified frequency inhibit the bifurcation process? How does the required excitation amplitude increase with the jet Reynolds number?

To address these questions, a low-speed apparatus was designed and built. Air served as the working fluid Several different techniques for producing the axial and helical excitation were considered. The insights gained from this preliminary investigation provided guidance for the design and fabrication of the high-speed version of the bifurcating jet apparatus.

Since the primary objectives of this study concern global features of the jet, flow visualization experiments were emphasized. With flow visualization, one can readily identify different flow structures, uniquely capture the instantaneous behavior of the entire flow, effectively determine the jet response to variations in excitation parameters, and quickly test system modifications. The velocity and pressure measurements quantify the initial conditions of the jet and the amplitude and phase of the excitation.

4.1 Low-speed jet apparatus

A schematic of the low-speed jet apparatus is shown in Fig. 4.1. Air is introduced into the outer annular section of the plenum through two 3.8-cm-diameter pipes. This outer section is bounded by an 8″ schedule-80 PVC pipe. The air bleeds through a 46-cm-long, 9.7-cm-diameter, porous, bronze cylinder into the inner cylindrical section of the plenum.

This cylinder, along with acoustic baffles in the outer annular section, effectively isolates the inner section from all but the lowest frequency upstream noise sources. Each baffle consists of a ring-like Plexiglas insert that fits between the PVC pipe and the bronze cylinder. The inserts are lined on both flat surfaces with open-cell foam for acoustic damping. Air flows through the baffles through several large holes in the inserts. This plenum design was used with good success by Kerschen and Johnston (1978), and its acoustic properties are documented by Roberts and Johnston (1974).

The air is supplied by an EG&G Rotron, 1/4-HP regenerative blower (model 101), which is connected to the plenum by a 6-m, 3.8-cm-diameter, flexible PVC hose. The air is filtered at the blower inlet. This blower provides a portable, independent flow source that is ideally matched to the pressure and flow rate requirements of the experiment. A series of gate valves regulates the amount of flow and allows one to bleed some of the air for secondary uses.

A circular duct, made of 4″ schedule 80 PVC pipe, directs the fluid from the plenum into the nozzle. The inner diameter of this duct is also 9.7 cm. For additional flow conditioning, a honeycomb disk is mounted inside this duct. A 1-mm-diameter pressure tap in the pipe wall provides access for monitoring plenum pressure.

The nozzle was made by cutting off the bottom and threaded ends of a clear, two-liter, plastic soda bottle. The nozzle is cemented onto a Plexiglas coupling which is rigidly mounted to the circular duct. This simple nozzle has significant advantages in addition to its low cost. Its clear walls allow visual access inside

the nozzle, and its light weight makes it possible to excite the jet by physically oscillating the nozzle. This type of excitation was anticipated but was not required.

Several different schemes for producing the helical and axial excitations were explored. These schemes involved mechanical, acoustic, and fluidic devices. Each scheme was tested, and one was chosen on the basis of success in producing bifurcation, ease of implementation, and flexibility in varying excitation parameters. The final version of the low-speed apparatus, shown in Fig. 4.1, incorporates an acoustic excitation system. A 60-watt, Pioneer, 9-cm, full-range speaker is used to produce the axial excitation. Four 120-watt, 15-cm, Morel woofers are flush mounted in a 70-cm by 70-cm particle board panel which is also flush with the nozzle exit. The woofers are positioned 90° apart, and their centers are located 11 cm from the jet centerline.

The Plexiglas coupling, shown in Fig. 4.1, also serves as a passage for smoke flow. Smoke enters through four ports into an annular chamber and is injected tangential to the core flow through a narrow annular slot. By injecting the smoke into the nozzle boundary layer, one clearly marks the shear layer and vortical structures of the jet.

The jet apparatus is oriented vertically by a rigid steel frame. The jet exit sits one meter above the floor. In all experiments, the jet is situated in a large room (at least 10m x 20m x 7m) and positioned at least one meter from the nearest wall.

4.2 High-speed jet apparatus

The low-speed apparatus was successfully used to produce bifurcating jets at moderate Reynolds numbers. These results are detailed in the next chapter. This success provided the motivation and guidance for designing another apparatus for studying high-speed, high-Reynolds number air jets. A schematic of this apparatus is shown in Fig. 4.2.

The plenum design is identical to the low-speed apparatus except for the method of bringing air into the plenum. Instead of two small-diameter pipes, one 9.7-cm-diameter pipe is used. An 8° (included angle) diffuser connects this large diameter pipe to the smaller diameter supply hose. The air is supplied by a 1-1/2-HP, EG&G Rotron regenerative blower (model 454). The air is filtered at the blower inlet. Two gate valves in parallel regulate the flow to the jet apparatus. The valves were arranged to minimize system resonances. The blower is connected to the jet apparatus by a 6-m, 3.8-cm-diameter, flexible PVC hose.

A two-piece, 2-cm-diameter, anodized aluminum nozzle was designed and machined for this high-speed jet apparatus. The nozzle profile is specified by a fifth-order polynomial with zero slope and curvature at inlet and exit. Tan-atichat (1980) demonstrated that this profile, when compared to a matched-cubic profile, has smaller streamwise velocity overshoot and smaller radially inward velocity at the jet exit. A numerically-controlled lathe provided the capability to match the specified profile to within 0.05 mm. The area-contraction ratio is 25-to-1, and the length-to-diameter ratio is 5-to-1.

The upper and lower halves of the nozzle meet at the inflection point of the profile. A thin annular slot is formed by these two halves. Smoke can be injected tangential to the main flow through this slot. This slot location was chosen since it is a region of favorable pressure gradient. The slot is connected by an axisymmetric passage to a small annular plenum in the outer portion of the nozzle. Smoke enters the nozzle assembly through four ports and is made azimuthally uniform by honeycomb in the annular plenum. A bottle of compressed air provides the air source for the injected smoke flow. This secondary air flow is regulated by a Matheson single-stage regulator (model 1L346). The flow rate is controlled by a high-precision needle valve connected to a Matheson rotameter (model 605).

The excitation source was chosen on the basis of estimations of the required excitation frequency and amplitude. From the definitions of the Reynolds and Strouhal numbers, one can derive the following expression for the excitation frequency, f:

$$f = \frac{\nu}{D^2} ReSt \qquad 4.1$$

The work of Lee and Reynolds demonstrated that bifurcating jets occur in the Strouhal number range of 0.4 to 0.7, based on the axial excitation frequency. Thus, generating bifurcating jets in this apparatus at Reynolds numbers up to 100,000 would require excitation frequencies over 2 kHz. Additionally, assuming that the perturbation pressure amplitude scales linearly with the mean jet exit velocity, one can conjecture from the low Reynolds number results that sound pressure levels of around 130 dB would be required.

To achieve these high levels of excitation, compression drivers are used. These high-power, high-efficiency acoustic drivers are frequently matched with horns as part of large sound systems. In this apparatus, one driver is attached to the plenum as shown in Fig. 4.2. The other four drivers surround the plenum. Each driver is connected to a 2-cm-diameter, 1.1-m-long, stainless steel, round tube. These tubes act as wave guides which carry the acoustic wave from the compression drivers to the acoustic passages in the nozzle assembly. Since shear layers are most susceptible to acoustic excitation at the trailing edge, these passages are designed to focus the acoustic signal at the jet exit. All five drivers are identical JBL 2485J, 120-watt, compression drivers.

The entire apparatus is supported by a rigid steel frame which sits on heavy-duty casters with leveling feet. This allows for easy transport and for adjusting the apparatus to be horizontally level regardless of the flatness of the floor. A 70-cm by 70-cm particle board panel surrounds the nozzle assembly and sits flush with the jet exit. The jet is oriented vertically, and its exit is 1.2 m above the floor.

Baffles made of particle board and Sonex standard, 7.6-cm-thick, acoustical foam surround the jet on all four sides. This Sonex foam has an absorption ratio of one down to 500 Hz. These baffles are located 1 m from the jet on each side. For visual access into the test cell, one of the baffles has a 46-cm by 61-cm rectangular opening covered with a thin Plexiglas sheet. One adjacent panel has a thin slit for passage of a laser light sheet. Entrained air flows into the test cell through the 0.8-m gap between the baffles and the floor. The air discharges to a positively-vented exhaust

hood located 1.3 m above the jet. This hood is lined with 'Hypalon'-coated Sonex 1 foam.

4.3 Excitation system

The acoustic excitation consists of signals of two different modes and frequencies. The axial mode is generated by either the acoustic driver in the jet plenum or by the four external drivers. An approximate first-order helical mode is produced by proper phasing of the sinusoidal signals routed to the four external drivers. The signals of adjacent drivers are 90° out of phase, and those of opposite drivers are 180° out of phase. A transverse instead of a helical mode is produced when only two opposite drivers are used. In the case of the bifurcating jet, the ratio, $\mathcal{R}_f$, of axial frequency, f_a, to helical frequency, f_h is exactly two.

A function generator (Circuitmate FG2) produces the reference sinusoidal signal at the helical excitation frequency. A PAR 121 lock-in amplifier uses this reference signal to generate a sinusoidal signal doubled in frequency. The reference signal is also fed into a custom, two-channel phase shifter. The first channel shifts the reference signal an arbitrary amount from 0° to 360° relative to the frequency-doubled signal. This phase shift corresponds to the relative phase between the axial and helical signals. The second channel shifts the output of the first channel an additional 90°. Sound measurements verify that the corresponding acoustic signals are also 90° out of phase. The outputs of these channels provide the signals for two adjacent external drivers. The properly-phased signals for the other two drivers are obtained by physically reversing the standard connection between these drivers and the amplifier or by electronically inverting the appropriate signals. The frequency-doubled signal is the axial excitation signal. Both excitation frequencies will typically be discussed in terms of the corresponding Strouhal numbers St_a and St_h, where $St_a \equiv f_a D/U$ and $St_h \equiv f_h D/U$.

These low-level signals are amplified with audio amplifiers. A Pioneer A-60, 100-watt/channel, integrated amplifier is used with the low-speed apparatus. Kenwood M1 (100-watt/channel) and Kenwood M2A (220-watt/channel) power amplifiers and a Kenwood C1 preamplifier are used with the high-speed apparatus. The low-level and amplified signals are monitored with a multi-channel oscilloscope (Iwatsu SS-5706), digital frequency counter (HP 5314A), and high-accuracy multimeter (Fluke 8842A). When only the four external drivers are used to produce both the axial and helical signals, the axial and helical signals are electronically added prior to amplification.

The relative phase between the axial and helical signals is typically set so as to produce the widest-spreading jet in the plane of the light sheet. Since $f_a/f_h = 2$, one only needs to shift the helical signal from 0° to 180° to cover the full range of relative phase angles. Phase angles that differ by 90° correspond to mirror images of the jet. When the light sheet coincides with the azimuthal plane containing two opposite drivers, the maximum spreading angle is observed when the relative phase of the axial and helical signals of either driver equals $47° \pm 15°$ (at $Re = 100{,}000$). The corresponding phase angle at $Re = 50{,}000$ is $31° \pm 15°$. These phase angles correspond to the approximate alignment of every other peak of the axial signal with a peak of the helical signal.

4.4 Flow-visualization techniques

To mark the shear layer and vortex structures, smoke is injected into the boundary layer in the nozzle. The smoke is illuminated with either an electronic stroboscope (General Radio 1531-A) or a 10-watt (2 mJ/pulse at 5-kHz repetition rate), copper-vapor, pulsed laser (Plasma Kinetics 151). A single flash from the light source provides instantaneous pictures. Phase-averaged pictures are obtained with multiple flashes by triggering the light source such that each flash occurs at the same phase of the reference signal. The strobe enables one to visualize the entire jet while the laser illuminates only cross-sections of the flow. The laser produces

the most detailed pictures not only because it is focused into a thin sheet but also because it has an extremely short pulse duration (30 ns vs. 1.2 μs for the strobe).

Most photographs are taken with a Nikon FE2 35-mm camera with a Nikon 2.8, 55-mm, micro Nikkor lens. The f-stop is set to 2.8, and the shutter speed is varied according to the desired number of laser pulses per exposure. For the instantaneous pictures at Re = 50,000 and 100,000, a Nikon 1.4, 50-mm, Nikkor lens is used with the f-stop set to 1.4. Kodacolor VRG (ASA 400) print film is significantly more sensitive to the green laser light than is Ektachrome (ASA 400) slide film. Thus slides are made from the prints rather than exposed directly. For black and white prints, either Kodak Tri-X (ASA 400) or Kodak TMAX (ASA 400) film is used. Kodak TMAX film was found to be the best option. It provided excellent results even when developed at ASA 800.

An external triggering circuit designed by Eaton (1986) controls the repetition rate of the copper-vapor laser. Since the laser is a very strong noise source, the triggering circuit is optically coupled to the laser power supply. This circuit includes a manually-adjustable internal trigger as well as inputs for a remotely-enabled external trigger.

For single instantaneous exposures, the laser repetition rate was set manually at various values between 200 and 250 Hz, and the camera shutter speed was set at 1/250. Occasionally, portions of the film were not exposed since the camera is not synchronized with the laser in this case. However, setting the repetition rate to 240 Hz was found virtually to eliminate this partial exposure problem. The appropriate combination of repetition rate and shutter speed will vary with different cameras. It should also be noted that this triggering scheme does *not* allow one to specify the phase of the laser pulse relative to the acoustic excitation.

For phase-averaged pictures, the laser is triggered to fire at a particular phase of the reference excitation signal. Zero-degrees phase corresponds to the peak of the reference signal. A pulse synchronization circuit converts the reference sinusoidal signal into a pulse and phase shifts that pulse from 0° to 360° as specified by the user. This pulse serves as the external trigger for the Eaton triggering circuit.

The triggering circuit is connected to the camera's autodrive (Nikon MD-12) such that the laser operates at the excitation frequency only when the camera shutter is enabled. At all other times the laser operates at its normal operating rate of 6 kHz. The triggering system is sketched in Fig. 4.12, and the corresponding timing diagram is given in Fig. 4.13. The number of laser flashes per exposure, F, is determined by the repetition rate and the camera shutter speed.

Visualizing an excited jet at successive phases of excitation is similar, thought not usually identical, to watching the time evolution of the jet. The two visualizations are identical only if the pictures at successive phases are taken within one period of the excitation. Referencing the flow pictures to the excitation phase allows one to determine the phase relationship between excitation and vortex formation. Because of the manner in which the laser is triggered, the phase of the excitation at which the laser flashes is only known for phase-averaged visualizations. The phase corresponding to instantaneous pictures can be estimated by comparing the instantaneous pictures with the phase-averaged pictures.

One can estimate the frequency associated with vortex structures from measurements of the distance between them. Let l represent the streamwise distance between the centers of the cores of two adjacent, fully-developed vortices. Let U be the local mean centerline velocity at z, and let U_e be the time-averaged centerline velocity at the jet exit. By approximating the vortex propagation speed by $U/2$, one obtains the following approximation for the vortex passage frequency, f_v:

$$f_v \simeq \frac{U}{2l} \qquad 4.2$$

From the definition of St and the approximation $U \simeq U_e$, which is valid near the jet exit, one obtains

$$St_D \simeq \frac{D}{2l} \qquad 4.3$$

and

$$St_\theta \simeq \frac{\theta}{2l} \qquad 4.4$$

where St_D is characteristic of the forcing and St_θ is characteristic of the jet's initial instability. From the definitions of St_D and St_θ, the ratio of the natural frequency, f_n, to the forcing frequency, f_a, can be expressed as

$$\frac{f_n}{f_a} = \frac{St_\theta D}{St_D \theta} \qquad 4.5$$

These equations are used in Ch. 5 to estimate from pictures the natural frequency of the shear layer.

Since the laser resides in an adjacent laboratory, a set of mirrors (Newport 20D20BD.1) and lenses are used to focus the beam into a thin sheet and to direct it into the test cell. A 2-m-focal-length, convex spherical lens (Melles-Griot 01 LDX 263/078) and a 200-mm-focal-length, concave spherical lens (Newport KPC 070AR.14) focus the beam while a 150-mm-focal-length, concave cylindrical lens (Melles-Griot 01 LCN 008/078) expands the beam in one plane. By changing the distance between the two spherical lenses, one can position the thinnest portion of the light sheet at the jet exit. This setup provides a light sheet that is less than 1-mm thick at the jet exit. A 5.1-cm laser window (Newport 20QB20XR.14) in the laboratory wall provides isolation between the two rooms. All mirrors are 99% reflective, and the lenses and window are 99% transmissive at the operating wavelengths.

The strobe is used with a VHS video camcorder (Panasonic PV-200D) primarily for preliminary studies and setup. The strobe frequency is manually set at a submultiple of the excitation frequency. When the strobe frequency is an exact submultiple, the flow structures are seen to sit motionless in space. Slight deviations from exact submultiples provide a sense of motion.

Several different smoke sources, including incense, cigarettes, cigars, vaporized mineral oil, and titanium tetrachloride (TiCl4), were considered. The titanium dioxide (TiO2) smoke, which is formed from TiCl4, scatters the most light but is also hardest to handle since hydrochloric acid is a by-product of the formation process. Neither the incense nor the mineral oil produced an adequately dense smoke. Tobacco smoke provided the best compromise between ease of handling and

amount of light scattering. Cigars are used instead of cigarettes since they burn much longer.

The smoke generation system consists of cigars (Phillies Titan), Pyrex flasks, and an air source. In the low-speed apparatus bypass air from the blower provides the necessary air. In the other apparatus the air is obtained from a compressed air cylinder, and the flow rate was maintained at 2% of the jet flow rate. This flow rate was chosen since the ratio of the injection-slot area to the nozzle cross-sectional area at the injection location is approximately 2%. The air is forced through the cigars burning in the flasks, and the cigars were found to burn most effectively if two small holes were made in the skin of each cigar near its unlit end.

The outlet ports of the flasks are connected to a mixing chamber. This chamber is in turn connected to each inlet port on the nozzle assembly through over two meters of copper and Tygon tubing. This long length of tubing allows the smoke flow to cool prior to entering the nozzle. The amount of smoke can be varied by varying the flow rate and/or the number of cigars. Four cigars were used in the high-speed experiments. The nozzle surface was cleaned regularly, and the room humidity was kept low to prevent the cigar smoke from leaving deposits on the nozzle's surface.

4.5 Velocity and pressure measurements

Both velocity and pressure measurements were made to document the jet initial conditions and the excitation signals. The time-averaged, centerline velocity at the jet exit was calculated from the plenum pressure, which was measured with a high-accuracy (± 0.005 in. H_2O), Meriam manometer (model 34FB2). A hot-wire anemometry system measured the streamwise velocity profiles, and a small condenser microphone positioned at the jet exit measured the level and phase of the acoustic excitation. Since the purpose of the acoustic measurement is to quantify the imposed perturbation and not to measure the jet noise, all acoustic measurements were made with no flow. It is assumed that for a fixed input signal to the excitation

system, the imposed perturbation is the same whether the flow is on or off. A theoretical argument for making *acoustic* measurements with *no* flow as a means of quantifying the acoustic excitation of a shear layer is given by Bechert (1988).

The hot-wire system consists of standard Dantec components. A 5-μm-diameter, platinum-coated tungsten wire with gold-plated ends is mounted on a straight probe (model 55P01) supported by a right-angle probe holder (model 55H22). The probe is connected to a multipurpose bridge (module 56C16) and signal conditioner (module 56N20). A two-dimensional, manually-actuated traverse moves the probe in a plane parallel to the jet's axis. A high-accuracy dial indicator enables setting the probe position to within 0.025 mm of a desired value.

A dedicated AT-type, 10-Mhz microcomputer (AST Premium 286) handled the data acquisition and processing. The data was acquired with a Data Translation analog-to-digital converter (model 2821-16SE-F) and stored directly in extended memory or on a 70-Mb MiniScribe hard disk. With this configuration single-channel data could be continuously acquired and stored at rates up to 130 kHz to memory and 50 kHz to disk.

All 'linearization' and temperature compensation of the hot-wire data was done in software. Calibration data were obtained with the hot-wire probe positioned at the center of the jet exit and were fit to the King's Law:

$$E^2 = E_0^2 + Ku^n, \tag{4.6}$$

where E is the bridge output voltage and u is the streamwise velocity. The coefficients E_0 and K and the exponent n were optimized to minimize the error. The temperature compensation used is that due to Bearman (1971):

$$E = E_{\text{ref}} \left(\frac{T_w - T}{T_w - T_{\text{ref}}} \right)^{1/2}, \tag{4.7}$$

where T_w is the wire temperature, T is the ambient temperature, and the reference state is that at calibration.

A 0.6-cm-diameter condenser microphone (Bruel & Kjaer 4136) was positioned one nozzle diameter (20 mm) from the jet exit and half a diameter (10 mm) from

the jet centerline. The microphone was oriented perpendicular to the jet's axis and pointed toward the jet centerline. In the azimuthal direction, the microphone was lined up with one of the wave guides. The microphone was connected to a preamplifier (Bruel & Kjaer 2619) which in turn was connected to a heterodyne analyzer (Bruel & Kjaer 2010). This analyzer was simply used to provide an accurate measurement of the sound pressure level (SPL), where

$$\mathrm{SPL} = 20 \log_{10} \left(\frac{p'}{p_{\mathrm{ref}}} \right). \tag{4.8}$$

The analyzer was set for a linear frequency response, and all pressure measurements are referenced to $p_{\mathrm{ref}} = 2 \times 10^{-5}$ Pa.

At a given frequency, doubling the amplitude of the excitation signal should, in theory, result in a 6 dB increase in the measured SPL. The deviation from theory was within ± 0.1 dB in the axial mode but was as high as ± 1 dB in the helical mode. From day to day, the measurement of the axial perturbation was repeatable to within 2% of the measured pressure fluctuation. At $z/D = 1$, the difference between the pressure fluctuations at $r/D = 0$ and $r/D = 0.5$ was also within 2% of the measured fluctuation. Measurements of the helical perturbation were repeatable to within 3% at high excitation amplitudes but deviated by as much as 25% at the lowest excitation amplitudes.

Calibration curves of rms pressure fluctuation, p', measured at $z/D = 1$ and $r/D = 0.5$, versus electrical signal amplitude were established at each frequency of interest for both the axial and helical modes. Each curve was essentially linear. During flow-visualization and hot-wire experiments, the electrical signal amplitudes are measured to within 0.5% of their actual value. The corresponding pressure fluctuations are calculated from the calibration curves and are reported in terms of the non-dimensional quantity $\bar{p}$, where $\bar{p} \equiv p'/(\frac{1}{2}\rho U^2)$. The velocity fluctuation at the jet exit increases linearly with the axisymmetric pressure fluctuation, p'_a. The streamwise velocity fluctuations corresponding to different values of $\bar{p}_a$ are presented in Fig. 4.3.

Chapter 5

EXPERIMENTAL RESULTS

The experimental methods and approach described in the previous chapter were applied to four different types of jet flows. The first is a natural jet. This unexcited jet provides a base case for the three other flows which all involve some type of excitation. Second, axially-excited jets are considered. Our study of these flows enhances our understanding of the effects of amplitude and phase on the control of the vortex formation process. The third type of jet is excited only by a first-order azimuthal mode. Since the bifurcating jet is generated by a combination of axial and helical excitation, it is instructive to consider the effect of the helical excitation alone. Finally, the main subject of this report, the bifurcating jet, is examined.

The range of parameters considered in this work both extends and parallels the range of parameters considered by Lee and Reynolds (1985b). They focused primarily on jets at a Reynolds number of 4300. This work investigates jets in the 10,000 to 100,000 range. The low-speed apparatus is used for $Re \leq 20,000$, while the high-speed apparatus is used for all higher Reynolds numbers flows. The axial and helical excitation amplitudes used by Lee and Reynolds were fixed at $u'/U = 17\%$ and $\delta/D = 4\%$, where δ represents the displacement of the nozzle tip. The range of amplitudes examined here cover several orders of magnitude. Since the experiments of Lee and Reynolds indicated that the bifurcation phenomenon occurs only for $0.40 \leq St \leq 0.65$, the same range is considered here. The key dimensionless and corresponding physical parameters are compared in Table C.2.

5.1 Natural jet

All the jets considered here are round, turbulent, free jets with initially thin shear layers. The natural jets are characterized in terms of Reynolds number, shear layer thickness, exit velocity profile, and exit centerline turbulence level. The Reynolds number Re is based on the time-averaged, centerline exit velocity, U, and nozzle

diameter, D. The shear layer thickness is specified in terms of the vorticity thickness δ_ω, where $\delta_\omega = U_{\max}/(du/dy)_{\max}$. The turbulence level is defined as u'/U, where u' is the root-mean-square of the fluctuating streamwise velocity. Measurements of the initial conditions of the natural jet were provided by Mr. Philippe Juvet for the high-speed jet and by Mr. Robert Koch for the low-speed jet. The initial shear layer appeared to be laminar in all cases, and the physical parameters of all the cases are summarized in Table C.3.

The low-speed facility was used to study jets at Reynolds numbers of 10,000 and 20,000. The centerline turbulence level at $z/D = 0.1$ is 1.3% at $Re = 10,000$ and 0.6% at $Re = 20,000$. The mean and fluctuating velocity profiles at $Re = 10,000$ are presented in Fig. 5.1. The corresponding vorticity thickness is approximately 1.3 mm ($\delta_\omega/R \simeq 0.12$).

The high-speed jet facility was used to study jets at Reynolds numbers of 25,000, 50,000, and 100,000. The corresponding centerline turbulence intensities are 0.5%, 0.3%, and 0.2% (at $z/D = 0.05$). The mean and fluctuating velocity profiles of these jets at $z/D = 0.05$ are presented in Figs. 5.2–5.4. In each case the velocity profiles are top-hat in shape. The shear layer profiles of these cases are compared in Fig. 5.5. The vorticity thickness decreases with increasing Reynolds number from 0.43 mm ($\delta_\omega/R = 0.043$) at $Re = 25,000$ to 0.25 mm ($\delta_\omega/R = 0.025$) at $Re = 50,000$ to 0.18 mm ($\delta_\omega/R = 0.018$) at $Re = 100,000$.

In all the cases studied in the high-speed facility, the flow rate of the injected air was two percent of the total flow rate. Figures 5.6 and 5.7 compare velocity profiles with and without air injection through the smoke slots. Note that the shape and size of the shear layer is not altered by the blowing. In the low-speed facility, the smoke flow was adjusted until it appeared to have no significant effect on the jet but was not separately metered.

Instantaneous cross-sections of unexcited jets at Reynolds numbers of 50,000 and 100,000 are displayed in Figs. 5.8 and 5.9. In both cases the shear layers are initially laminar but undergo transition to turbulent layers within one jet diameter.

The process of transition consists of the formation of very small vortex rings followed by one stage of vortex ring merging and the subsequent breakdown of those rings into turbulent puffs. The vortex merging occurs asymmetrically. In one case (Fig. 5.8), two vortex cores are seen merging on the left side while apparently three are combining on the right side at the same downstream location ($z/D = 0.7$). This indicates that different azimuthal sections of a vortex ring do not always behave the same. It is also evident from this picture that the smoke interface between the jet core fluid and the ambient fluid sometimes disappears between adjacent vortex cores. This observation suggests that the ring formation and merging processes locally stretch the shear layer so strongly that it is torn.

Using Eqn. 4.4 to estimate the initial vortex formation frequency from Fig. 5.8 and using the approximation $\theta \simeq \delta_\omega/4$ to determine θ (see Monkewitz & Huerre 1982), one obtains $St_\theta = 0.014$. This is fairly close to the shear layer's initial most amplified frequency, which is typically taken to be $St_\theta = 0.017$ (Ho & Huerre 1984). Since Eqn. 4.4 is merely an approximation and since background disturbances can cause the observed most-amplified frequency to differ from the theoretical one, it is not surprising that these two values are slightly different. The fact that the estimate is as close as it is to the actual value indicates that this 'back-of-the-envelope' analysis can be useful. Substituting $St_\theta = 0.014$ and $St_D = 0.55$ into Eqn. 4.5, one notes that typical forcing frequencies are about eight times lower in frequency than the initial vortex formation frequency. Thus, the amplification rate corresponding to the forcing frequency is at least an order of magnitude lower than the maximum amplification rate (Michalke & Hermann 1982).

Another striking feature of these natural jets are their strong three dimensionality. The smoke boundaries on both the interior and exterior surfaces of the shear layer are very ragged. In general, the shear layer spreads more rapidly on its exterior side. Beyond $z/D = 1$, large-scale structures are not clearly evident though they are suggested by various patterns in the shear layer. Two large blobs of smoke at $z/D = 2$ and 3 are apparent on the left side of the jet (Fig. 5.8). In the other jet (Fig. 5.9), two blobs of smoke are seen on the right side at $z/D = 6$ and 8. It is not

surprising that the distance between these blobs is much larger than that between the other pair of blobs since these structures are much farther downstream. One would expect the largest length scales to increase with downstream location. Between these two blobs is a thick strand-like structure reminiscent of the vortex sheet connecting adjacent rollers in a plane mixing layer. In some instances (Fig. 5.10), the potential core wanders left and right as a meandering river. It will be shown in Sec. 5.3 that this zig-zag pattern is a signature of the first-order helical instability in jet flows.

Multiple-exposure cross-sections of natural jets at Reynolds numbers of 50,000 and 100,000 are pictured in Figs. 5.11 and 5.12. The raggedness of the shear layer is smoothed away by the 'averaging' achieved by the multiple exposures. Small vortices are still somewhat visible in the near field. Comparing Figs. 5.11 and 5.12, one can see that increasing the Reynolds number results in an earlier transition to turbulence and an apparently longer potential core. In both cases the jet *appears* fairly symmetric about its centerline. As was seen in the instantaneous pictures, the length of the potential core increases with Reynolds number while the length of the laminar portion of the shear layer decreases. One would not expect the helical instability to be distinct in multiple-exposure pictures since the jet does not always succumb to that instability and since the zig-zag pattern could take any azimuthal orientation. The contrast between the instantaneous and multiple-exposure views clearly demonstrates the importance of having both views to get an accurate concept of the features of a flow.

Multiple-exposure pictures at $Re = 25{,}000$ reveal many of the same features of the higher Reynolds number jets. Laminar and turbulent vortical structures of differing scales and asymmetric ring merging are evident in Figs. 5.13 and 5.14. Since only four exposures are combined in these pictures, many of the fine details remain.

5.2 Axially-excited jet

By imposing a single-frequency, axial excitation, one can control the frequency at which the shear layer rolls up into distinct vortex rings. As a result, phase-averaged pictures can capture these structures. This section illustrates the effects of differing excitation amplitudes and present the phase evolution of the vortex structures. Additionally, the internal and external means of introducing the axial excitation are compared. Unless otherwise stated, the axial excitation is introduced internally by the acoustic driver in the plenum at Re = 10,000 and 20,000 and is generated by the external drivers at the higher Reynolds numbers. In most cases, the Strouhal number, St_a, given by $f_a D/U$, equals 0.55.

One example of the differences between natural and axially-excited jets at $Re = 10,000$ is depicted by the instantaneous strobe pictures in Fig. 5.15. The shear layer and initial vortices in the natural jet remain laminar for a much longer distance than those in the higher Reynolds number jets. The axial excitation causes the shear layer to start to roll up sooner and results in the vortices being larger and more regularly arranged. The mushroom-shaped structure at $z/D = 5$ is the consequence of one ring being pulled through and wrapped around another ring.

Instantaneous cross-sections through the center of the jet show interesting differences in jet response to $\bar{p}_a$. At low levels of streamwise forcing, one controls the vortex formation frequency by causing a periodic collective interaction of the thin closely-spaced rings near the jet exit. The axially-pulsed jet at $Re = 20,000$ and $\bar{p}_a = 1.6\%$ is an example of this (Fig. 5.16). The thin rings form independently of the forcing while the large rings form because of the forcing. Looking at the larger vortex structure at $z/D = 3$, one can note differences in the shape of the jet core around this structure. Upstream of the structure, the core's two sides are convex. Downstream of the structure, the core looks like an arrowhead. The oblong mass of vortical fluid at the tip of this 'arrowhead' is the result of a vortex merging.

At higher levels ($\bar{p}_a = 12\%$), the thin vortex rings are no longer visible, and instead, one sees the initial formation of rings whose spacing is on the order of the jet diameter (Fig. 5.17). The stronger excitation causes a tight roll-up of the shear

layer and the formation of very large laminar rings. The structure of the vortex cores shows many interfaces between the jet fluid and the entrained fluid. Several diameters from the exit, a vortex ring exhibits severe deformation and elongation due to the pairing process. As pairing occurs, the core of the upstream vortex ring changes from a circular to an oblong structure.

Instantaneous pictures at different phases of excitation at $Re = 10,000$ are presented in Fig. 5.18. The pictures are arranged in successive phases of the initial roll-up of the shear layer. From these pictures one can see that a vortex ring grows by wrapping more and more of the shear layer around itself as it propagates downstream. Eventually, the roll-up process stops, and consequently the independent growth of the vortex structure does also. Further growth is no longer achieved by additional roll up of the shear layer but by the amalgamation of vortex rings. In certain instances as many as five vortex rings remain distinctly visible and organized at one time (Fig. 5.18d). This contrasts sharply with the natural jet seen in Fig. 5.15.

Phase-averaged pictures of a jet at $Re = 100,000$ and at phase intervals of 90° are presented in Fig. 5.19. Since the laser is triggered by the excitation signal, the fact that the positions of the rings remains the same over 17 exposures demonstrates that the large rings are being formed at the forcing frequency. In both the instantaneous and phase-averaged pictures (Figs. 5.17–5.19), the spacing between adjacent, fully-developed vortex rings that are not pairing is about one diameter. These two cases differ in Re by a factor of ten but are identical in St, and hence, the spacing between rings is essentially identical.

The effects of amplitude variations seen at the lower Reynolds numbers are also seen at the higher Reynolds numbers. Instantaneous pictures of axially-excited jets at $Re = 50,000$ and 100,000 are shown in Figs. 5.20 and 5.21. In both cases one sees varying scales of vortex structures that are very distinct from each other. The axial excitation is effective in generating the desired large vortices. Since the amplitude is a factor of 4 higher in the $Re = 100,000$ case, the vortex rings in that jet are much more distinct and organized. The pronounced circular void of vortical fluid

in the large vortex ring is the consequence of ambient fluid being engulfed during a pairing event.

Several cases with different amplitudes at $Re = 50,000$ are compared in Fig. 5.22. The large vortex structures become more distinct as the amplitude is increased, however, the formation of the small, initial vortex rings appears unaffected except at the very highest amplitude. The highest amplitude is a factor of 9 greater than the lowest one. In Fig. 5.22d, the helical instability is present downstream of the potential core.

The same cases considered in Fig. 5.22 are visualized by the phase-averaged technique in Fig. 5.23. It is important to remember that while the phase-averaged pictures all correspond to the same phase of excitation, the instantaneous pictures do not. As in the instantaneous pictures (Fig. 5.22), the vortex cores in the phase-averaged pictures (Fig. 5.23) become more distinct as the amplitude is increased. The vortex cores form a staggered array as the amplitude is increased. This would be expected of a helically-excited jet but *not* of an axially-excited jet. The explanation for this phenomenon is not clear, though one might conjecture that energy is being transferred from the axial to the helical instability.

A comparison of axially-excited jets at $Re = 100,000$ and at different amplitudes is provided by the instantaneous visualizations in Fig. 5.24. The excitation at the two lowest amplitudes appears to have little or no effect on the shear layer. The excitation at the highest amplitudes is quite sufficient to generate distinct vortex rings. At the very highest amplitude, the eye of the vortex is completely clear of vortical fluid. The deformation of a vortex ring due to pairing is also evident in Fig. 5.24d.

The corresponding phase-averaged pictures are given in Fig. 5.25. From these pictures, one can see that even the low amplitude excitations do alter the structure of the shear layer in a fashion characteristic of the excitation frequency. Comparing Figs. 5.23 and 5.25 demonstrates that the same absolute level of forcing does not produce the same effect at these two different Reynolds numbers.

In Fig. 5.25d, the cores of the vortices are still quite clear in spite of averaging over 17 exposures. The fact that two different scales of structures remain distinct and localized indicates that the smaller structure corresponds to the first harmonic of the frequency characteristic of the larger structures. The vortices corresponding to the forcing frequency are the result of at least two stages of vortex coalescence.

A close-up of an axially-excited jet at $Re = 25,000$ is given in Fig. 5.26. Since only four exposures were taken, this phase-averaged picture appears much like instantaneous pictures. The large, turbulent rings are fixed in space, but the small laminar ones are not. Thus, the large structures do not correspond to an exact subharmonic of the small structures. Multiple rings combine to form the large structures by a 'collective interaction' process like that described by Ho and Huang (1982). The effects of different amplitudes are compared in Fig. 5.27. The highest amplitude considered is sufficient to bypass the collective interaction process and produce the large structures directly.

A comparison of excited jets at different St_a but the same excitation amplitude is presented in Fig. 5.28. Figure 5.28a corresponds to $St_a = 0.55$. The Strouhal numbers of Figs. 5.28b and 5.28c are slightly higher at 0.60 and 0.65. These small variations in St_a result in noticeable changes in the spacing of the vortex structures. As one would expect, the rings are closer at higher St_a.

In the high-Reynolds-number facility, when the axial excitation is produced by the *internal* acoustic driver, increasing the excitation amplitude can cause separation of the boundary layer in the nozzle (Fig. 5.29). When the separation occurs, the smoke issuing from the nozzle is no longer only a thin laminar stream but is also a large turbulent structure. The separation appears to occur periodically. Additionally, the boundary layer of the flow at $Re = 100,000$ is more robust and does not separate until much higher levels of forcing. When the axial perturbation is produced by the external drivers, no separation is observed.

Though the separation is linked to certain levels of forcing from the internal driver, its exact cause is not known. It is possible that the shear layer formed

inside the nozzle by the main and injected flows is adversely affected by the acoustic forcing. Another plausible explanation is that the compression driver produces vortex rings that propagate through the plenum and interact with the nozzle boundary layer. No production of vortex structures away from the plenum walls would be expected in the low-speed apparatus since the speaker is a conventional conical-diaphragm loudspeaker whose diameter is approximately equal to the plenum diameter. In the high-speed apparatus, however, the acoustic signal leaves the compression driver through a 5-cm-diameter opening which is coupled to the 10-cm-diameter plenum by a wide-angle conical diffuser.

A jet at $Re = 100,000$ was excited by both internal and external axial forcing to compare the effects of these two different means of introducing the same forcing mode. Figure 5.30 compares these effects at low excitation amplitudes while Fig. 5.31 provides a comparison at high excitation amplitude. Both means of forcing control the vortex formation process. The difference shows up in the minimum amplitude required to generate distinct vortex rings and in the size of those vortices. It appears that the internally introduced excitation is much more effective in causing vortex roll-up and hence produces larger structures at a given forcing level.

Figures 5.30 and 5.31 also provide an unintended example of particle-tracking. A particle track is seen to the right of the jet near its exit in Fig. 5.30a. Another track is seen in the upper left corner of Fig. 5.31b. These tracks provide an indication of the movement of the entrained flow. Velocities could be deduced from these tracks since the laser repetition rate is known. For example, the particle track consisting of the four dots near the jet exit in Fig. 5.30 corresponds to a velocity of 17 m/s in the plane of the light sheet. It is interesting that the particle in Fig. 5.31b moves downstream and then upstream as it nears the jet. This cusped pattern suggests that organized structures might exist in the jet even where they are no longer visible due to the limitations of the smoke-visualization technique.

5.3 Helically-excited jet

Even as a regular array of coaxial vortex rings indicates an axially-excited jet, a spiral deformation of a jet's shape is a signature of a helically-excited jet (Fig. 5.32). This signature takes different forms as the level of excitation is changed. At higher levels of forcing, the spiral shape is more pronounced and the vortex structures are larger (Figs. 5.33 and 5.34). The staggered orientation of the vortical structures in these cross-sections suggests that the structures are sections of tilted rings or of a spiral tube.

As was seen in the axially-excited jets, the same absolute excitation level does not have the same effect at different Reynolds numbers. Figures 5.33 and 5.34 correspond to the same absolute level of excitation but different Re. Phase-averaged realizations of helically-excited jets at different excitation amplitudes and Reynolds numbers are given in Figs. 5.35 and 5.36. From Fig. 5.36, one can note that increasing amplitude increases the global spreading angle of the jet. This correlation of amplitude and angle is not seen in the axially-excited jet (Fig. 5.25).

The effect of St_h at a fixed excitation amplitude is seen in Fig. 5.37. A similar comparison at a higher amplitude is presented in Fig. 5.38. Figures 5.39 and 5.40 provide an enlarged view of the near field of these flows. The primary effect of increasing St_h is the decrease of the spacing between vortex structures. Two vortex cores are seen coalescing on the right side of the jet in Fig. 5.40c.

The values of St_h considered here were chosen to be one half of the values used in the axially-excited jet (Fig. 5.28). This choice follows from the fact that in the bifurcating jet the helical frequency is half of the axial frequency.

The phase evolution of a helically-excited jet is shown at Reynolds number 100,000 in Fig. 5.41. Successive pictures are separated by 45° in phase. Focusing on the phase evolution of the shear layer around $z/D = 2$, one notes that the shear layer initially thickens, then forms a large vortical structure, and subsequently thins as the vortical structure propagates downstream. Another way to consider the phase-evolution of the jet is to watch the changing shape of the jet core. At

some phases the initial bend of the jet core is to the right while at other phases it is to the left. Comparing views that are 180° apart in phase is like looking at mirror images of the same flow.

5.4 Bifurcating jet

The structure of the bifurcating jet differs dramatically from those of the axially and helically excited jets. Figure 5.42 displays a cross-section of a bifurcating jet in the plane of bifurcation at $Re = 10,000$ and $St_a = 0.55$. The jet appears similar to an axially-excited jet near the exit except for the slight displacement and tilt of the vortices. Farther downstream, however, the flow abruptly splits into two distinct jets with an included angle of 70°. Initially adjacent vortex rings propagate along different branches of the jet. This results in the jet fluid being stretched back and forth between the two branches of the jet. Eventually, the vortex sheet connecting adjacent vortex rings vanishes.

In this case a transverse rather than helical excitation is used. The transverse forcing is achieved by turning off the two external speakers that do not lie in the plane of bifurcation. Bifurcation occurs only when the phase between the axial and transverse signals is properly adjusted.

Figure 5.43 presents this bifurcating jet at different phases of the transverse excitation. Figures 5.43a–d correspond to one half of the excitation period, and Figs. 5.43e and 5.43f correspond to the other half. During each half of the period one vortex ring is produced near the jet exit. This is consistent with the fact that the ratio f_a/f_t exactly equals two. Since these two rings evolve during different halves of the transverse signal, they tilt toward opposite sides of the jet.

Looking at the third ring downstream from the jet exit, one can see vortical fluid being pulled through the center of the vortex. In Fig. 5.43e, it appears that the entrained vortical fluid originated from the vortex sheet connecting the second and third vortices. As this segment of the vortex sheet passes through the third

vortex, it closes on itself to form the observed closed element. It is subsequently stretched toward the outer surfaces of the vortex ring as seen in Fig. 5.43f.

Figures 5.43c and 5.43d show that the vortex rings do not always remain intact as they separate onto alternate trajectories. The left half of the fourth vortex ring seen in Fig. 5.43c is swallowed by the fifth vortex ring in Fig. 5.43d.

A bifurcating jet at $Re = 50,000$ is displayed in Fig. 5.44. Unlike laminar vortex rings in the low Re jet, the vortex rings in this flow are very turbulent. Additionally, the large vortical structures are formed from the coalescence of much smaller ones rather than directly from the initially laminar shear layer. The cross-sections of several vortex rings can be seen on the left branch of the jet. Bifurcating jets at $Re = 100,000$ and at different combinations of axial and helical amplitudes are presented in Figs. 5.45 and 5.46.

The phase-evolution of a bifurcating jet at $Re = 100,000$ and $St_a = 0.55$ is presented in Fig. 5.47. Each phase-averaged picture corresponds to a different phase of the helical excitation. The phase difference between successive views is 45°. Within the first two diameters, one can see adjacent vortex rings tilted toward opposite sides of the jet. In this case, however, the vortex structures are not able to separate from each other onto alternate trajectories. Instead, sections of two adjacent rings combine. In a full, three-dimensional view, one might see an array of vortex rings tilting toward alternate sides of the jet with one side of a given ring coalescing with a section of the ring downstream of it while its other side combines with a portion of an upstream ring.

The bifurcating jet exhibits different behavior in the bifurcating and bisecting planes. The *bifurcating plane* is the plane passing through the nozzle axis and containing the two branches of the bifurcating jet. The *bisecting plane* is the plane passing through the nozzle axis and perpendicular to the bifurcating plane. A bifurcating jet at $Re = 100,000$ is viewed in both the bifurcating and bisecting planes in Fig. 5.48. Note that the bifurcating jet does not spread axisymmetrically. Instead, it spreads dramatically in the bifurcating plane while in the bisecting plane the smoke disappears several diameters downstream from the jet exit. However,

each branch of the jet spreads as a single jet along its own axis (Lee & Reynolds 1985b).

Unlike combined axial and transverse excitations, the relative phase between axial and helical excitations does not determine whether the jet bifurcates but rather determines the plane in which the jet bifurcates. One can rotate the bifurcating jet about its centerline by simply changing the relative phase. Thus, one can look at different cross-sections of the flow without moving the light sheet. Varying the relative phase in 30° steps, one obtains the cross-sections in Fig. 5.49. Abrupt changes in spreading angle are seen as the bifurcation plane is rotated away from the plane of illumination. Views that are 180° apart are mirror images of each other since they correspond to viewing the jet from opposite sides of the flow.

The effect of varying $\bar{p}_h$ while keeping $\bar{p}_a$ fixed is considered in Fig. 5.50. A similar comparison at a higher value of $\bar{p}_a$ is presented in Fig. 5.51. The corresponding phase-averaged visualizations are given in Figs. 5.52 and 5.53. Figure 5.54 is an enlarged view of Fig. 5.53c. One can see that the spreading angle definitely increases with $\bar{p}_h$. Figures 5.50d and 5.51d suggest that increases of $\bar{p}_h$ above a certain level results in the spreading angle decreasing. However, one would not make the same conclusion from the phase-averaged visualizations. Part of the explanation of this discrepancy might lie in the fact that the instantaneous and phase- averaged pictures do not generally correspond to the same phase of excitation. As Fig. 5.55 illustrates, when the phases of excitation are essentially identical, the two different visualization schemes are consistent.

A similar comparison of amplitude variations at $Re = 100,000$ is presented in Fig. 5.56. When $\bar{p}_h$ is low, the jet is almost identical to an axially-excited jet. Noticeable differences along with larger spreading angles result from higher levels of $\bar{p}_h$.

The effect of varying $\bar{p}_a$ while keeping $\bar{p}_h$ fixed is considered in Fig. 5.57. The phase-averaged pictures in Fig. 5.58 correspond to the same value of $\bar{p}_h$ but to a partially different set of values of $\bar{p}_a$. If $\bar{p}_a$ is too small, little difference is seen from the helically-excited jet (Figs. 5.57a and 5.57b). At certain levels, increasing $\bar{p}_a$

increases the spreading angle (Figs. 5.57c, 5.57d, 5.58b, and 5.58c). The increases in spreading angle are minimal when $\bar{p}_a \geq 2.8\%$ (Compare Figs. 5.56d & 5.59 and Figs. 5.58c and 5.58d.).

Bifurcating jets at different St_a are compared in Fig. 5.60. The corresponding phase-averaged views are given in Fig. 5.61. A comparison at lower excitation levels is presented in Fig. 5.62. Over this range of St_a, the changes in spreading angle are minimal although Fig. 5.60 does suggest a small increase in spreading angle with St_a.

Along with excitation amplitude and frequency, the method of forcing also affects the spreading angle. Figures 5.63 and 5.64 illustrate the effects of two means of forcing on a bifurcating jet at $Re = 100,000$. In Figs. 5.63a and 5.64a, the axial and helical excitations are introduced *separately* through the internal and external acoustic drivers. In Figs. 5.63b and 5.64b, the two signals are *combined* and are introduced through the external drivers alone. At the lower excitation level (Fig. 5.63), there is only a small difference in the spreading angle between the two means of forcing. At the higher level (Fig. 5.64), the bifurcating jet produced by the separate excitations spreads much more rapidly.

Many of the trends observed in this section can be summarized by plotting the spreading angle as a function of excitation amplitudes. The spreading angle is taken to be the angle formed by the edges of the smoke. Except at $Re = 10,000$, only phase-averaged pictures are used to determine spreading angles. Since the vortex structures are very distinct and well organized at $Re = 10,000$, one can easily determine the spreading angle from instantaneous pictures. The dependence of spreading angle on excitation amplitudes at $Re = 100,000$ and 50,000 is presented in Fig. 5.65 for the method of combined excitations. Figure 5.65a clearly shows that the spreading angle increases as either excitation amplitude is increased. The spreading angles range from around 17° (typical of natural jets) to over 40°. This trend is not as distinct at $Re = 50,000$ (Fig. 5.65b).

The largest spreading angles (up to 70°) resulted when separate excitations were used. Figure 5.66 displays the spreading angle characteristics of bifurcating

jets at $Re = 10,000$ and 100,000 produced by separate excitation. These results also indicate that the spreading angle increases with both excitations amplitudes.

The mean velocity field of a bifurcating jet at $Re = 100,000$ is compared with that of a natural jet in Fig. 5.67. Since a single-wire probe was used to make this measurement, the measured velocity is actually the magnitude of the velocity vector in the plane of bifurcation. This result indicates that the double-peak profile seen in low-Re flows (Fig. 1.4) is also characteristic of high-Re bifurcating jets.

5.5 Summary

This chapter contains the results of a flow-visualization study of excited jets. The effects of axial, helical, and combined excitations on the structure of round jets were considered. While a regular array of coaxial vortex rings are produced by axial excitation, the shear layer of a helically-excited jet appears to form a spiral-shaped vortex. Combining axial and helical excitations with $f_a/f_h = 2$ produces a bifurcating jet.

Reynolds number and excitation amplitudes were the primary parameters considered in this experimental study. The Reynolds number was varied by changing the mean velocity of the jet. As one would expect, a wider range of length scales and turbulent rather that laminar vortex structures are seen at the higher Reynolds numbers. Increasing the excitation amplitude produces more distinct vortex structures and, in the case of the bifurcating jet, generally increases the jet spreading angle. The excitation amplitudes required to produce bifurcating jets was found to increase with Re, but no general scaling relationship could be determined.

Chapter 6
DISCUSSION

Properly-combined axial and helical excitations can cause a turbulent round jet to split into two distinct jets. This unique flow, known as a bifurcating jet, exhibits spreading angles as high as 70°. This work has focused on determining the mechanism of bifurcation, extending previous work to higher Reynolds number flows, and understanding the effects of excitation frequency, amplitude, and phase on the evolution of bifurcating jets.

This research effort involved both a numerical and experimental investigation of bifurcating jets. The numerical work primarily targeted the questions concerning the mechanism of bifurcation and the role of excitation frequency. The experimental work extended the bifurcation phenomenon to $Re = 100,000$ and documented the effects of various excitation parameters.

The research methods and results were described in Chapters 2–5. The significance of those results is discussed in the following sections on natural states of round jets, the structure and features of bifurcating jets, the role of excitation frequency, the role of excitation amplitude and phase, and the mechanism of bifurcation. The effect of Reynolds number is touched on in each of these sections. The reasons for the discrepancies between computations and experiments are not completely clear, but several possible causes are presented in Section 6.5. Finally, the chapter concludes with some thoughts on the implications of this specific work on the general issue of jet flow control.

6.1 Natural states of round jets

Stability theory predicts the existence of both axisymmetric and helical modes in round jets (Michalke & Hermann 1982). This prediction is consistent with the visualizations of unexcited jets (Figs. 5.8–5.10). Axisymmetric vortices of varying scales are found in the near field, and the spacing of the initially-formed vortices

corresponds to the natural frequency of the shear layer. The interaction of the ring structures is quite asymmetric at the higher Reynolds numbers. Downstream of the potential core region, the jet sometimes exhibits a helical structure.

Axial forcing produces an orderly arrangement of large axisymmetric structures. At $Re = 10,000$, these structures are initially laminar, and the roll-up of the shear layer is clearly visible within the vortex cores (Fig. 5.17). At all higher Reynolds numbers, the structures are turbulent, and pockets of ambient fluid within the core are only seen at the highest forcing amplitudes (Fig. 5.24).

Helical forcing generates asymmetric vortex structures. We have demonstrated this at Re up to 100,000 but expect it to be true at all Re for subsonic flows. The cross-sectional view suggests that the complete structure is a single vortex coil like that seen by Koch *et al.* (1988) at $Re = 10,000$. The phase-evolution of the helical structure at $Re = 100,000$ indicates that the structure rotates as time progresses (Fig. 5.41). Thus, the time-averaged, net axial vorticity is zero.

6.2 Structure and features of bifurcating jets

The most striking feature of the bifurcating jet is its wide-angle, Y-shaped structure. This structure is formed by the jet splitting into two distinct jets. Superimposed on this flow are the distinct vortex rings formed by the axial excitation. Initially adjacent rings propagate along alternate branches of the jet (Fig. 5.43). In the cross-sectional views, portions of the shear layer appear as filaments connecting the initially adjacent rings. As the rings get far enough apart, the vortex sheet connecting them is apparently torn apart. Eventually, the vortex rings break down into turbulent puffs of smoke. The stretching of the vortex sheet and the breakdown of the vortex rings results in smaller-scale secondary structures.

At the higher Reynolds numbers ($Re > 10,000$), there is a much wider range of scales, and the structures are much more turbulent. As a result, the characteristic Y-shaped structure seen at lower Re is not seen. Instead, one simply sees a jet that spreads rapidly in one plane but not in the perpendicular plane. In the near field,

however, vortex rings tilting in opposite directions are observed as in the bifurcating jet at $Re = 10,000$.

These observations about the bifurcating jet lead to an interesting question of semantics. How should a bifurcating jet be defined? Two criteria are proposed. First, do visualizations indicate that the jet splits into two separate jets? Second, does the velocity profile of the jet consist of two separate peaks that persist into the far field of the jet? Satisfaction of either of these criteria should be considered as sufficient for classifying a jet as a bifurcating jet. The fact that a jet spreads much more rapidly in one direction than in the perpendicular direction is not a sufficient condition since elliptic and indeterminate-origin jets also exhibit this characteristic. In the case where the turbulence of the flow obscures the structure of the jet, the flow-visualization criterion should be that the jet fluid disappears as one moves downstream in the transverse plane. This secondary criterion is consistent with the pictures and velocity measurements presented in Figs. 5.48 and 5.67. Based on these ideas, one might consider many of the "bifurcating jets" discussed in Ch. 5 to correspond actually to a transition state linking natural and bifurcating jets.

6.3 Role of excitation frequency

The role of the excitation frequency can be characterized in terms of the frequency ratio R_f and the axial Strouhal number St_a. Dual-mode excitation will cause a jet to split into two distinct, stationary jets only if $R_f = 2$. The flow phenomena that occur when $R_f \neq 2$ are well documented by Lee and Reynolds (1985b).

The axial Strouhal number determines the frequency characteristic of the largest vortex rings. Consequently, St_a also determines the spacing between rings, and the spacing decreases as St_a increases (Fig. 5.28). In a similar manner, the helical Strouhal number determines the length-scale characteristic of helical structures (Figs. 5.39 and 5.40). Both the computations and the experiments of Lee and Reynolds (1985b) demonstrate that within a range of Strouhal numbers, the

spreading angle increases. Outside that range the jet does not exhibit two distinct branches. Below that range the jet appears much like a natural jet.

The range of St_a over which the bifurcation phenomenon occurs does not depend on δ_ω/R. The vorticity thickness at Re = 10,000 is about seven times larger than that at Re = 100,000, yet in both cases the maximum jet spreading occurs around $St_a = 0.55$. At very high excitation amplitudes, the bifurcating jet at $Re = 10,000$ and $St_a = 0.55$ (Fig. 5.42) spreads at an angle identical to a bifurcating jet at $Re = 3700$ and $St_a = 0.55$ (Fig. 4.26e in Lee & Reynolds 1985b). These observations imply that it is the large vortex rings formed by pairings or collective interactions and not the small ones formed by the initial roll-up of the shear layer that are important in the bifurcation process. The invariance of St_a over this Reynolds number range also suggests that the key mechanism causing bifurcation is an inviscid instability.

6.4 Role of excitation amplitude and phase

While the mode of excitation determines the type of structures formed, the amplitude of excitation determines how distinct and how large those structures are. The amplitude also affects how structures are formed. In the case of axially-excited jets, low and moderate levels of forcing produce large vortices by causing a collective interaction or multiple pairings of the smaller vortices. Distinct structures first appear in the phase-averaged views at Re = 50,000 and 100,000 when $\bar{p}_a \simeq 1\%$ (Figs. 5.23 and 5.25). A large forcing level ($\bar{p}_a = 12\%$) can produce the large structures directly at $Re = 10,000$ (Fig. 5.18).

In the case of thin laminar exit boundary layers, θ/D scales with $Re^{-1/2}$. Combining this scaling relationship with Eqn. 4.5, one can show that the ratio of the natural to the forcing frequency at fixed St_D and St_θ scales with $Re^{1/2}$. Consequently, as one increases Re, one moves farther from the peak of the amplification curve of linear stability theory. Therefore, stronger forcing is required as Re increases.

The Reynolds number also has an effect through the mean velocity, which is an important scaling parameter in stability analysis. No clear Reynolds-number scaling of the total amplification at a fixed St_D was found. This is not surprising since both linear amplification and nonlinear saturation, as well as laminar and turbulent structures, are involved.

In the bifurcating jet, increasing either the axial or helical excitation can increase the jet spreading angle. The results suggest that bifurcation does not occur below certain levels and that jet spreading does not continue to increase beyond certain limits. The bounds of this amplitude range could not be clearly defined.

Typically, it is the axial amplitude that must be larger. One might expect it to be the other way around since the jet splits in the direction of the helical forcing. However, it is the interaction of vortex rings that splits the jet and causes the wide spreading angles, and it is the axial amplitude that governs the production of those rings. The higher the axial amplitude, the more concentrated is the vorticity of the rings and the stronger are their interactions. Also, linear stability predicts that helical disturbances are more strongly amplified even in the near field when the disturbance frequency is much less than the natural frequency (Michalke & Hermann 1982).

Along with the amplitude, the phase of excitation is very important. The phase referred to here is the relative phase between the axial and helical/transverse signals. When a helical excitation is used, this phase determines the azimuthal plane in which the jet bifurcates. When a transverse excitation is used, the phase determines whether or not bifurcation occurs. As discussed in Ch. 4, bifurcation occurs in the azimuthal plane in which every other peak of the axial signal coincides with a peak of the helical signal.

6.5 Comparison of computations and experiments

A comparison of the numerical results with the experimental results of Lee & Reynolds (1985b) reveals both major similarities and significant differences. The

Y-shaped structure of the bifurcating jet, the alternating trajectories of the vortex rings, the increase of spreading angle with Strouhal number and excitation amplitude, and the inviscid vortex-interaction model are common conclusions. Another interesting area of comparison is the relative spacing of the vortex rings. The parameter $\mathcal{R}_s$ was defined in Ch. 3 to be the ratio of the distance between rings on a branch of the bifurcating jet to that on the trunk of the jet. The analysis of a train of rings yields $\mathcal{R}_s$ =1.6–1.7 over a wide range of St. The simulation of a bifurcating jet at $St = 0.42$ predicts a value of $\mathcal{R}_s = 1.5$. Experimental results indicate a value of about 1.5 (Figs. 1.1, 5.17, and 5.42). The fact that the jet splits into two distinct jets requires that the characteristic frequency of branch rings equal half that of the axial perturbation. However, $\mathcal{R}_s$ does not equal two because of the decrease of convection velocity with increased ring spacing.

The two sets of results differ in the specification of spreading angle dependence on A_0 or St_a. The numerical simulation requires an order of magnitude higher amplitude to achieve comparable spreading angles. Additionally, the computations conclude that bifurcating jets with distinct branches do not occur for $St_a > 0.42$ while the experiments specify a bound of $St_a > 0.65$.

These discrepancies exist, in part, because of the approximations made by the numerical simulation. First, the numerical scheme represents vortex rings by piecewise linear segments. Second, to keep the number of parameters low, the tilt of the nozzle in the experiments of Lee and Reynolds (1985b) is not included. Finally, the roll-up of the shear layer is assumed rather than simulated, and only a single filament represents each vortex ring. Nevertheless, the numerical simulation does clearly demonstrate the central role of vortex interactions, and elimination of these approximations would require a much more complex and costly simulation.

6.6 Mechanism of bifurcation

The evolution of imposed disturbances in shear flows is often discussed in terms of instability waves or vortex interactions. The dominant presence of vortex struc-

tures in bifurcating jets, the nonlinearity of the bifurcation process, and the approach of the numerical simulations suggest reasoning in terms of vortex concepts. One could possibly explain the physical mechanism of bifurcating jets in terms of instability waves, but a vortex-interaction model is more intuitive and follows more directly from the results of this work.

The mechanism causing bifurcation can be described in terms of vortex interactions. The shear layer rolls up into a periodic array of vortex rings in response to the axial forcing. The helical or transverse forcing displaces these rings eccentrically. The resulting staggered array of rings is unstable. As a result, the rings tilt away from each other until initially adjacent rings eventually propagate along two different trajectories.

The instability of an eccentric arrangement of rings follows from their mutual induction. Each ring causes its neighboring rings to tilt away from itself. The strength of this interaction depends on the spacing and eccentricity of the rings and their circulation. Thus, both excitation frequency and amplitude affect this interaction and, consequently, the spreading angle of the jet. Once two separate trajectories are established, the rings on each branch are concentric with each other, and hence each branch evolves as a separate jet. Similar reasoning can be used to explain the blooming jets.

8.7 Some thoughts on jet flow control

This work along with that of Lee and Reynolds indicates that one can dramatically modify the evolution of jet flows with moderate perturbations. The effectiveness of these perturbations lies in their ability to trigger flow instabilities that amplify the effects of the imposed excitations. Additionally, it is important to note that the proper triggering of two different instabilities produces an effect that neither can achieve on its own.

The specific means of introducing the required perturbations is not critical to generating a bifurcating jet as long as the excitation is focused on the shear layer

at the exit. Both mechanical and acoustic systems are effective, and in acoustic systems, the different modes can be introduced separately or together. However, these systems are not equally effective. Generation of the axial excitation by the internal rather than the external acoustic drivers was found to be more effective. Additionally, a helical excitation that only oscillates the origin of the jet can not force the shear layer to roll up into a coil-like structure (Lee & Reynolds 1985b) whereas a system that produces an azimuthally-varying helical perturbation can (Koch *et al.* 1988).

There are two ideas inherent to the concept of flow control. One is the modification of a flow from its natural state to some desired state. This is primarily a question of physics. The other is the control system required to achieve those modifications. Since the roles of most of the key parameters are well understood, one could automate a bifurcating jet with an open-loop control system. Sensing the jet velocity, a control system could easily calculate the required excitation frequencies. This system could maintain a bifurcating jet in the presence of variations of the mean flow. A closed-loop controller would be required to optimize the excitation to achieve a desired system characteristic or to implement the bifurcating jet in widely-varying ambient conditions.

Chapter 7

CONCLUSIONS AND RECOMMENDATIONS

A combined numerical and experimental investigation of bifurcating jets has been described. The numerical scheme is based on the discrete-vortex method. The experiment involved dual-mode, dual-frequency, acoustic excitation of round jets at Reynolds numbers from 10,000 to 100,000. The effects of excitation amplitude, frequency, and phase and the significance of Reynolds number were considered.

7.1 Conclusions

On the basis of the work described in the previous chapters, several conclusions can be made that affirm and extend the previous understanding of bifurcating jet flows. Those conclusions are as follows:

1. Dual-mode acoustic excitation can produce bifurcating jets in air at Reynolds numbers up to 100,000 and Mach numbers up to 0.22.
2. The structure of the bifurcating jet consists of a Y-shaped jet with adjacent vortex rings propagating along alternate branches of the jet. This jet spreads at angles up to 70° in the plane of bifurcation. The characteristic frequency of the rings on a branch is half that of the rings on the trunk of the jet. The spacing between rings is about 1.5 times greater on the branch than on the trunk.
3. The bifurcation phenomenon can be modeled as an inviscid, vortex-interaction process. Axial excitation periodically creates vortex rings. Helical or transverse excitation causes the rings to be displaced and tilted away from each other. The array of vortex rings produced by the combination of these two excitations is unstable as a result of the rings' mutually-induced motions.
4. Bifurcation occurs only within a range of Strouhal numbers. Within that range, the spreading angle increases with Strouhal number. The numerical simulations predict that range to be 0.30–0.42. However, the experiments show that the

upper limit should be around 0.65. Bifurcation occurs only when the ratio, R_f, of axial to helical frequency is two.

5. The relative phase between the axial and helical signals determines the plane in which the jet bifurcates. The relative phase between axial and transverse signals determines whether or not a jet bifurcates.
6. The spreading angle increases with both excitation amplitudes. The results suggest that bifurcation does not occur below certain levels and that jet spreading does not continue to increase beyond certain limits. The bounds of this amplitude range could not be clearly defined.
7. For a given nozzle geometry, the required excitation levels increase with Reynolds number. This is partly due to the fact that θ/D decreases with increasing Re, resulting in a larger disparity between the imposed and naturally most amplified frequencies. The increase of mean velocity with Re is another factor. The useful range of excitation Strouhal numbers is independent of Reynolds number.

7.2 Recommendations

Further study in the area of bifurcating and blooming jets needs to address the following issues concerning amplitude scaling, receptivity, and competing mechanisms:

1. Determination of the excitation required under different flow conditions requires formulation and understanding of the scaling parameters. Further work is needed to establish how the required helical excitation amplitude and power scale with jet diameter.
2. Since increases in jet velocity require increases in excitation amplitude, producing the excitation levels required to control high-velocity flows is difficult and costly. Thus, techniques of enhancing the receptivity of the shear layer to the excitation signal need to be developed.

3. Many flows of practical interest involve supersonic velocities, combustion, and forward flight. The effectiveness of dual-mode forcing in the presence of shock-shear-layer interactions, additional forcing produced by combustion, large density gradients, and external flow is not known.

Research in these areas is important not only to provide new insights about the physics of excited jet flows but also to make practical applications of bifurcating jets more feasible.

Appendix A

DERIVATION OF INDUCED-VELOCITY FUNCTIONS

A.1 Vortex segment

Consider the point at $\mathbf{r}$ and the vortex segment defined by $\mathbf{e} \equiv \mathbf{r}_1 - \mathbf{r}_0$. Let $\mathbf{r}_j(\xi) = \mathbf{r}_0 + \xi\mathbf{e}$, for $0 \leq \xi \leq 1$. Then by Eqn. 2.6, the velocity induced by the vortex segment is given by

$$\mathbf{u}(\mathbf{r}) = -\frac{\Gamma}{4\pi}[(\mathbf{r}-\mathbf{r}_0)\times\mathbf{e}]\int_0^1 \frac{d\xi}{[|(\mathbf{r}-\mathbf{r}_0)-\xi\mathbf{e}|^2+\alpha\sigma_j^2]^{3/2}}. \qquad A.1$$

Using the definitions of p and q given in Eqn. 2.10, one can rewrite Eqn. A.1 as

$$\mathbf{u}(\mathbf{r}) = -\frac{\Gamma}{4\pi}\frac{[(\mathbf{r}-\mathbf{r}_0)\times\mathbf{e}]}{|\mathbf{e}|^3}\int_0^1 \frac{d\xi}{[\xi^2-2p\xi+q^2]^{3/2}}. \qquad A.2$$

Solving the definite integral in Eqn. A.2, one obtains

$$\mathbf{u}(\mathbf{r}) = -\frac{\Gamma_j}{4\pi}\left[\frac{(1-p)}{\sqrt{(1-p)^2+\lambda^2}}+\frac{p}{q}\right]\frac{[(\mathbf{r}-\mathbf{r}_j(n,t))\times\mathbf{e}]}{\lambda^2|\mathbf{e}|^3}, \qquad A.3$$

where $\lambda^2 \equiv q^2 - p^2$.

A.2 Circular vortex filament

Consider the point P located at (r, z, θ) and a circular vortex filament having radius R and circulation Γ and centered at the origin. Applying Eqn. 2.6 and making use of the symmetry of the filament about the plane defined by P and the filament's centerline, one obtains the following components of the induced velocity:

$$u_r = \frac{\Gamma R}{2\pi}\int_0^\pi \frac{z\cos\theta}{[R^2+z^2+r^2+\alpha\sigma^2-2Rr\cos\theta]^{3/2}}\,d\theta, \qquad A.4a$$

$$u_z = \frac{\Gamma R}{2\pi} \int_0^{\pi} \frac{R - r\cos\theta}{[R^2 + z^2 + r^2 + \alpha\sigma^2 - 2Rr\cos\theta]^{3/2}}\, d\theta, \qquad A.4b$$

and

$$u_\theta = 0. \qquad A.4c$$

Simplifying Eqn. A.4a and A.4b by substitution of the non-dimensional variables defined in Eqn. 2.13 gives

$$u_r = \frac{(\Gamma/R)\bar{z}}{2\pi\bar{\nu}^{3/2}} \int_0^{\pi} \frac{\cos\theta}{(1 - \bar{\eta}\cos\theta)^{3/2}}\, d\theta, \qquad A.5a$$

and

$$u_z = \frac{(\Gamma/R)}{2\pi\bar{\nu}^{3/2}} \int_0^{\pi} \frac{1 - \bar{r}\cos\theta}{(1 - \bar{\eta}\cos\theta)^{3/2}}\, d\theta. \qquad A.5b$$

Solving the definite integrals in Eqn. A.5 yields

$$u_r = \frac{(\Gamma/R)\bar{z}}{2\pi\bar{r}\sqrt{\bar{\nu} + 2\bar{r}}} \left[\frac{1}{(1 - \bar{\eta})} E(1 - m_1) - K(1 - m_1)\right], \qquad A.6a$$

and

$$u_z = \frac{(\Gamma/R)}{\pi\bar{\nu}^{3/2}\sqrt{1 + \bar{\eta}}} \left[\frac{(1 - \frac{\bar{\nu}}{2})}{(1 - \bar{\eta})} E(1 - m_1) + \frac{\bar{\nu}}{2} K(1 - m_1)\right], \qquad A.6b$$

where K and E are complete elliptic integrals of the first and second kind and m_1 is given by Eqn. 2.13f. These complete elliptic integrals are defined as follows:

$$K(m) \equiv \int_0^{\pi/2} \frac{d\theta}{\sqrt{1 - m\sin^2\theta}}, \qquad A.7a$$

and

$$E(m) \equiv \int_0^{\pi/2} \sqrt{1 - m\sin^2\theta}\, d\theta. \qquad A.7b$$

Polynomial approximations for $K(m)$ and $E(m)$ are given in Sec. A.4.

A.3 Semi-infinite cylindrical vortex sheet

Consider a semi-infinite, cylindrical vortex sheet extending along the z-axis from $-\infty$ to 0 and having a circulation per unit length equal to γ. The velocity induced at a point (r, z, θ) can be found by adapting Eqn. A.4 to this geometry as follows:

$$u_r = \frac{\gamma R}{2\pi} \int_{-\infty}^{0} \int_{0}^{\pi} \frac{(z - z') \cos\theta}{[R^2 + (z - z')^2 + r^2 + \alpha\sigma^2 - 2Rr\cos\theta]^{3/2}} \, d\theta \, dz', \qquad A.8a$$

$$u_z = \frac{\gamma R}{2\pi} \int_{-\infty}^{0} \int_{0}^{\pi} \frac{R - r\cos\theta}{[R^2 + (z - z')^2 + r^2 + \alpha\sigma^2 - 2Rr\cos\theta]^{3/2}} \, d\theta \, dz', \qquad A.8b$$

and

$$u_\theta = 0. \qquad A.8c$$

Simplifying Eqns. A.8a and A.8b by the dimensionless variables and integrals defined in Eqns. 2.13, 2.15, and A.7, one obtains

$$u_r(\bar{r}, \bar{z}) = \frac{\gamma}{2\pi\sqrt{\bar{\nu}}} I(\bar{\eta}), \qquad A.9a$$

and

$$u_z(\bar{r}, \bar{z}) = \frac{\gamma}{2\pi\bar{\rho}} \left\{ \frac{\pi}{2} \left[\frac{(2 - \bar{\rho})}{\sqrt{1 - \bar{\mu}^2}} + \bar{\rho} \right] - \frac{\bar{z}}{\sqrt{\bar{\nu}}} \left[\frac{2}{\sqrt{1 + \bar{\eta}}} K(1 - m_1) + (\bar{\mu} - \bar{r}) \, T(\bar{\mu}, \bar{\eta}) \right] \right\}, \qquad A.9b$$

Let $\phi \equiv (\pi - \vartheta)/2$. Then by Eqn. 2.15c,

$$I(\bar{\eta}) = 2 \int_{0}^{\pi/2} \frac{1 - 2\cos^2\phi}{\sqrt{1 - \bar{\eta} + 2\bar{\eta}\cos^2\phi}} \, d\phi. \qquad A.10$$

The definite integral in Eqn. A.10 can be split into two definite integrals that match the complete elliptic integrals (Eqn. A.7) such that

$$I(\bar{\eta}) = \frac{2}{\bar{\eta}\sqrt{1 + \bar{\eta}}} [K(1 - m_1) - (1 + \bar{\eta}) \, E(1 - m_1)]. \qquad A.11$$

A.4 Approximations of elliptic integrals

When evaluating $K(m)$ and $E(m)$ numerically, it is valuable to have simple and accurate approximations for them. The following approximations are from the *Handbook of Mathematical Functions* by Abramowitz and Stegun (Dover Press):

$$K(m) = 1.3862944 + 0.1119723m_1 + 0.0725296m_1^2 + (0.5 + 0.1213478m_1 + 0.0288729m_1^2)\ln(1/m_1) + \epsilon_K(m), \qquad A.12a$$

and

$$E(m) = 1 + 0.4630151m_1 + 0.1077812m_1^2 + (0.2452727m_1 + 0.0412496m_1^2)\ln(1/m_1) + \epsilon_E(m), \qquad A.12a$$

where $|\epsilon_K(m)| \leq 3 \times 10^{-5}$, $|\epsilon_E(m)| < 4 \times 10^{-5}$, and $m + m_1 = 1$.

Appendix B

PROGRAM LISTINGS

B.1 BIJET

```
C*********************************************************************
C
C
C              BIFURCATING/BLOOMING  JET  SIMULATION
C
C
C          This program uses vortex filaments to simulate 3-D
C     bifurcating/blooming jets.  The calculation uses a vortex
C     filament technique to represent the vorticity in the jet.
C     An analytical function is used to account for the vorticity
C     in the boundary layer in the nozzle.  These two components
C     of the simulation are combined by superposition.
C
C          A single filament is used to represent each vortex ring.
C     The user chooses STNUM (Strouhal number based on axial-
C     excitation frequency) and FRATIO (frequency ratio, FRATIO =
C     axial/orbital).  The program calculates the corresponding
C     axial and orbital frequencies of excitation and the
C     circulation/length of the nozzle function.
C
C
C     Output:        Unit 6
C
C     Written by:    David Parekh
C     Date:          October 1983
C
C*********************************************************************
C  *  Dimension variables and define common blocks.
      DIMENSION RNODE(3,5000),CRAD2(500),GAMMA(500)
      DIMENSION NSTART(500),NEND(500)
      DIMENSION POSNZ(3,1000),POSRNG(5,3,64),CENTER(3)
      COMMON /CORE/ CRAD2
      COMMON /RING/ NPERRG,NRINGS,NNODES,NSTART,NEND
      COMMON /MANYPI/ HALFPI,PI,TWOPI
      COMMON /PARM/ GAMMA,ALPHA,COEF
      COMMON /POS/ RNODE
```

```
C  *  Specify constants and parameters and initialize variables.
      DATA ALPHA/0.2065/      !  vorticity-distribution factor
      PI = 2.  * ASIN(1.)
      HALFPI = PI / 2.
      TWOPI = 2.  * PI
      COEF = -1.  / (4.  * PI)
      AMP = 0.3               !  amplitude of nozzle excitation
      NOZEXC = 1              !  type of nozzle excitation:
                              !  (NOZEXC = 0) => none
                              !  (NOZEXC < 0) => sinusoidal flapping
                              !  (NOZEXC > 0) => orbital
      STNUM = 0.32            !  Strouhal number based on axial frequency
      FRATIO = 2.0            !  ratio of axial to orbital frequency; must
                              !  have integer value </= 1st dim of POSRNG
      GAM = 1.0               !  circulation of ring
      VDELT = 2.0 / (GAM * (STNUM*STNUM))  ! time between ring creations
      GAMJET = SQRT(2.  * GAM / VDELT)      ! circulation/length of jet
      PRDA = 20.              !  period of axial excitation in DELT units
      PRDO = FRATIO * PRDA    ! period of orbital excitation (< dim POSJ)
      NPRDA = PRDA
      NPRDO = PRDO
      DELT = VDELT / PRDA     ! time step of simulation
      DELTO2 = DELT/2.0
      NSTEPS = 120            !  total number of time steps in simulation
      NSPACE = 1000           !  time step at which to change SPACE size
      NEWVTX = NPRDA          ! see SUBROUTINE GENRNG
      NPLOT = 10              !  see SUBROUTINE PLOT
      IOUT = 40               !  see SUBROUTINE OUTPUT
      TIME = 0.0
      NRINGS = 0              !  current number of rings
      ITH = IOUT              ! counter for SUBROUTINE OUTPUT
      NPTH = NPLOT            ! counter for SUBROUTINE PLOT
      INEWV = NEWVTX          ! counter for SUBROUTINE GENRNG
      NPHASE = FRATIO         ! counter for SUBROUTINE GENRNG
      INOZ = NPRDO            ! counter for SUBROUTINE RUNGE
C  *  Print output header.
      WRITE(6,100)
  100 FORMAT('1',9X,' NODE',15X,'X',25X,'Y',21X,'Z',///)
C  *  Calculate position of center of jet exit.
      CALL NOZPOS(AMP,PRDO,NPRDO,NOZEXC,  POSNZ)
C  *  Specify ring parameters and generate first ring at time zero.
C  *  *  Specify geometry of ring.
         NPERRG = 32          !  number of nodes per ring
```

```
      RAD = 1.0              !  radius of ring
      CORE2 = 0.01           !  square of the filament core radius
C  *  *  Generate array of coordinates of initial ring node positions.
      CALL RNGPOS(TWOPI,RAD,NPERRG,NPRDA,FRATIO,POSNZ,  POSRNG)
C  *  *  Generate initial ring.
      CALL GENRNG(GAM,CORE2,FRATIO,POSRNG, INEWV,NPHASE, NNODES)
C  *  *  Print initial coordinates of ring.
      CALL OUTPUT(NNODES,TIME,ITH)
C  *  Initialize plotting routine and plot initial ring.
C  *  *  Initialize GWE.
      CALL IGWE(23)
C  *  *  Define space boundaries.
      CALL SPACE(-0.5,25.0,-3.0,3.0,-3.0,3.0)
C  *  *  Plot initial ring.
      CENTER(1) = POSNZ(1,1)
      CENTER(2) = POSNZ(2,1)
      CENTER(3) = POSNZ(3,1)
      CALL PLOT(NPTH,NPLOT,CENTER)
C  *  Carry out the simulation for NSTEPS time steps.
      DO 1000 ISTEP=1,NSTEPS
C  *  *  Increment counters at beginning of time step.
      INEWV = INEWV + 1
      ITH = ITH + 1
      NPTH = NPTH + 1
      TIME = TIME + DELT
      IF(INOZ.NE.NPRDO)THEN
         INOZ = INOZ + 1
            ELSE
               INOZ = 1
      END IF
C  *  *  Assign position of center of jet exit.
      CENTER(1) = POSNZ(1,INOZ)
      CENTER(2) = POSNZ(2,INOZ)
      CENTER(3) = POSNZ(3,INOZ)
C  *  *  Update node positions by 2nd order Runge-Kutta.
      CALL RUNGE(DELT,DELTO2,NNODES,NPERRG,GAMJET,CENTER)
C  *  *  Generate a new vortex ring as specified.
      IF(INEWV.EQ.NEWVTX)
     &    CALL GENRNG(GAM,CORE2,FRATIO,POSRNG, INEWV,NPHASE, NNODES)
C  *  *  Print node positions as specified.
      IF(ITH.EQ.IOUT) CALL OUTPUT(NNODES,TIME,ITH)
C  *  *  Plot rings as specified.
      IF(ISTEP.EQ.NSPACE) CALL SPACE(-0.5,50.0,-5.0,5.0,-5.0,5.0)
```

```
         IF(NPTH.EQ.NPLOT) CALL PLOT(NPTH,NPLOT,CENTER)
 1000 CONTINUE
C  *   Specify end of plotting file.
      CALL FLASH
      STOP
      END


      SUBROUTINE RNGPOS(TWOPI,RAD,NPERRG,NPRDA,FRATIO,POSNZ,  POSRNG)
CCCCCCCCCCCCCCCCCCCCCCCCCCCCCCCCCCCCCCCCCCCCCCCCCCCCCCCCCCCCCCCCCCCCCCCCCC
C
C     This subroutine (SUBROUTINE RNGPOS) calculates the various
C     initial positions of the ring filaments and assigns these
C     coordinates to the array POSRNG.  POSRNG is a three-dimensional
C     array.  Its first index designates one of FRATIO possible
C     filament locations.  The second index designates a coordinate
C     direction, and the last index corresponds to the particular
C     nodes.  Thus, POSRNG(2,1,23) contains the x-coordinate of
C     the 23 node on the filament that is generated at position 2.
C     The various filament positions correspond to the index I in
C     DO-loop 20 in the subroutine.
C
CCCCCCCCCCCCCCCCCCCCCCCCCCCCCCCCCCCCCCCCCCCCCCCCCCCCCCCCCCCCCCCCCCCCCCCCCC
      DIMENSION POSRNG(5,3,64),POSNZ(3,1000),CIRCLE(3,64)
C  *   Calculate the coordinates of a circle of radius RAD, centered
C     about the origin in the Y-Z plane.
      SECT = NPERRG
      THETA = TWOPI / SECT
      DO 10 L=1,NPERRG
         DIV = L - 1
         ANGLE = DIV * THETA
         CIRCLE(1,L) = 0.0
         CIRCLE(2,L) = RAD * COS(ANGLE)
         CIRCLE(3,L) = RAD * SIN(ANGLE)
   10 CONTINUE
C  *   Calculate the position of the filament nodes.
      II = FRATIO    ! assumes FRATIO has an integer value
      K = 1          !  K designates which coordinate in array POSNZ
                     !  is the nozzle position corresponding to POSRNG
      DO 20 I=1,II
         DO 21 J=1,NPERRG
            POSRNG(I,1,J) = POSNZ(1,K) + CIRCLE(1,J)
            POSRNG(I,2,J) = POSNZ(2,K) + CIRCLE(2,J)
```

```
            POSRNG(I,3,J) = POSNZ(3,K) + CIRCLE(3,J)
   21     CONTINUE
          K = K + NPRDA
   20  CONTINUE
       RETURN
       END


       SUBROUTINE GENRNG(GAM,CORE2,FRATIO,POSRNG, INEWV,NPHASE)
CCCCCCCCCCCCCCCCCCCCCCCCCCCCCCCCCCCCCCCCCCCCCCCCCCCCCCCCCCCCCCCCCCCCCCCCCCCCCCC
C
C      This subroutine (SUBROUTINE GENRNG) specifies the initial
C      coordinates and core size of the nodes on the newly created
C      vortex ring.
C
CCCCCCCCCCCCCCCCCCCCCCCCCCCCCCCCCCCCCCCCCCCCCCCCCCCCCCCCCCCCCCCCCCCCCCCCCCCCCCC
       DIMENSION RNODE(3,5000),CRAD2(500),NSTART(500),NEND(500),
      &          GAMMA(500),POSRNG(5,3,64)
       COMMON /CORE/ CRAD2
       COMMON /RING/ NPERRG,NRINGS,NNODES,NSTART,NEND
       COMMON /PARM/ GAMMA,ALPHA,COEF
       COMMON /POS/ RNODE
C  *   Initialize and increment counters.
       INEWV = 0
       NRINGS = NRINGS + 1
       NNODES = NPERRG*NRINGS
       NRATIO = FRATIO
       IF(NPHASE.NE.NRATIO)THEN
          NPHASE = NPHASE + 1
             ELSE
                NPHASE = 1
       END IF
C  *   Specify node numbers, circulation, and core radius of ring NRINGS.
       NEND(NRINGS) = NNODES
       NSTART(NRINGS) = NNODES - NPERRG + 1
       GAMMA(NRINGS) = GAM
       CRAD2(NRINGS) = CORE2
C  *   Specify the initial coordinates of the nodes of ring NRINGS.
       NSN = NSTART(NRINGS)
       NEN = NEND(NRINGS)
       INDEX = (NRINGS - 1) * NPERRG
       DO 10 I=NSN,NEN
          K = I - INDEX
```

```
         RNODE(1,I) = POSRNG(NPHASE,1,K)
         RNODE(2,I) = POSRNG(NPHASE,2,K)
         RNODE(3,I) = POSRNG(NPHASE,3,K)
   10 CONTINUE
      RETURN
      END


      SUBROUTINE NOZPOS(AMP,PRDO,NPRDO,NOZEXC,  POSNZ)
CCCCCCCCCCCCCCCCCCCCCCCCCCCCCCCCCCCCCCCCCCCCCCCCCCCCCCCCCCCCCCCCCCCCCCCCCCCCCCC
C
C     This subroutine (SUBROUTINE NOZPOS) calculates the position
C     of the center of the jet exit as a function of time step and
C     the type of excitation specified by NOZEXC.  This subroutine
C     also assigns the calculated positions to the array POSNZ.
C
CCCCCCCCCCCCCCCCCCCCCCCCCCCCCCCCCCCCCCCCCCCCCCCCCCCCCCCCCCCCCCCCCCCCCCCCCCCCCCC
      DIMENSION POSNZ(3,1000)
      COMMON /MANYPI/ HALFPI,PI,TWOPI
C  *  Calculate jet center positions.
      THETA = TWOPI / PRDO
      IF(NOZEXC.GT.0)THEN
         DO 10 I=1,NPRDO
            DIV = I - 1
            ANGLE = DIV * THETA
            POSNZ(1,I) = 0.0
            POSNZ(2,I) = AMP*COS(ANGLE)
            POSNZ(3,I) = AMP*SIN(ANGLE)
   10    CONTINUE
         ELSE IF(NOZEXC.LT.0)THEN
            DO 20 I=1,NPRDO
               DIV = I - 1
               ANGLE = DIV * THETA
               POSNZ(1,I) = 0.0
               POSNZ(2,I) = AMP*COS(ANGLE)
               POSNZ(3,I) = 0.0
   20       CONTINUE
            ELSE
               DO 30 I=1,NPRDO
                  POSNZ(1,I) = 0.0
                  POSNZ(2,I) = 0.0
                  POSNZ(3,I) = 0.0
   30          CONTINUE
```

```
      END IF
      RETURN
      END


      SUBROUTINE OUTPUT(NNODES,TIME,ITH)
CCCCCCCCCCCCCCCCCCCCCCCCC CCCCCCCCCCCCCCCCCCCCCCCCCCCCCCCCCCCCCCCCCCCCCCC
C
C     This subroutine (SUBROUTINE OUTPUT) writes the coordinates of
C     the nodes to UNIT 6 every IOUTth time step.
C
CCCCCCCCCCCCCCCCCCCCCCCCCCCCCCCCCCCCCCCCCCCCCCCCCCCCCCCCCCCCCCCCCCCCCCCCC
      DIMENSION RNODE(3,5000)
      COMMON /POS/ RNODE
      ITH = 0
      WRITE(6,200) TIME
      WRITE(6,201) (J,(RNODE(K,J), K=1,3), J=1,NNODES)
      WRITE(6,202)
  200 FORMAT(10X,'TIME  = ',F6.3,/)
  201 FORMAT(10X,I5,5X,F19.14,5X,F19.14,5X,F19.14)
  202 FORMAT(1X,/)
      RETURN
      END


      SUBROUTINE PLOT(NPTH,NPLOT,CENTER)
CCCCCCCCCCCCCCCCCCCCCCCCCCCCCCCCCCCCCCCCCCCCCCCCCCCCCCCCCCCCCCCCCCCCCCCCC
C
C     This subroutine (SUBROUTINE PLOT) generates a frame of data
C     for the Evans and Sutherland every NPLOTth time step.
C
CCCCCCCCCCCCCCCCCCCCCCCCCCCCCCCCCCCCCCCCCCCCCCCCCCCCCCCCCCCCCCCCCCCCCCCCC
      DIMENSION RNODE(3,5000),NSTART(500),NEND(500),
     &          CENTER(3),SCRTCH(45),
     &          COOR(3075)  !  Good for NPERRG < 1025
      COMMON /POS/ RNODE
      COMMON /RING/ NPERRG,NRINGS,NNODES,NSTART,NEND
      NPTH = 0
C  *  Plot a small sphere to mark the origin.
      CALL COLOR(0)
      RHO = 0.1
      NVSEC = 4
      NHSEC = 4
```

```
      IPTS = 15
      MODE = 0
      CALL SPHERE(CENTER,RHO,NVSEC,NHSEC,SCRTCH,IPTS,MODE)
C  *  Draw NRINGS rings with NPERRG nodes.
      CALL COLOR(4)
      DO 100 NR=1,NRINGS
C  *  *  Assign node positions to plotting array.
         I = 1
         NSN = NSTART(NR)
         NEN = NEND(NR)
         DO 110 J=NSN,NEN
            COOR(I) = RNODE(1,J)
            COOR(I+1) = RNODE(2,J)
            COOR(I+2) = RNODE(3,J)
            I = I + 3
  110    CONTINUE
         COOR(I) = RNODE(1,NSN)
         COOR(I+1) = RNODE(2,NSN)
         COOR(I+2) = RNODE(3,NSN)
C  *  *  Draw ring(s).
         NPTS = NPERRG + 1
         CALL DRAW3D(COOR,NPTS,2,2)
  100 CONTINUE
      CALL FRAME
      RETURN
      END


      subroutine runge(Delt,Delt02,NNodes,NPerRg,GamJet,Center)
CCCCCCCCCCCCCCCCCCCCCCCCCCCCCCCCCCCCCCCCCCCCCCCCCCCCCCCCCCCCCCCCCCCCCCCCCC
C
C   FUNCTION:
C      This subroutine (SUBROUTINE RUNGE) calls SUBROUTINE INDVEL
C      to calculate the filament-node velocity induced by the
C      filaments in the flow field.  The node positions at the end
C      of the time step are caluculated by 2nd order Runge-Kutta.
C
C   READ-ONLY PARAMETERS:
C      Delt -> time step
C      Delt02 -> half of a time step
C      NNodes -> total number of nodes in simulation
C      NPerRg -> number of nodes per ring
C      GamJet -> circulation of jet function
```

```
C       Center -> current position of center of jet exit
C
C   AUTHOR:
C       David Parekh   (July 1983; revised:  July 1984)
C
CCCCCCCCCCCCCCCCCCCCCCCCCCCCCCCCCCCCCCCCCCCCCCCCCCCCCCCCCCCCCCCCCCCCCCC
      dimension RNode(3,5000),RNew(3,5000),RRef(3),Center(3),
     &          VelInd(3,5000),VelJet(3,5000),VelRef(3),CRad2(500)
      common /POS/ RNode
      common /CORE/ CRad2
C  *  Predict using the Euler method.
C  *  *  Calculate node velocities due to mutual induction.
         call indvel(RNode,VelInd)
C  *  *  Calculate node velocities due to jet function.
         do 10 N = 1,NNodes
            RRef(1) = RNode(1,N)
            RRef(2) = RNode(2,N)
            RRef(3) = RNode(3,N)
            Index = ((N - 1) / NPerRg) + 1
            CRef2 = CRad2(Index)
            call jetvel(GamJet,RRef,CRef2,Center,VelRef)
            VelJet(1,N) = VelRef(1)
            VelJet(2,N) = VelRef(2)
            VelJet(3,N) = VelRef(3)
   10    continue
      do 100 N = 1,NNodes
         RNew(1,N) = RNode(1,N) + (DeltO2 * (VelInd(1,N) + VelJet(1,N)))
         RNew(2,N) = RNode(2,N) + (DeltO2 * (VelInd(2,N) + VelJet(2,N)))
         RNew(3,N) = RNode(3,N) + (DeltO2 * (VelInd(3,N) + VelJet(3,N)))
  100 continue
C  *  Correct using the midpoint rule.
C  *  *  Calculate node velocities due to mutual induction.
         call indvel(RNew,VelInd)
C  *  *  Calculate node velocities due to jet function.
         do 20 N = 1,NNodes
            RRef(1) = RNew(1,N)
            RRef(2) = RNew(2,N)
            RRef(3) = RNew(3,N)
            Index = ((N - 1) / NPerRg) + 1
            CRef2 = CRad2(Index)
            call jetvel(GamJet,RRef,CRef2,Center,VelRef)
            VelJet(1,N) = VelRef(1)
            VelJet(2,N) = VelRef(2)
```

```
            VelJet(3,N) = VelRef(3)
   20     continue
          do 200 N = 1,NNodes
             RNode(1,N) = RNode(1,N) + (Delt * (VelInd(1,N) + VelJet(1,N)))
             RNode(2,N) = RNode(2,N) + (Delt * (VelInd(2,N) + VelJet(2,N)))
             RNode(3,N) = RNode(3,N) + (Delt * (VelInd(3,N) + VelJet(3,N)))
  200     continue
          return
          end


          subroutine indvel(RNode,  VelInd)
CCCCCCCCCCCCCCCCCCCCCCCCCCCCCCCCCCCCCCCCCCCCCCCCCCCCCCCCCCCCCCCCCCCCCCCCCCCC
C
C   FUNCTION:
C      This subroutine (SUBROUTINE INDVEL) calculates the filament-
C      node velocity induced by the vortex filaments in the flow
C      field.    The segments joining each pair of nodes is a straight
C      line.    The vorticity is distributed about the filament as
C      specified by a spherically symmetric polynomial.    The nodes
C      are grouped in rings.    The innermost loop calculates the
C      velocity induced by a particular segment.
C
C   READ-ONLY PARAMETERS:
C      RNode -> the coordinates of each node
C
C   WRITE-ONLY PARAMETERS:
C      VelInd -> the node velocities induced by the filaments
C
C   AUTHORS:
C      David Parekh  &  Tony Leonard    (July 1983; revised:  July 1984)
C
CCCCCCCCCCCCCCCCCCCCCCCCCCCCCCCCCCCCCCCCCCCCCCCCCCCCCCCCCCCCCCCCCCCCCCCCCCCC
C  *  Dimension variables and define common block.
      dimension VelInd(3,5000),RNode(3,5000),CRad2(500),
     &          Gamma(500),NStart(500),NEnd(500),
     &          DR(3),RDif(3),RDfXDR(3)
      common /CORE/ CRad2
      common /PARM/ Gamma,Alpha,Coef
      common /RING/ NPerRg,NRings,NNodes,NStart,NEnd
C  *  Initialize velocity vector.
      do 100 N = 1,NNodes
         VelInd(1,N) = 0.0
```

```
            VelInd(2,N) = 0.0
            VelInd(3,N) = 0.0
  100 continue
C   *  Calculate the induced velocities by solving the Biot-Savart integral.
      do 200 NR = 1,NRings
         Gam = Gamma(NR)
         NTail = NEnd(NR)
         CNR2 = CRad2(NR)
         do 210 NHead = NStart(NR),NEnd(NR)
            DR(1) = RNode(1,NHead) - RNode(1,NTail)
            DR(2) = RNode(2,NHead) - RNode(2,NTail)
            DR(3) = RNode(3,NHead) - RNode(3,NTail)
            do 211 N = 1,NNodes
               RDif(1) = RNode(1,N) - RNode(1,NTail)
               RDif(2) = RNode(2,N) - RNode(2,NTail)
               RDif(3) = RNode(3,N) - RNode(3,NTail)
               RDif2 = (RDif(1) * RDif(1)) + (RDif(2) * RDif(2)) +
     &                 (RDif(3) * RDif(3))
               DR2 = (DR(1) * DR(1)) + (DR(2) * DR(2)) + (DR(3) * DR(3))
               RDifDR = (RDif(1) * DR(1)) + (RDif(2) * DR(2)) +
     &                  (RDif(3) * DR(3))
               Index = ((N - 1) / NPerRg) + 1
               BSDen = RDif2 + (Alpha * (CNR2 + CRad2(Index)))
               C1 = (BSDen + DR2) - (RDifDR + RDifDR)
               C2 = ((DR2-RDifDR) / sqrt(C1)) + (RDifDR / sqrt(BSDen))
               C3 = C2 / ((DR2 * BSDen) - (RDifDR * RDifDR))
               RDfXDR(1) = (RDif(2) * DR(3)) - (RDif(3) * DR(2))
               RDfXDR(2) = (RDif(3) * DR(1)) - (RDif(1) * DR(3))
               RDfXDR(3) = (RDif(1) * DR(2)) - (RDif(2) * DR(1))
               VelInd(1,N) = VelInd(1,N) + (C3 * Gam * RDfXDR(1))
               VelInd(2,N) = VelInd(2,N) + (C3 * Gam * RDfXDR(2))
               VelInd(3,N) = VelInd(3,N) + (C3 * Gam * RDfXDR(3))
  211       continue
            NTail = NHead
  210    continue
  200 continue
      do 300 N = 1,NNodes
         VelInd(1,N) = Coef * VelInd(1,N)
         VelInd(2,N) = Coef * VelInd(2,N)
         VelInd(3,N) = Coef * VelInd(3,N)
  300 continue
      return
      end
```

```
      subroutine jetvel(GamJet,RRef,Core2,Center,  VelRef)
CCCCCCCCCCCCCCCCCCCCCCCCCCCCCCCCCCCCCCCCCCCCCCCCCCCCCCCCCCCCCCCCCCCCCCCCCCCCCCC
C
C     This subroutine (SUBROUTINE JETVEL) calculates the velocity
C     induced at the point (R,Z) by a semi-infinite sheet of
C     vorticity.  Analytical expressions (FUNCTION RVFUNC and
C     FUNCTION ZVFUNC) for the velocity field of a semi-infinite
C     sheet of vorticity are used.
C
CCCCCCCCCCCCCCCCCCCCCCCCCCCCCCCCCCCCCCCCCCCCCCCCCCCCCCCCCCCCCCCCCCCCCCCCCCCCCCC
      dimension RRef(3),VELREF(3),Center(3)
      real Mu,Nu
C  *  Assign values of distribution factor, and core radius squared
C     of vortex sheet.
      DATA ALPHA,SIGMA2 /0.2065,0.01/
C  *  Transform position vector RREF to RVFUNC-&-ZVFUNC coordinates.
      X = RREF(2) - CENTER(2)
      Y = RREF(3) - CENTER(3)
      R = SQRT((X*X) + (Y*Y))
      Z = RREF(1) - CENTER(1)
C  *  Calcualte velocity function arguments.
      RHO = 1.  + (R * R) + (ALPHA * (SIGMA2 + CORE2))
      NU = RHO + (Z * Z)
      MU = 2.  * (R / RHO)
      ETA = 2.  * (R / NU)
C  *  Calculate the induced velocity.
      RVEL = RVFUNC(NU,ETA,GAMJET)
      ZVEL = ZVFUNC(R,Z,RHO,MU,NU,ETA,GAMJET)
      VELREF(1) = ZVEL
      VELREF(2) = (X * (RVEL/R))
      VELREF(3) = (Y * (RVEL/R))
      RETURN
      END


      FUNCTION RVFUNC(NU,ETA,GAM)
CCCCCCCCCCCCCCCCCCCCCCCCCCCCCCCCCCCCCCCCCCCCCCCCCCCCCCCCCCCCCCCCCCCCCCCCCCCCCCC
C
C     This function computes the r-component of velocity.
C
CCCCCCCCCCCCCCCCCCCCCCCCCCCCCCCCCCCCCCCCCCCCCCCCCCCCCCCCCCCCCCCCCCCCCCCCCCCCCCC
      REAL I,NU
      COMMON /MANYPI/ HALFPI,PI,TWOPI
```

```
      COEF = GAM / (2.  * PI * SQRT(NU))
      IF(ETA.GT.0.05)THEN
         RVFUNC = COEF * I(ETA)
      ELSE
         RVFUNC = COEF * T(0.,ETA)
      END IF
      RETURN
      END


      FUNCTION ZVFUNC(R,Z,RHO,MU,NU,ETA,GAM)
CCCCCCCCCCCCCCCCCCCCCCCCCCCCCCCCCCCCCCCCCCCCCCCCCCCCCCCCCCCCCCCCCCCCCCCCCCCCCC
C
C     This function computes the z-component of velocity.
C
CCCCCCCCCCCCCCCCCCCCCCCCCCCCCCCCCCCCCCCCCCCCCCCCCCCCCCCCCCCCCCCCCCCCCCCCCCCCCC
      REAL K,M1,MU,NU
      COMMON /MANYPI/ HALFPI,PI,TWOPI
      M1 = (1.  - ETA) / (1.  + ETA)
      COEF = GAM / (TWOPI * RHO)
      A = HALFPI * (((2.  - RHO) / SQRT(1.  - MU*MU)) + RHO)
      B1 = (2./SQRT(1.  + ETA)) * K(M1)
      B2 = (MU - R) * T(MU,ETA)
      ZVFUNC = COEF * (A - ((Z/SQRT(NU)) * (B1 + B2)))
      RETURN
      END


      FUNCTION T(MU,ETA)
CCCCCCCCCCCCCCCCCCCCCCCCCCCCCCCCCCCCCCCCCCCCCCCCCCCCCCCCCCCCCCCCCCCCCCCCCCCCCC
C
C     This function calculates the value of the Terry function for
C     specified values of MU and ETA by means of the a 4-panel
C     Newton-Cotes scheme (SUBROUTINE DNC4).  N is a parameter of
C     DNC4.
C
CCCCCCCCCCCCCCCCCCCCCCCCCCCCCCCCCCCCCCCCCCCCCCCCCCCCCCCCCCCCCCCCCCCCCCCCCCCCCC
      REAL MU
      COMMON /TERRY/ TMU,TETA
      COMMON /MANYPI/ HALFPI,PI,TWOPI
      EXTERNAL TFI
      TMU = MU
      TETA = ETA
```

```
      N = 3.  + (6.*MU) + (3.*ETA)
      T = DNC4(TFI,0.,PI,N)
      RETURN
      END


      FUNCTION TFI(PHI)
CCCCCCCCCCCCCCCCCCCCCCCCCCCCCCCCCCCCCCCCCCCCCCCCCCCCCCCCCCCCCCCCCCCCCCCCCCCCCCCCCC
C
C     This subroutine defines the Terry function integrand.
C
CCCCCCCCCCCCCCCCCCCCCCCCCCCCCCCCCCCCCCCCCCCCCCCCCCCCCCCCCCCCCCCCCCCCCCCCCCCCCCCCCC
      REAL MU
      COMMON /TERRY/ TMU,TETA
      COSPHI = COS(PHI)
      TFI = COSPHI / ((1.DO - TMU*COSPHI) *
     &      SQRT(1.DO - TETA*COSPHI))
      RETURN
      END


      FUNCTION DNC4(TFI,A,B,N)
CCCCCCCCCCCCCCCCCCCCCCCCCCCCCCCCCCCCCCCCCCCCCCCCCCCCCCCCCCCCCCCCCCCCCCCCCCCCCCCCCC
C
C     This subroutine integrates the function TFI from A to B by
C     a modified 4-panel Newton-Cotes scheme.  The points where TFI
C     is evaluated were chosen to give the greatest resolution at
C     the ends of the intervals.  N is the initial step size
C     criterion, where HO = (B-A)/(2**N) and N > 2.
C
C     Written by:  David Parekh
C     Date:        August 1983
C
CCCCCCCCCCCCCCCCCCCCCCCCCCCCCCCCCCCCCCCCCCCCCCCCCCCCCCCCCCCCCCCCCCCCCCCCCCCCCCCCCC
C  *  Calculate initial step size and loop parameter.
      EXP = N
      FRAC = 2.**EXP
      HO = (B-A)/FRAC
      IEND = N - 3
C  *  Integrate using a modified 4-panel Newton-Cotes formula.
C  *  *  Integrate first subinterval.
         H = HO
         PHI1 = A
```

```
      PHI2 = PHI1 + H
      PHI3 = PHI2 + H
      PHI4 = PHI3 + H
      PHI5 = PHI4 + H
      TFI5 = TFI(PHI5)
      SUM = (H/22.5) * (7.*TFI(PHI1) + 32.*TFI(PHI2) +
     &       12.*TFI(PHI3) + 32.*TFI(PHI4) + 7.*TFI5)
C  *  *  Integrate the rest of the first half of the interval,
C        doubling H every subinterval.
      DO 10 I=1,IEND
         TFI1 = TFI5
         PHI1 = PHI5
         PHI2 = PHI1 + H
         PHI3 = PHI2 + H
         PHI4 = PHI3 + H
         PHI5 = PHI4 + H
         TFI5 = TFI(PHI5)
         SUM = SUM + ((H/22.5) * (7.*TFI1 +
     &                32.*TFI(PHI2) + 12.*TFI(PHI3) +
     &                32.*TFI(PHI4) + 7.*TFI5))
         H = 2.*H
   10    CONTINUE
C  *  *  Integrate the last subinterval.
      H = HO
      PHI5 = B
      PHI4 = PHI5 - H
      PHI3 = PHI4 - H
      PHI2 = PHI3 - H
      PHI1 = PHI2 - H
      TFI1 = TFI(PHI1)
      SUM = SUM + ((H/22.5) * (7.*TFI1 +
     &             32.*TFI(PHI2) + 12.*TFI(PHI3) +
     &             32.*TFI(PHI4) + 7.*TFI(PHI5)))
C  *  *  Integrate the rest of the last half of the interval.
      DO 20 I=1,IEND
         TFI5 = TFI1
         PHI5 = PHI1
         PHI4 = PHI5 - H
         PHI3 = PHI4 - H
         PHI2 = PHI3 - H
         PHI1 = PHI2 - H
         TFI1 = TFI(PHI1)
         SUM = SUM + ((H/22.5) * (7.*TFI1 +
```

```
     &                    32.*TFI(PHI2) + 12.*TFI(PHI3) +
     &                    32.*TFI(PHI4) + 7.*TFI5))
           H = 2.*H
  20    CONTINUE
        DNC4 = SUM
        RETURN
        END


        REAL FUNCTION I(ETA)
CCCCCCCCCCCCCCCCCCCCCCCCCCCCCCCCCCCCCCCCCCCCCCCCCCCCCCCCCCCCCCCCCCCCCCCCCCCC
C
C       This function is a combination of the elliptic integrals K & E.
C
CCCCCCCCCCCCCCCCCCCCCCCCCCCCCCCCCCCCCCCCCCCCCCCCCCCCCCCCCCCCCCCCCCCCCCCCCCCC
        REAL K,M1
        M1 = (1.  - ETA) / (1.  + ETA)
        COEF = 2.  / (ETA * SQRT(ETA + 1.))
        I = COEF * (K(M1) - ((1.  + ETA) * E(M1)))
        RETURN
        END


        REAL FUNCTION K(M1)
CCCCCCCCCCCCCCCCCCCCCCCCCCCCCCCCCCCCCCCCCCCCCCCCCCCCCCCCCCCCCCCCCCCCCCCCCCCC
C
C       This function is a polynomial approximation of the complete
C       elliptic integral of the first kind (from HMF 17.3.33) with
C       e(m1) < 3E-5.
C
CCCCCCCCCCCCCCCCCCCCCCCCCCCCCCCCCCCCCCCCCCCCCCCCCCCCCCCCCCCCCCCCCCCCCCCCCCCC
        REAL M1
        DATA AO, A1, A2 /1.3862944, 0.1119723, 0.0725296/
        DATA BO, B1, B2 /0.5, 0.1213478, 0.0288729/
        K = (AO+(M1*(A1+(M1*A2)))) + ((BO+(M1*(B1+(M1*B2))))*ALOG(1./M1))
        RETURN
        END


        FUNCTION E(M1)
CCCCCCCCCCCCCCCCCCCCCCCCCCCCCCCCCCCCCCCCCCCCCCCCCCCCCCCCCCCCCCCCCCCCCCCCCCCC
C
C       This function is a polynomial approximation of the complete
```

```
C     elliptic integral of the second kind (from HMF 17.3.35) with
C     e(m1) < 4E-5.
C
CCCCCCCCCCCCCCCCCCCCCCCCCCCCCCCCCCCCCCCCCCCCCCCCCCCCCCCCCCCCCCCCCCCCCCCCCCCCCCC
      REAL M1,M12
      DATA A1, A2 /0.4630151, 0.1077812/
      DATA B1, B2 /0.2452727, 0.0412496/
      E = (1.+(M1*(A1+(M1*A2)))) + ((M1*(B1+(M1*B2)))*ALOG(1./M1))
      RETURN
      END
```

B.2 AXLAYER

```
C*************************************************************************
C
C                     AXISYMMETRIC  RINGS
C
C          This program uses analytical expressions to calcualte
C     the motion of axisymmetric, incompressible, inviscid
C     vortex rings.  The boundary condition at the location of
C     creation of the rings is imposed by a jet function.  The jet
C     function specifies the velocity field induced by a semi-
C     infinite axisymmetric sheet of vorticity.
C
C     Output:       Unit 10
C
C     Written by:   David Parekh
C     Date:         September 1984
C
C*************************************************************************
C  *  Define logical variables, common blocks and output unit.
      logical Image,CorCon
      common /JET/ ALPHA, GamJet, Cr2Jet
      common /PARM/ Sigma2(1000),Gam(1000),Sig2I(1000),GamI(1000)
      common /POS/ RPos(1000),ZPos(1000),RPosI(1000),ZPosI(1000)
      common /RING/ GamRng, CORE, RAD, VOLUME
      open(unit=10,file='RESULTS')
C  *  Specify constants and parameters.
      Image = .TRUE.          !  specifies whether images are to be included
      CorCon = .TRUE.         !  specifies whether cores are constant in time
      GAMJ = 1.0              !  nominal circulation/length of jet
      RAD = 1.0               !  nominal radius of rings
```

```
      CORE = 0.1              !  nominal core radius of rings
      STNUM = 0.4             !  Strouhal number based on axial frequency
      NSTEPS = 400            !  total number of time steps in simulation
      PRDA = 100.             !  period of axial excitation in DELT units
      PRDF = 10.              !  period of filament generation in DELT units
      AXAMP = 0.2             !  amplitude of axial excitation / GAMJ
      IOUT = 5                !  time steps between calls to "output"
      NEWVTX = PRDF           ! time steps between calls to "genRng"
      call initJet
      ExFac = 1.  + (AXAMP**2) / 2       !  excitation factor
      AxFreq = 4 * asin(1.)  / PRDA      ! axial frequency (rad / step)
      FPerA = PRDA / PRDF                  ! filaments per axial period
      VDelT = 2 / (GAMJ * FPerA * STNUM)   ! time between ring creations
      DelT = VDelT / PRDF                  ! time step of simulation
      DelT02 = DelT / 2
      GamDot = GAMJ**2 / 2                 !  nominal circulation flux rate
      CIRC = ExFac * VDelT * GamDot        !  nominal circulation of rings
      VOLUME = RAD * CORE**2               !  nominal volume of rings
      Coef1 = 2 * AXAMP * DelT / AxFreq
      Coef2 = AXAMP / 8
C  *  Initialize counters.
      INewV = NEWVTX
      Ith = IOUT
      NRings = 0
      Time = 0.0
C  *  Print output header.
      write(10,100) CIRC,RAD,CORE,GAMJ,AXAMP,STNUM,DelT,FPerA
      if (Image) then
         write(10,110)
      else
         write(10,120)
      end if
C  *  Carry out simulation for NSTEPS time steps.
      do 1000 IStep = 1,NSTEPS
C  *  *  Calculate instantaneous circulations of jet and filament.
C         Phi0 = AXFREQ * (IStep - 1)
C         Phi1 = Phi0 + AXFREQ * PRDF
C         GamJet = (1.  - AXAMP * cos(Phi0)) * GAMJ
C         GamRng = GamDot * (ExFac * VDelT + Coef1 *
C     &            (Coef2 * (sin(2 * Phi1) - sin(2 * Phi0)) -
C     &             (sin(Phi1) - sin(Phi0))))
         GamJet = (1.  - AXAMP * cos(AXFREQ * (IStep - 1))) * GAMJ
C  *  *  Generate a new vortex ring as specified.
```

```
         if (INewV.eq.NEWVTX) then
            call genRng(Image,INewV,NRings)
            Phi0 = AXFREQ * (IStep - 1)
         end if
         RelStp = INewV + 1
         Phi1 = Phi0 + AXFREQ * RelStp
         Gam(NRings) = GamDot * (ExFac * DelT * RelStp + Coef1 *
     &                 (Coef2 * (sin(2 * Phi1) - sin(2 * Phi0)) -
     &                  (sin(Phi1) - sin(Phi0))))
         GamI(NRings) = -Gam(NRings)
C  *  *  Print ring positions as specified.
         if (Ith.eq.IOUT) call output(NRings,Time,Ith)
C  *  *  Update node positions by 2nd order Runge-Kutta.
         call runKut(NRings,DelT,DelT02,CorCon,Image)
C  *  *  Increment counters at end of time step.
         INewV = INewV + 1
         Ith = Ith + 1
         Time = Time + DelT
 1000 continue
C  *  Write final coordinates of rings.
      GamJet = (1.  - AXAMP * cos(AXFREQ * IStep)) * GAMJ
C      if (INewV.eq.NEWVTX) call genRng(Image,INewV,NRings)
         if (INewV.eq.NEWVTX) then
            call genRng(Image,INewV,NRings)
            Phi0 = AXFREQ * (IStep - 1)
         end if
         RelStp = INewV + 1
         Phi1 = Phi0 + AXFREQ * RelStp
         Gam(NRings) = GamDot * (ExFac * DelT * RelStp + Coef1 *
     &                 (Coef2 * (sin(2 * Phi1) - sin(2 * Phi0)) -
     &                  (sin(Phi1) - sin(Phi0))))
         GamI(NRings) = -Gam(NRings)
      call output(NRings,Time,Ith)
      close(10)
C  *  I/O formats.
  100 format(1x,'Circulation =',t17,f7.4,/,
     &       1x,'Ring Radius =',t17,f6.2,/,
     &       1x,'Core Radius =',t19,f6.4,//,
     &       1x,'Jet Circulation =',t20,f8.4,/,
     &       1x,'Axial Excitation =',t20,f8.4,//,
     &       1x,'Strouhal Number =',t20,f8.4,/,
     &       1x,'Time Step =',t21,f8.5,//,
     &       1x,'Filaments per Pulse =',t23,f5.0,///)
```

```
  110 format(1x,'***   Images included in simulation   ***',///)
  120 format(1x,'***   Images not used in simulation   ***',///)
      stop
      end


      subroutine genRng(Image, INewV,NRings)
CCCCCCCCCCCCCCCCCCCCCCCCCCCCCCCCCCCCCCCCCCCCCCCCCCCCCCCCCCCCCCCCCCCCCCCCCCC
C
C     This subroutine (SUBROUTINE GENRNG) specifies the coordinate
C     of the center of the newly generated vortex ring and assigns
C     the circulation and core radius of the new ring.
C
CCCCCCCCCCCCCCCCCCCCCCCCCCCCCCCCCCCCCCCCCCCCCCCCCCCCCCCCCCCCCCCCCCCCCCCCCCC
C  *  Define variables and common blocks.
      logical Image
      common /PARM/ Sigma2(1000),Gam(1000),Sig2I(1000),GamI(1000)
      common /POS/ RPos(1000),ZPos(1000),RPosI(1000),ZPosI(1000)
      common /RING/ GamRng, CORE, RAD, VOLUME
C  *  Initialize and increment counters.
      INewV = 0
      NRings = NRings + 1
C  *  Specify ring parameters.
      RPos(NRings) = RAD
      ZPos(NRings) = 0.0 + CORE
C      Gam(NRings) = GamRng
      Sigma2(NRings) = CORE**2
C  *  Specify image ring if required.
      if (Image) then
         RPosI(NRings) = RAD
         ZPosI(NRings) = 0.0 - CORE
C         GamI(NRings) = -GamRng
         Sig2I(NRings) = CORE**2
      end if
      return
      end


      subroutine output(NRings,Time,Ith)
CCCCCCCCCCCCCCCCCCCCCCCCCCCCCCCCCCCCCCCCCCCCCCCCCCCCCCCCCCCCCCCCCCCCCCCCCCC
C
C     This subroutine (SUBROUTINE OUTPUT) writes the coordinates of
C     the centers of the vortex rings and their radii to UNIT 10
```

```
C     every IOUTth time step.
C
CCCCCCCCCCCCCCCCCCCCCCCCCCCCCCCCCCCCCCCCCCCCCCCCCCCCCCCCCCCCCCCCCCCCCCCCCCC
C  *  Define variables and common blocks.
      common /JET/ ALPHA, GamJet, Cr2Jet
      common /PARM/ Sigma2(1000),Gam(1000),Sig2I(1000),GamI(1000)
      common /POS/ RPos(1000),ZPos(1000),RPosI(1000),ZPosI(1000)
C  *  Reset counter.
      ITH = 0
C  *  Write results.
      Write(10,200) Time,GamJet,sqrt(Cr2Jet)
      Write(10,201)
      Write(10,202) (J,RPos(J),ZPos(J),sqrt(Sigma2(J)),Gam(J),
     &               J=1,NRINGS)
      Write(10,203)
C  *  Format statements.
  200 Format(1X,'TIME  = ',F9.3,//,
     &       1x,'GAMJET = ',F7.3,/,
     &       1x,'CORE OF JET = ',F10.5,/)
  201 Format(1X,' RING',8X,'RADIUS',12X,'Z',12x,'CORE RADIUS',
     &       6x,'CIRCULATION',//)
  202 Format(1X,I5,5X,F10.5,5X,F10.5,10X,F10.5,10x,F10.5)
  203 Format(1X,/)
      return
      end


      subroutine runKut(NRings,DelT,DelT02,CorCon,Image)
CCCCCCCCCCCCCCCCCCCCCCCCCCCCCCCCCCCCCCCCCCCCCCCCCCCCCCCCCCCCCCCCCCCCCCCCCCC
C
C     This subroutine (SUBROUTINE RUNKUT) calls SUBROUTINE VELOCITY
C     to calculate the induced velocity at a particular node point
C     and calculates the node positions at the next time step by
C     2nd order Runge-Kutta.
C
CCCCCCCCCCCCCCCCCCCCCCCCCCCCCCCCCCCCCCCCCCCCCCCCCCCCCCCCCCCCCCCCCCCCCCCCCCC
C  *  Dimension variables and define common block.
      logical Image,CorCon
      dimension RRunge(1000), ZRunge(1000)
      common /POS/ RPos(1000),ZPos(1000),RPosI(1000),ZPosI(1000)
      common /VEL/ RVel(1000), ZVel(1000)
C  *  Predict using the Euler method.
      call velocity(NRings,Image)
```

```
      do 100 NR = 1,NRings
         RRunge(NR) = DelT02 * RVel(NR)
         ZRunge(NR) = DelT02 * ZVel(NR)
         RPos(NR) = RPos(NR) + RRunge(NR)
         ZPos(NR) = ZPos(NR) + ZRunge(NR)
  100 continue
      if (Image) then
         do 110 NR = 1,NRings
            RPosI(NR) = RPos(NR)
            ZPosI(NR) = -ZPos(NR)
  110    continue
      end if
      if (.not.CorCon) call newCore(NRings,Image)
C  *  Correct using the midpoint rule.
      call velocity(NRings,Image)
      do 200 NR = 1,NRings
         RRunge(NR) = DelT * RVel(NR) - RRunge(NR)
         ZRunge(NR) = DelT * ZVel(NR) - ZRunge(NR)
         RPos(NR) = RPos(NR) + RRunge(NR)
         ZPos(NR) = ZPos(NR) + ZRunge(NR)
  200 continue
      if (Image) then
         do 210 NR = 1,NRings
            RPosI(NR) = RPos(NR)
            ZPosI(NR) = -ZPos(NR)
  210    continue
      end if
      if (.not.CorCon) call newCore(NRings,Image)
      return
      end


      subroutine velocity(NRings,Image)
CCCCCCCCCCCCCCCCCCCCCCCCCCCCCCCCCCCCCCCCCCCCCCCCCCCCCCCCCCCCCCCCCCCCCCCCCCC
C
C   FUNCTION:
C      To calculate the velocity and stretching of rings due to
C      the influence of the rings and the sheet of vorticity.
C      The influence of image rings are included as specified.
C
C   AUTHOR:
C      David Parekh   (October 1984)
C
```

```
CCCCCCCCCCCCCCCCCCCCCCCCCCCCCCCCCCCCCCCCCCCCCCCCCCCCCCCCCCCCCCCCCCCCCCCCCCCCCCC
C  *  Dimension variables and define common block.
      logical Image
      common /PARM/ Sigma2(1000),Gam(1000),Sig2I(1000),GamI(1000)
      common /POS/ RPos(1000),ZPos(1000),RPosI(1000),ZPosI(1000)
      common /VEL/ RVel(1000), ZVel(1000)
C  *  Calculate velocities induced by jet.
      do 100 NR = 1,NRings
         call jetVel(RPos(NR),ZPos(NR),Sigma2(NR),RVel(NR),ZVel(NR))
  100 continue
C  *  Calculate velocities induced by other rings.
      do 200 NR = 1,NRings
         do 210 IR = 1,NRings
            ZDif = ZPos(IR) - ZPos(NR)
            call rngVel(RPos(NR),Gam(NR),Sigma2(NR),RPos(IR),ZDif,
     &                  Sigma2(IR),VelInR,VelInZ)
            RVel(IR) = RVel(IR) + VelInR
            ZVel(IR) = ZVel(IR) + VelInZ
  210    continue
         if (Image) then
            do 220 IR = 1,NRings
               ZDif = ZPos(IR) - ZPosI(NR)
               call rngVel(RPosI(NR),GamI(NR),Sig2I(NR),RPos(IR),ZDif,
     &                     Sigma2(IR),VelInR,VelInZ)
               RVel(IR) = RVel(IR) + VelInR
               ZVel(IR) = ZVel(IR) + VelInZ
  220       continue
         end if
  200 continue
      return
      end


      subroutine newCore(NRings,Image)
CCCCCCCCCCCCCCCCCCCCCCCCCCCCCCCCCCCCCCCCCCCCCCCCCCCCCCCCCCCCCCCCCCCCCCCCCCCCCCC
C
C   FUNCTION:
C      To calculate the core size of the rings based on conservation
C      of volume constraints.
C
C   AUTHOR:
C      David Parekh   (September 1984)
C
```

```
CCCCCCCCCCCCCCCCCCCCCCCCCCCCCCCCCCCCCCCCCCCCCCCCCCCCCCCCCCCCCCCCCCCCCCCCCCC
C  *  Define variables and common blocks.
      logical Image
      common /PARM/ Sigma2(1000),Gam(1000),Sig2I(1000),GamI(1000)
      common /POS/ RPos(1000),ZPos(1000),RPosI(1000),ZPosI(1000)
      common /RING/ GamRng, CORE, RAD, VOLUME
C  *  Calculate new core sizes.
      do 100 NR = 1,NRings
         Sigma2(NR) = VOLUME / RPos(NR)
  100 continue
      if (Image) then
         do 110 NR = 1,NRings
            Sig2I(NR) = Sigma2(NR)
  110    continue
      end if
      return
      end


      subroutine rngVel(RadRng,GamRng,Cr2Rng,R,Z,Core2, RVel,ZVel)
CCCCCCCCCCCCCCCCCCCCCCCCCCCCCCCCCCCCCCCCCCCCCCCCCCCCCCCCCCCCCCCCCCCCCCCCCCC
C
C   FUNCTION:
C      To calculate the velocity induced by a circular vortex ring
C      at a particular field point.
C
C   READ-ONLY PARAMETERS:
C      RadRng -> radius of vortex ring
C      GamRng -> circulation of vortex ring
C      Cr2Rng -> square of radius of vortex core
C      R -> r-coordinate of field point
C      Z -> z-coordinate of field point
C      Core2 -> square of vortex core associated with field point
C
C   WRITE-ONLY PARAMETERS:
C      RVel -> r-component of velocity induced by ring
C      ZVel -> z-component of velocity induced by ring
C
C   NOTES:
C      1.  If the field point is in zero-vorticity fluid, Core2
C          should be equal to Cr2Rng.
C
C      2.  The calculated velocities may be considered to be
```

```
C          non-dimensionalized by nominal circulation and ring-radius
C          parameters, each having a value of unity.
C
C      3.  Subroutine "initJet" should be called once prior to the
C          first call of this subroutine.
C
C   AUTHOR:
C      David Parekh   (September 1984)
C
CCCCCCCCCCCCCCCCCCCCCCCCCCCCCCCCCCCCCCCCCCCCCCCCCCCCCCCCCCCCCCCCCCCCCCCCCC
C  *  Define common block.
      common /KE/ AO, A1, A2, BO, B1, B2, C1, C2, D1, D2
      common /MANYPI/ HALFPI, PI, TWOPI
C  *  Define elliptic integral functions.
      RK(RM1) = (AO + (RM1 * (A1 + (RM1 * A2)))) +
     &          ((BO + (RM1 * (B1 + (RM1 * B2)))) * ALOG(1.  / RM1))
      E(RM1) = (1.  + (RM1 * (C1 + (RM1 * C2)))) +
     &         ((RM1 * (D1 + (RM1 * D2))) * ALOG(1.  / RM1))
C  *  Define constants.
      data ALPHA /0.2065/
C  *  Calculate parameters.
      RBar = R / RadRng
      ZBar = Z / RadRng
      RNu = 1.  + ZBar**2 + RBar**2 + ALPHA * (Cr2Rng+Core2) / RadRng**2
      Eta = 2 * RBar / RNu
      RM1 = (1.  - Eta) / (1.  + Eta)
C  *  Calculate velocity components.
      if (R.ne.0.0) then
         RVel = GamRng * ZBar * (E(RM1) / (1.  - Eta) - RK(RM1)) /
     &          (TWOPI * R * sqrt(RNu + 2 * RBar))
      else
         RVel = 0.0
      end if
      ZVel = (E(RM1) * (1.  - RNu / 2) / (1.  - Eta) + RK(RM1) * RNu / 2)
     &       * GamRng / (PI * RadRng * RNu**1.5 * sqrt(1.  + Eta))
      return
      end
```

```
      subroutine jetVel(R,Z,Core2,  RJtVel,ZJtVel)
CCCCCCCCCCCCCCCCCCCCCCCCCCCCCCCCCCCCCCCCCCCCCCCCCCCCCCCCCCCCCCCCCCCCCCCCCCCCCCC
C
C   FUNCTION:
C      To calculate the velocity induced at the point (R,Z) by a
C      semi-infinite axisymmetric sheet of vorticity.  Analytical
C      expressions (function rVFunc and function zVFunc) for the
C      induced velocity field are used.
C
C   READ-ONLY PARAMETERS:
C      R -> r-coordinate of field point
C      Z -> z-coordinate of field point
C      Core2 -> square of core radius associated with field point
C
C   WRITE-ONLY PARAMETERS:
C      RJtVel -> r-component of induced velocity
C      ZJtVel -> z-component of induced velocity
C
C   NOTES:
C      1.  If the field point coincides with zero-vorticity fluid,
C          the parameter Core2 should be set to Cr2Jet, which is
C          specified by subroutine initJet.
C
C      2.  The length variables are nondimensionalized by the jet
C          radius which is assumed to have a value of unity.
C
C      3.  Subroutine initJet must be called once prior to the first
C          call of this subroutine.
C
C   AUTHOR:
C      David Parekh   (September 1984)
C
CCCCCCCCCCCCCCCCCCCCCCCCCCCCCCCCCCCCCCCCCCCCCCCCCCCCCCCCCCCCCCCCCCCCCCCCCCCCCCC
C  *  Define common blocks.
      common /JET/ ALPHA, GamJet, Cr2Jet
      common /KE/ A0, A1, A2, B0, B1, B2, C1, C2, D1, D2
      common /MANYPI/ HALFPI, PI, TWOPI
C  *  Define elliptic integral functions.
      rK(RM1) = (A0 + (RM1 * (A1 + (RM1 * A2)))) +
     &          ((B0 + (RM1 * (B1 + (RM1 * B2)))) * alog(1.  / RM1))
      E(RM1) = (1.  + (RM1 * (C1 + (RM1 * C2)))) +
     &         ((RM1 * (D1 + (RM1 * D2))) * alog(1.  / RM1))
      rI(RM1,Eta) = 2 * (rK(RM1) - (1.  + Eta) * E(RM1)) /
```

```
     &              (Eta * sqrt(1.  + Eta))
C  *  Calcualte velocity function arguments.
      Rho = 1.  + R**2 + ALPHA * (Cr2Jet + Core2)
      RNu = Rho + Z**2
      RMu = 2 * R / Rho
      Eta = 2 * R / RNu
      RM1 = (1.  - Eta) / (1.  + Eta)
C  *  Calculate velocity components.
      Gam = 2 * GamJet
      if (Eta.gt.0.05) then
         RJtVel = Gam * rI(RM1,Eta) / (TWOPI * sqrt(RNu))
      else
         RJtVel = Gam * Teri(0.0,Eta) / (TWOPI * sqrt(RNu))
      end if
      ZJtVel = (HALFPI * (Rho + (2.  - Rho) / sqrt(1.  - RMu**2)) -
     &          (2 * rK(RM1) / sqrt(1.  + Eta) +
     &           (RMu - R) * Teri(RMu,Eta)) * Z / sqrt(RNu)) *
     &         Gam / (TWOPI * Rho)
      return
      end


      subroutine initJet
cccccccccccccccccccccccccccccccccccccccccccccccccccccccccccccccccccccccc
c
c   FUNCTION:
c      To initialize various constants and arrays used by subroutine
c      jetVel and by the functions jetVel calls.
c
c   AUTHOR:
c      David Parekh   (September 1984)
c
cccccccccccccccccccccccccccccccccccccccccccccccccccccccccccccccccccccccc
C  *  Define common blocks.
      common /JET/ ALPHA, GamJet, Cr2Jet
      common /KE/ A0, A1, A2, B0, B1, B2, C1, C2, D1, D2
      common /MANYPI/ HALFPI, PI, TWOPI
C  *  Set values of constants and variables.
      data ALPHA /0.2065/
      data A0, A1, A2 /1.3862944, 0.1119723, 0.0725296/
      data B0, B1, B2 /0.5, 0.1213478, 0.0288729/
      data C1, C2, D1, D2 /0.4630151, 0.1077812, 0.2452727, 0.0412496/
      HALFPI = asin(1.)
```

```
      PI = 2 * HALFPI
      TWOPI = 2 * PI
      Cr2Jet = 0.1**2
C  *  Initialize Teri function arrays.
      call initTF
      return
      end


      subroutine initTF
CCCCCCCCCCCCCCCCCCCCCCCCCCCCCCCCCCCCCCCCCCCCCCCCCCCCCCCCCCCCCCCCCCCCCCCCCCCC
C
C   FUNCTION:
C      To initialize various arrays used by function Teri.
C
C   AUTHOR:
C      David Parekh   (September 1984)
C
CCCCCCCCCCCCCCCCCCCCCCCCCCCCCCCCCCCCCCCCCCCCCCCCCCCCCCCCCCCCCCCCCCCCCCCCCCCC
C  *  Dimension variables and define common block.
      dimension CoefNC(0:6)
      common /TF/ TCoef(55,8),CosPhi(55,8),NOrder,NPanel
C  *  Initialize constants.
      data NOrder,NPanel /8,6/
      PI = 2 * asin(1.)
      CoefNC(0) = 41.  / 840.
      CoefNC(1) = 216.  / 840.
      CoefNC(2) = 27.  / 840.
      CoefNC(3) = 272.  / 840.
      CoefNC(4) = CoefNC(2)
      CoefNC(5) = CoefNC(1)
      CoefNC(6) = CoefNC(0)
C  *  Calculate coefficient and cosine arrays used by function Teri.
      do 100 N = 1,NOrder
C  *  *  Initialize counters and arguments.
         M = 0
         Ang = 0.
         DelAng = (PI / 2**N)
         DelPhi = DelAng / NPanel
C  *  *  Set first set of values.
         do 110 NC = 0,NPanel
            M = M + 1
            Phi = Ang + NC * DelPhi
```

```
            TCoef(M,N) = CoefNC(NC) * DelAng
            CosPhi(M,N) = cos(Phi)
  110     continue
C  *  *  Set rest of the values.
          do 120 Int = N,1,-1
C  *  *  *  Update subinterval sizes.
             Ang = Ang + DelAng
             DelAng = PI / 2**Int
             DelPhi = DelAng / NPanel
C  *  *  *  Handle case of a point shared by adjacent subintervals.
             TCoef(M,N) = TCoef(M,N) + CoefNC(0) * DelAng
C  *  *  *  Set values at points in current subinterval.
             do 121 NC = 1,NPanel
                M = M + 1
                Phi = Ang + NC * DelPhi
                TCoef(M,N) = CoefNC(NC) * DelAng
                CosPhi(M,N) = cos(Phi)
  121        continue
  120     continue
  100 continue
      return
      end


      function Teri(TMu,TEta)
CCCCCCCCCCCCCCCCCCCCCCCCCCCCCCCCCCCCCCCCCCCCCCCCCCCCCCCCCCCCCCCCCCCCCCCCCCCC
C
C   FUNCTION:
C      To evaluate the Teri function at the specified values of
C      TMu and TEta.
C
C   READ-ONLY PARAMETERS:
C      TMu, TEta -> arguments of the Teri function
C
C   NOTES:
C      1.  A semi-adaptive quadrature scheme based on n-panel
C          Newton-Cotes is used to evaluate the Teri function.
C
C      2.  Subroutine initTF must be called to initialize various
C          arrays prior to the first call to this routine.
C
C   AUTHOR:
C      David Parekh   (September 1984)
```

```
C
CCCCCCCCCCCCCCCCCCCCCCCCCCCCCCCCCCCCCCCCCCCCCCCCCCCCCCCCCCCCCCCCCCCCCCCCCCC
C  *  Define common block.
      common /TF/ TCoef(55,8),CosPhi(55,8),NOrder,NPanel
C  *  Initialize variables.
      Teri = 0
      NumInt = 1.0 + NOrder * amax1(TMu,TEta)    !subintervals in 1st half
      IEnd = (NumInt + 1) * NPanel + 1           !number of points in interval
C  *  Evaluate Teri function by quadrature.
      do 1 I=1,IEnd
         Teri = Teri + (TCoef(I,NumInt) * CosPhi(I,NumInt)) /
     &                 ((1.  - TMu * CosPhi(I,NumInt)) *
     &                  sqrt(1.  - TEta * CosPhi(I,NumInt)))
    1 continue
      return
      end
```

B.3 SIVSPLINE

```
C*************************************************************************
C
C                        VORTEX  RING  SPEED
C
C          This program uses a spline technique to approximate
C     the self-induced velocity of an axisymmetric, inviscid
C     vortex ring.  The calculated speed is compared with the
C     theoretical approximation of the self-induced velocity of
C     an inviscid ring with a Gaussian core.
C     (For best match of velocities, use ALPHA = 0.2065)
C
C     Input:        Unit 5
C     Output:       Unit 6  (program prompts)
C
C     Written by:   David Parekh
C     Date:         August 1984
C
C*************************************************************************
C  *  Dimension variables and define common blocks.
      implicit real*8 (a-h,o-z)
      dimension VelInd(3),RRef(3),RNode(3,10000)
      common /POS/ RNode
      common /PARM/ Gamma,Nodes,ALPHA,COEF
```

```
C  *  Specify constants and parameters and initialize variables.
      data VCONST /0.558d0/
      PI = 2.d0 * dasin(1.d0)
      TWOPI = 2.d0 * PI
      COEF = -1.d0 / (4.d0 * PI)
C  *  Specify ring coordinates.
C  *  *  Specify geometry and circulation of ring.
         write(6,999)
  999    format(1x,'enter:',/,1x,'nodes, core, rad, gamma, alpha',/)
         read(5,*)Nodes,Core,Rad,Gamma,Alpha
C  *  *  Generate ring.
         Core2 = Core * Core
         call genrng(TWOPI,Rad,Nodes,Core2)
C  *  Calculate self-induced velocity by spline approximation.
      RRef(1) = RNode(1,1)
      RRef(2) = RNode(2,1)
      RRef(3) = RNode(3,1)
      call splvel(RRef,Core2,VelInd)
      VelMg2 = (VelInd(1) * VelInd(1)) + (VelInd(2) * VelInd(2)) +
     &         (VelInd(3) * VelInd(3))
      VelMag = dsqrt(VelMg2)
C  *  Calculate theoretical value of self-induced velocity.
      Fac1 = Gamma / (4.d0 * PI * Rad)
      Fac2 = dlog(8.d0 * Rad / Core) - VCONST
      SIVel = Fac1 * Fac2
      Error = VelMag - SIVel
      PerErr = (dabs(Error) / SIVel) * 100.d0
C  *  Write results.
      write(6,996)
      write(6,*) (VelInd(K), K=1,3)
  996 format(1x,//,2x,'xyz components of induced velocity:',/)
      write(6,995) SIVel,Error,PerErr
  995 format(//,5x,'Theoretical Velocity = ',f10.7,/,
     &       5x,'Error = ',f10.7,/,
     &       5x,'Percent Absolute Error = ',f10.7,/)
      write(10,994) Nodes,Core,Rad,Gamma
      write(10,996)
      write(10,*) (VelInd(K), K=1,3)
      write(10,995) SIVel,Error,PerErr
  994 format(/,5x,'Nodes = ',i6,
     &       /,5x,'Core = ',f7.4,
     &       /,5x,'Rad = ',f5.2,
     &       /,5x,'Gamma = ',f5.2,/)
```

```
      stop
      end


      SUBROUTINE GENRNG(TWOPI,RAD,CORE2)
CCCCCCCCCCCCCCCCCCCCCCCCCCCCCCCCCCCCCCCCCCCCCCCCCCCCCCCCCCCCCCCCCCCCCCCCCCCCCCC
C
C     This subroutine (SUBROUTINE GENRNG) specifies the initial
C     coordinates and core size of the nodes on the newly created
C     vortex ring.
C
CCCCCCCCCCCCCCCCCCCCCCCCCCCCCCCCCCCCCCCCCCCCCCCCCCCCCCCCCCCCCCCCCCCCCCCCCCCCCCC
      implicit real*8 (a-h,o-z)
      DIMENSION RNODE(3,10000)
      COMMON /POS/ RNODE
      COMMON /PARM/ GAMMA,NODES,ALPHA,COEF
C  *  Calculate the initial coordinates.
      NDIV = 0
      SECT = NODES
      THETA = TWOPI/SECT
      DO 10 I=1,NODES
         DIV = NDIV
         ANGLE = DIV*THETA
         RNODE(1,I) = RAD*DCOS(ANGLE)
         RNODE(2,I) = RAD*DSIN(ANGLE)
         RNODE(3,I) = 0.
         NDIV = NDIV + 1
   10 CONTINUE
      RETURN
      END


      subroutine splvel(RRef,Core2,VelInd)
CCCCCCCCCCCCCCCCCCCCCCCCCCCCCCCCCCCCCCCCCCCCCCCCCCCCCCCCCCCCCCCCCCCCCCCCCCCCCCC
C
C     This subroutine (subroutine splvel) calculates the velocity
C     induced at the location of a specified node as a result of
C     the vorticity of the filament(s).  A spline is used to
C     evaluate the Biot-Savart integrand at the node points.  The
C     trapezoid rule is used to evaluate the integral.
C
CCCCCCCCCCCCCCCCCCCCCCCCCCCCCCCCCCCCCCCCCCCCCCCCCCCCCCCCCCCCCCCCCCCCCCCCCCCCCCC
C  *  Dimension variables, define common block, and set constants.
```

```
      implicit real*8 (a-h,o-z)
      dimension VelInd(3),RRef(3),RNode(3,10000),Dr(3),RDif(3),RDfXDx(3)
      dimension DxDs(3,10000),Vec(10000)
      common /POS/ RNode
      common /PARM/ Gamma,Nodes,ALPHA,COEF
      data SMIN,SDEL /1.d0,1.d0/
      GCoef = Gamma * COEF
C  *  Evaluate DxDs at the node points by spline approximation.
      call dpsplder(Nodes,SMin,SDel,RNode,DxDs)
C  *  Initialize velocity vector.
      VelInd(1) = 0.d0
      VelInd(2) = 0.d0
      VelInd(3) = 0.d0
C  *  Solve the Biot-Savart integral by the trapezoid rule.
      do 200 N = 1,Nodes
C  *  *  Calculate relative position vector.
         RDif(1) = RRef(1) - RNode(1,N)
         RDif(2) = RRef(2) - RNode(2,N)
         RDif(3) = RRef(3) - RNode(3,N)
         RDif2 = (RDif(1) * RDif(1)) + (RDif(2) * RDif(2)) +
     &           (RDif(3) * RDif(3))
C  *  *  Calculate Biot-Savart integrand at node points.
         BSDen = (RDif2 + (ALPHA * (Core2 + Core2)))**(-1.5d0)
         RDfXDx(1) = (RDif(2) * DxDs(3,N)) - (RDif(3) * DxDs(2,N))
         RDfXDx(2) = (RDif(3) * DxDs(1,N)) - (RDif(1) * DxDs(3,N))
         RDfXDx(3) = (RDif(1) * DxDs(2,N)) - (RDif(2) * DxDs(1,N))
         VelInd(1) = VelInd(1) + (RDfXDx(1) * BSDen)
         VelInd(2) = VelInd(2) + (RDfXDx(2) * BSDen)
         VelInd(3) = VelInd(3) + (RDfXDx(3) * BSDen)
  200 continue
      VelInd(1) = GCoef * VelInd(1)
      VelInd(2) = GCoef * VelInd(2)
      VelInd(3) = GCoef * VelInd(3)
      return
      end
```

```
      subroutine dpsplder(NumPts,XMin,Delta,YData,  DfDx)
C***********************************************************************
C
C   FUNCTION:
C      This subroutine (DPSPLDER) fits a set of evenly-spaced data
C   with a periodic cubic spline and evaluates the value of the
C   first derivative at the data points.  Double precision is used.
C
C   READ-ONLY PARAMETERS:
C      NumPts -> number of data points
C      XMin -> value of independent variable at first data point
C      Delta -> size of subinterval
C      YData -> vector of 3-D data
C
C   WRITE-ONLY PARAMETERS:
C      DfDx -> value of first derivative of spline function at nodes
C
C   NOTES:
C      The coefficient matrix of the vector of unknown second
C   derivatives is tridiagonal with the exception of the elements
C   (1,N) and (N,1).  The matrix is stored in the three vectors
C   DiagUp, DiagMn, and DiagLw, which represent the three diagonals.
C   The elements DiagUp(N) and DiagLw(N) are not used.
C      The vectors RowN and ColN represent the Nth row and column
C   of the coefficient matrix.  The last elements of RowN and
C   ColN are not used.
C      The vector YData should not include the last data point of the
C   the periodic curve since it is assumed to be equal to the first.
C   The number of data points must be at least 3 and at most 10000.
C
C   AUTHOR:
C      David Parekh   (August 1984)
C
C***********************************************************************
      implicit real*8 (a-h,o-z)
      dimension YData(3,NumPts + 2),DfDx(3,NumPts)
      dimension DiagUp(10000),DiagMn(10000),DiagLw(10000)
      dimension RowN(10000),ColN(10000)
      dimension YVec(3,10000),D2fDx2(3,10002)
C  *  Initialize vectors and NP1.
      do 1 N = 1,NumPts
         DiagUp(N) = 0.25d0
         DiagMn(N) = 1.d0
```

```
            DiagLw(N) = 0.25d0
            RowN(N) = 0.d0
            ColN(N) = 0.d0
         1 continue
           NP1 = NumPts - 1
           NP2 = NumPts - 2
           RowN(1) = 0.25d0
           RowN(NP1) = 0.25d0
           ColN(1) = 0.25d0
           ColN(NP1) = 0.25d0
C  *  Compute vector on right hand side of matrix equation.
           do 10 I = 1,3
              do 11 N = 2,NP1
                 YVec(I,N) = YData(I,N-1) - (2 * YData(I,N)) + YData(I,N+1)
        11    continue
              YVec(I,1) = YData(I,NumPts) - (2 * YData(I,1)) + YData(I,2)
              YVec(I,NumPts) = YData(I,NP1) - (2 * YData(I,NumPts)) +
          &                    YData(I,1)
        10 continue
C  *  Solve system of equations by Gauss-Jordan technique.
C  *  *  Perform forward elimination and normalize diagonal elements.
C        (Note:  the lower diagonal is not updated to 0 to save cost.)
C        (Note:  the (1,1) element is assumed to be initially 1.)
C  *  *  *  Do all but the last set of operations.
              do 20 NF = 2,NP1
                 NF1 = NF - 1
C  *  *  *  *  Forward elimination of lower diagonal.
                 Factor = DiagLw(NF1) / DiagMn(NF1)
                 DiagMn(NF) = DiagMn(NF) - (Factor * DiagUP(NF1))
                 ColN(NF) = ColN(NF) - (Factor * ColN(NF1))
                 do 21 I = 1,3
                    YVec(I,NF) = YVec(I,NF) - (Factor * YVec(I,NF1))
        21       continue
C  *  *  *  *  Normalization of row NF.
                 DiagUp(NF) = DiagUp(NF) / DiagMn(NF)
                 ColN(NF) = ColN(NF) / DiagMn(NF)
                 do 22 I = 1,3
                    YVec(I,NF) = YVec(I,NF) / DiagMn(NF)
        22       continue
                 DiagMn(NF) = 1.d0
C  *  *  *  *  Forward elimination of bottom row.
                 Factor = RowN(NF1)
                 RowN(NF) = RowN(NF) - (Factor * DiagUp(NF1))
```

```
            DiagMn(NumPts) = DiagMn(NumPts) - (Factor * ColN(NP1))
            do 23 I = 1,3
               YVec(I,NumPts) = YVec(I,NumPts) - (Factor*YVec(I,NP1))
 23         continue
 20      continue
C  *  *  *  Update certain elements.
         DiagLw(NP1) = RowN(NP1)
         DiagUp(NP1) = ColN(NP1)
C  *  *  *  Complete forward elimination process.
         Factor = DiagLw(NP1) / DiagMn(NP1)
         DiagMn(NumPts) = DiagMn(NumPts) - (Factor * DiagUp(NP1))
         do 25 I = 1,3
            YVec(I,NumPts) = YVec(I,NumPts) - (Factor * YVec(I,NP1))
            YVec(I,NumPts) = YVec(I,NumPts) / DiagMn(NumPts)
 25      continue
         DiagMn(NumPts) = 1.d0
C  *  *  Perform back elimination and scale D2fDx2.    Without scaling,
C     the result would be (D2fDx2 / Coef) instead of D2fDx2.
C     (Note:  the upper diagonal is not updated to 0 to save cost.)
      Delta2 = Delta * Delta
      Coef = 6.d0 / (4.d0 * Delta2)
C  *  *  *  Start back elimination process.
         do 35 I = 1,3
            D2fDx2(I,NumPts) = Coef * YVec(I,NumPts)
            YVec(I,NP1) = YVec(I,NP1) - (DiagUp(NP1)*YVec(I,NumPts))
            D2fDx2(I,NP1) = Coef * YVec(I,NP1)
 35      continue
C  *  *  *  Complete back elimination process.
         do 30 NB = NP2,1,-1
            NB1 = NB + 1
            do 31 I = 1,3
               YVec(I,NB) = YVec(I,NB) - (DiagUp(NB) * YVec(I,NB1))
     &                                 - (ColN(NB) * YVec(I,NumPts))
               D2fDx2(I,NB) = Coef * YVec(I,NB)
 31         continue
 30      continue
C  *  *  *  Specify periodicity conditions.
         N1 = NumPts + 1
         N2 = NumPts + 2
         do 36 I = 1,3
            D2fDx2(I,N1) = D2fDx2(I,1)
            D2fDx2(I,N2) = D2fDx2(I,2)
            YData(I,N1) = YData(I,1)
```

```
                YData(I,N2) = YData(I,2)
   36         continue
C  *  Evaluate DfDx.
      Fac = Delta / (-6.d0)
      do 40 NP = 1,NumPts
         NP1 = NP + 1
         do 41 I = 1,3
            Term1 = (YData(I,NP1) - YData(I,NP)) / Delta
            Term2 = Fac * ((2.d0 * D2fDx2(I,NP)) + D2fDx2(I,NP1))
            DfDx(I,NP) = Term1 + Term2
   41    continue
   40 continue
      return
      end
```

Appendix C

TABLES OF PARAMETERS

Table C.1. Parameters of Bifurcating Jet Simulations

Index	Excitation	A_a	St_a	$\bar{\sigma}$	N
01	flapping	0.1	0.50	0.10	32
02	flapping	0.2	0.50	0.10	32
03	flapping	0.1	0.30	0.10	32
04	flapping	0.5	0.50	0.10	32
05	flapping	0.5	0.30	0.10	32
06	helical	0.5	0.30	0.10	32
07	helical	0.5	0.30	0.03	32
08	helical	0.5	0.30	0.10	32
09	helical	0.5	0.40	0.10	32
10	helical	0.5	0.35	0.10	32
11	helical	0.5	0.45	0.10	32
12	helical	0.5	0.25	0.10	32
13	helical	0.5	0.43	0.10	32
14	helical	0.5	0.42	0.10	32
15	helical	0.1	0.20	0.10	32
16	helical	0.3	0.35	0.10	32
17	helical	0.3	0.32	0.10	16
18	helical	0.3	0.38	0.10	16
19	helical	0.3	0.30	0.10	16
20	helical	0.3	0.30	0.10	32

Table C.2. Comparison of Physical Parameters

	Lee & Reynolds (1985b)	Current Work
Fluid	Water	Air
Re	2,800–10,000	10,000–100,000
St_a	0.3–0.7	0.40–0.65
U (m/s)	0.2–0.8	7–75
f (Hz)	5–40	130–2,400
D (cm)	1.27	2.15 & 2.00

Table C.3. Parameters of Bifurcating Jet Experiments

Nominal Re	10,000	20,000	25,000	50,000	100,000
U (m/s)	7.1	14	18.4	36.9	75.6
D (cm)	2.15	2.15	2.00	2.00	2.00
ν (cm^2/s)	0.15	0.15	0.154	0.155	0.162
Actual Re	10,000	20,000	23,900	47,700	93,400
f_a (Hz)	180	386	516	1030	2060
f_h (Hz)	90	193	258	515	1030
St_a	0.55	0.59	0.561	0.558	0.545
St_h	0.27	0.30	0.280	0.279	0.273
δ_ω / R	0.12	—	0.043	0.025	0.018
u'/U	0.013	0.006	0.005	0.003	0.002

REFERENCES

Arbey, H. & Ffowcs Williams, J. E. 1984 Active cancellation of pure tones in an excited jet. *J. Fluid Mech.* **149**, 445–454.

Ashurst, W. T. & Meiburg, E. 1988 Three-dimensional shear layers via vortex dynamics. *J. Fluid Mech.* **189**, 87–116.

Batchelor, G. K. 1967 *An Introduction to Fluid Dynamics.* Cambridge University Press.

Bearman, P. W. 1971 Corrections for the effect of ambient temperature drift on hot-wire measurements in incompressible flow. DISA Info. Bull. **11**.

Bechert, D. W. 1988 Excitation of instability waves in free shear layers. Part 1. Theory. *J. Fluid Mech.* **186**, 47–62.

Bouchard, E. E. & Reynolds, W. C. 1981 The effects of forcing on the mixing-layer region of a round jet. In *Proc. IUTAM Symp. on Unsteady Turbulent Shear Flows.* 370–379.

Bouchard, E. E. & Reynolds, W. C. 1982 The structure and growth of the mixing layer region of a round jet. Ph.D. dissertation, Thermosciences Division, Department of Mechanical Engineering, Stanford University.

Brown, G. B. 1935 On vortex motion in gaseous jets and the origin of their sensitivity to sound. *Physical Society* **47**, 703–732.

Brown, G. L. & Roshko, A. 1974 On density effects and large structure in turbulent mixing layers. *J. Fluid Mech.* **64**, 775–816.

Cantwell, B. J. 1981 Organized motion in turbulent flow. *Ann. Rev. Fluid Mech.* **13**, 457–515.

Chan, Y. Y. 1977 Wavelike eddies in a turbulent jet. *AIAA J.* **15**, 992–1001.

Crow, S. C. & Champagne, F. H. 1971 Orderly structure in jet turbulence. *J. Fluid Mech.* **48**, 547–591.

Eaton, A. 1986 Private communication.

Gaster, M., Kit, E. & Wygnanski, I. 1985 Large-scale structures in a forced turbulent mixing layer. *J. Fluid Mech.* **150**, 23–39.

Gutmark, E. & Ho, C. M. 1983 Preferred modes and the spreading rates of jets. *Phys. Fluids* **26**, 2932–2938.

Ho, C. M. & Gutmark, E. 1987 Vortex induction and mass entrainment in a small-aspect-ratio elliptic jet. *J. Fluid Mech.* **179**, 383–405.

Ho, C. M. & Huang, L. S. 1982 Subharmonics and vortex merging in mixing layers. *J. Fluid Mech.* **119**, 443–473.

Ho, C. M. & Huerre, P. 1984 Perturbed free shear layers. *Ann. Rev. Fluid Mech.* **16**, 365–424.

Hussain, A. K. M. F. & Clark, A. R. 1981 On the coherent structure of the axisymmetric mixing layer: a flow-visualization study. *J. Fluid Mech.* **104**, 263–294.

Hussain, A. K. M. F. & Zaman, K. B. M. Q. 1981 The "preferred mode" of the axisymmetric jet. *J. Fluid Mech.* **110**, 39–71.

Kerschen, E. J. & Johnston, J. P. 1978 Modal content of noise generated by a coaxial jet in a pipe. Report MD-38, Thermosciences Division, Department of Mechanical Engineering, Stanford University.

Koch, C. R., Mungal, M. G., Reynolds, W. C. & Powell, J. D. 1988 Helical modes in round jets. Poster presented in 6th Ann. Picture Gallery of Fluid Motion, Amer. Phys. Soc., Fluid Dynamics Division.

Lamb, H. 1932 *Hydrodynamics.* Cambridge University Press.

Leconte, J. 1858 On the influence of musical sounds on the flame of a jet of coal gas. *Phil. Mag.* **15**, 235–239.

Lee, M. & Reynolds, W. C. 1982 Bifurcating and blooming jets. *Bull. Amer. Phys. Soc.* **27**, 1185.

Lee, M. & Reynolds, W. C. 1985a Bifurcating and blooming jets. *Fifth Symp. on Turbulent Shear Flows*, Ithaca, New York. 1.7–1.12.

Lee, M. & Reynolds, W. C. 1985b Bifurcating and blooming jets. Report TF-22, Thermosciences Division, Department of Mechanical Engineering, Stanford University.

Leonard, A. 1980 Vortex methods for flow simulation. *J. Comp. Phys.* **37**, 289–335.

Leonard, A. 1985 Computing three-dimensional incompressible flows with vortex elements. *Ann. Rev. Fluid Mech.* **17**, 523–559.

Leonard, A., Couet, B. & Parekh, D. 1985 Two studies in three-dimensional vortex dynamics: a perturbed round jet and an inhomogeneous mixing layer. Presented at *International Symp. on Separated Flow around Marine Structures*, Trondheim, Norway.

Lepicovsky, J., Ahuja, K. K., Brown, W. H. & Morris, P. J. 1985 Acoustic control of free jet mixing. *J. Propulsion* **2**, 323–330.

Michalke, A. 1972 The instability of free shear layers. In *Progress in Aerospace Science* **12**. Pergamon Press.

Michalke, A. & Hermann, G. 1982 On the inviscid instability of a circular jet with external flow. *J. Fluid Mech.* **114**, 343–359.

Monkewitz, P. A. 1988 Subharmonic resonance, pairing and shredding in the mixing layer. *J. Fluid Mech.* **188**, 223–252.

Monkewitz, P. A. & Huerre, P. 1982 The influence of the velocity ratio on the spatial instability of mixing layers. *Phys. Fluids* **25**, 1137–1143.

Moore, D. W. & Saffman, P. G. 1972 The motion of a vortex filament with axial flow. *Phil. Trans. R. Soc. London Ser. A* **272**, 403–429.

Oshima, Y. 1978 Head on collision of two vortex rings. *J. Phys. Soc. Japan* **44**, 328ff.

Oshima, Y. & Kuwahara, K. 1984 Experimental and numerical study of vortex interactions. *AIAA* paper 84–1546.

Parekh, D. E., Leonard, A. & Reynolds, W. C. 1983 A vortex-filament simulation of a bifurcating jet. *Bull. Amer. Phys. Soc.* **28**, 1353.

Parekh, D. E., Reynolds, W. C. & Mungal, M. G. 1987 Bifurcation of round air jets by dual-mode acoustic excitation. *AIAA* paper 87–0164.

Parekh, D. E. & Reynolds, W. C. 1987 Bifurcating air jets at higher subsonic speeds. Presented at *Sixth Symp. on Turbulent Shear Flows*, Toulouse, France.

Petersen, R. A. & Samet, M. M. 1987 On the preferred mode of jet instability. Submitted to *J. Fluid Mech.*

Roberts, D. W. & Johnston, J. P. 1974 Development of a new internal flow aeroacoustic facility—aerodynamic and acoustic experiments on square-edged orifices. Report PD-18, Thermosciences Division, Department of Mechanical Engineering, Stanford University.

Saffman, P. G. 1970 The velocity of viscous vortex rings. *Studies in Appl. Math.* **49**, 371–380.

Saffman, P. G. & Baker, G. R. 1979 Vortex interactions. *Ann. Rev. Fluid Mech.* **11**, 95–122.

Samet, M. M. & Petersen, R. A. 1987 Effects of forcing level on the stability of an axisymmetric mixing layer. Submitted to *Phys. Fluids.*

Tan-atichat, J. 1980 Effects of axisymmetric contractions of various scales. Ph.D. thesis, Illinois Institute of Technology.

Tso, J. & Hussain, A. K. M. F. 1987 Organized motion in a fully developed turbulent axisymmetric jet. Submitted to *J. Fluid Mech.*

Tyndall, J. 1867 On the action of sonorous vibrations on gaseous and liquid jets. *Phil. Mag.* **33**, 375–391.

Winant, C. D. & Browand, F. K. 1974 Vortex pairing: the mechanism of turbulent mixing-layer growth at moderate Reynolds number. *J. Fluid Mech.* **63**, 237–255.

Wlezien, R. W. & Kibens, V. 1984 Passive control of jets with indeterminant origins. *AIAA* paper 84–2299.

Zaman, K. B. M. Q. & Hussain, A. K. M. F. 1980 Vortex pairing in a circular jet under controlled excitation. Part 1. General jet response. *J. Fluid Mech.* **101**, 449–491.

Figure 1.1. Side and end views of bifurcating jet at $Re = 4300$ and $St = 0.46$ (from Lee & Reynolds 1985b).

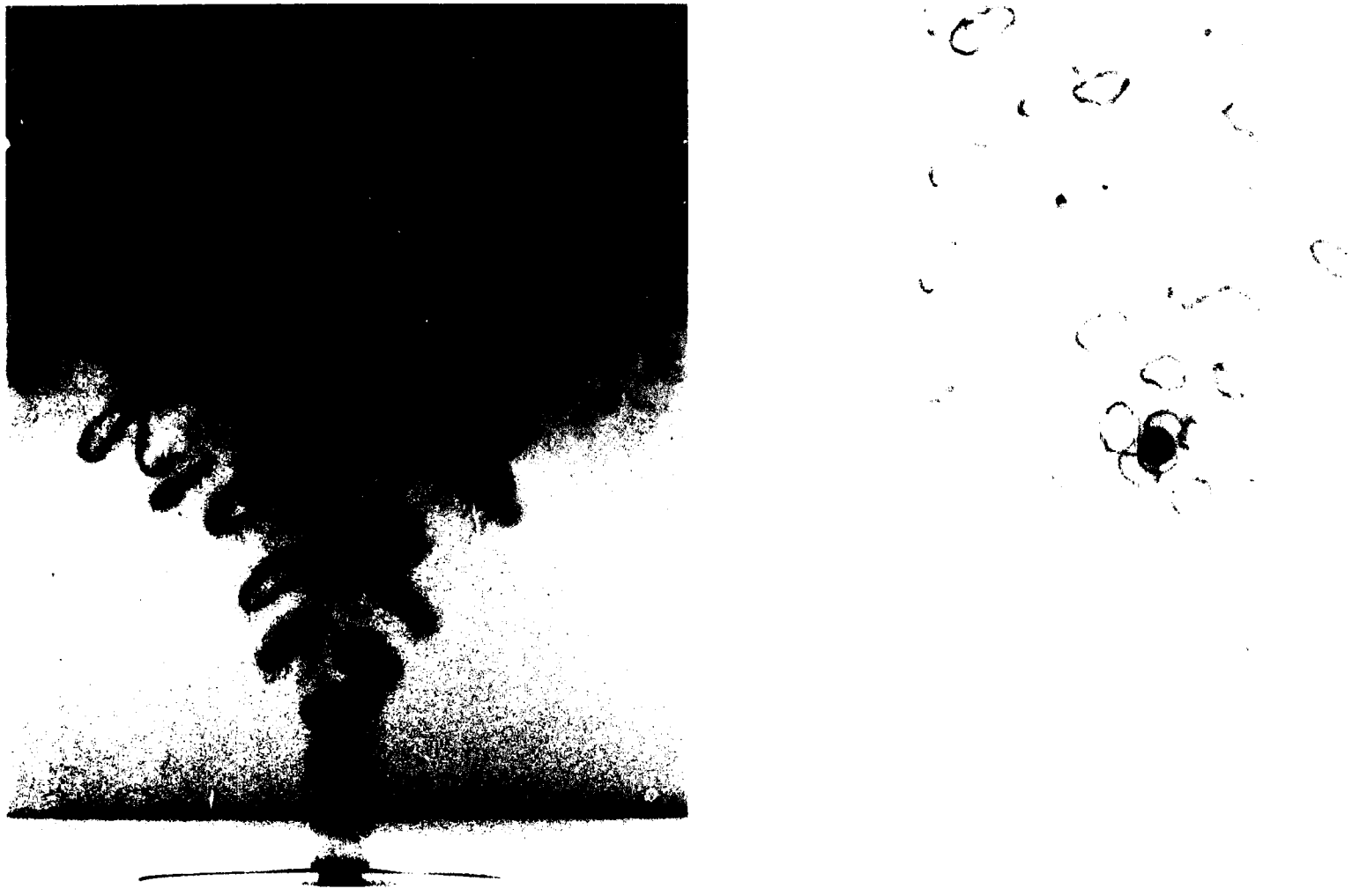

Figure 1.2. Side and end views of blooming jet at $Re = 4300$ and $St = 0.46$ (from Lee & Reynolds 1985b).

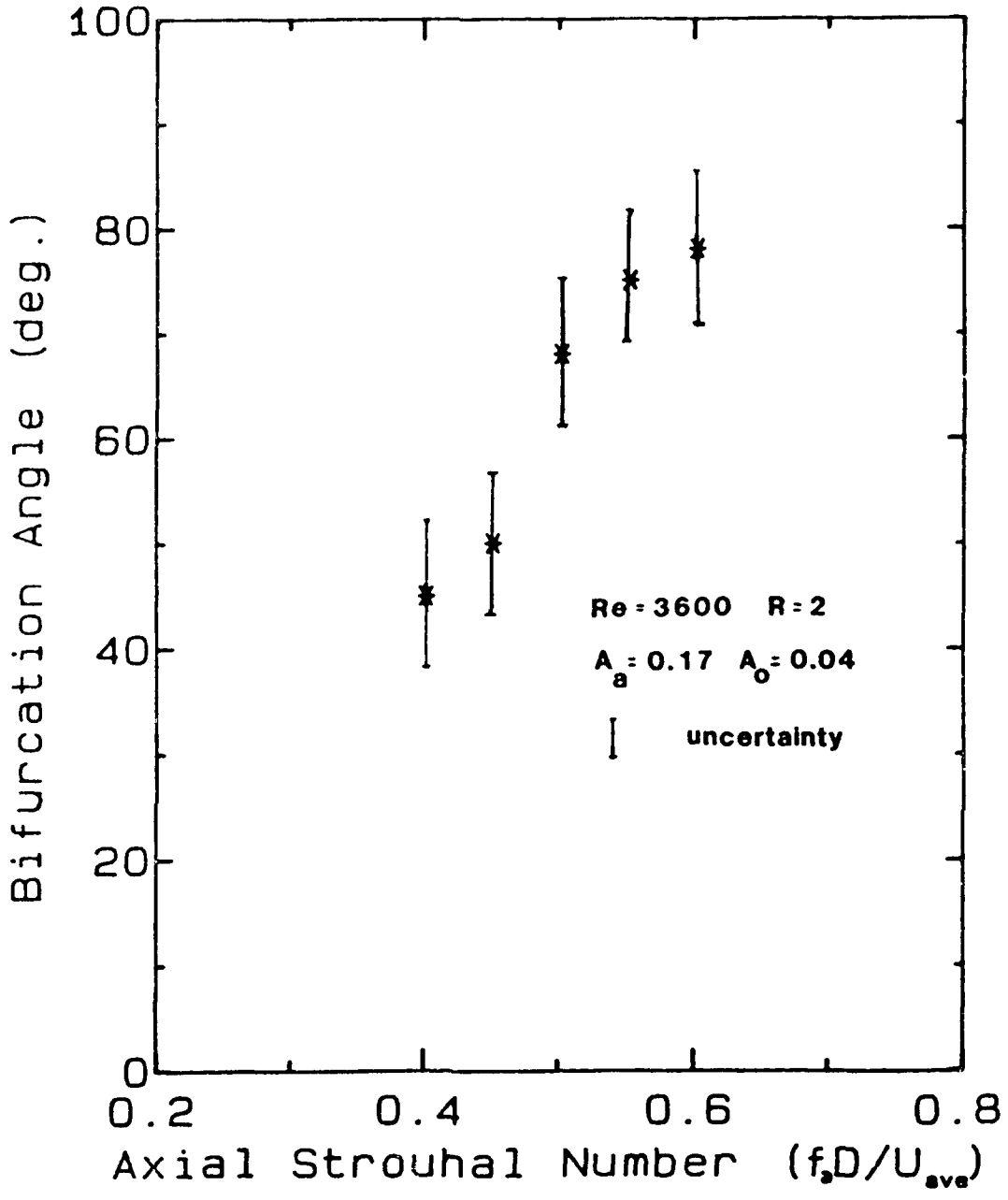

Figure 1.3. Dependence of bifurcation angle on axial excitation frequency (from Lee & Reynolds 1985b).

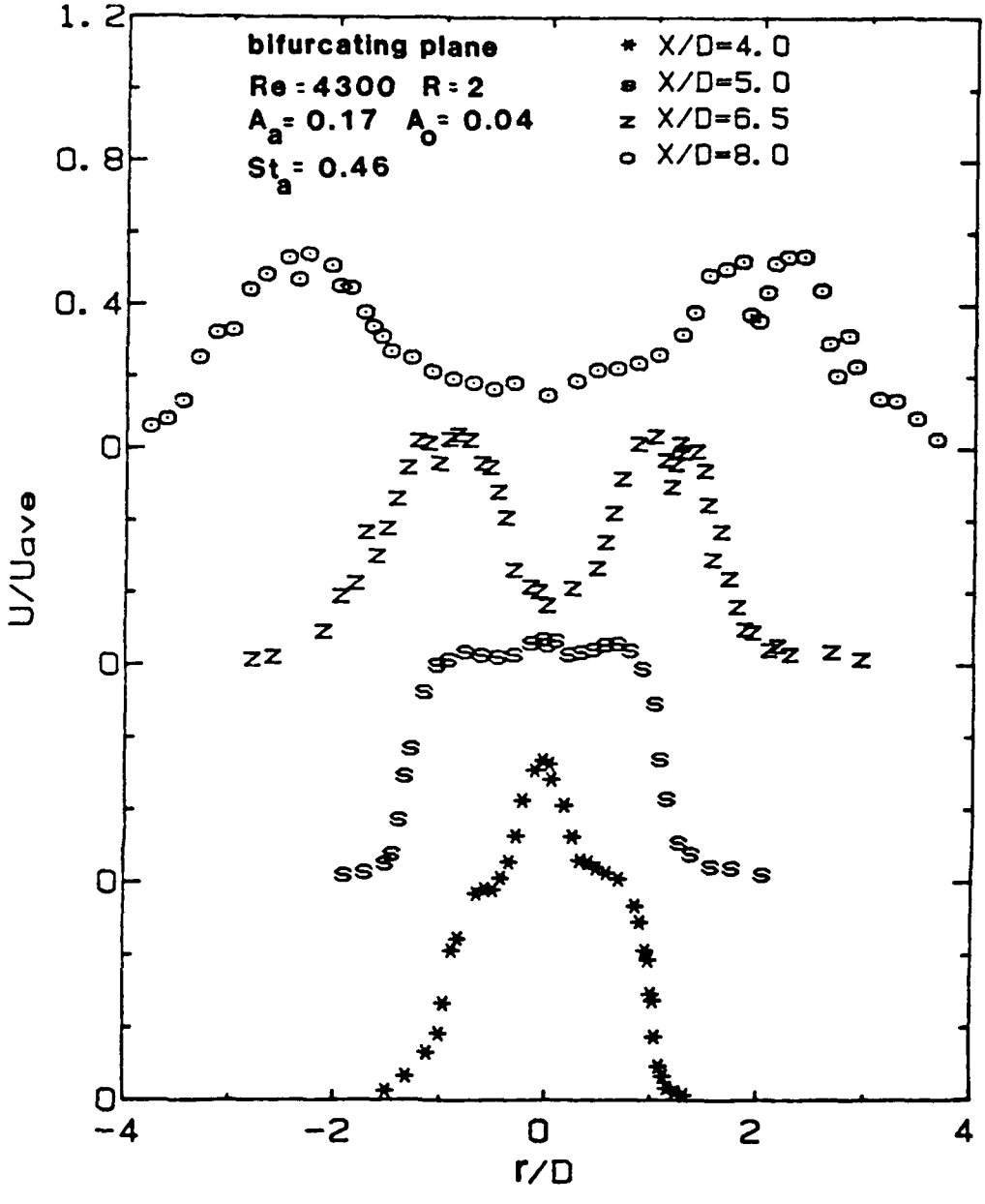

Figure 1.4. Mean velocity profile of bifurcating jet in the bifurcating plane (from Lee & Reynolds 1985b). $Re = 4300$ and $St = 0.46$.

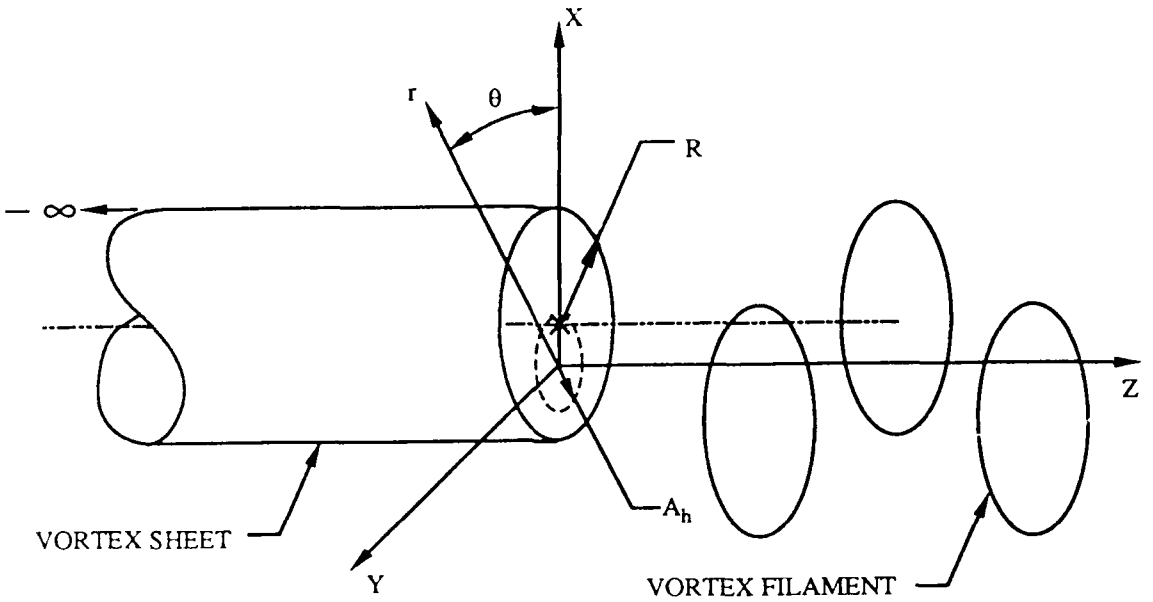

Figure 2.1. Schematic of numerical model.

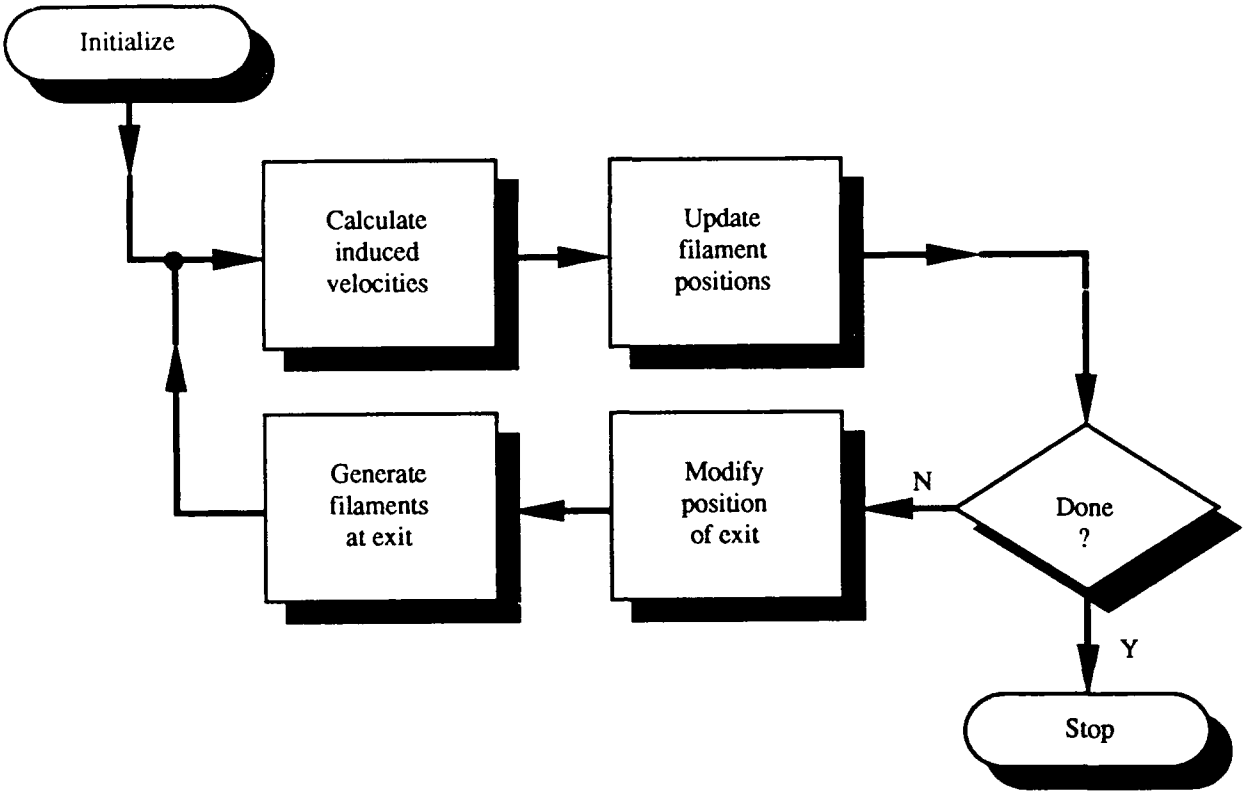

Figure 2.2. Flow chart of numerical algorithm.

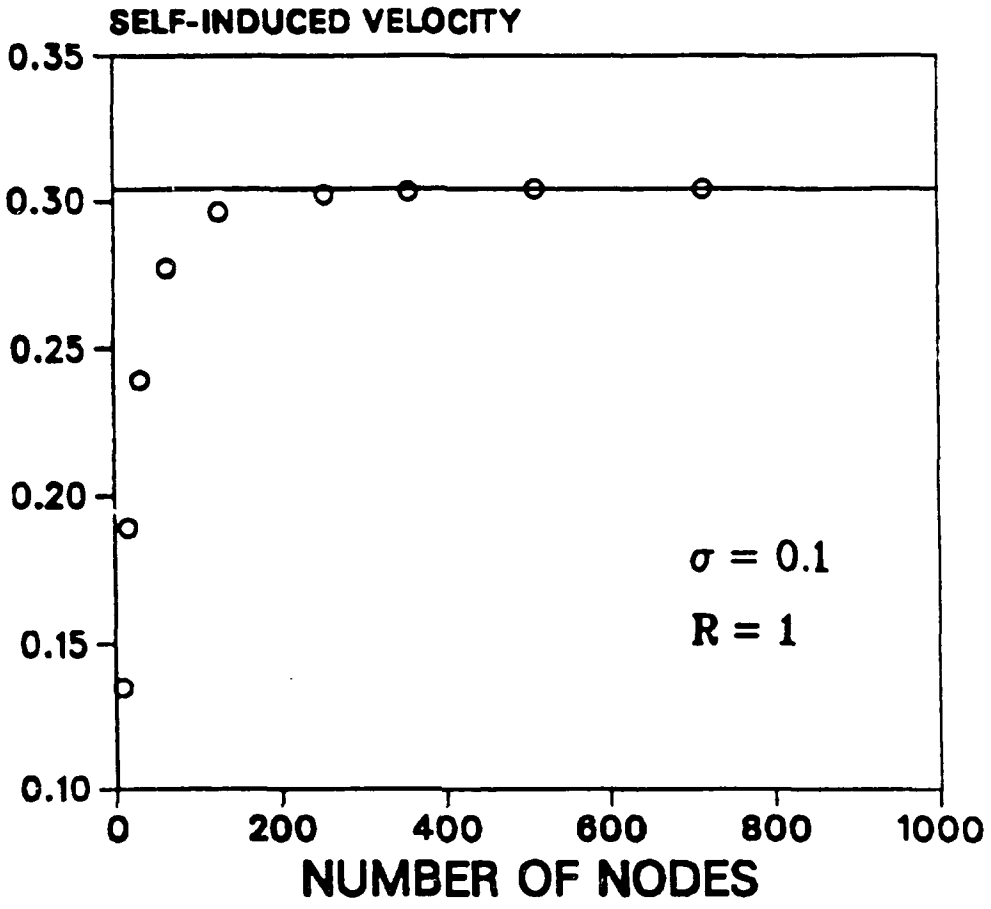

Figure 3.1. Calculation of self-induced velocity.

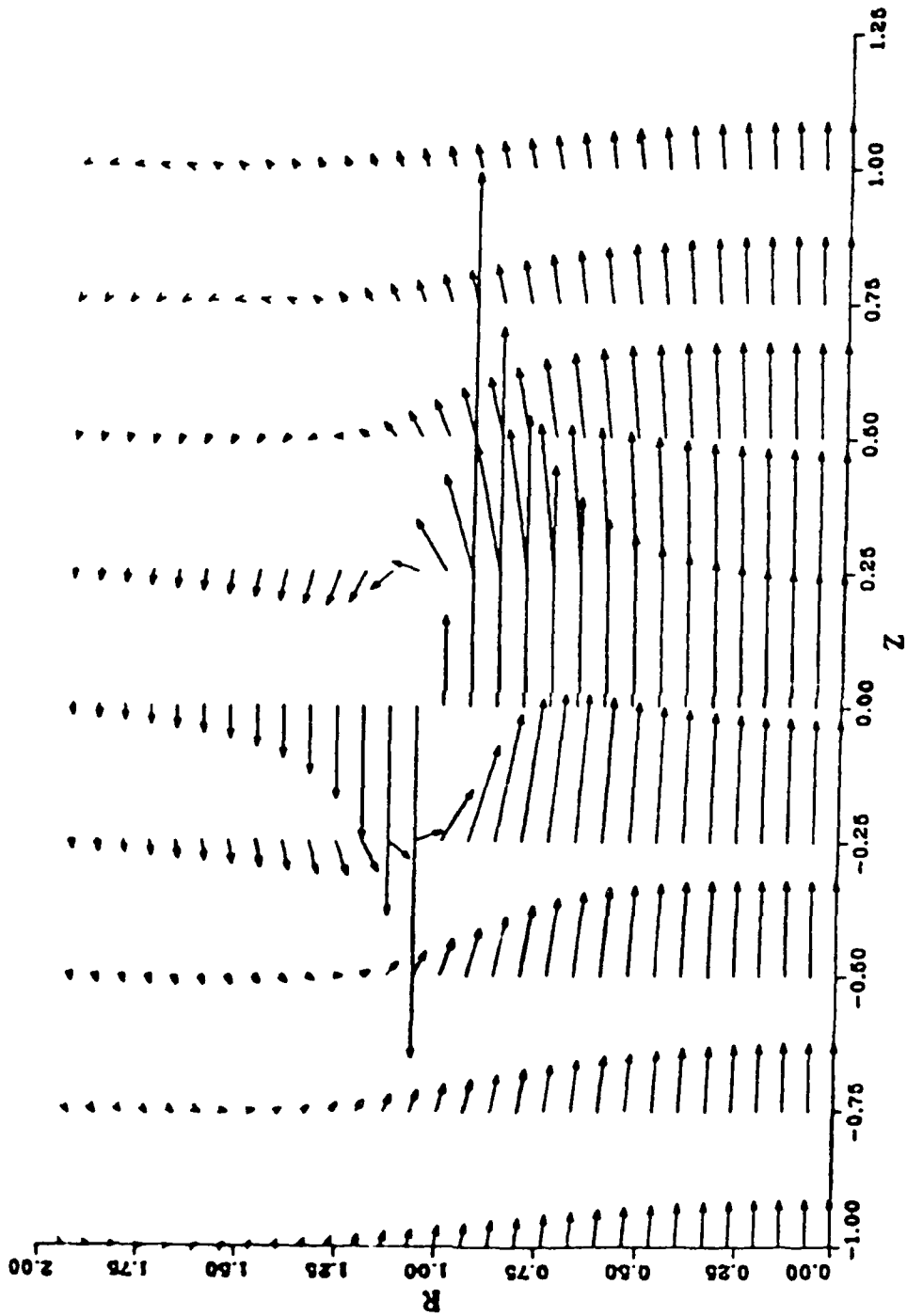

Figure 3.2. Velocity field of a vortex ring. $\bar{\sigma} = 0.1$.

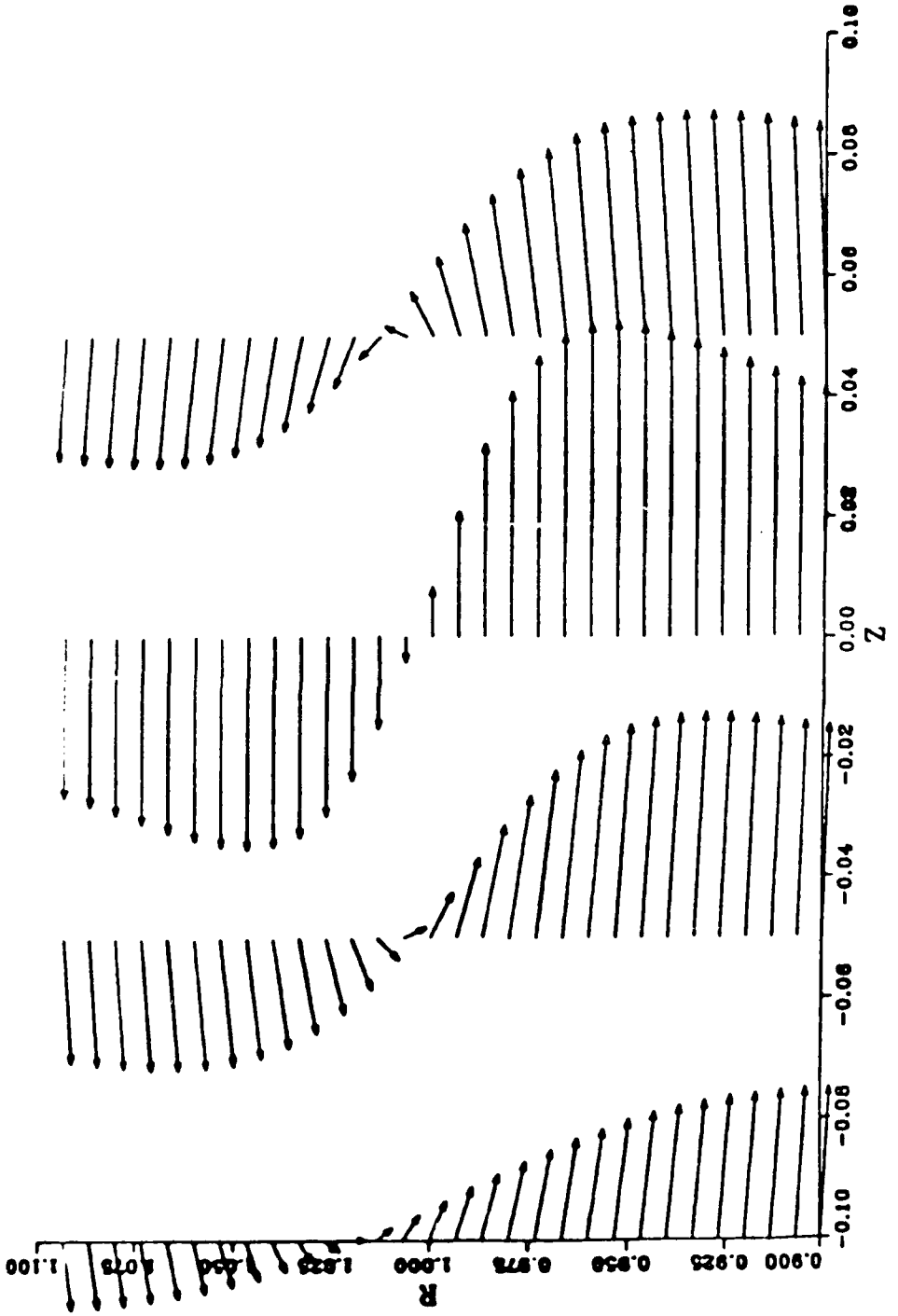

Figure 3.3. Velocity field in the core of a vortex ring. $\bar{\sigma} = 0.1$.

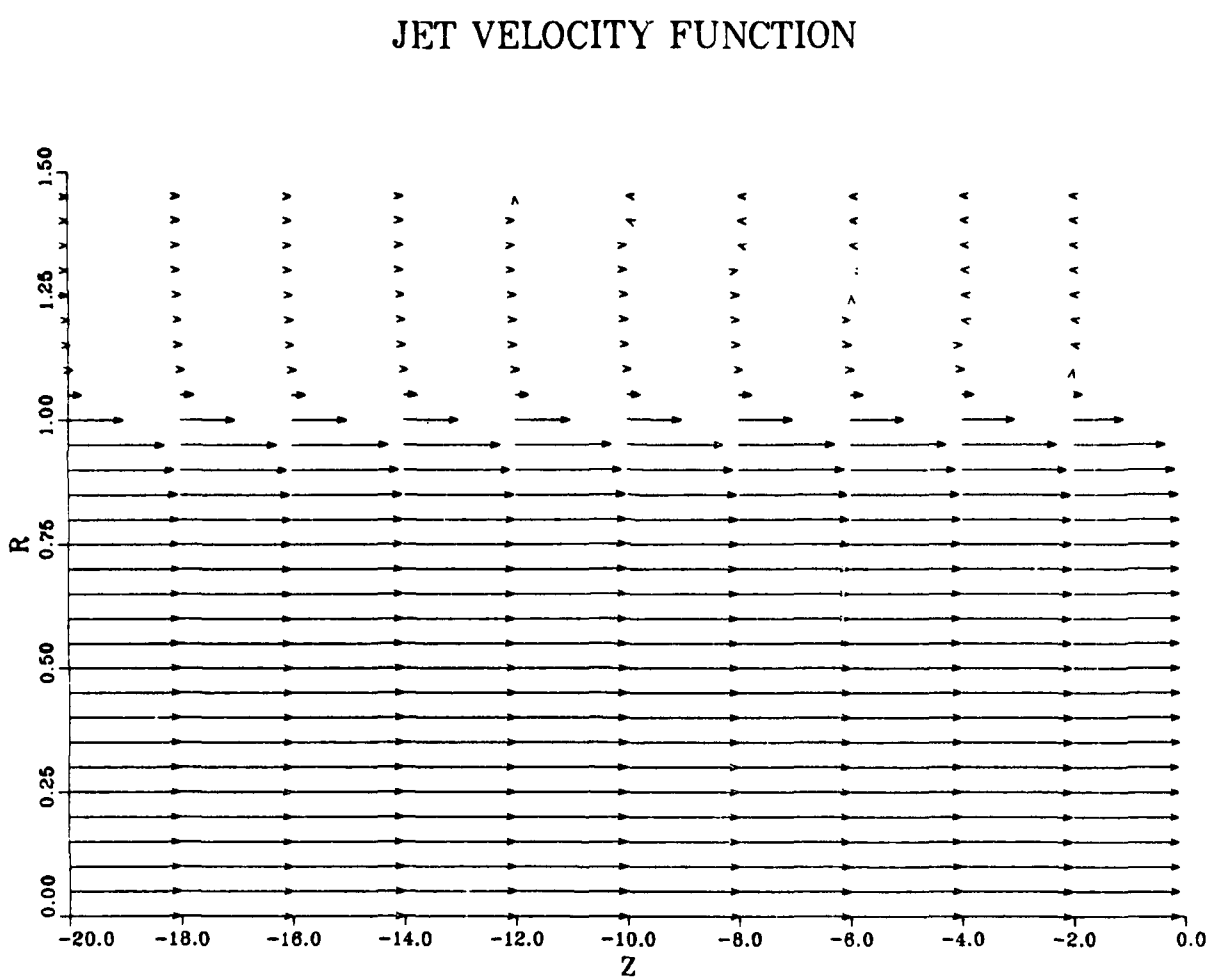

Figure 3.4. Upstream velocity field of jet source flow.

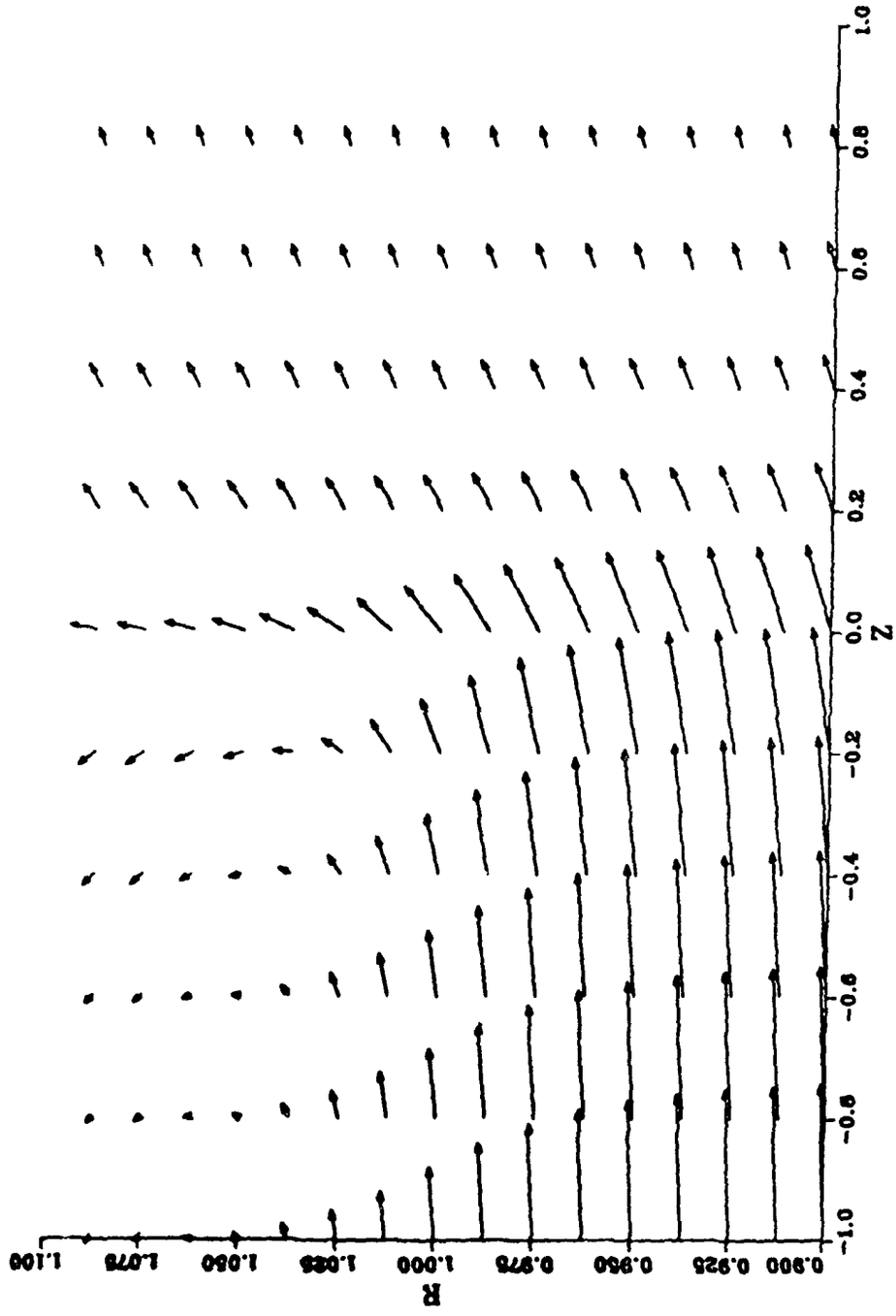

Figure 3.5. Velocity field near the exit of jet source flow.

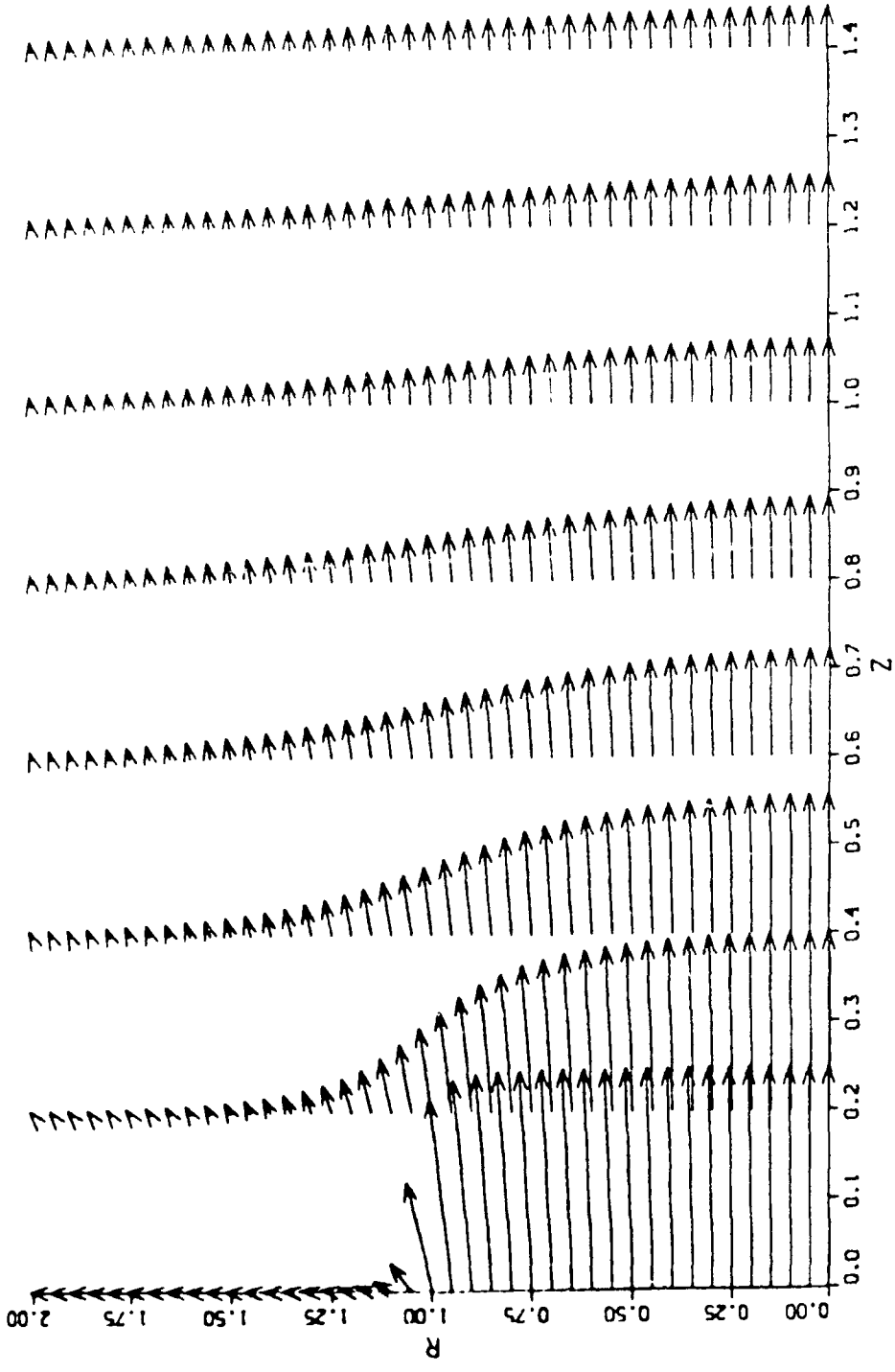

Figure 3.6. Downstream velocity field of jet source flow.

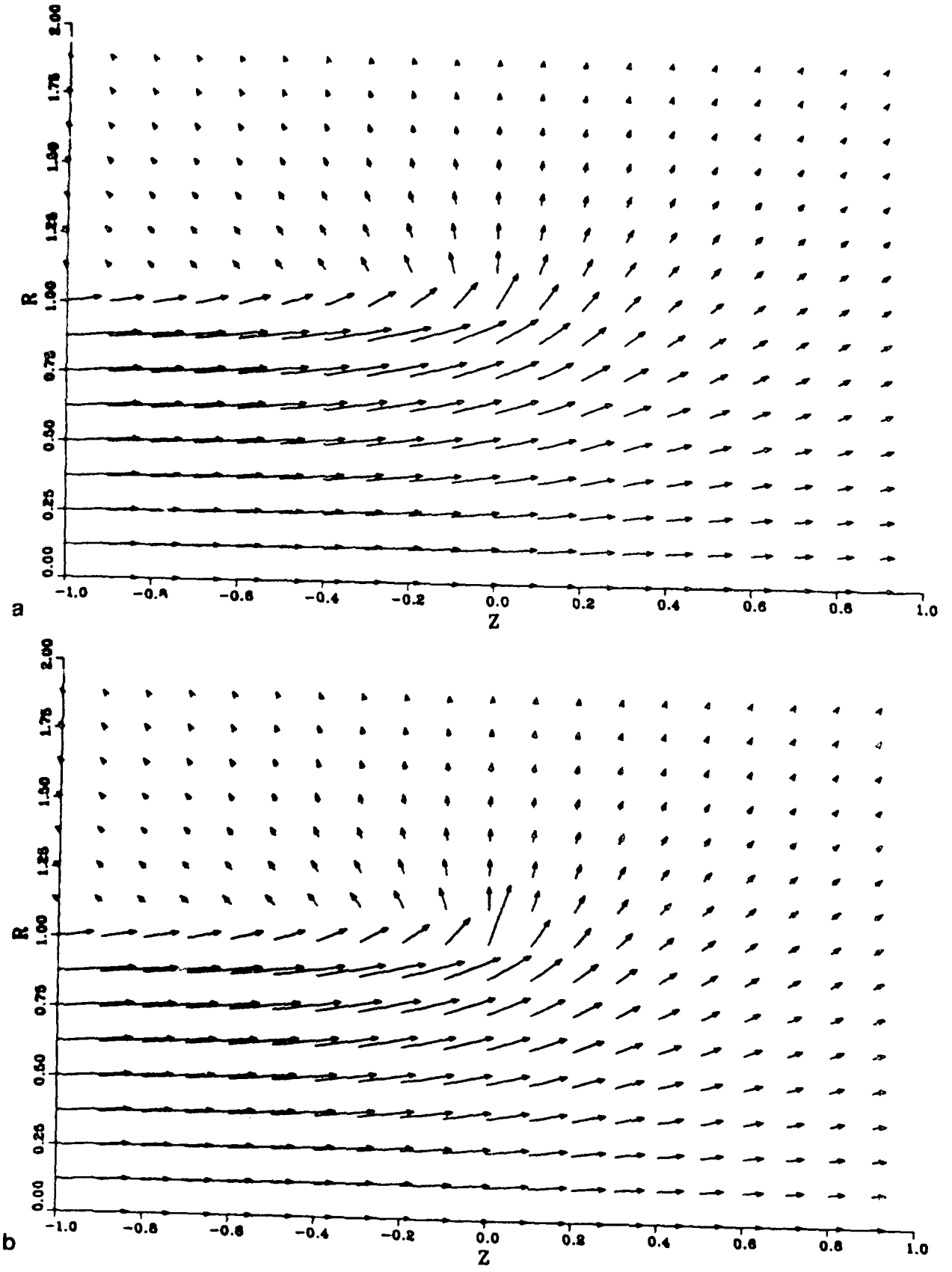

Figure 3.7. Comparison of jet function velocity fields at different $\bar{\sigma}$: (a) $\bar{\sigma} = 0.1$, (b) $\bar{\sigma} = 0.01$.

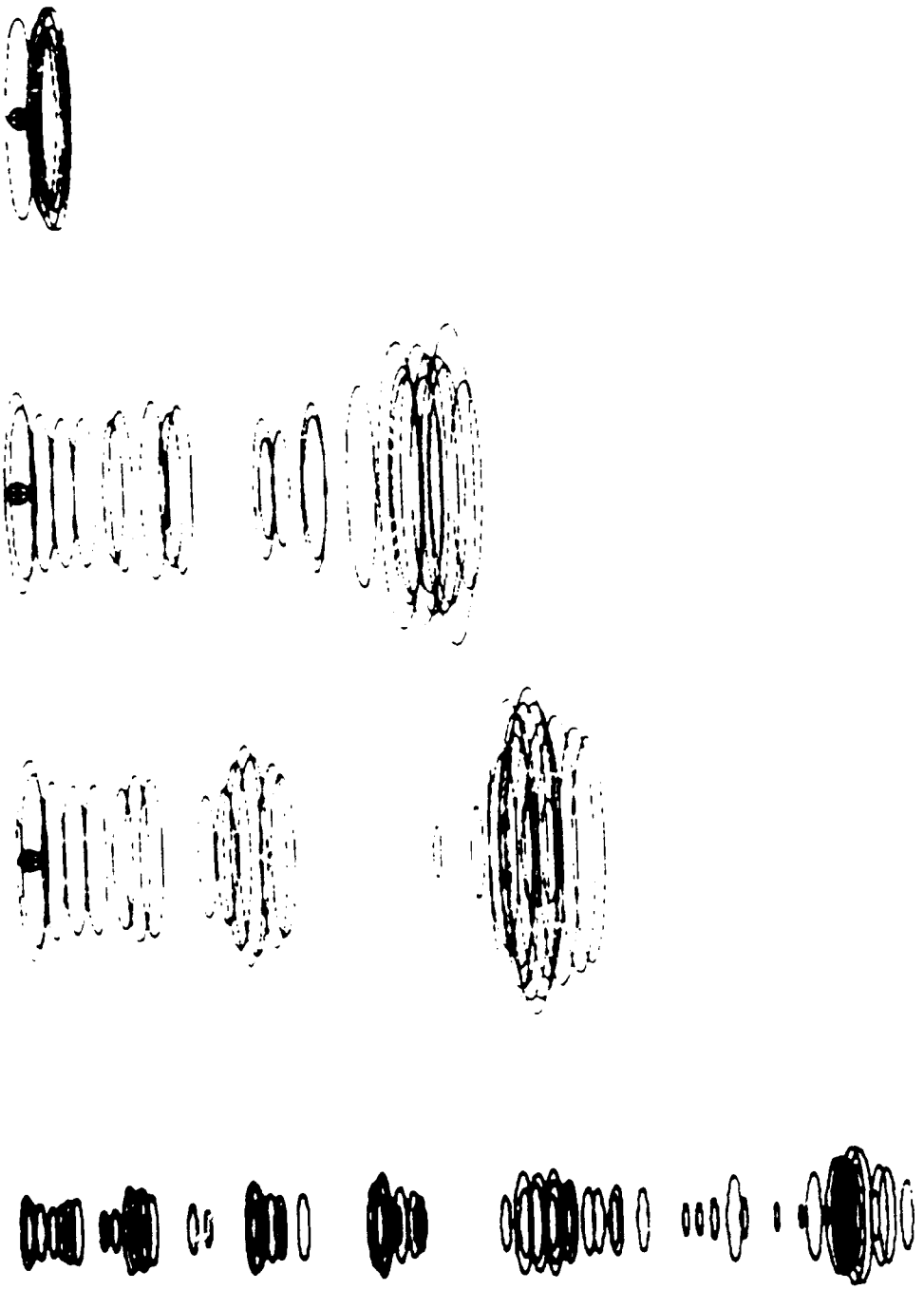

Figure 3.8. Evolution of unexcited, axisymmetric shear layer (source flow not included).

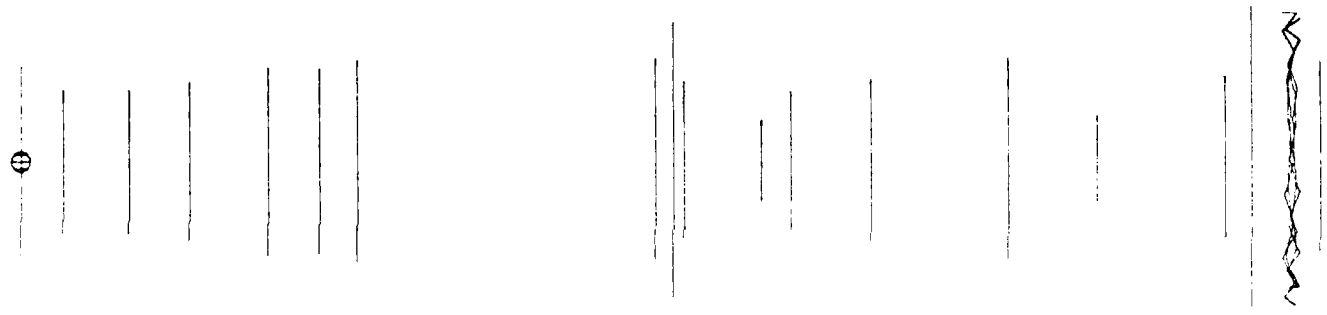

Figure 3.9. Example of numerical instability in axisymmetric shear layer calculations.

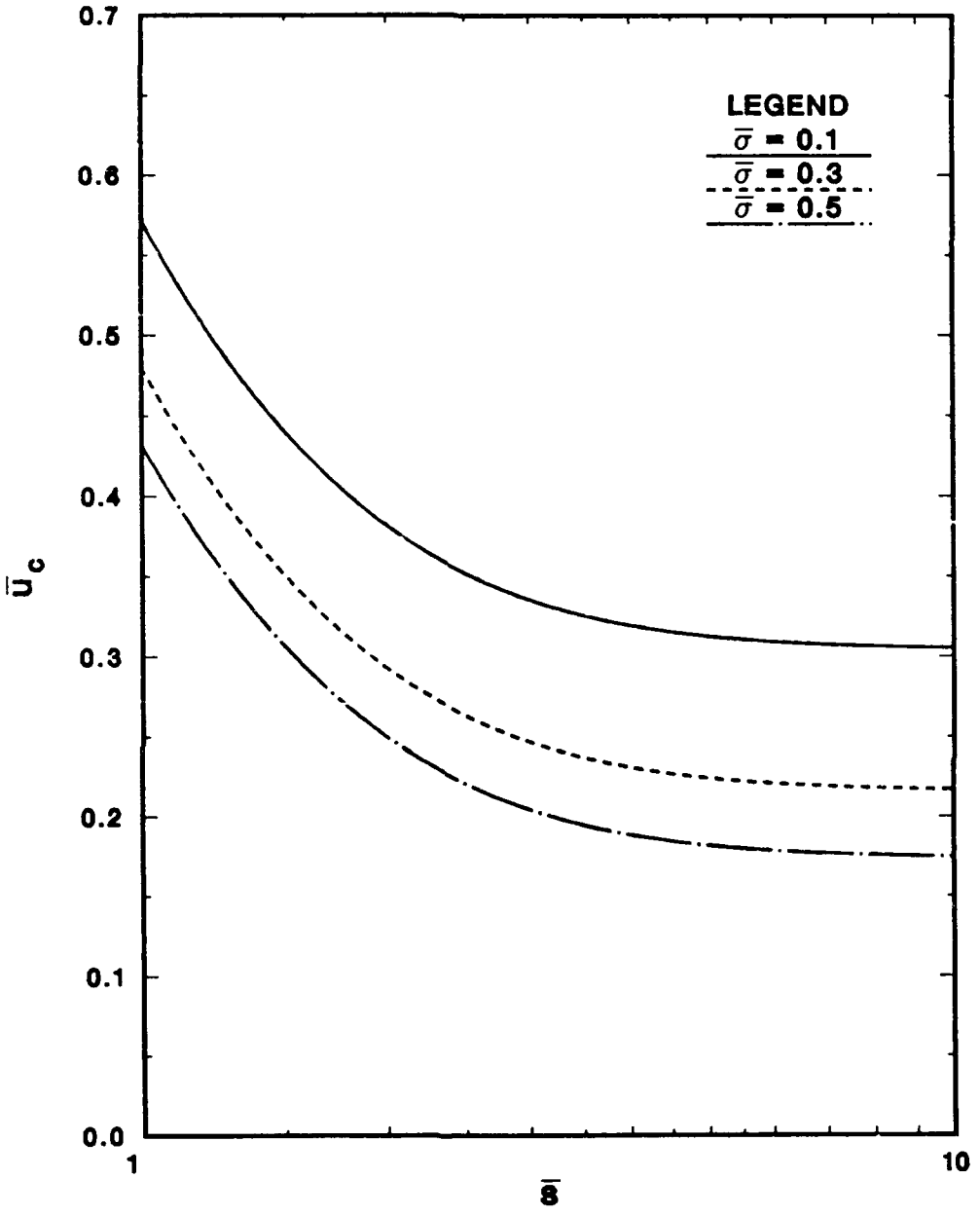

Figure 3.10. Convection velocity of a train of rings ($N_v = 41$).

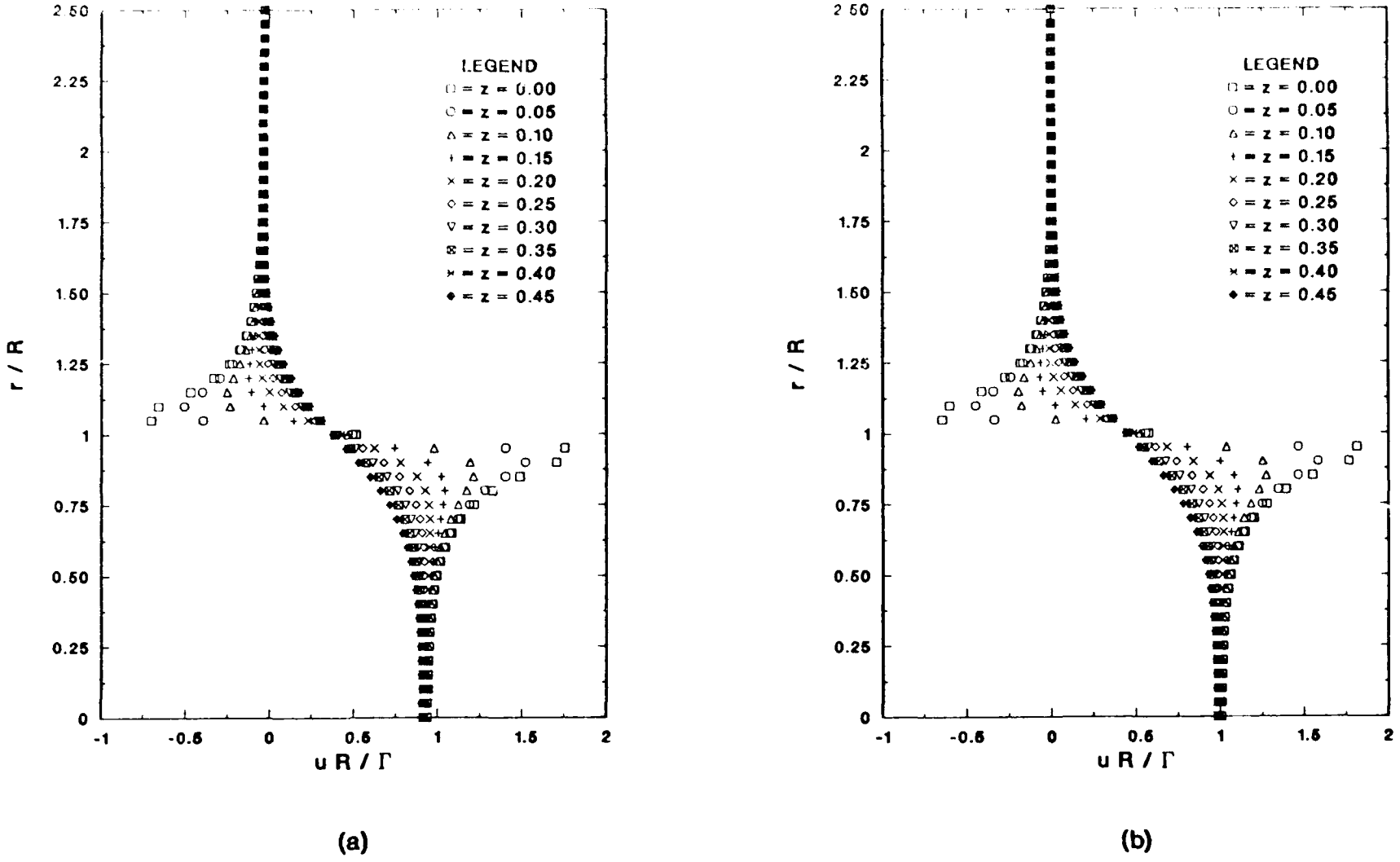

Figure 3.11. Instantaneous velocity profiles of a train of rings for (a) $N_v = 5$ and (b) $N_v = 41$.

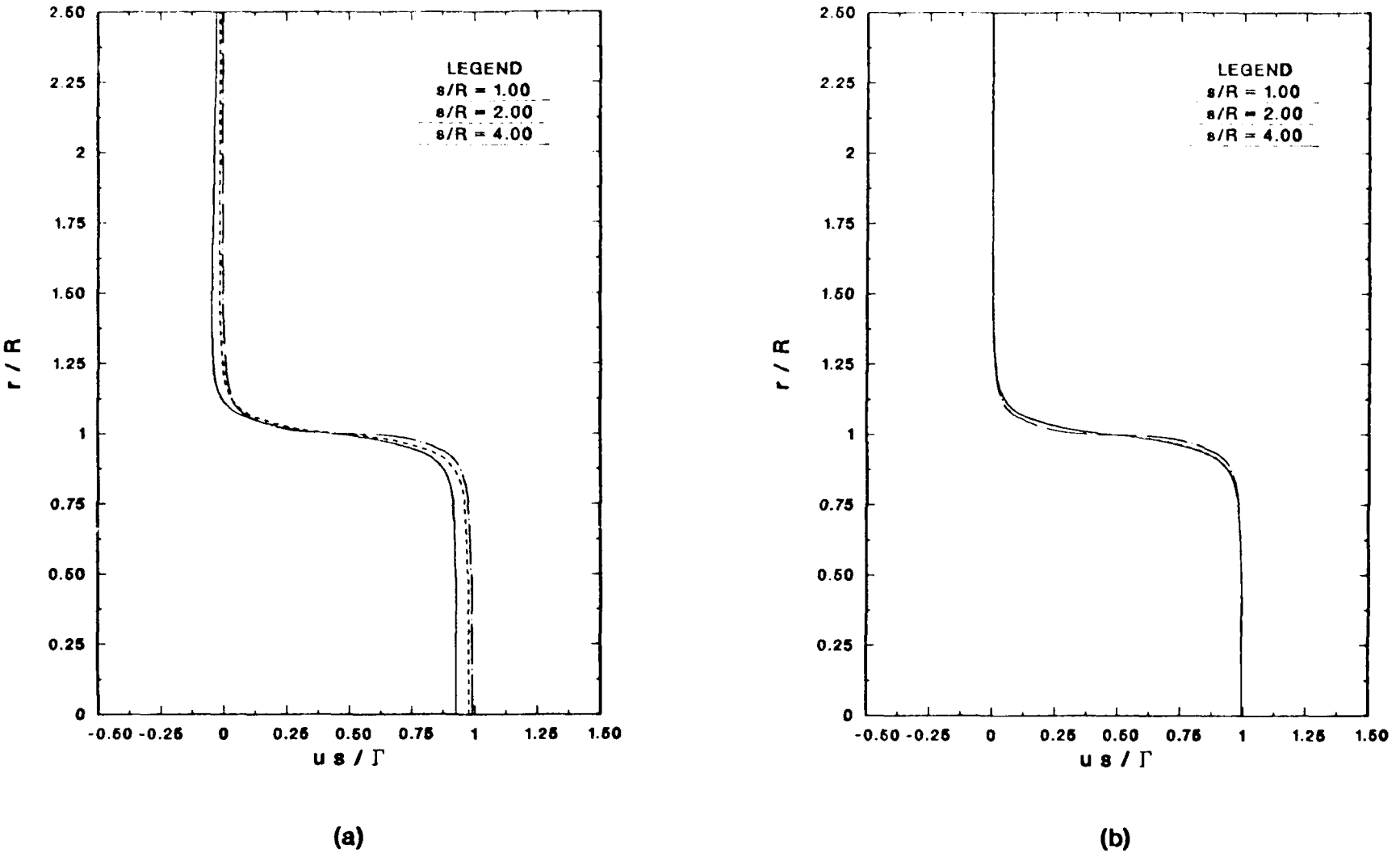

Figure 3.12. Mean streamwise velocity profile of a train of rings for (a) $N_v = 5$ and (b) $N_v = 41$.

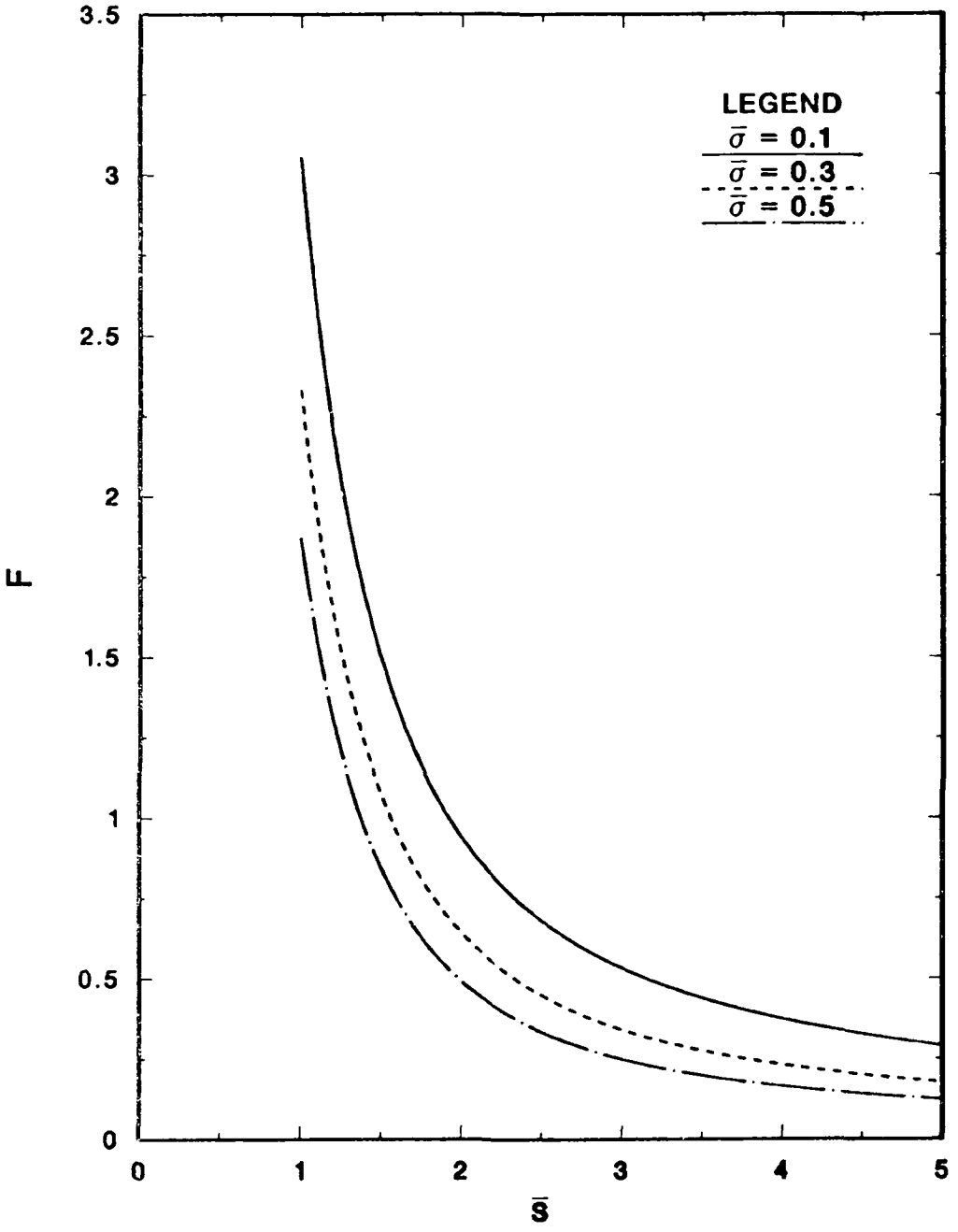

Figure 3.13. Momentum flux of a train of rings ($N_v = 41$).

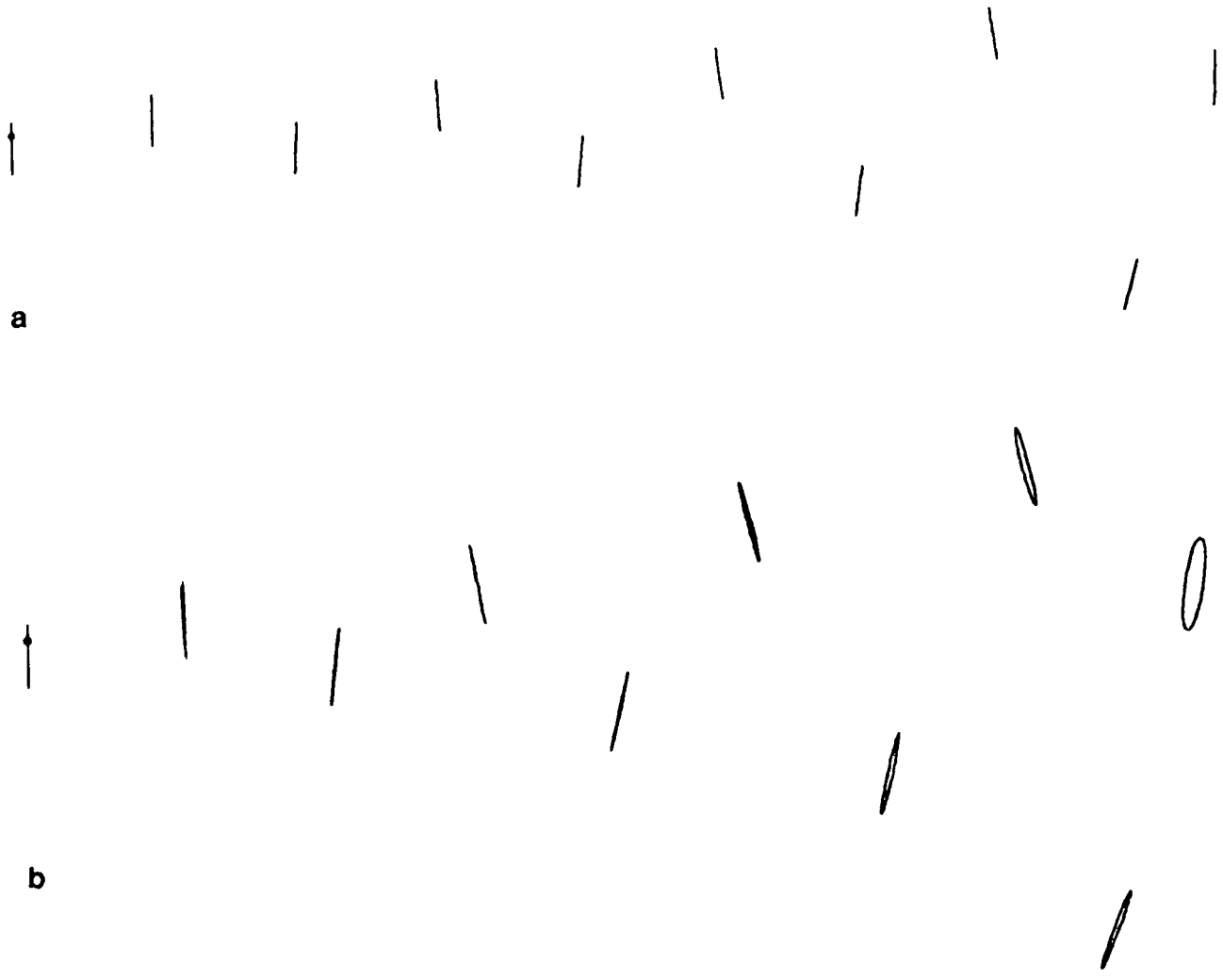

Figure 3.14. Comparison of bifurcating jet simulations at $St_a = 0.3$
(a) without and (b) with source flow.

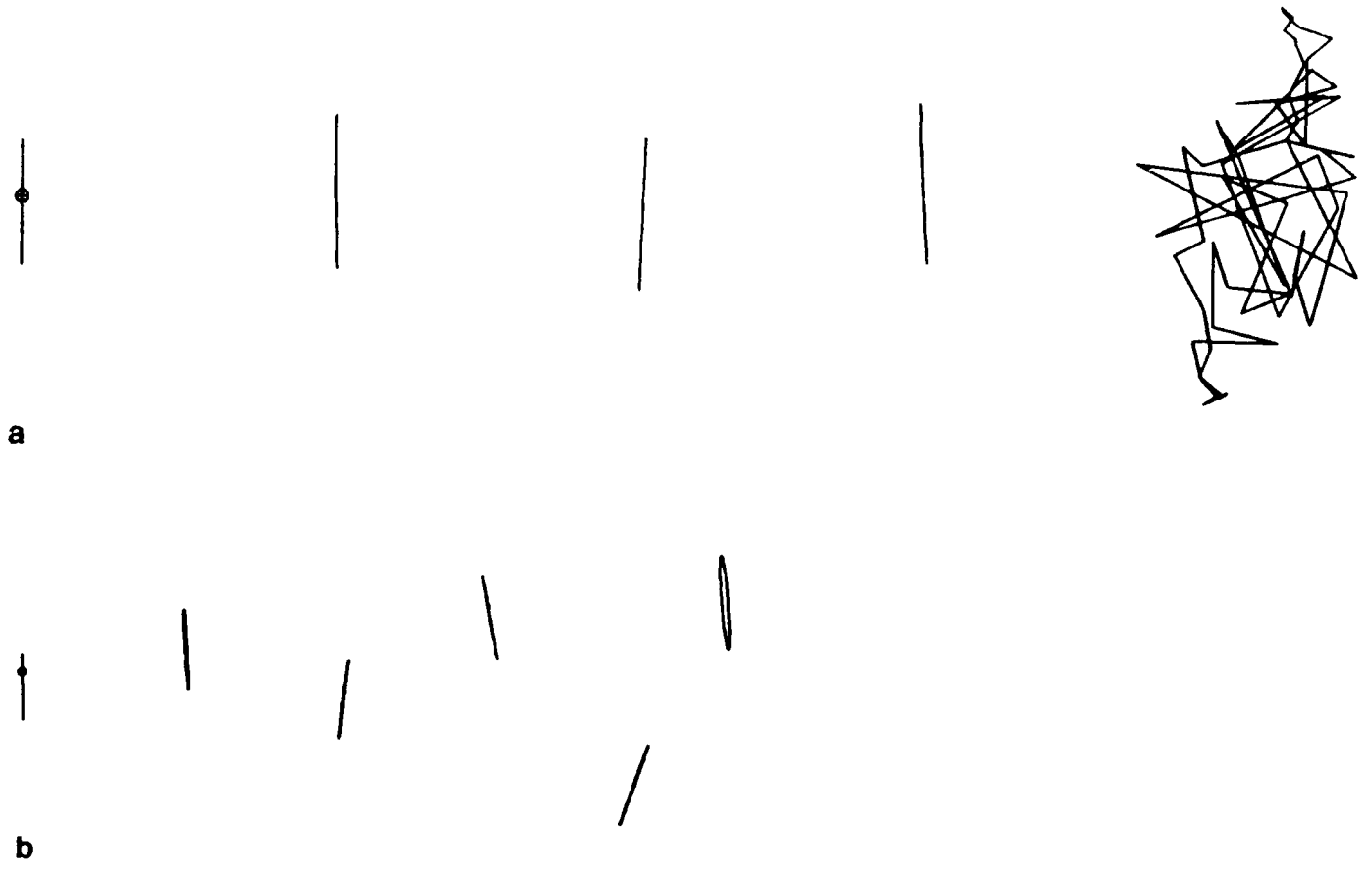

Figure 3.15. Comparison of bifurcating jets at $St_a = 0.30$ and at (a) $A_h = 0.1$ and (b) $A_h = 0.5$.

Figure 3.16. Comparison of bifurcating jets at $St_a = 0.35$ and at (a) $A_h = 0.3$ and (b) $A_h = 0.5$.

Figure 3.17. Evolution of bifurcating jet at $St_a = 0.30$ and $A_h = 0.5$.

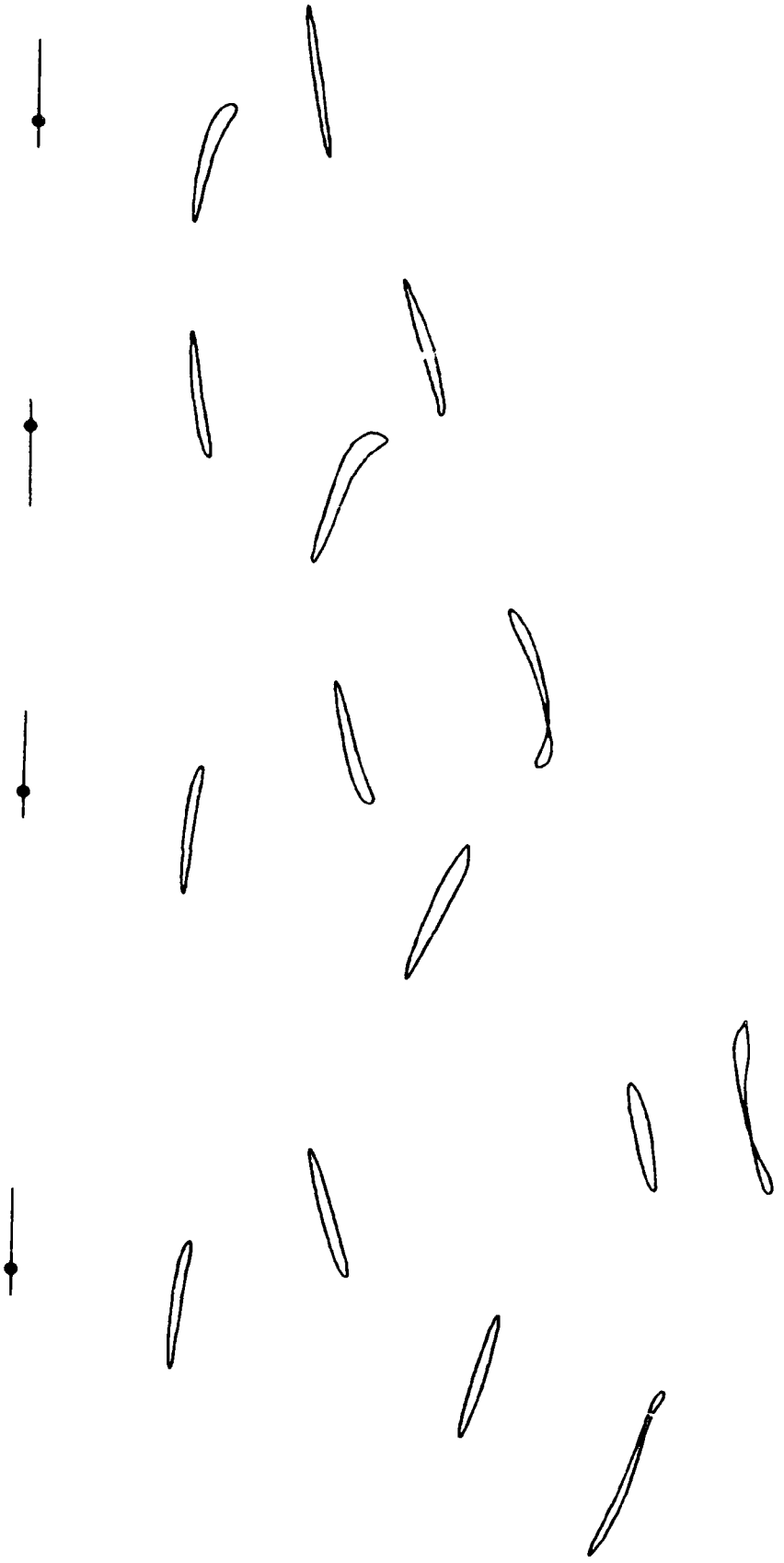

Figure 3.18. Evolution of bifurcating jet at $St_a = 0.40$ and $A_h = 0.5$.

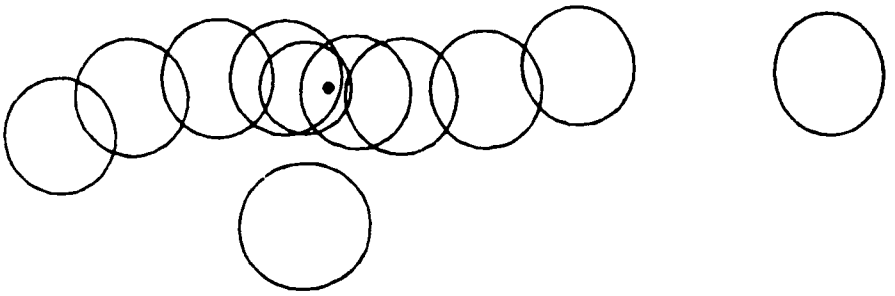

a

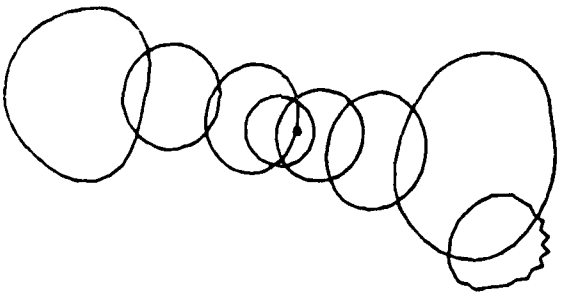

b

Figure 3.19. End views of bifurcating jets at $A_h = 0.5$ and at (a) $St_a = 0.30$ and (b) $St_a = 0.40$.

Figure 3.20. Bifurcating jet at $St_a = 0.42$ and $A_h = 0.5$ and at two different times.

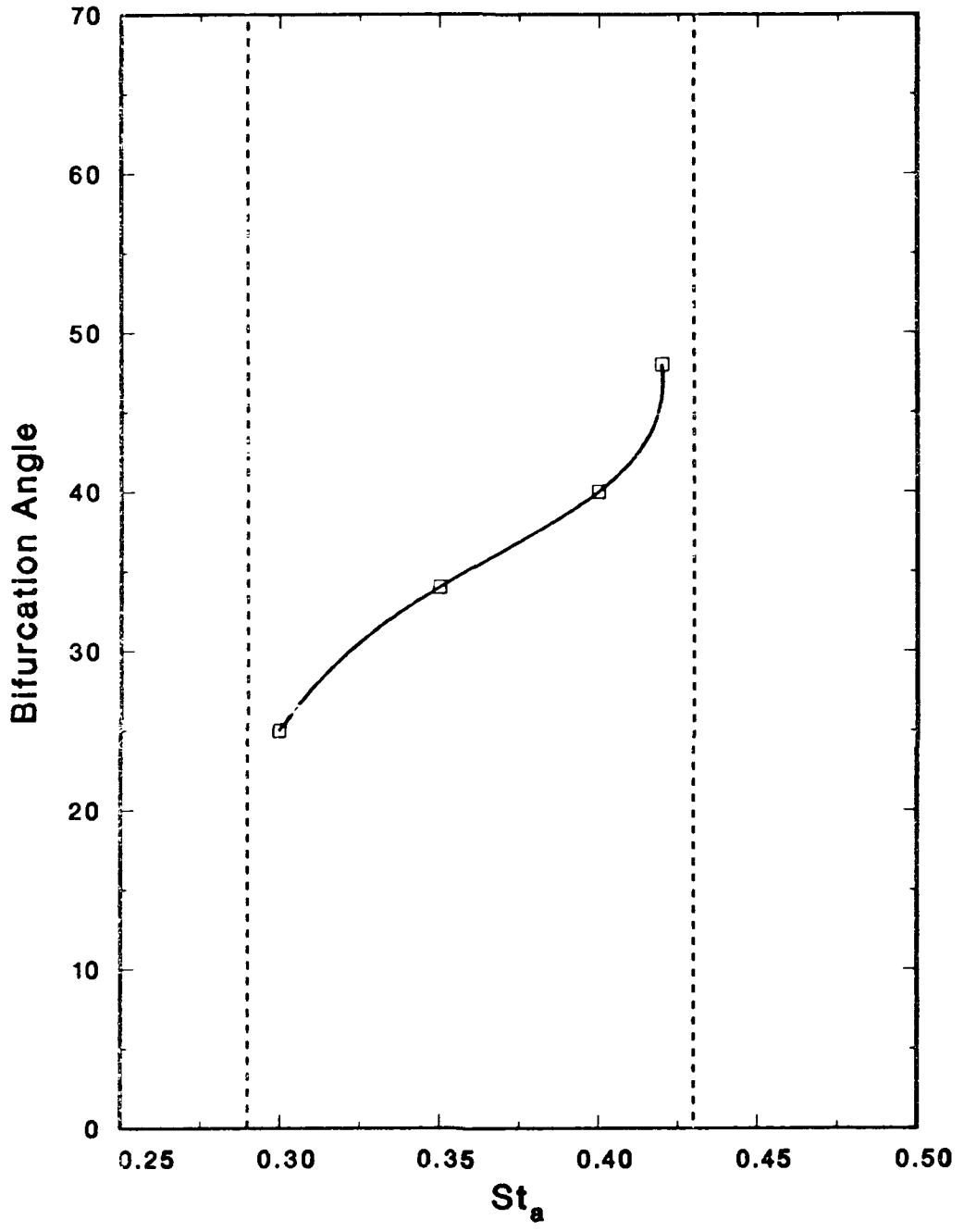

Figure 3.21. Dependence of bifurcation angle on St_a ($A_h = 0.5$).

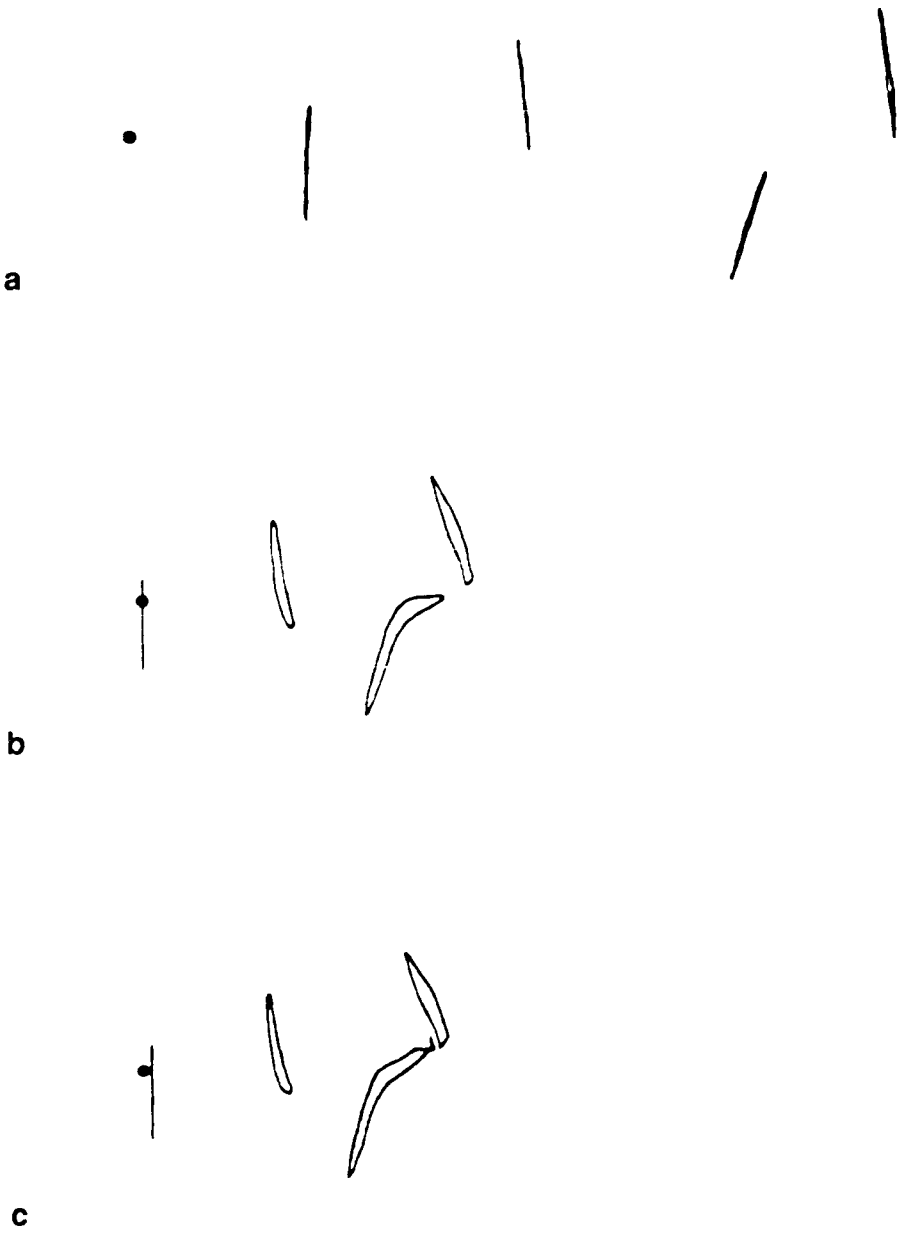

Figure 3.22. Onset of bifurcation at (a) $St_a = 0.30$, (b) $St_a = 0.42$, and (c) $St_a = 0.43$.

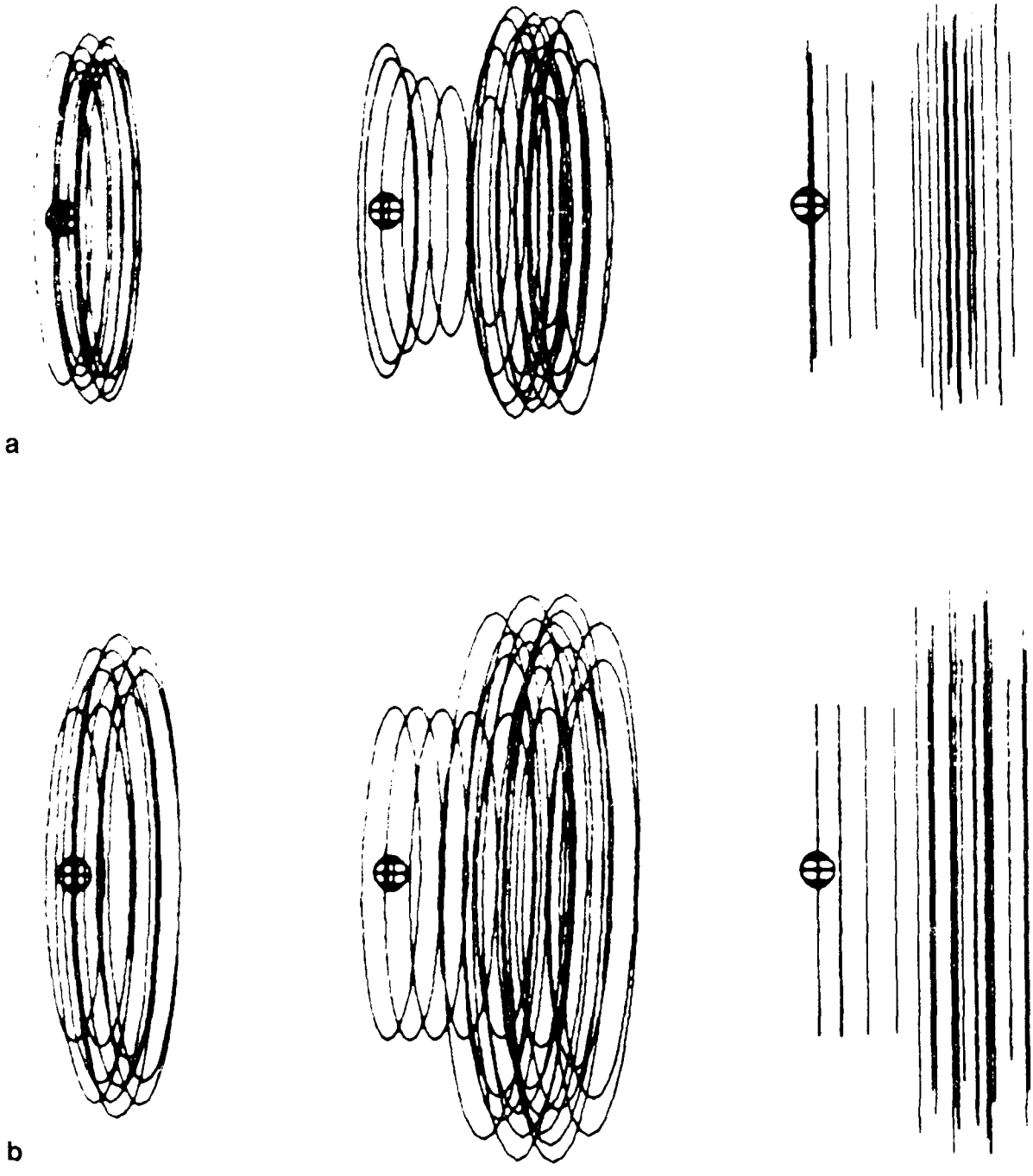

Figure 3.23. Initial ring formation in the (a) absence and (b) presence of source flow.

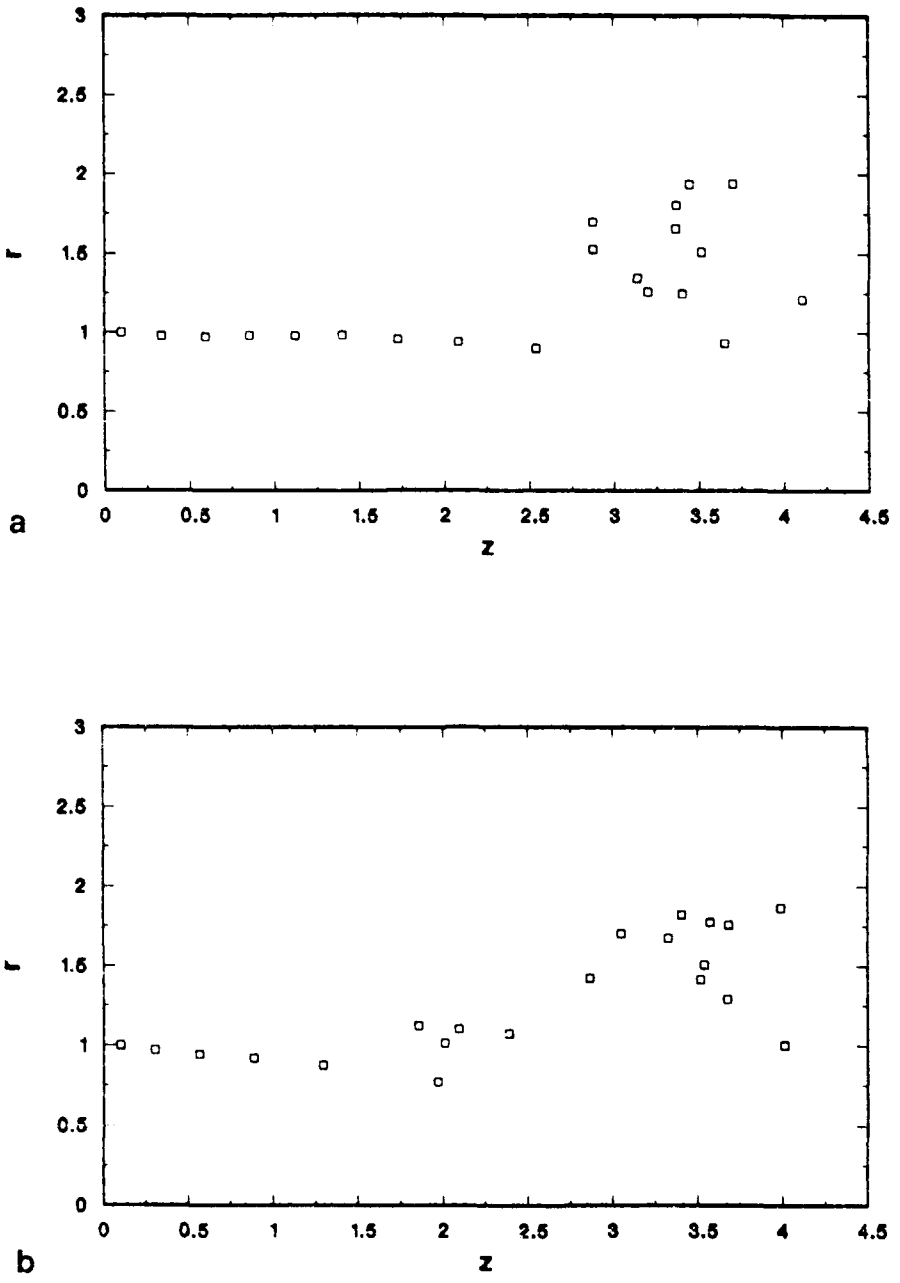

Figure 3.24. Comparison of (a) unforced and (b) forced ($A_a = 0.2$) axisymmetric shear layers.

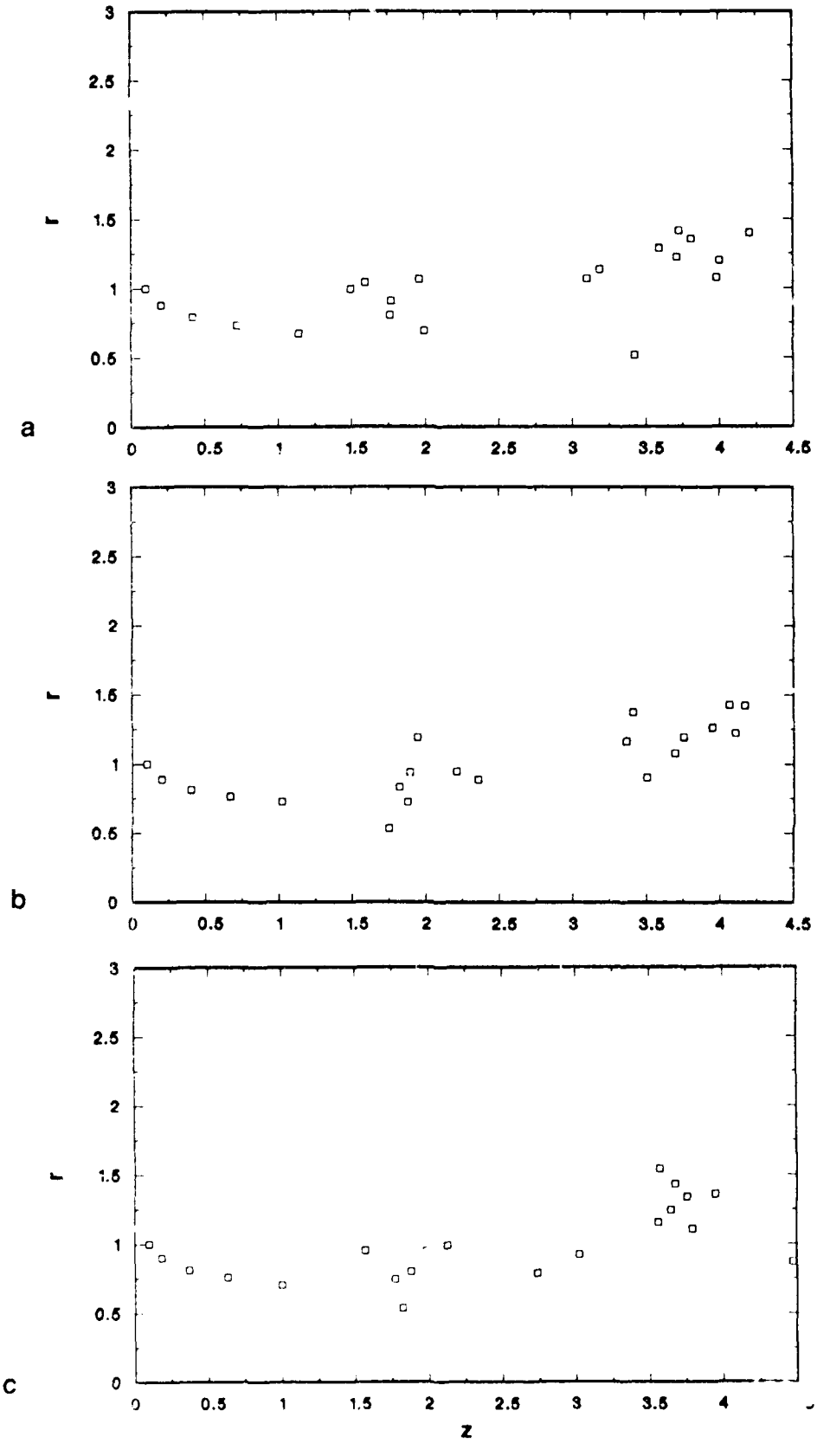

Figure 3.25. Forced axisymmetric shear layers corresponding to different matching schemes at $St_a = 0.4$ and $A_a = 0.2$: (a) quadrature, (b) integral, and (c) growth.

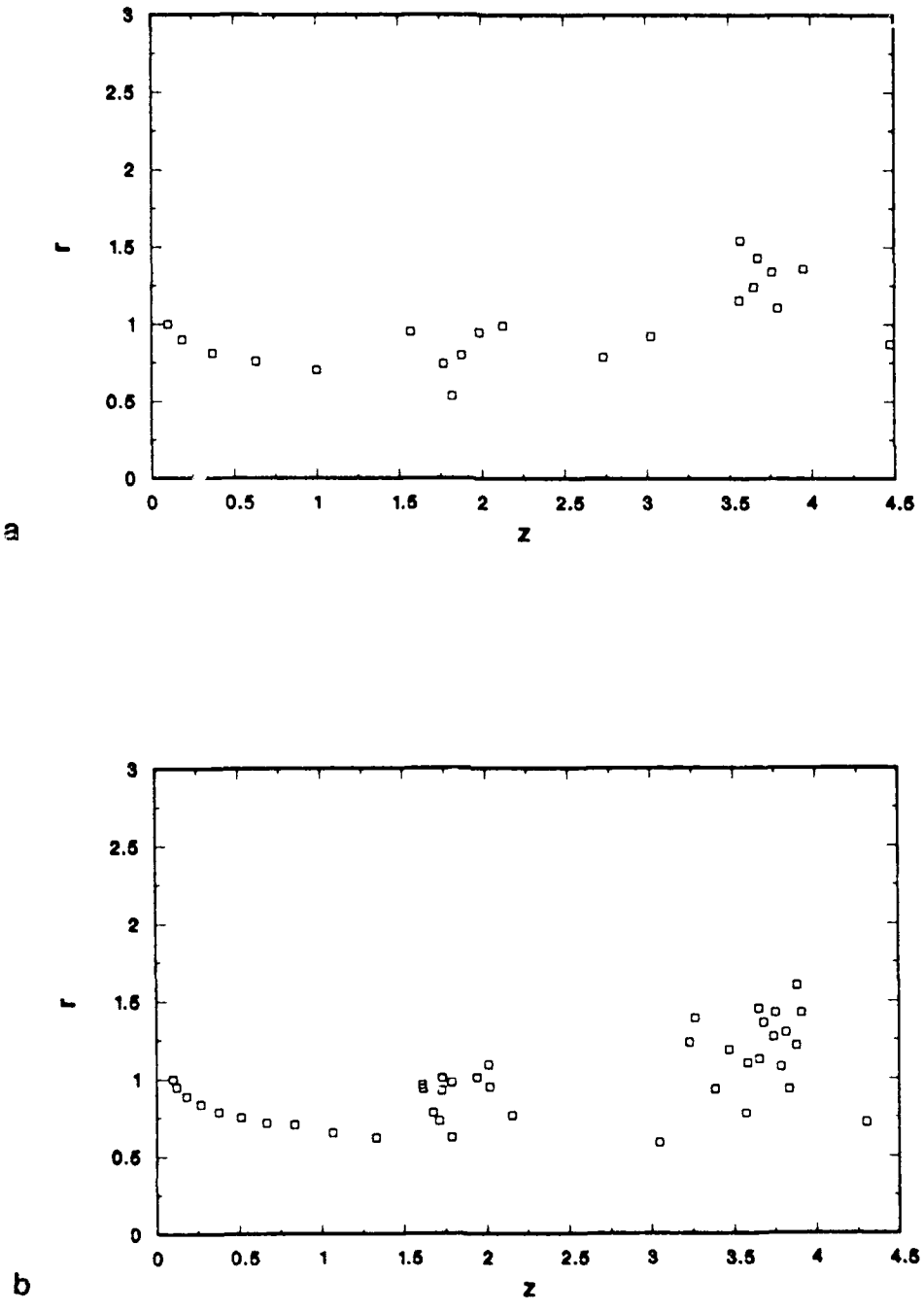

Figure 3.26. Axisymmetric shear layer simulations using (a) 10 and (b) 20 filaments per excitation period (growth matching).

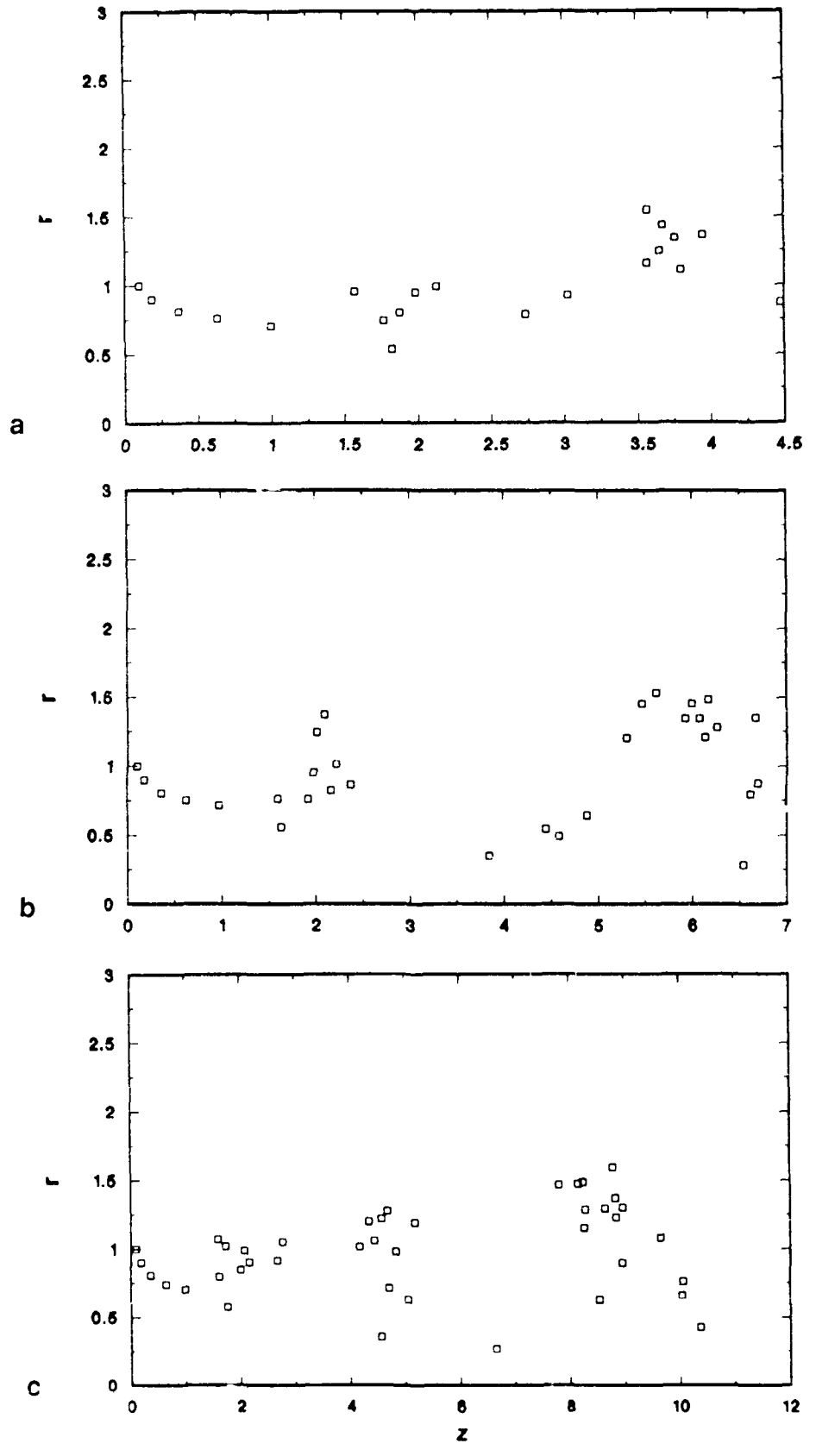

Figure 3.27. Evolution of forced axisymmetric shear layer at $St_a = 0.4$ and $A_a = 0.2$.

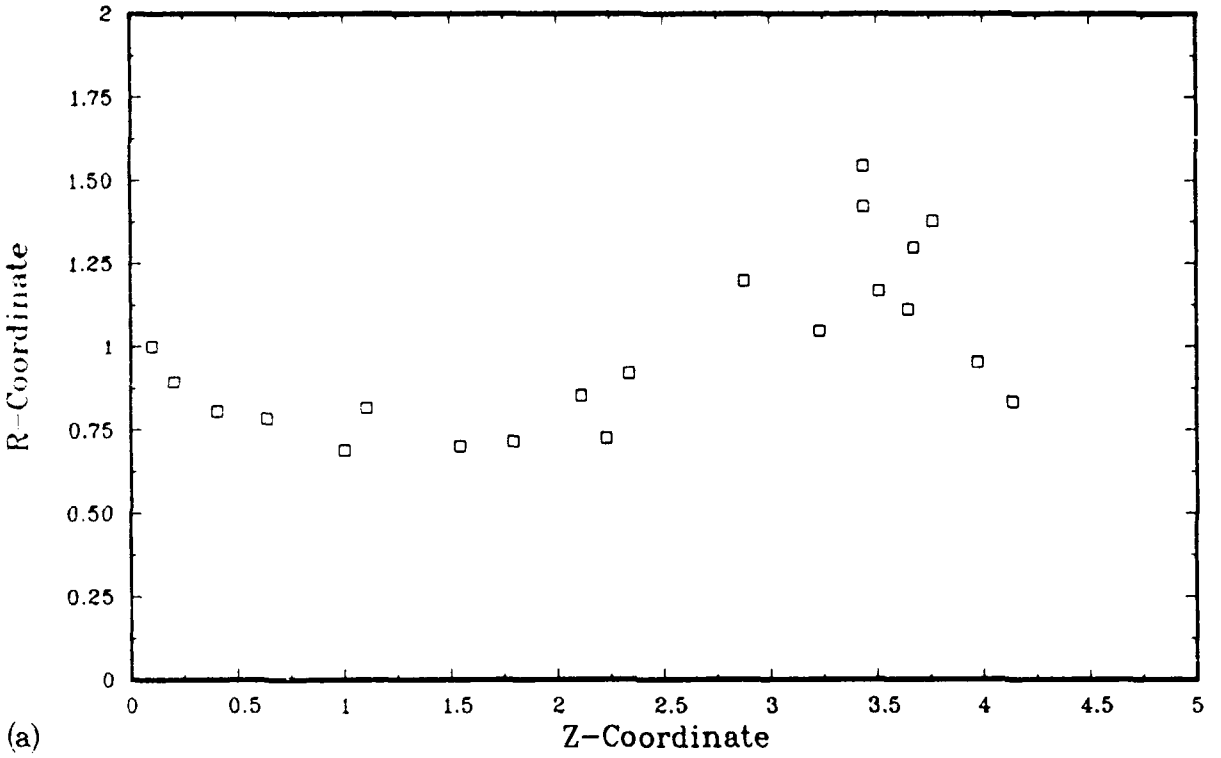

(a)

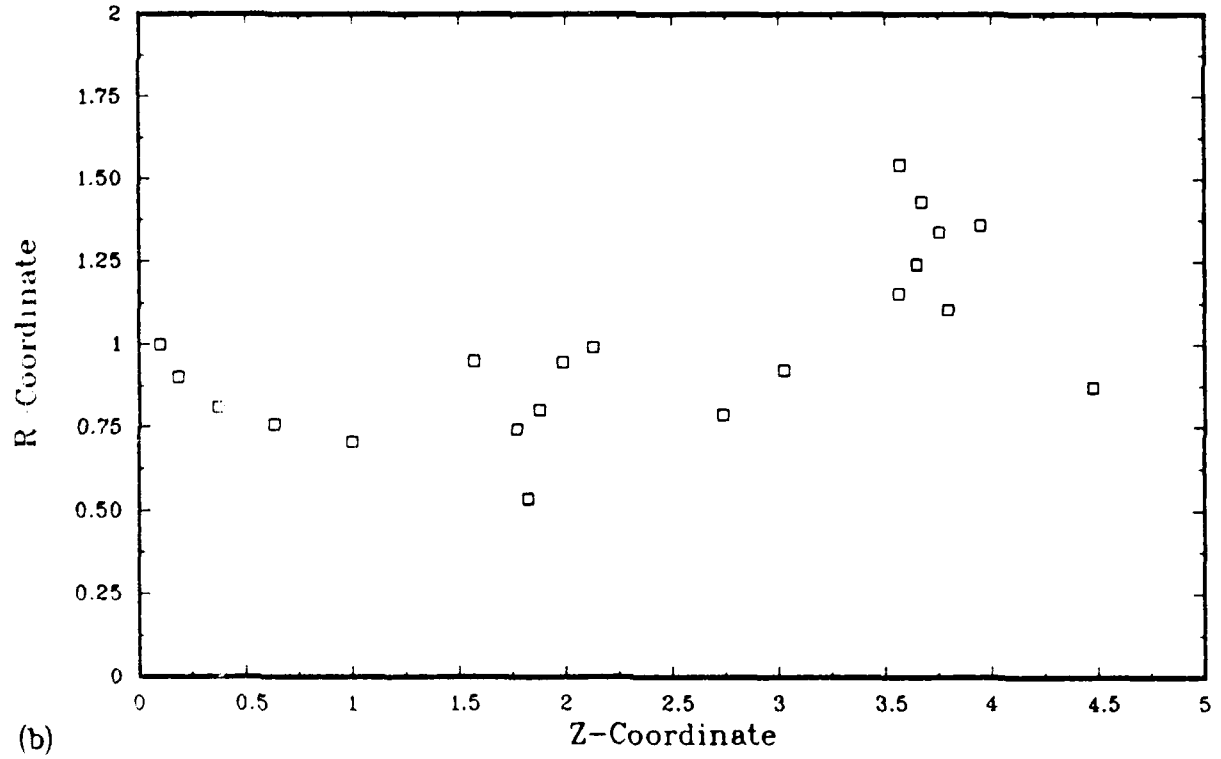

(b)

Figure 3.28. Effect of forcing level ((a) $A_a = 0.5$ and (b) $A_a = 0.20$) on axisymmetric shear layer development at $St_a = 0.4$.

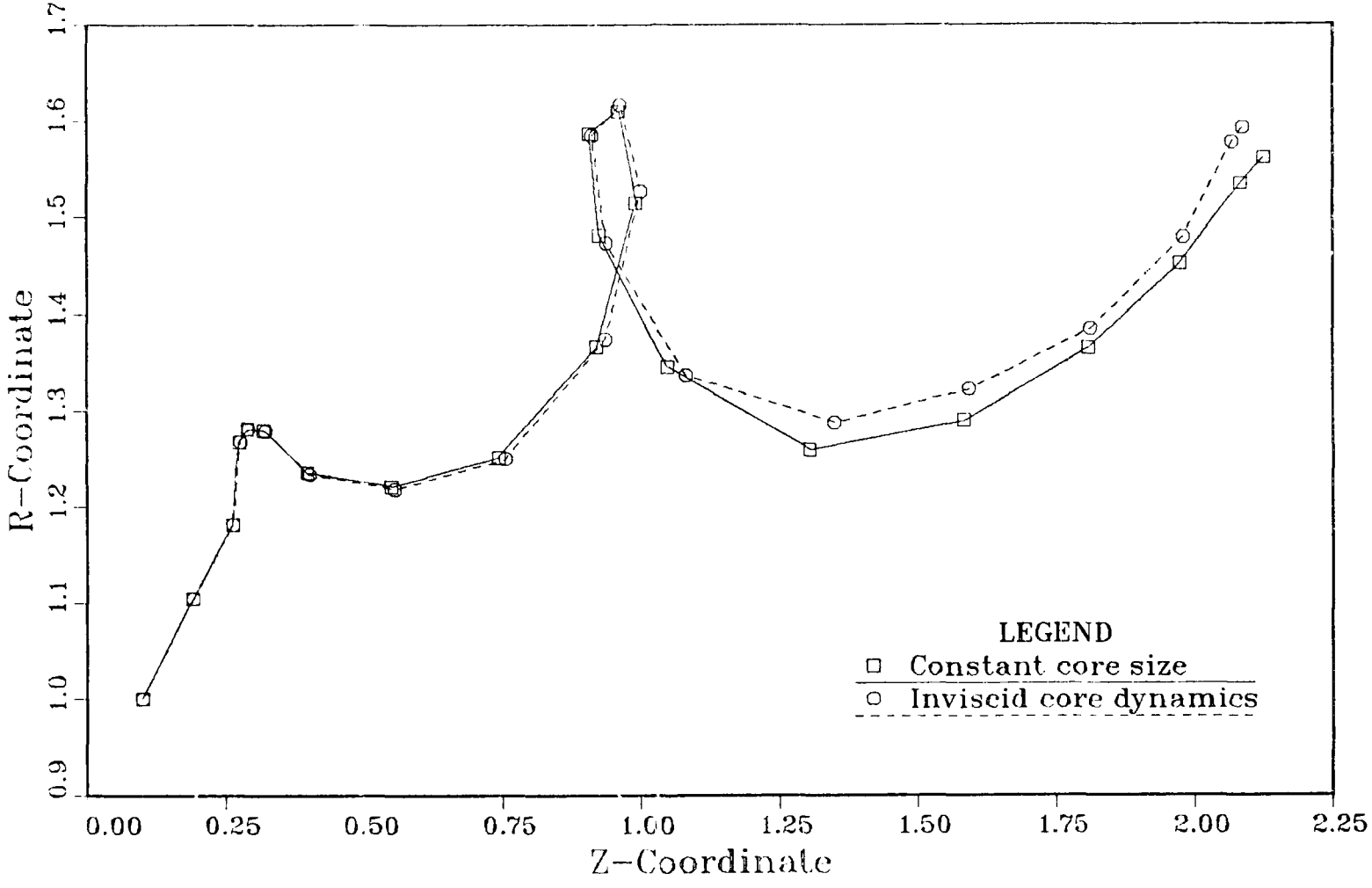

Figure 3.29. Effect of temporal variations of core radius.

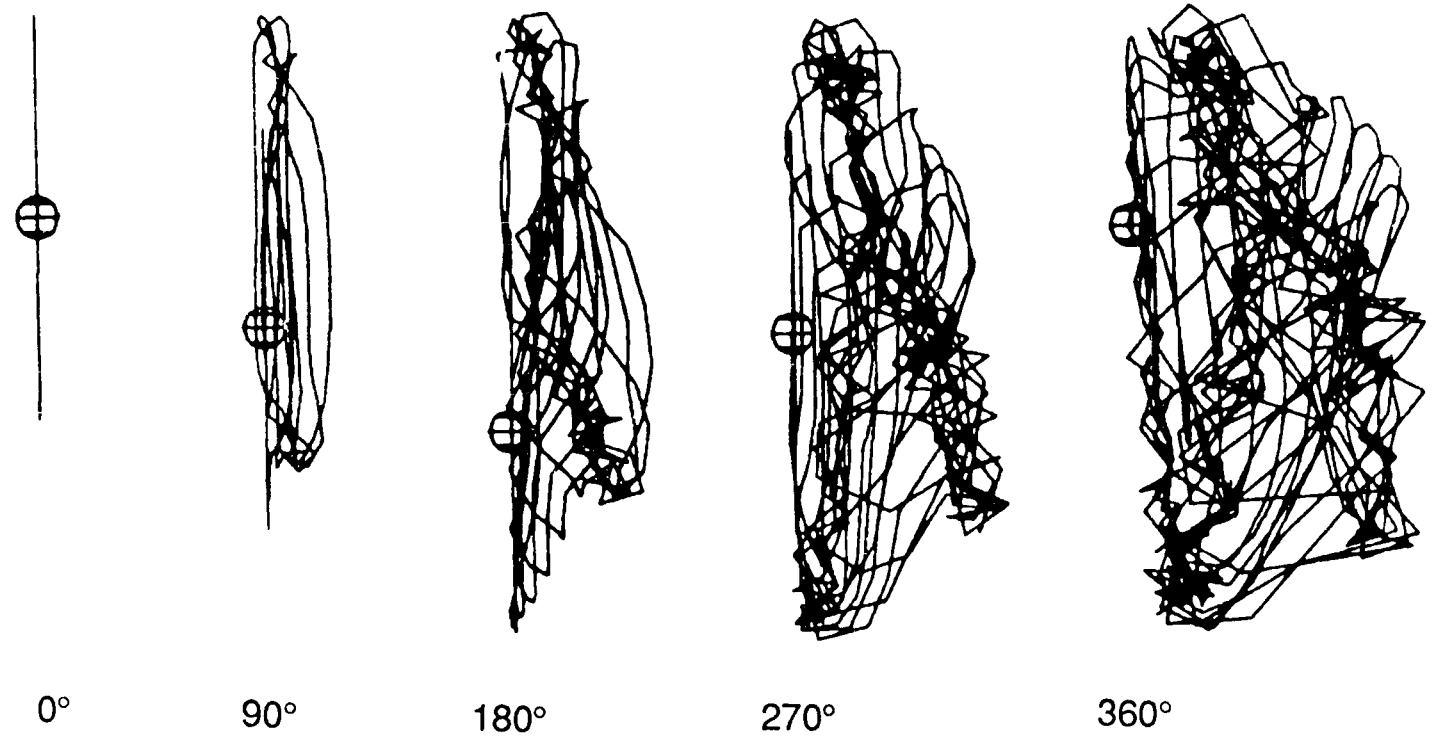

Figure 3.30. Side view of initial development of helically- excited jet ($A_h = 0.5$).

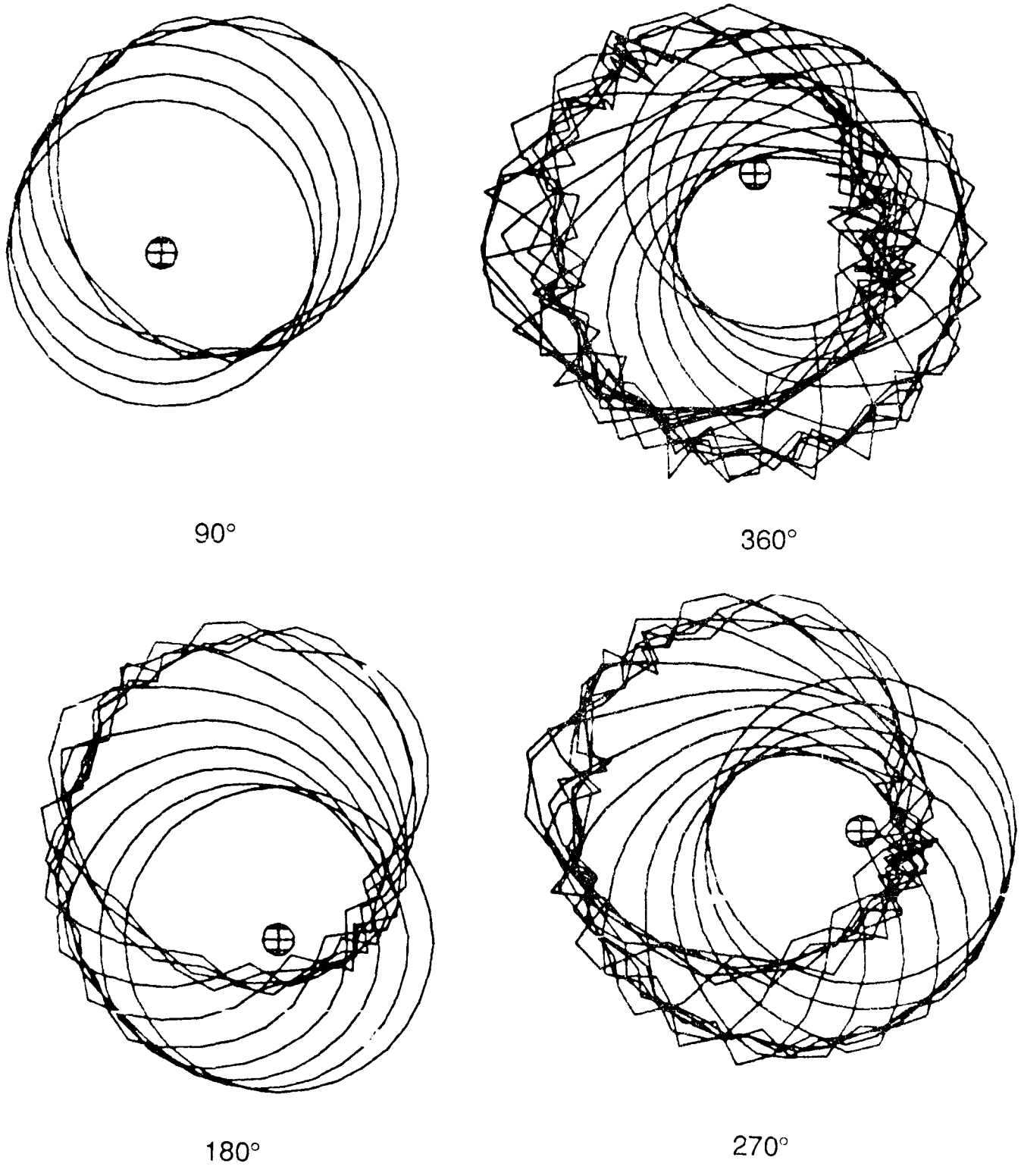

Figure 3.31. End view of initial development of helically- excited jet (A_{θ} = 0.5).

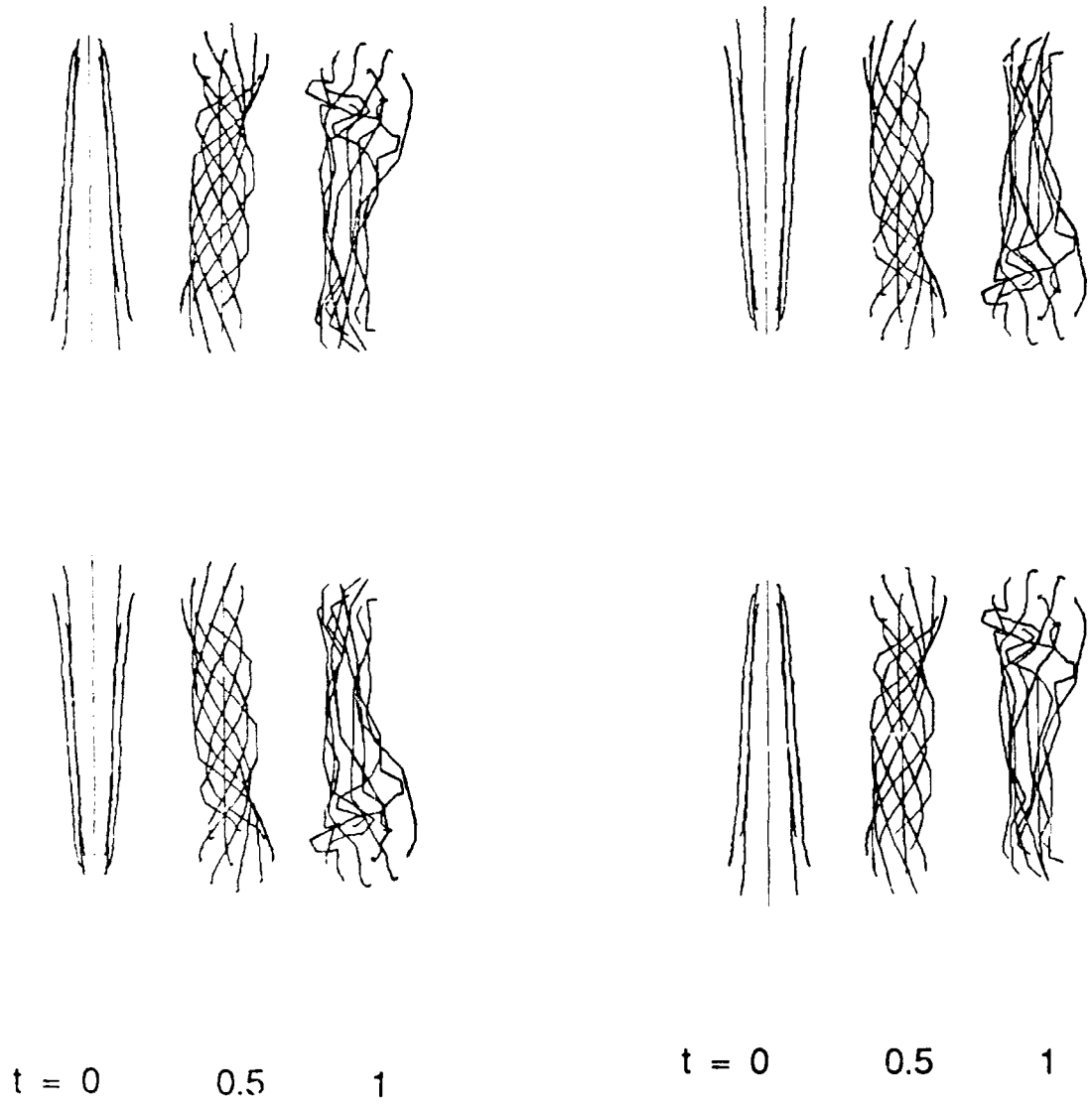

Figure 3.32. Interaction of a pair of side-by-side, multi- filament rings.

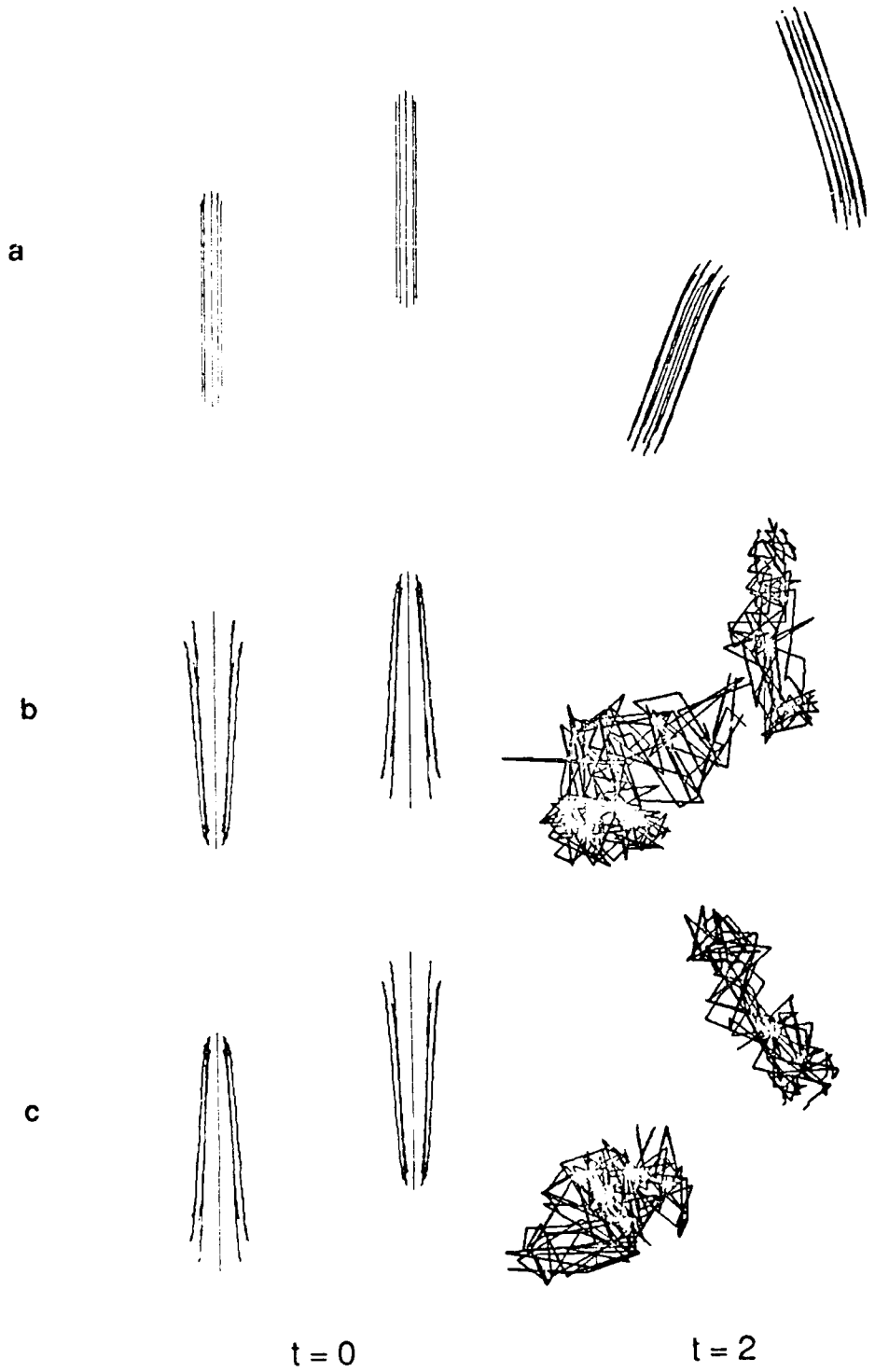

Figure 3.33. Interaction of a pair of eccentric, multi- filament rings.

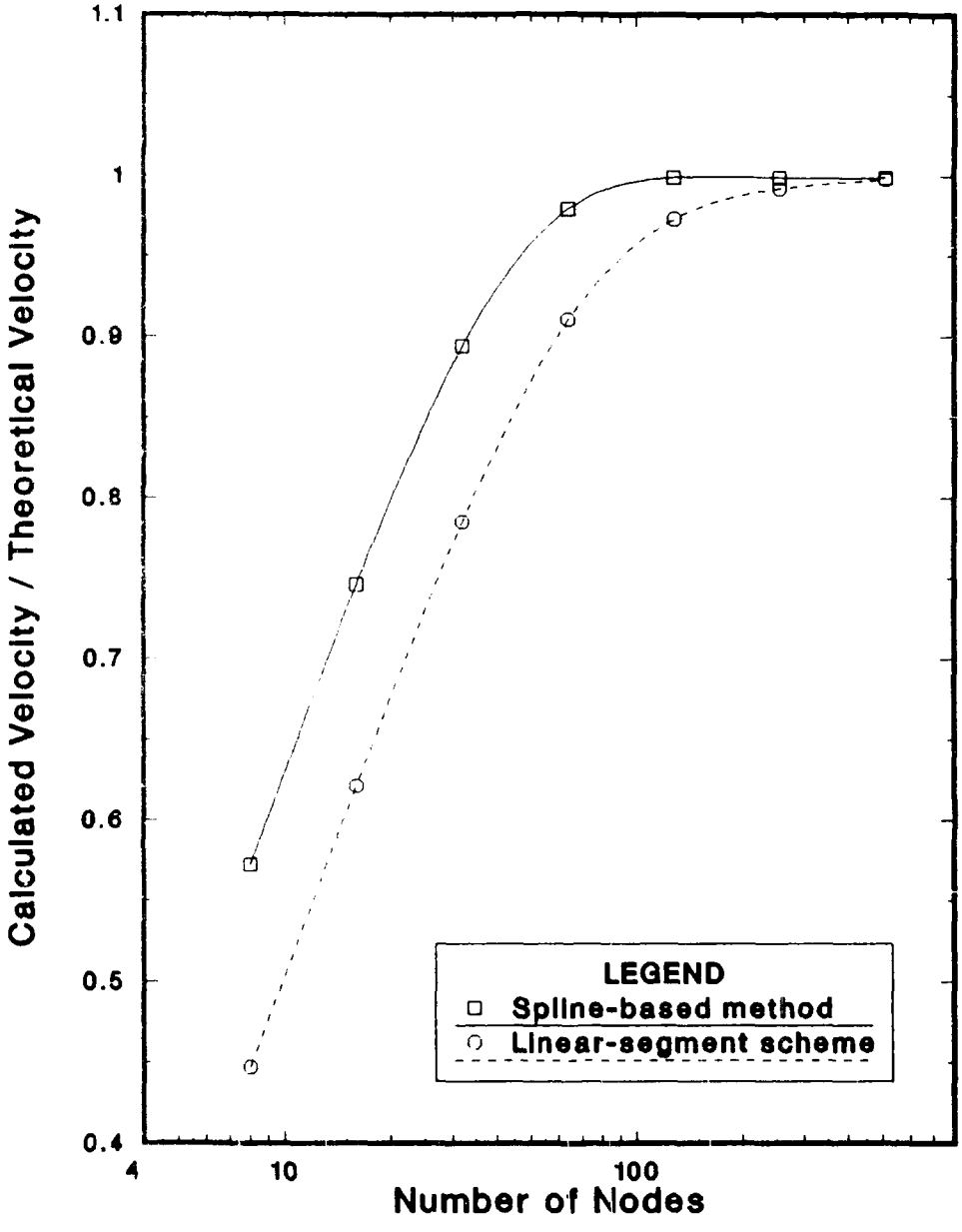

Figure 3 34. Calculation of self-induced velocity by linear-segment and cubic-spline methods.

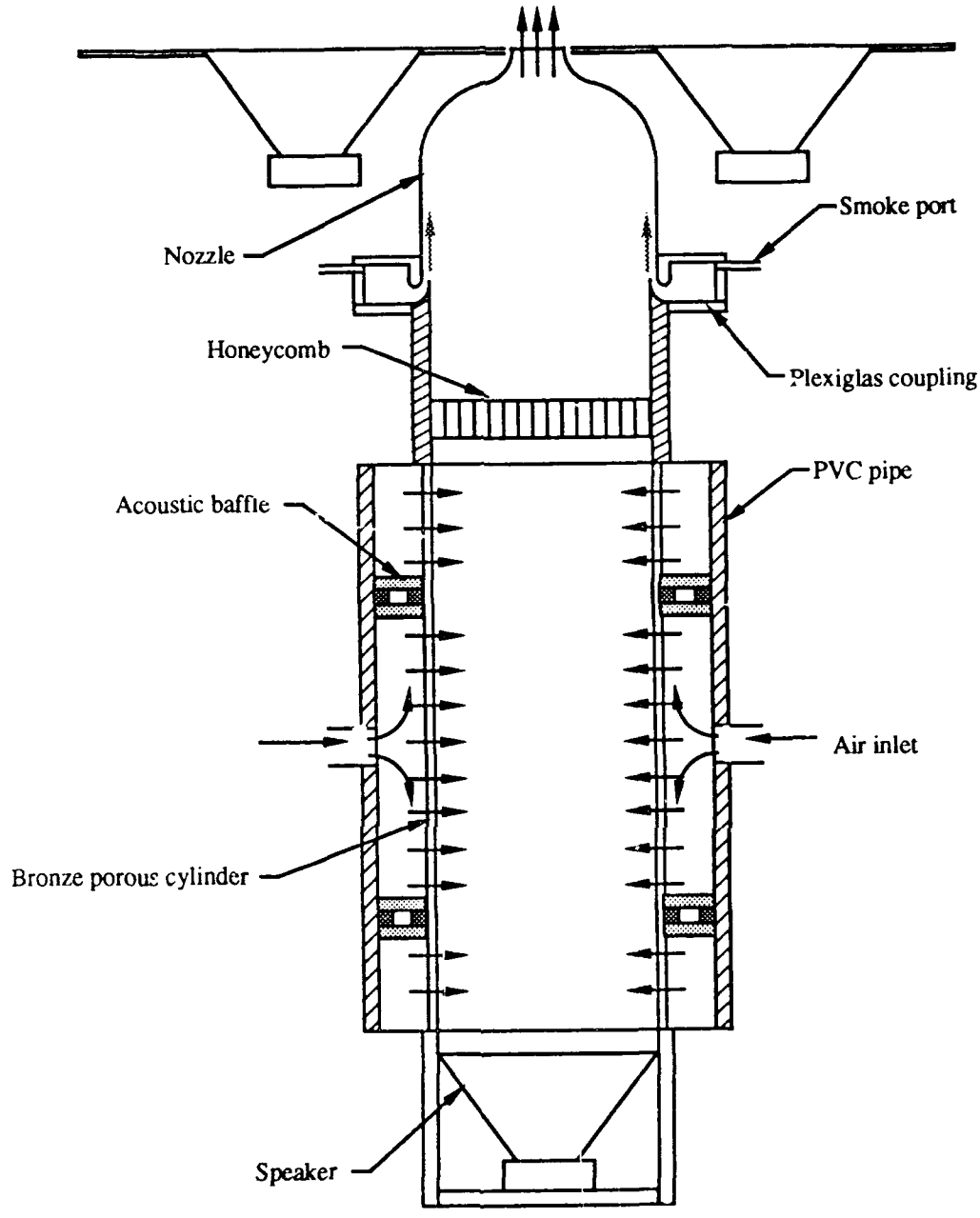

Figure 4.1. Schematic of low-speed apparatus.

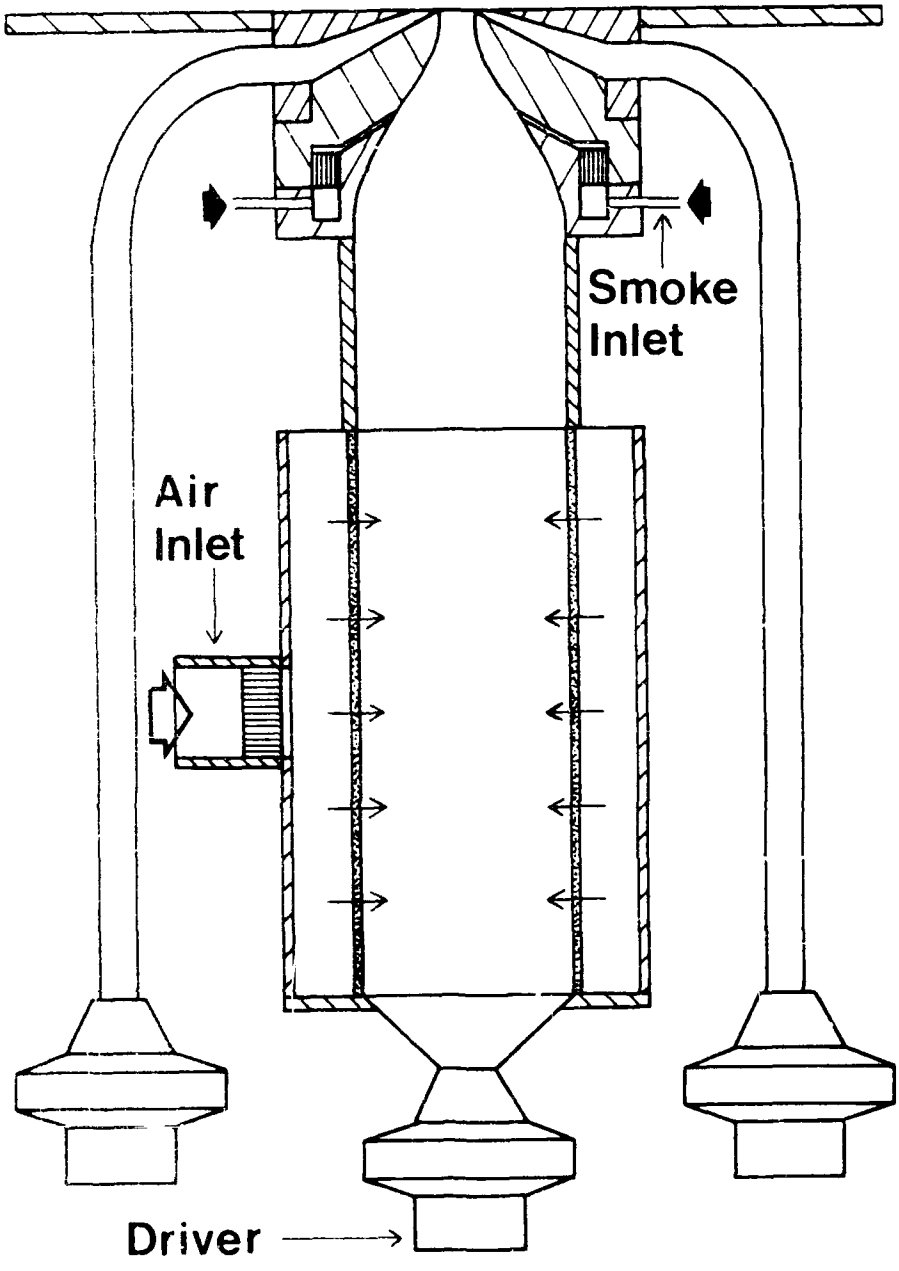

Figure 4.2. Schematic of high-speed apparatus.

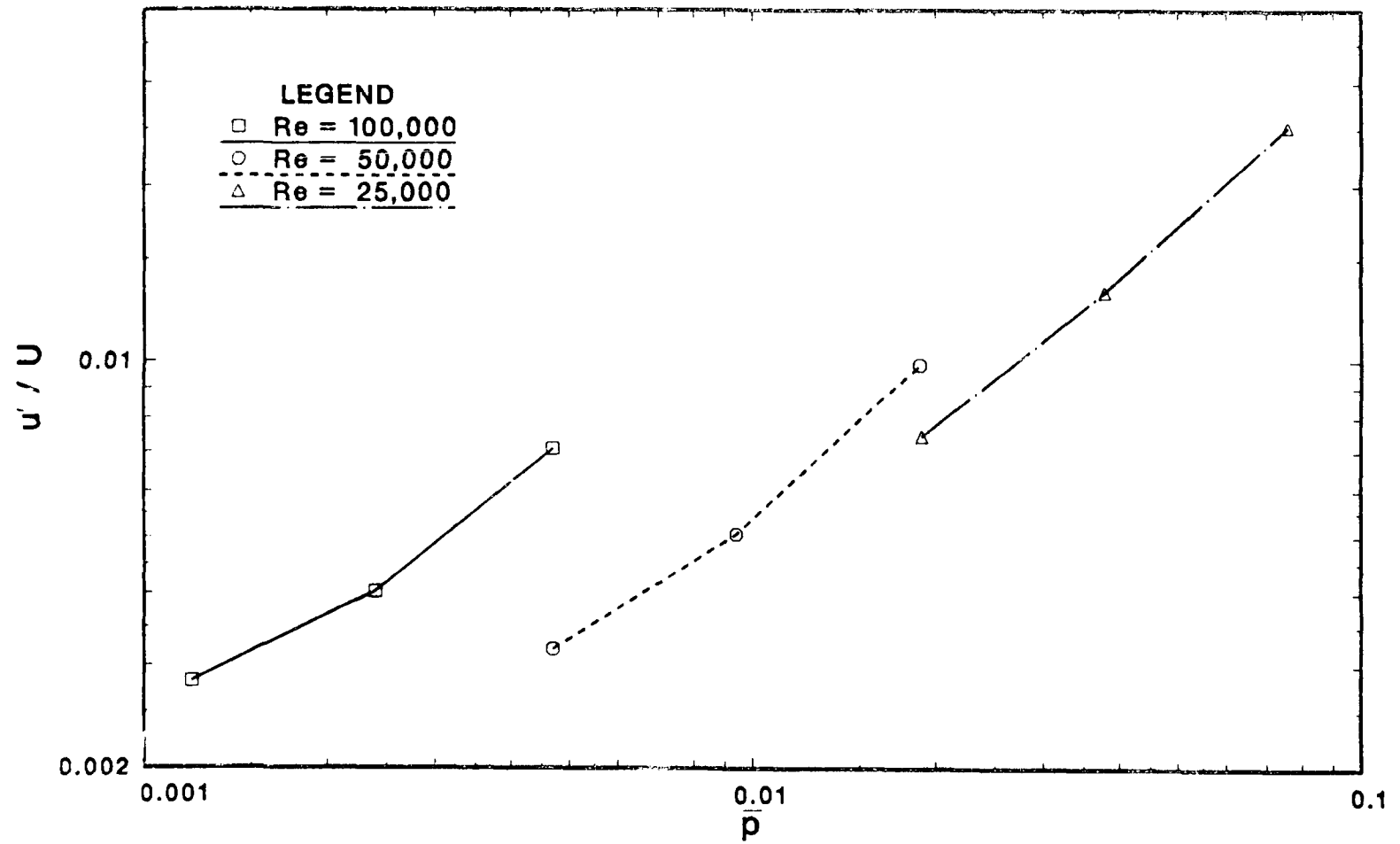

Figure 4.3. Streamwise velocity fluctuations (at $z/D = 0.05$ and $r/D = 0.0$) corresponding to different excitation levels produced by internal driver at 2060 Hz.

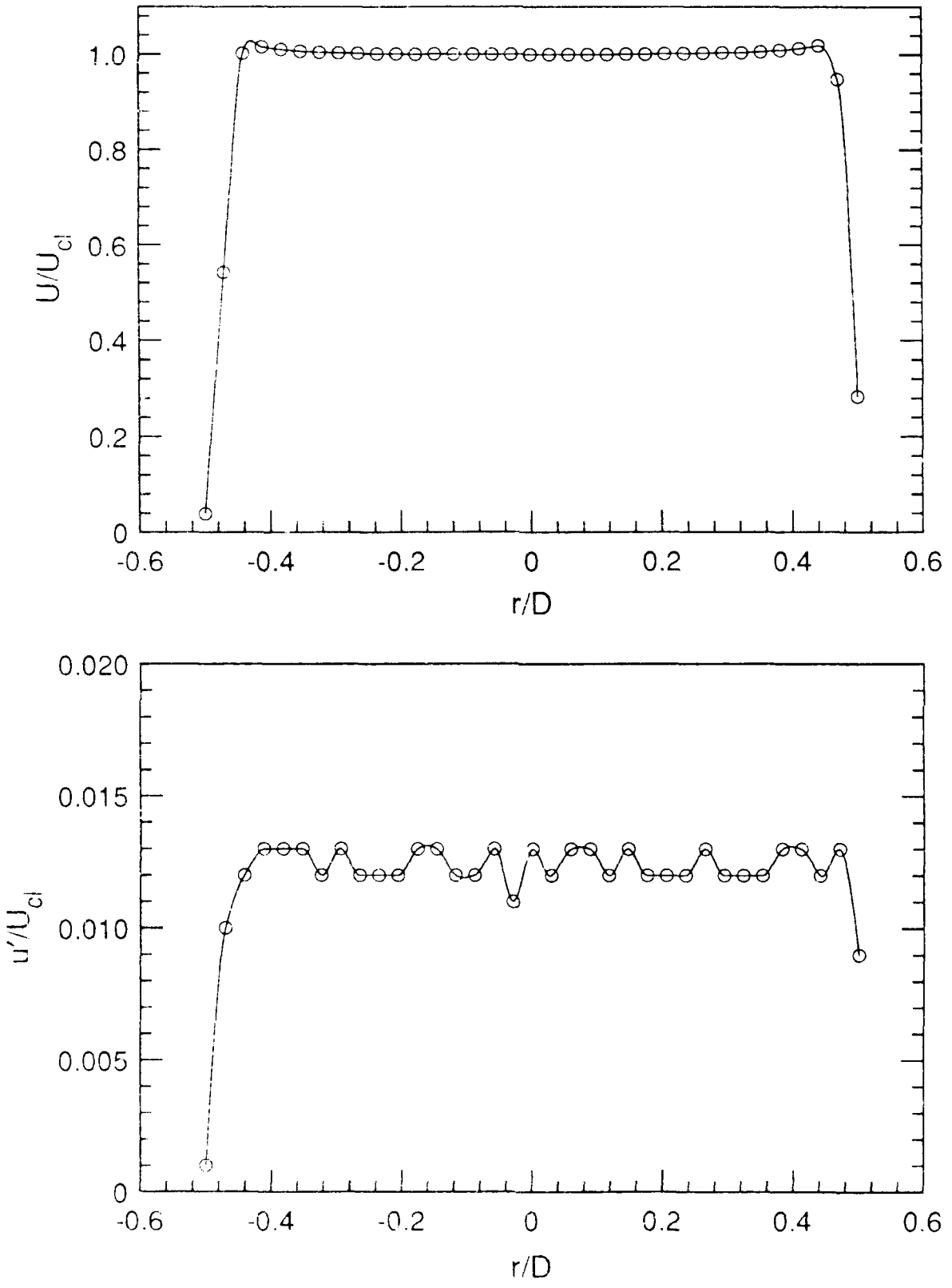

Figure 5.1. Mean and fluctuating velocity profiles at $Re = 10,000$ and $z/D = 0.1$.

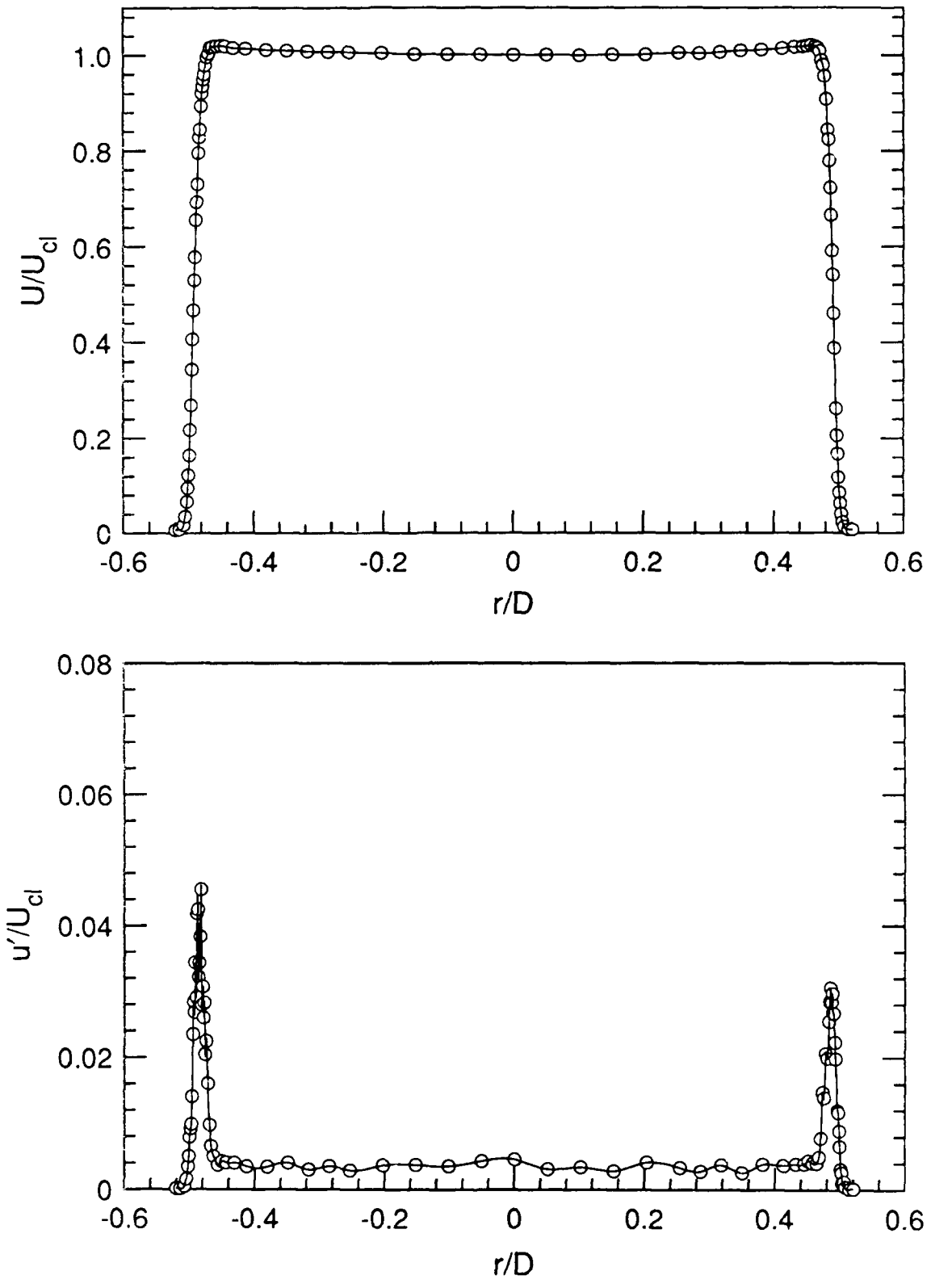

Figure 5.2. Mean and fluctuating velocity profiles at $Re = 25,000$ and $z/D = 0.05$.

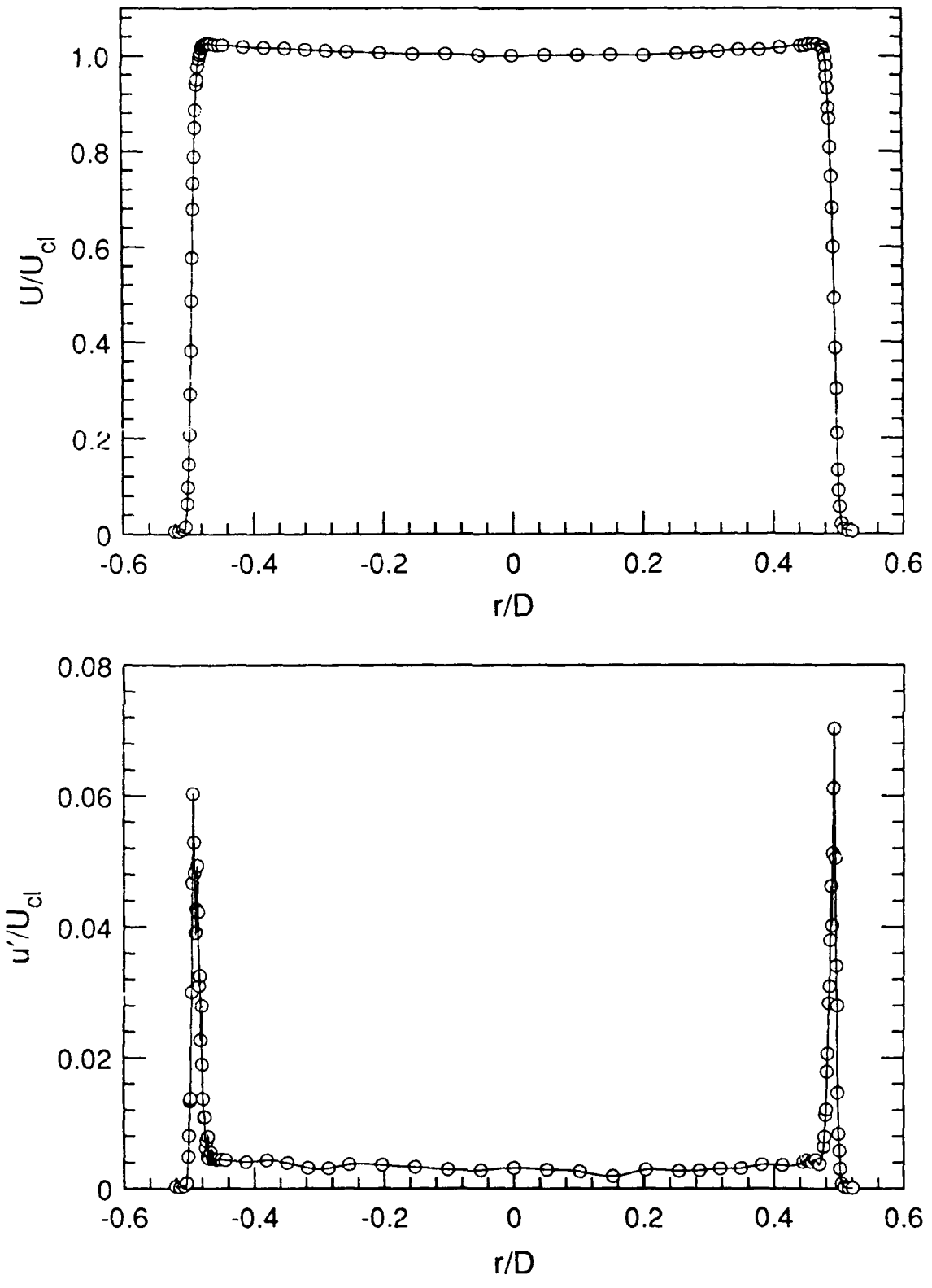

Figure 5.3. Mean and fluctuating velocity profiles at $Re = 50,000$ and $z/D = 0.05$.

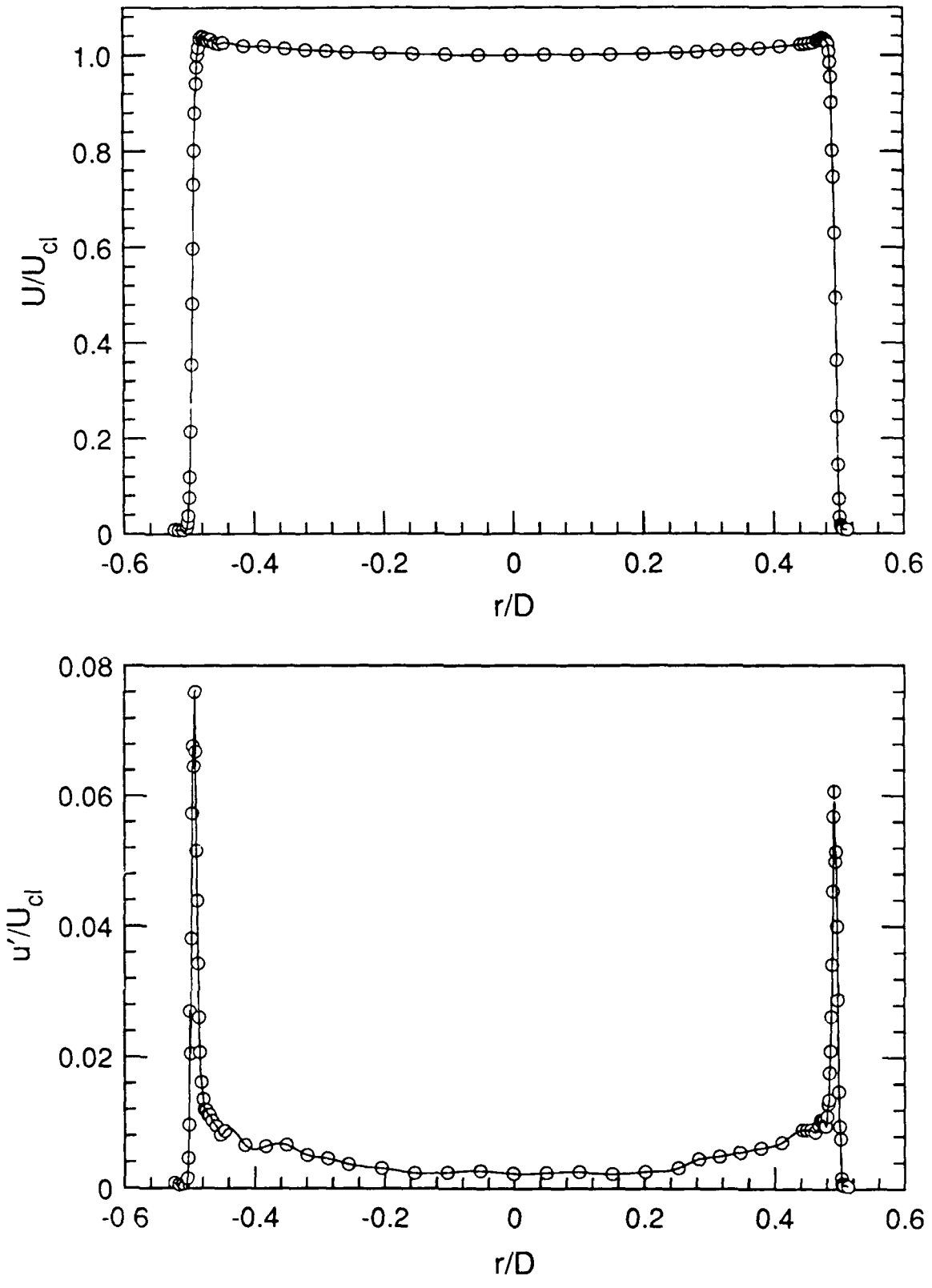

Figure 5.4. Mean and fluctuating velocity profiles at $Re = 100,000$ and $z/D = 0.05$.

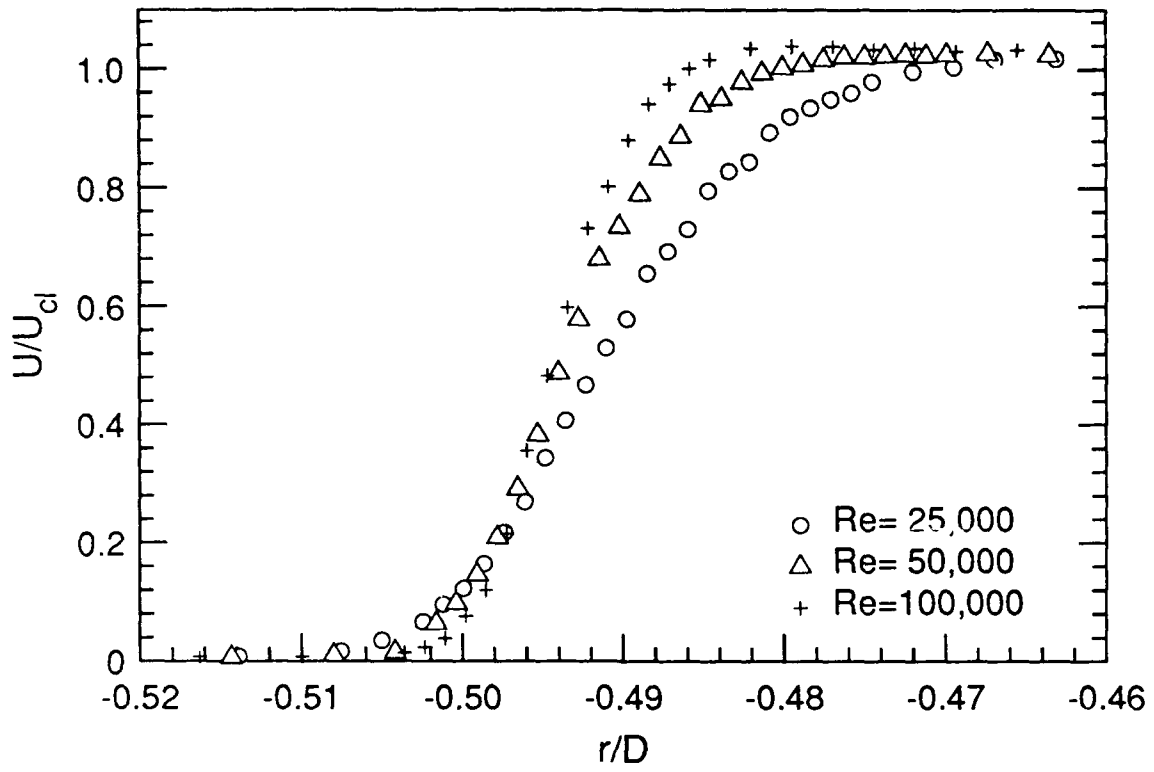

Figure 5.5. Axisymmetric shear layer profiles at various Reynolds numbers.

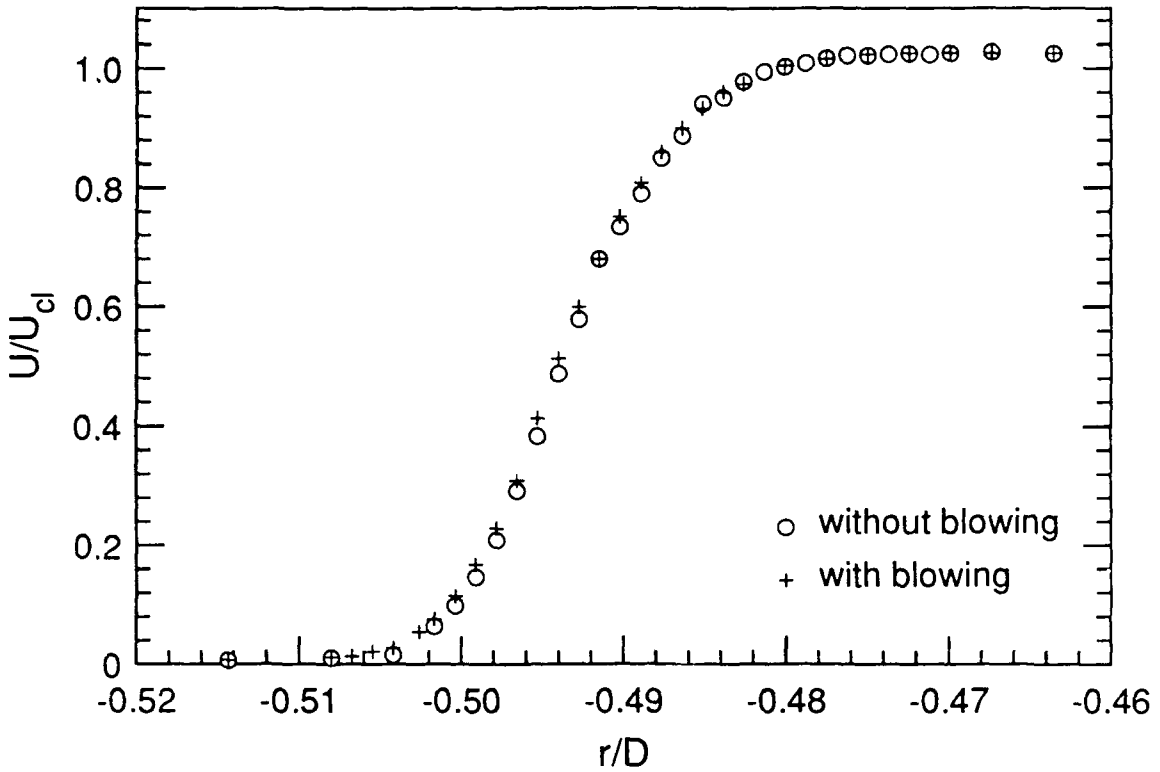

Figure 5.6. Comparison of shear layer profiles with and without blowing ($Re = 50,000$).

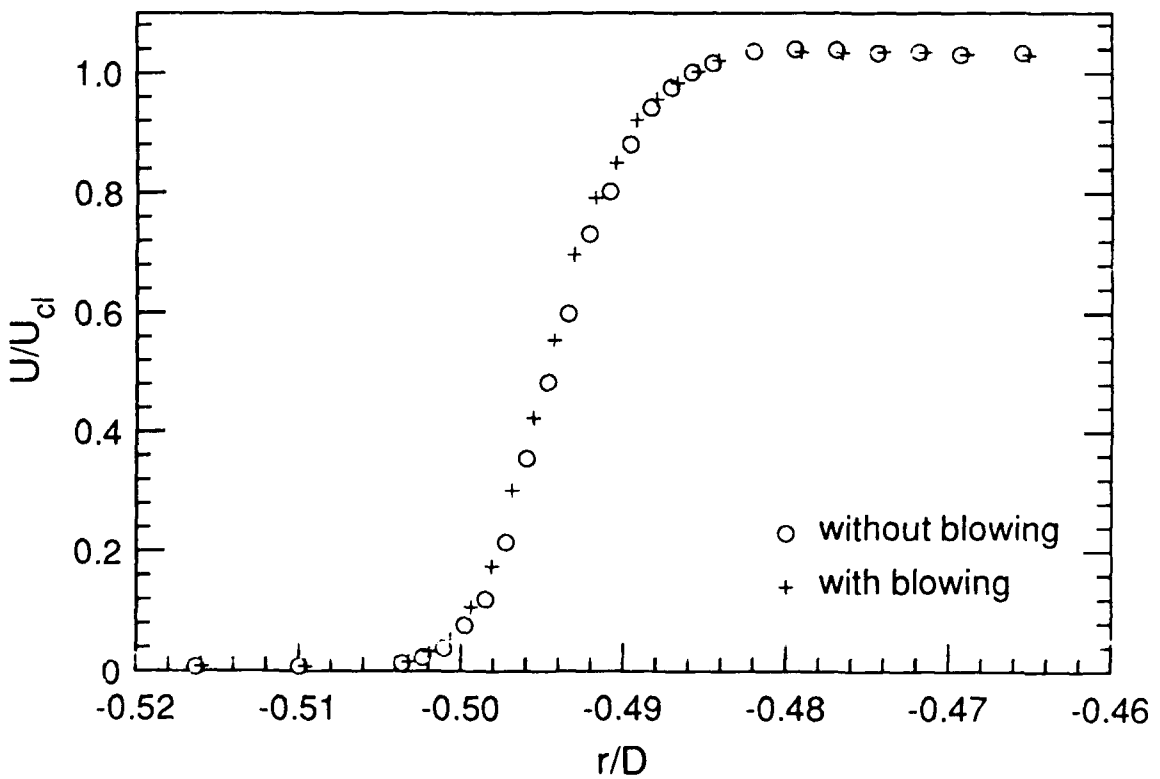

Figure 5.7. Comparison of shear layer profiles with and without blowing ($Re = 100,000$).

Figure 5.10. Instantaneous cross-section of natural jet at Re 100,000.

Figure 5.13. Multiple-exposure cross-section of natural jet at Re 25,000 (F 4).

Figure 5.14. Multiple-exposure cross-section of natural jet at Re 25,000 (F 4).

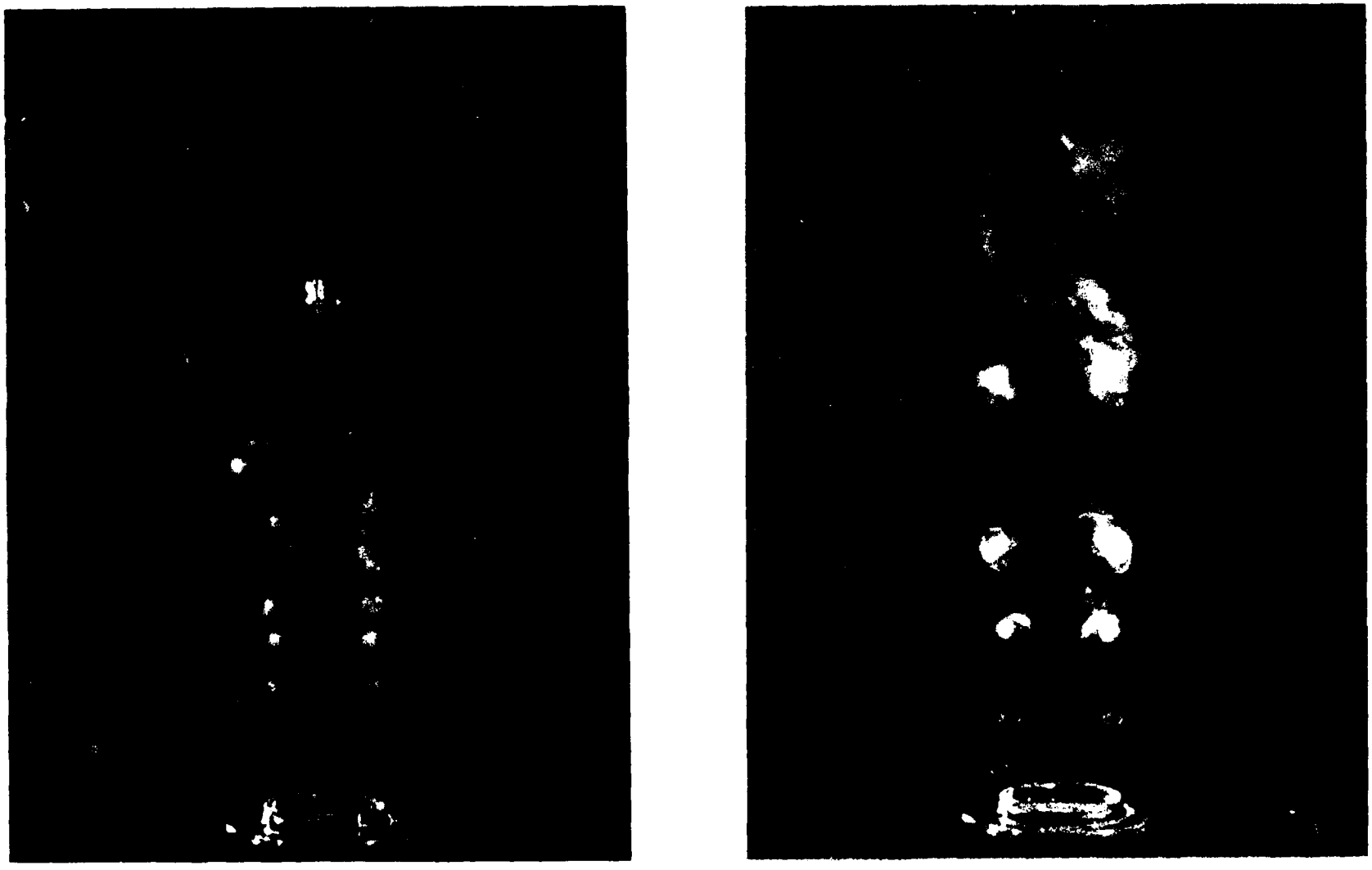

Figure 5.15. Comparison of natural and axially-excited jets at $Re = 10,000$.

Figure 5.16. Axially-excited jet at $Re = 20,000$, $St_a = 0.55$, and $p_a = 1.6\%$ ($F = 1$).

Figure 5.17. Axially-excited jet at $Re = 10,000$, $St_a = 0.55$, and p_a 12% (F 1).

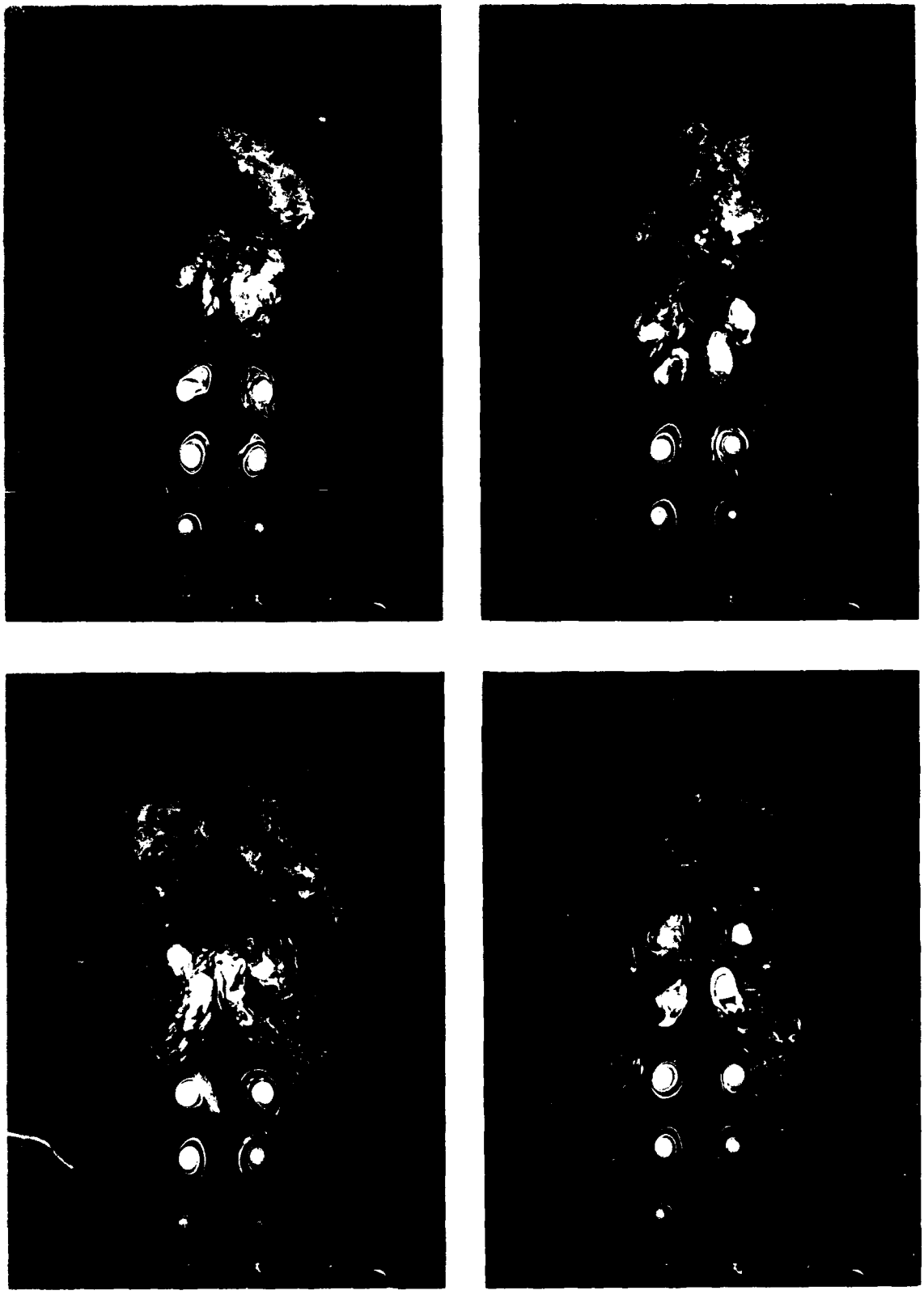

Figure 5.18. Instantaneous pictures of axially-excited jet at different phases of excitation ($Re = 10,000$, $St_a = 0.55$, and $\bar{p}_a = 12\%$).

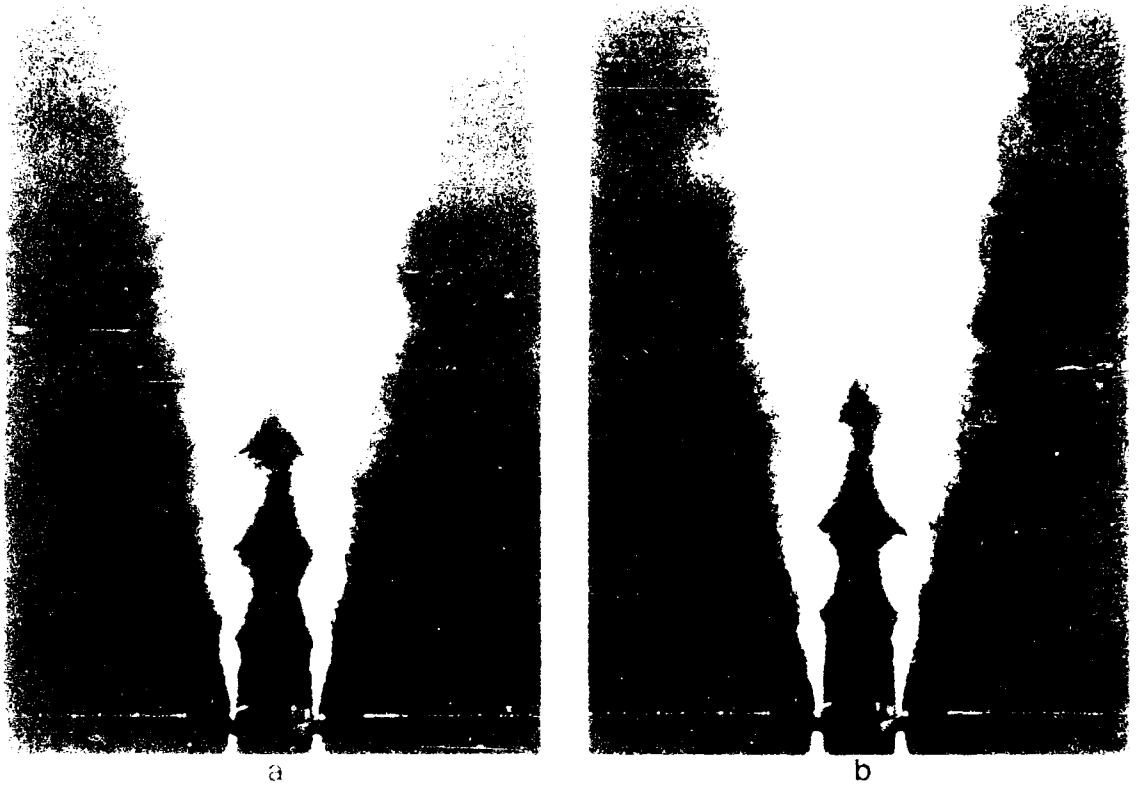

a b

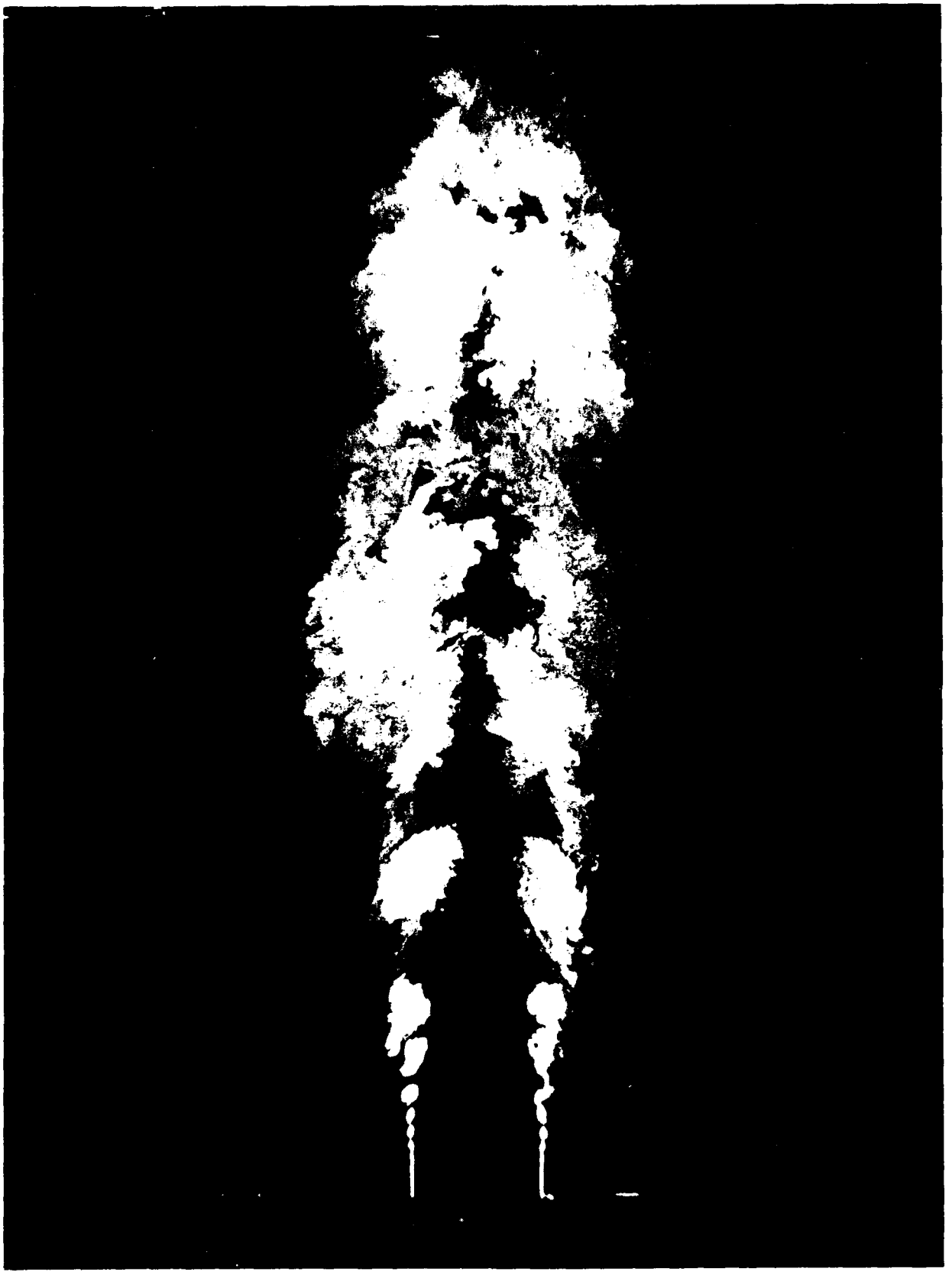

Figure 5.20. Axially-excited jet at $Re = 50{,}000$, $St_a = 0.55$, and $p_a = 1.4\%$ ($F = 1$).

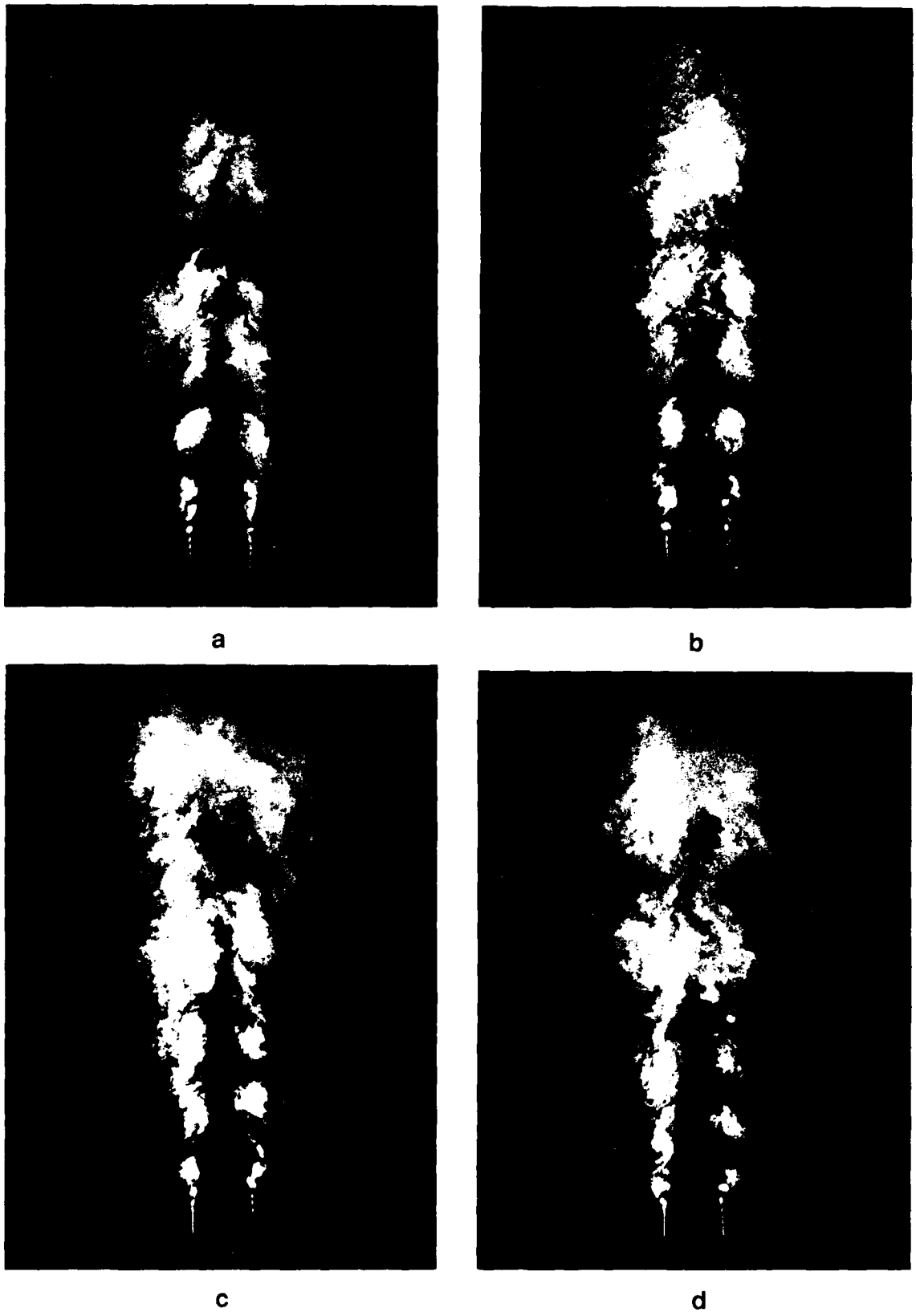

Figure 5.22. Axially-excited jet at $Re = 50{,}000$ and $St_a = 0.55$ and at different $\tilde{p}_a$: (a) 1.4%, (b) 2.7%, (c) 6.5%, and (d) 13%. $F = 1$.

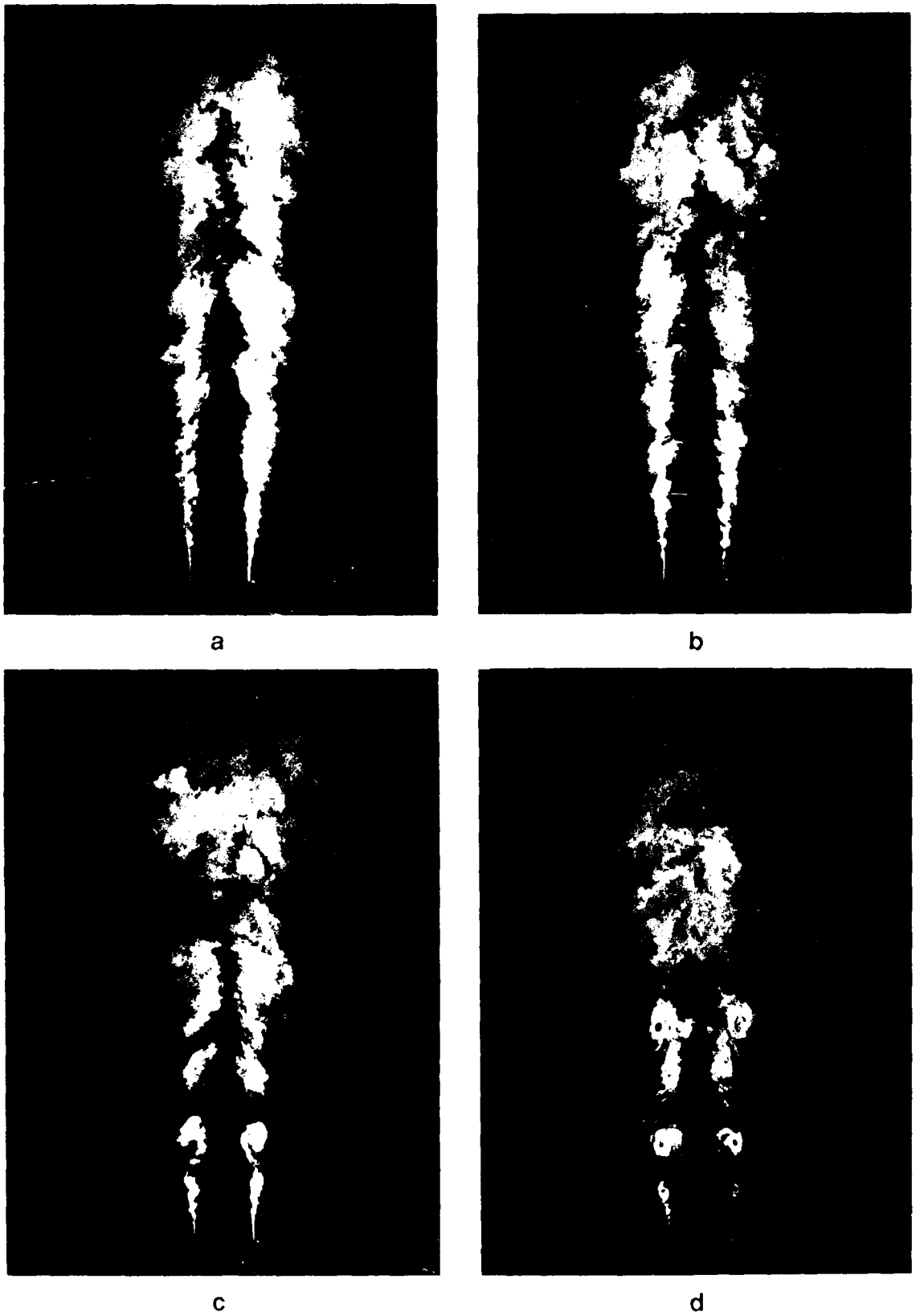

Figure 5.24. Axially-excited jet at Re 100,000 and St_a 0.55 and at different p_a: (a) 0.3%, (b) 0.6%, (c) 2.8%, and (d) 5.5%. F 1.

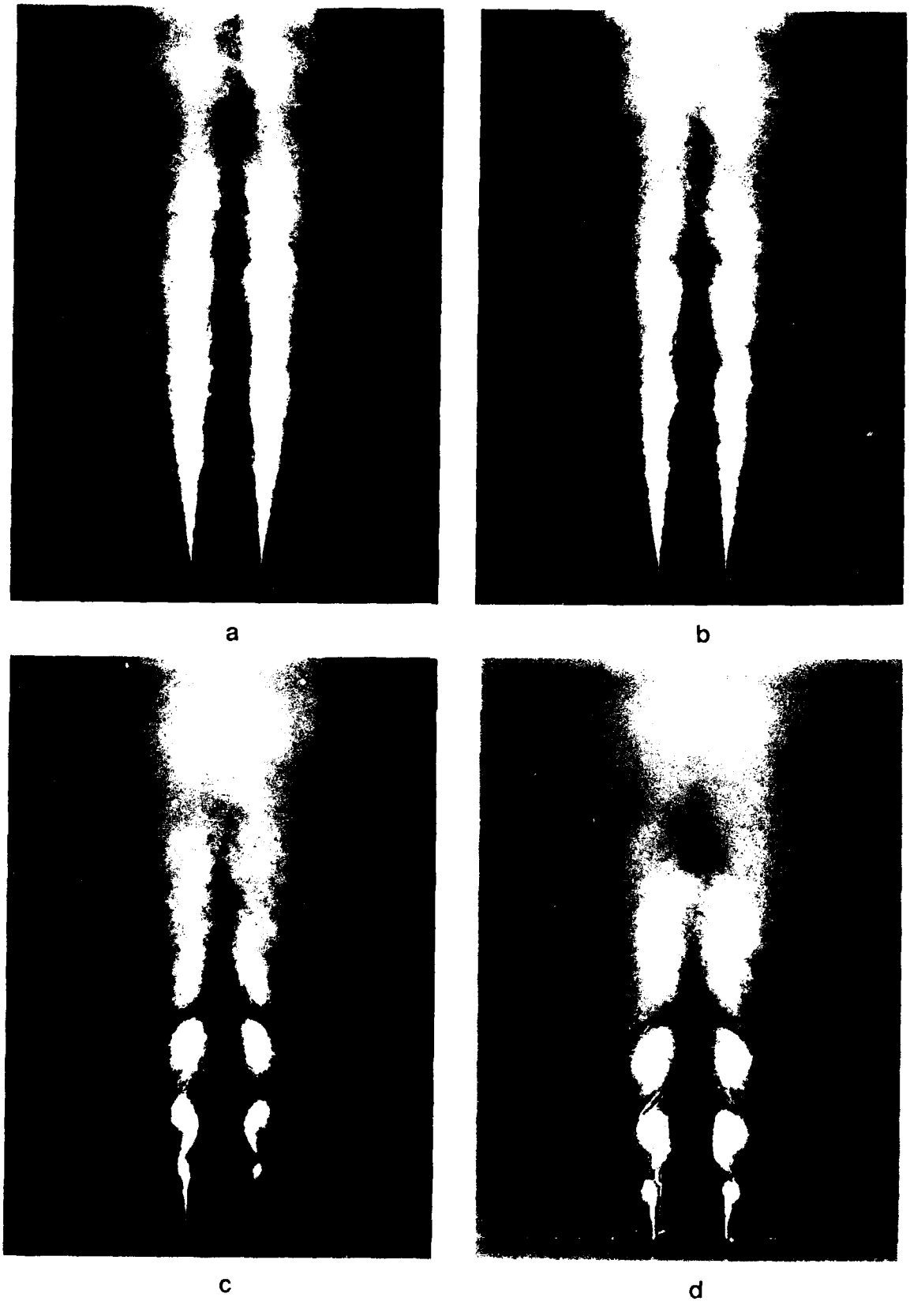

Figure 5.25. Axially-excited jet at $Re = 100,000$ and $St_a = 0.55$ and at different p_a: (a) 0.3%, (b) 0.6%, (c) 2.8%, and (d) 5.5%. $F = 17$.

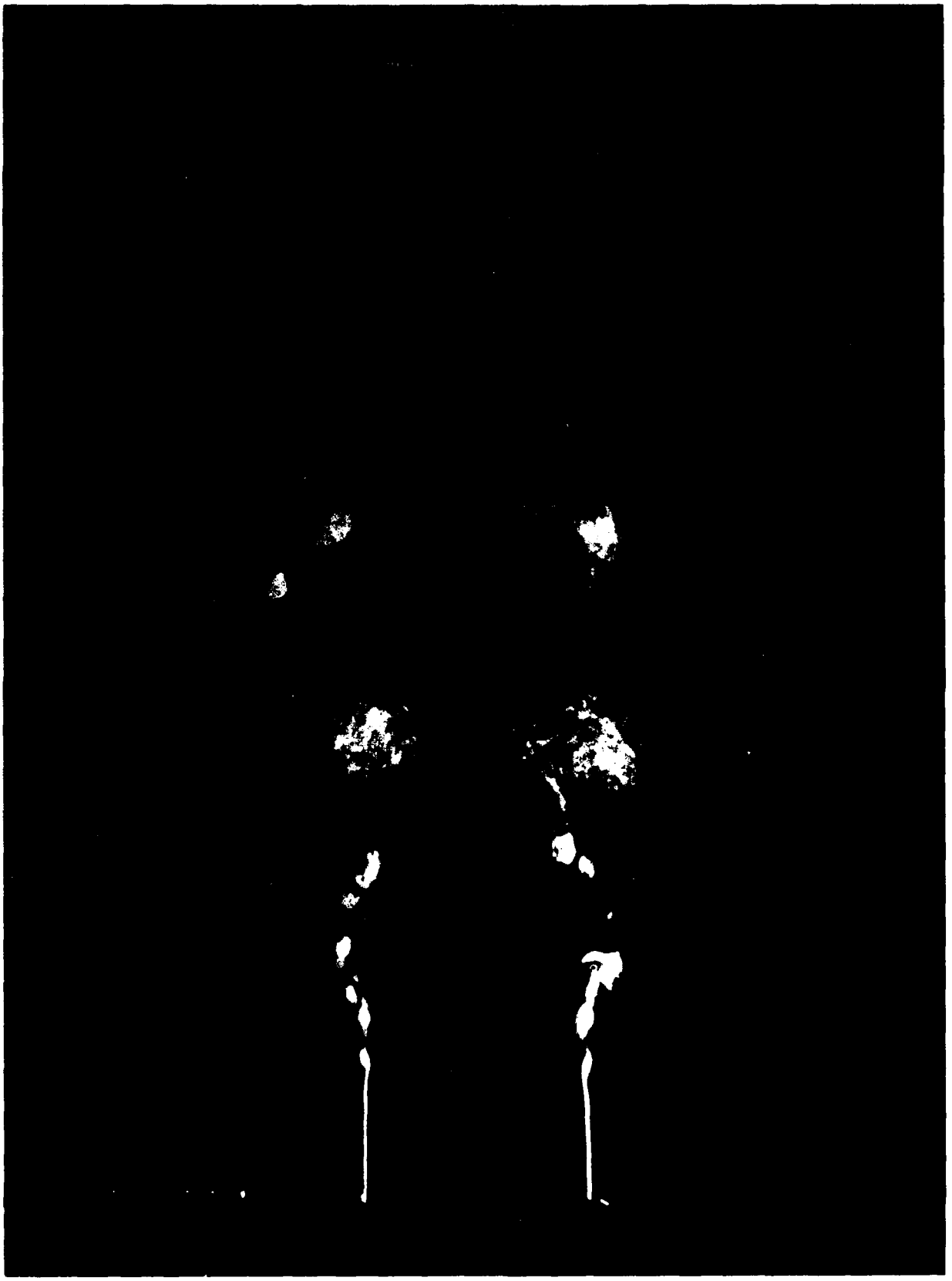

Figure 5.26. Axially-excited jet at $Re = 25,000$, $St_a = 0.55$, and $\bar{p}_a = 18\%$ ($F = 4$).

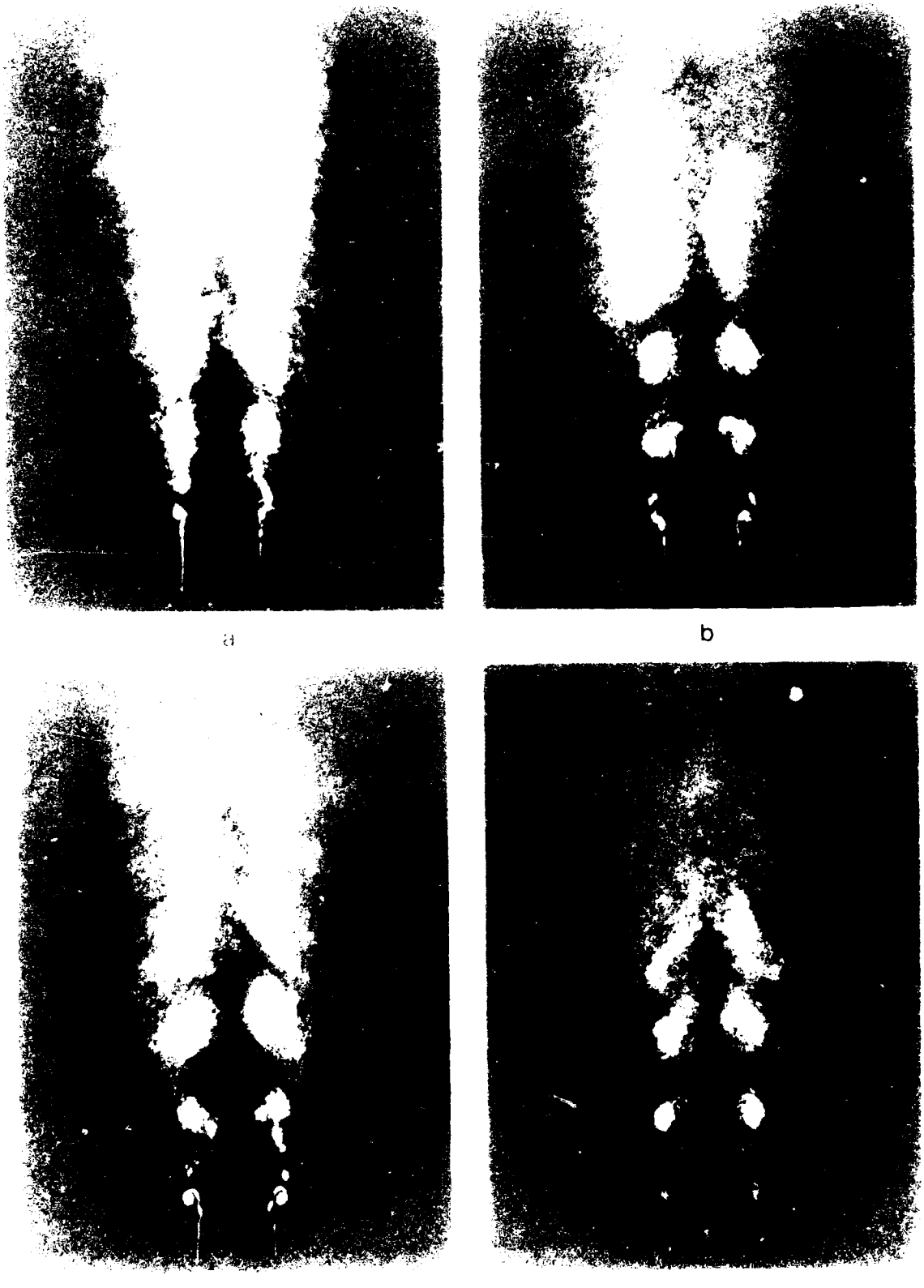

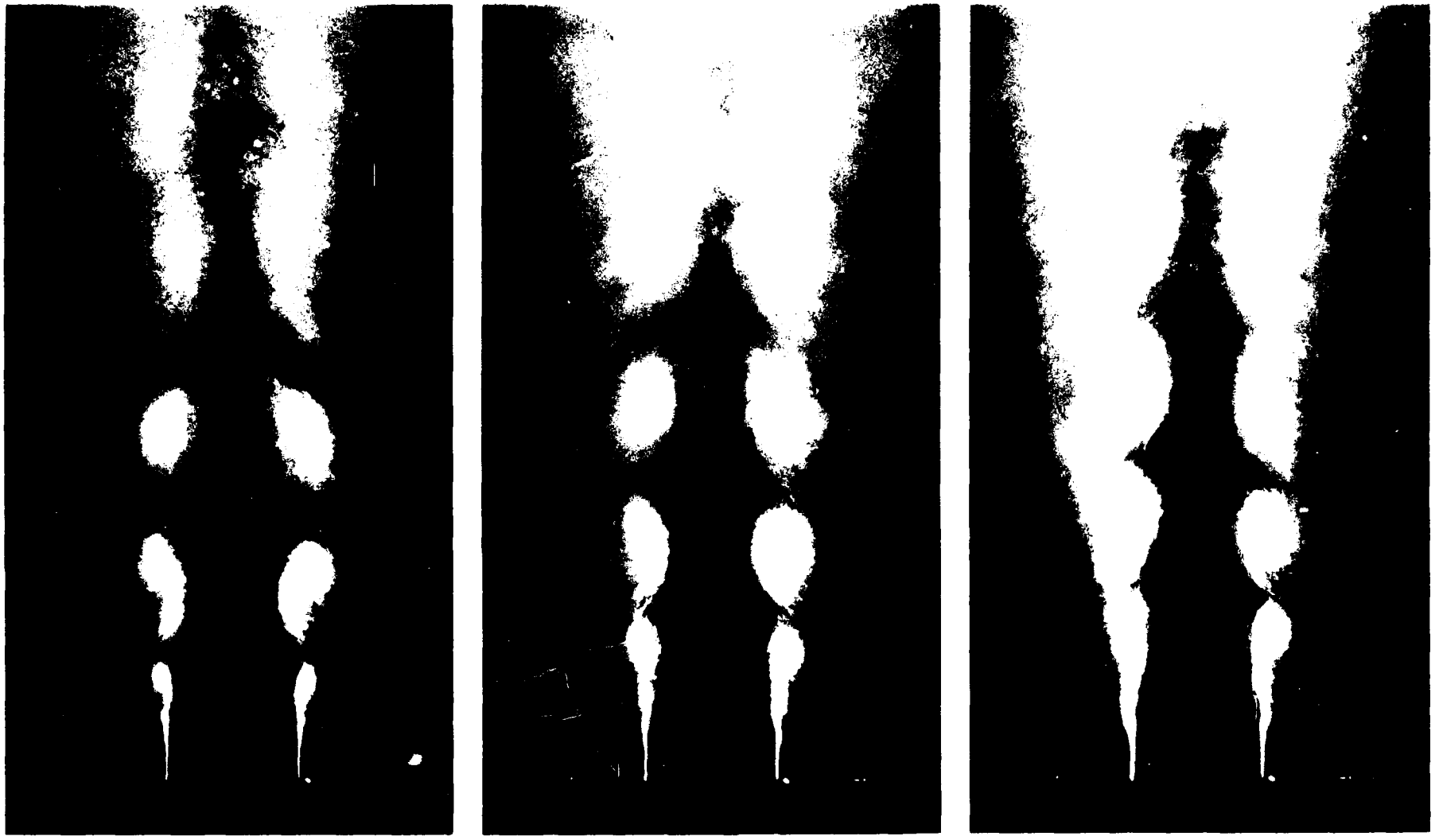

Figure 5.28. Axially-excited jet at $Re = 100,000$ and $\tilde{p}_a = 2.8\%$ and at different St_a: (a) 0.55, (b) 0.60, and (c) 0.65. $F = 17$.

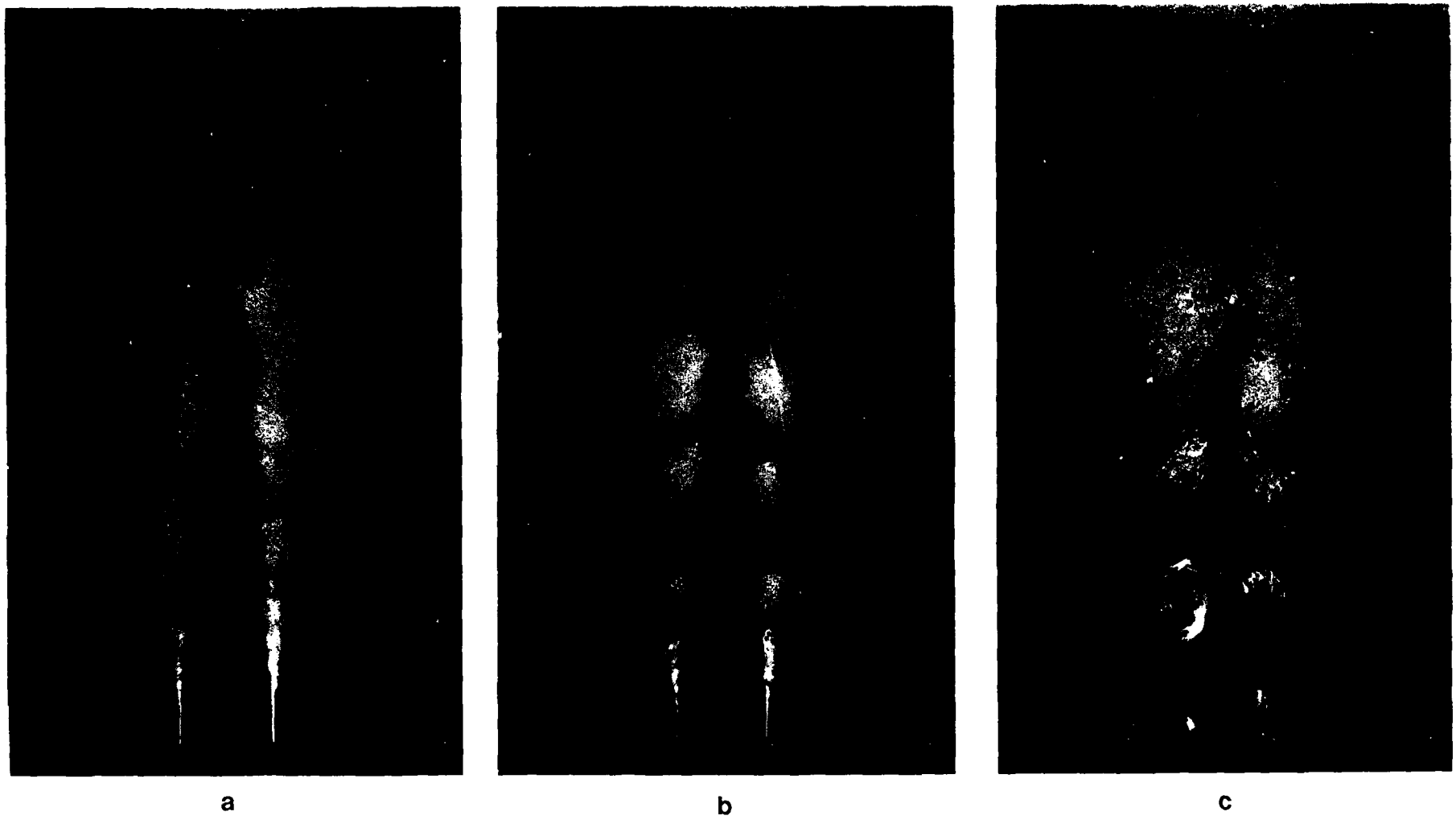

Figure 5.29. Axially-excited jet at $Re = 50,000$ and $St_a = 0.55$ and different $\bar{p}_a$: (a) 0%, (b) 0.5%, and (c) 2.1%. $F = 8$.
The axial excitation is produced by the driver in the plenum.

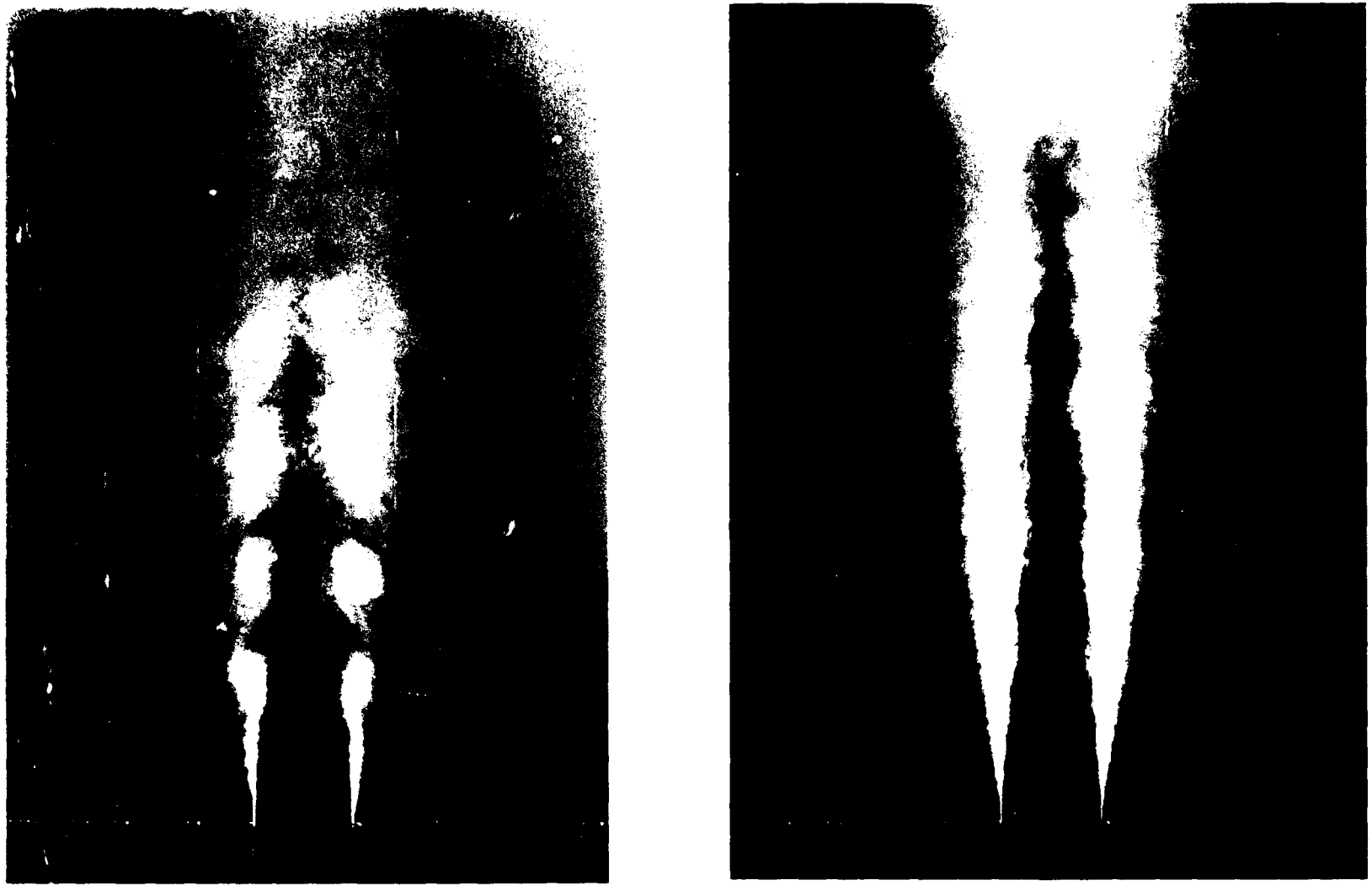

Figure 5.30. Comparison of the effects of (a) internal ($\bar{p} = 0.24\%$ and $F = 8$) and (b) external ($\bar{p} = 0.30\%$ and $F = 17$) axial forcing at $Re = 100{,}000$ and $St_a = 0.55$.

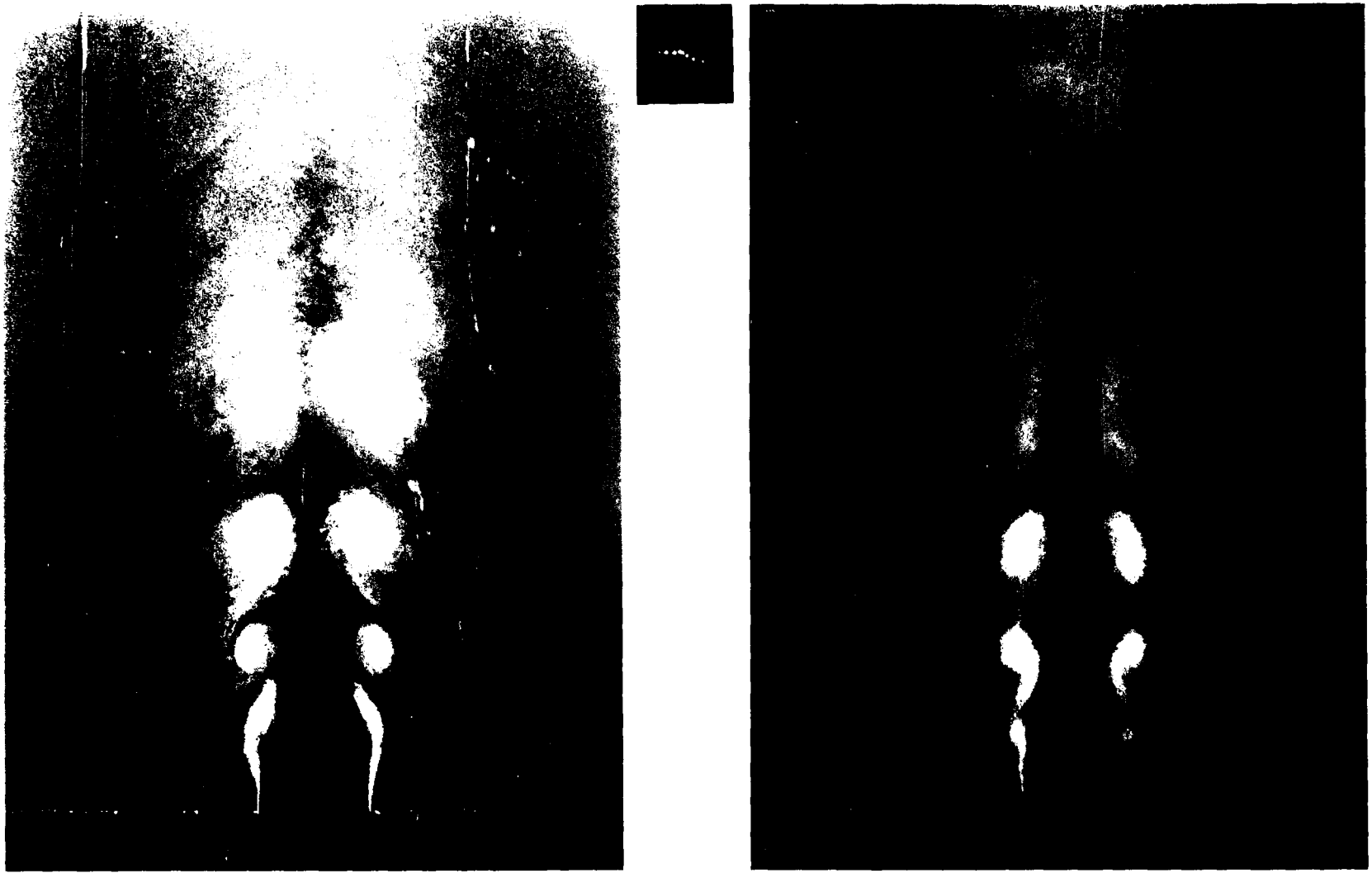

Figure 5.31. Comparison of the effects of (a) internal ($\bar{p} = 1.9\%$ and $F = 8$) and (b) external ($\bar{p} = 2.7\%$ and $F = 17$) axial forcing at $Re = 100,000$ and $St_a = 0.55$.

Figure 5.32. Helically-excited jet at $Re = 25,000$, $St_h = 0.28$, and $p_h = 0.2\%$ $(F = 1)$.

Figure 5.34. Helically-excited jet at Re 100,000, St_h 0.27, and p_h 0.7% (F 1).

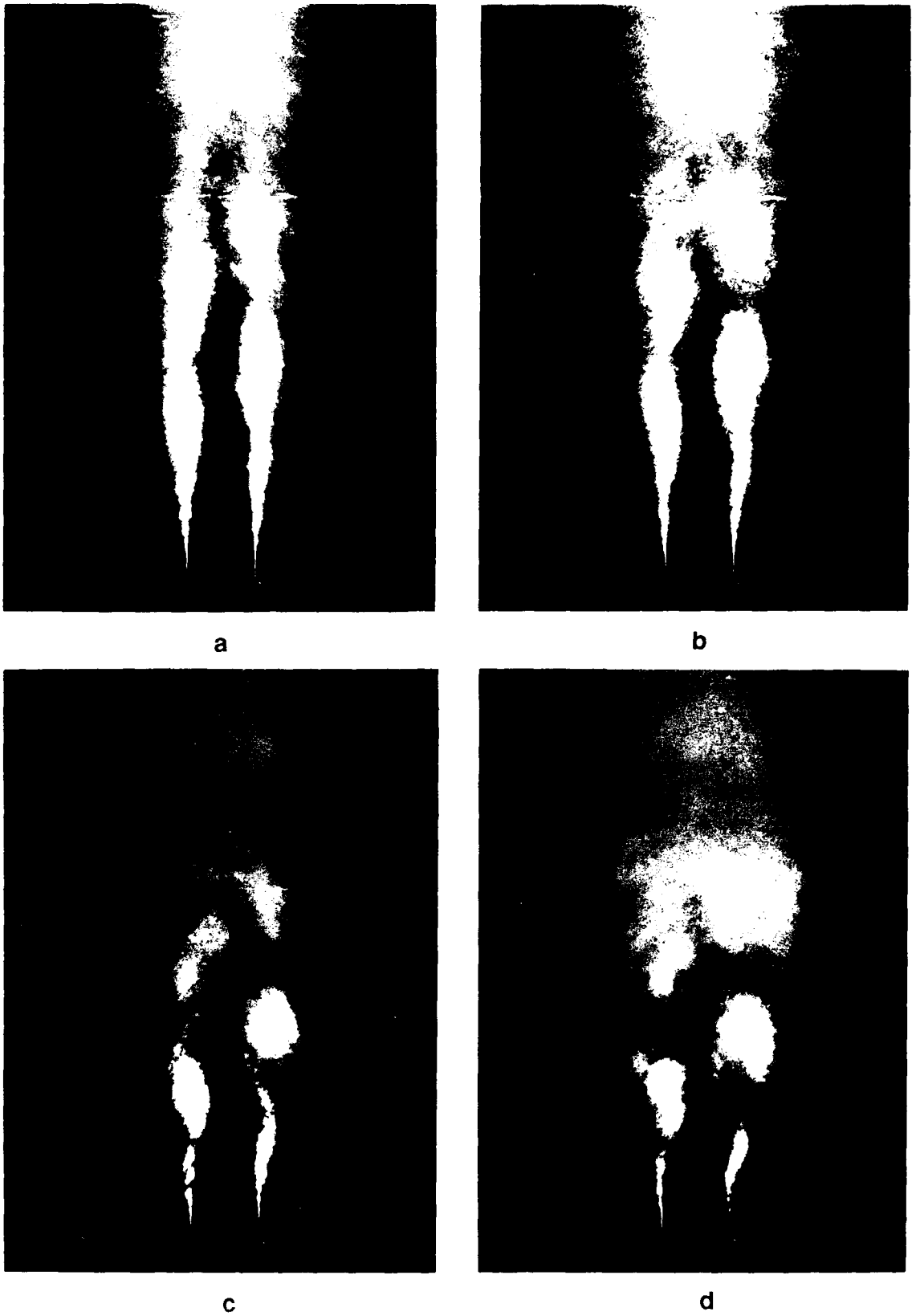

Figure 5.35. Helically-excited jet at $Re = 50,000$ and $St_a = 0.28$ and at different p_h: (a) 0.3%, (b) 0.6%, (c) 1.2%, and (d) 2.4%. F 17.

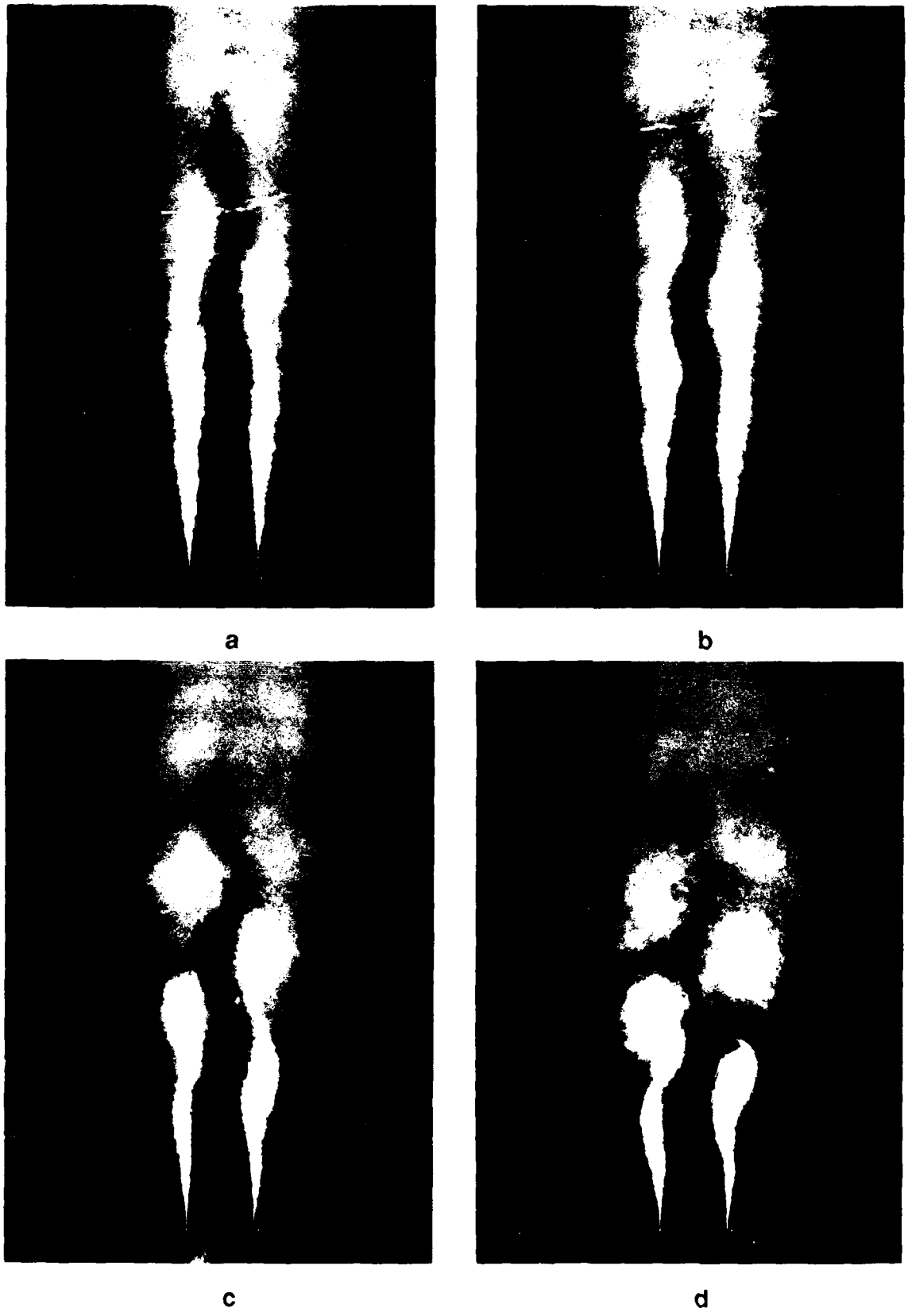

Figure 5.36. Helically-excited jet at $Re = 100,000$ and $St_a = 0.27$ and at different $\bar{p}_h$: (a) 0.1%, (b) 0.2%, (c) 0.4%, and (d) 0.7%. F 17.

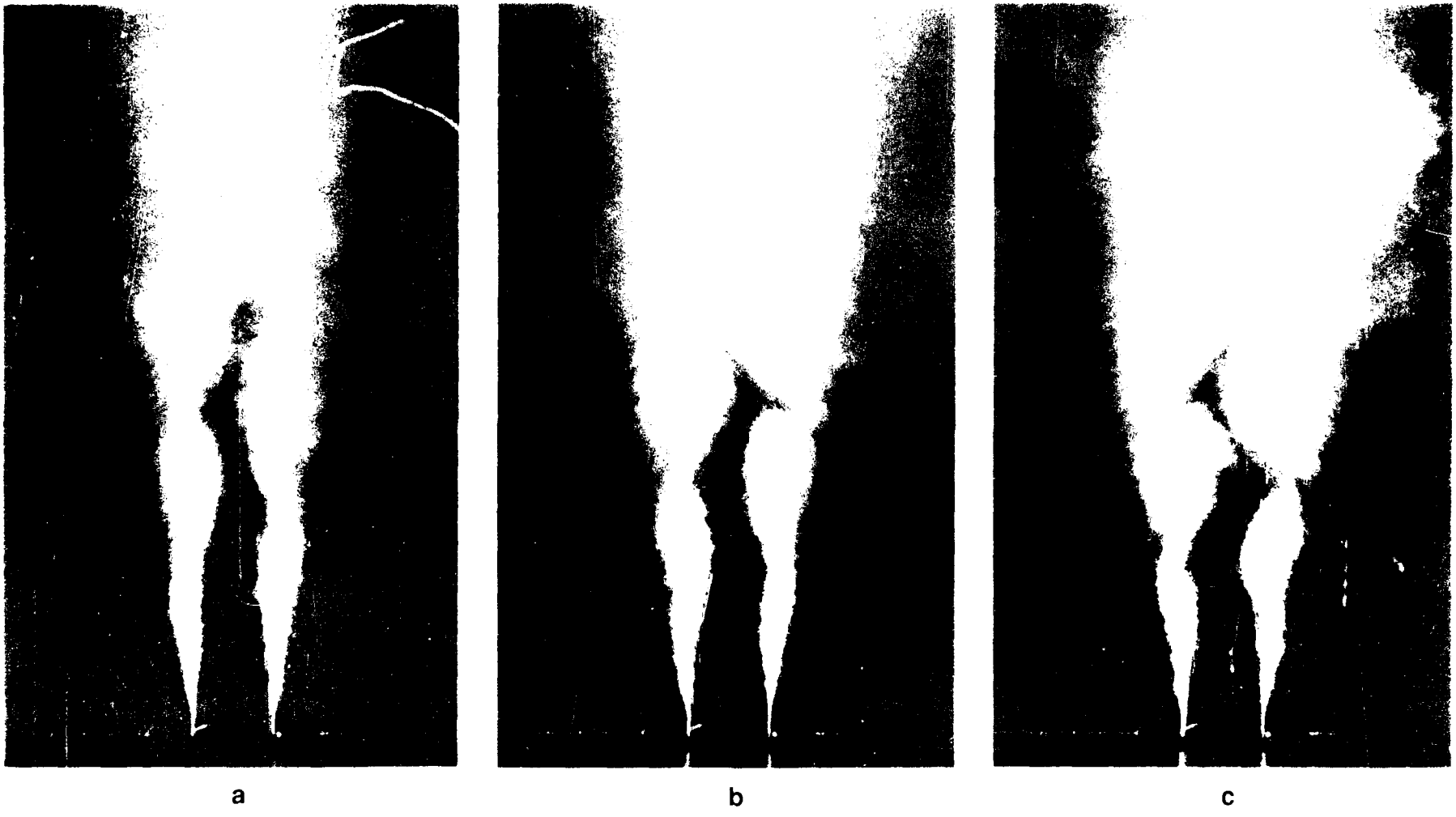

Figure 5.37. Helically-excited jet at $Re = 100,000$ and $\bar{p}_h = 0.3\%$ and at different St_h: (a) 0.27, (b) 0.30, and (c) 0.32. $F = 17$.

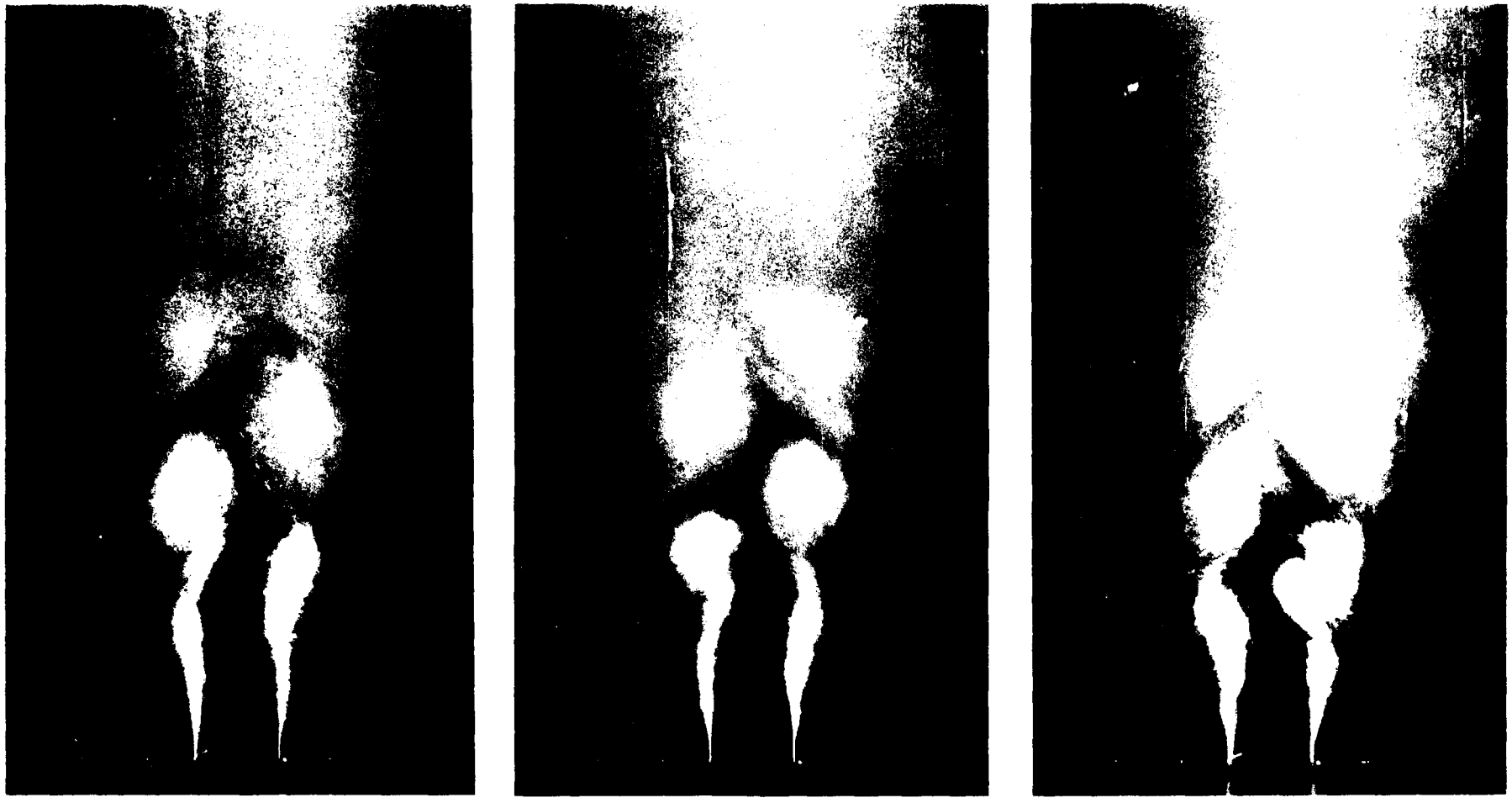

Figure 5.38. Helically-excited jet at $Re = 100,000$ and $\bar{p}_h = 0.7\%$ and at different St_h: (a) 0.27, (b) 0.30, and (c) 0.32. $F = 17$.

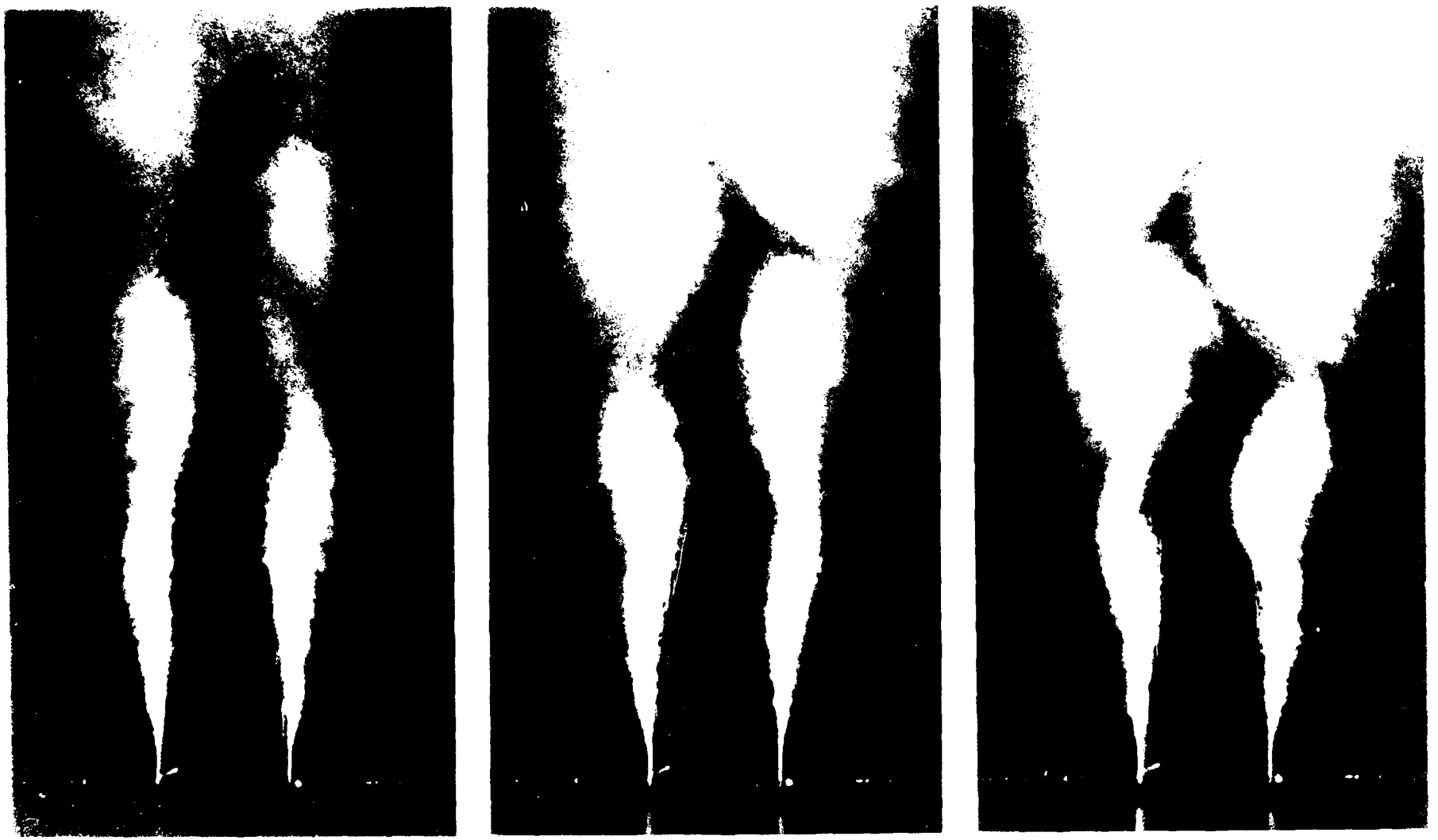

Close up view of helically excited jet at Re [illegible] μ_a 0.3% and at different St_D: (a) 0.27, (b) 0.30, and [illegible] F 17.

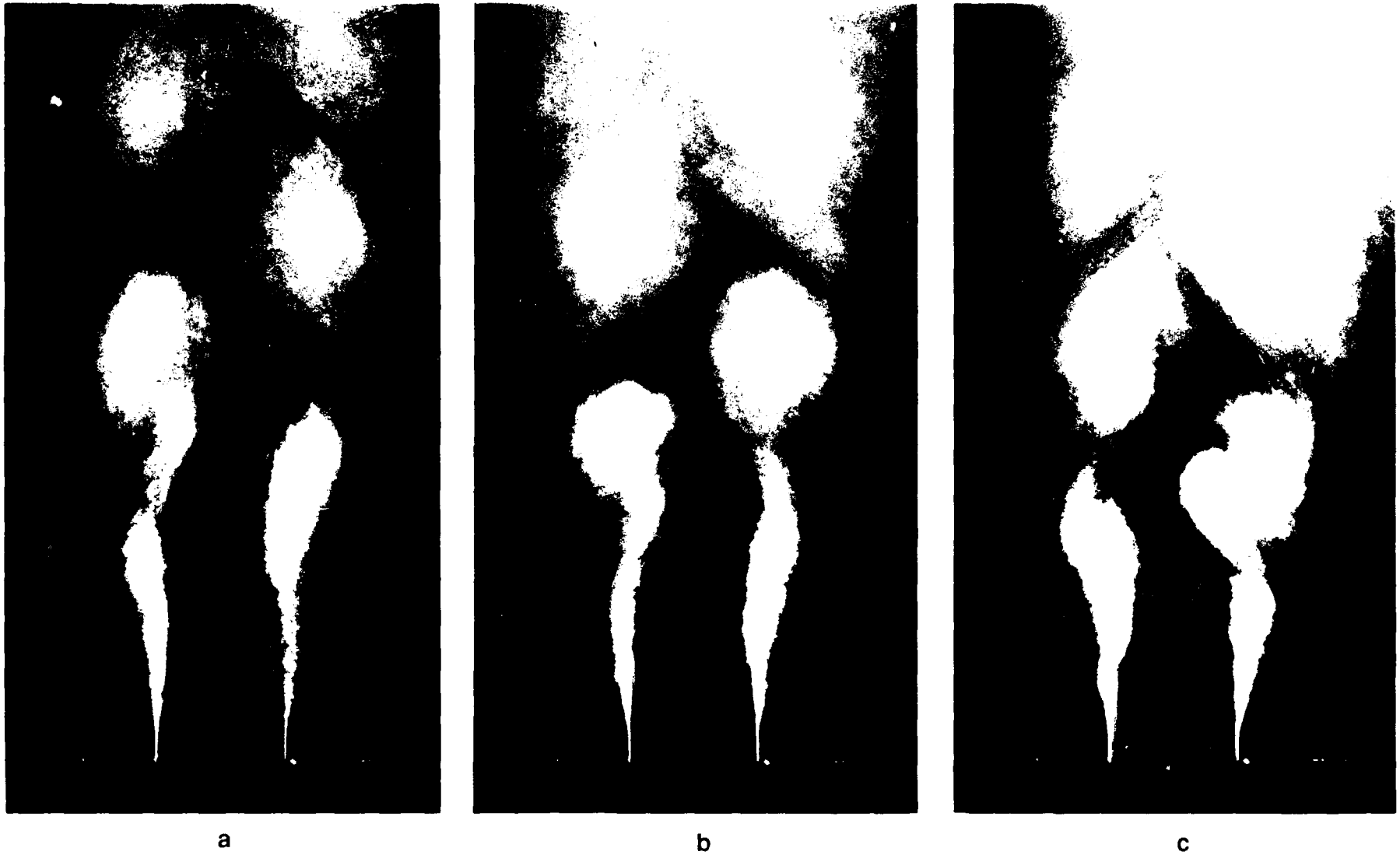

Figure 5.40. Close-up view of helically-excited jet at $Re = 100,000$ and $\bar{p}_h = 0.7\%$ and at different St_h: (a) 0.27, (b) 0.30, and (c) 0.32. $F = 17$.

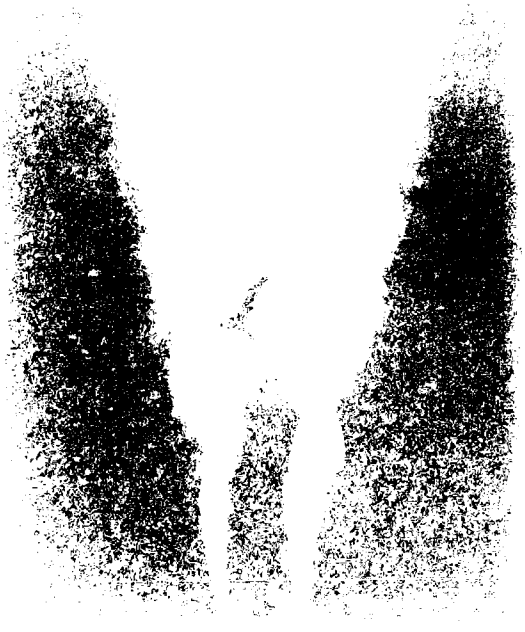

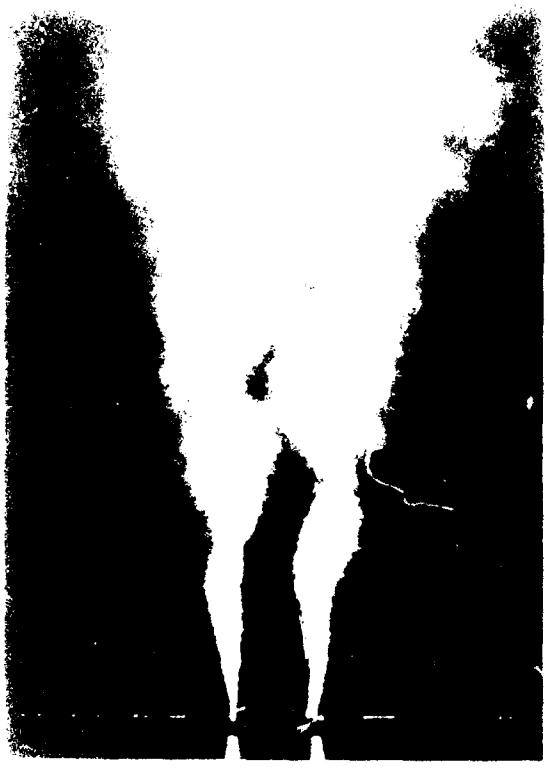

e

f

g

h

Figure 5.42. Bifurcating jet at Re = 10,000, St_a = 0.55, p_a = 12%, and p_b = 3.8%. F = 1.

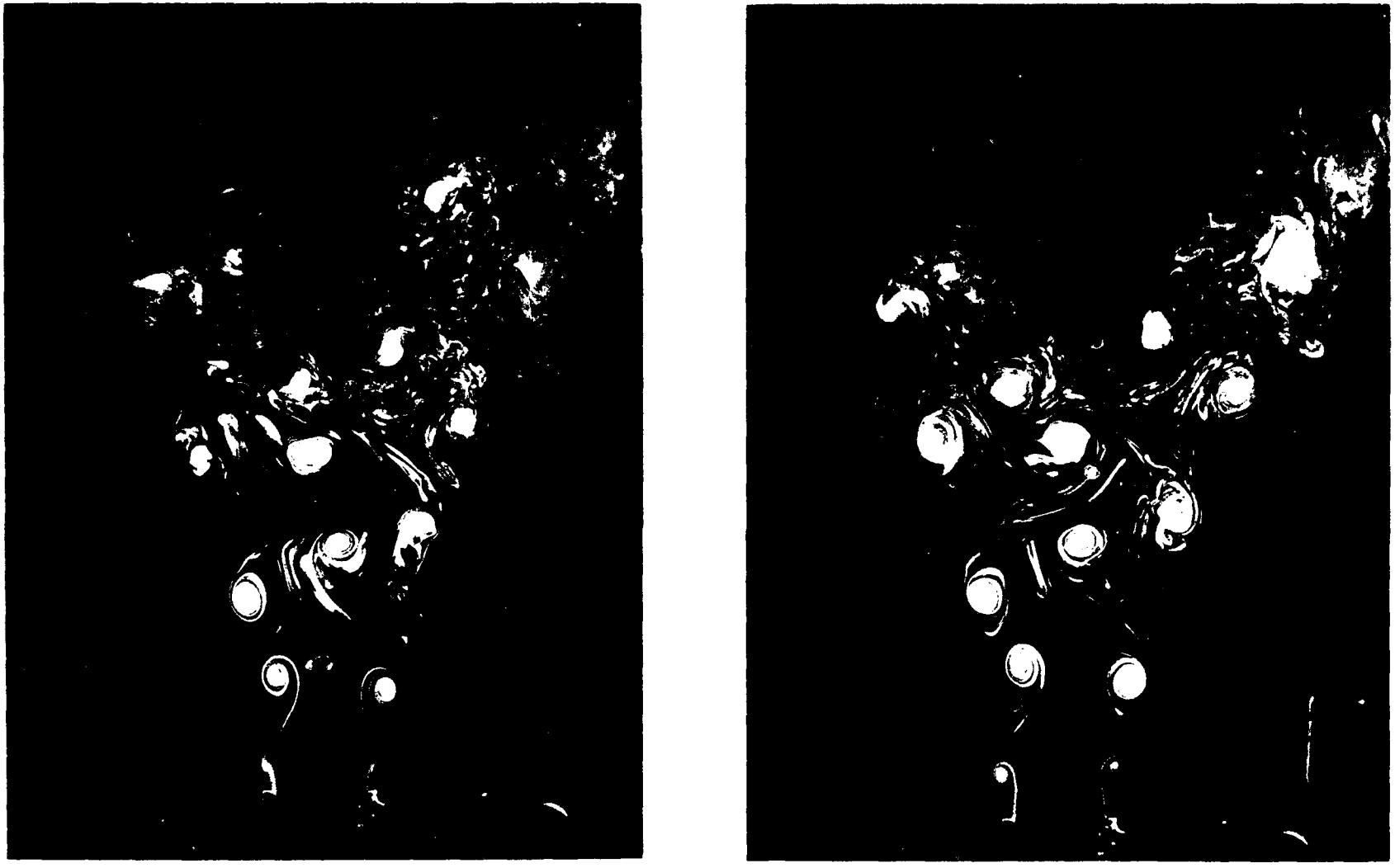

a b

Figure 5.43. Phase-evolution of bifurcating jet at $Re = 10,000$, $St_a = 0.55$, $\bar{p}_a = 12\%$, and $\bar{p}_h = 3.8\%$. $F = 1$.

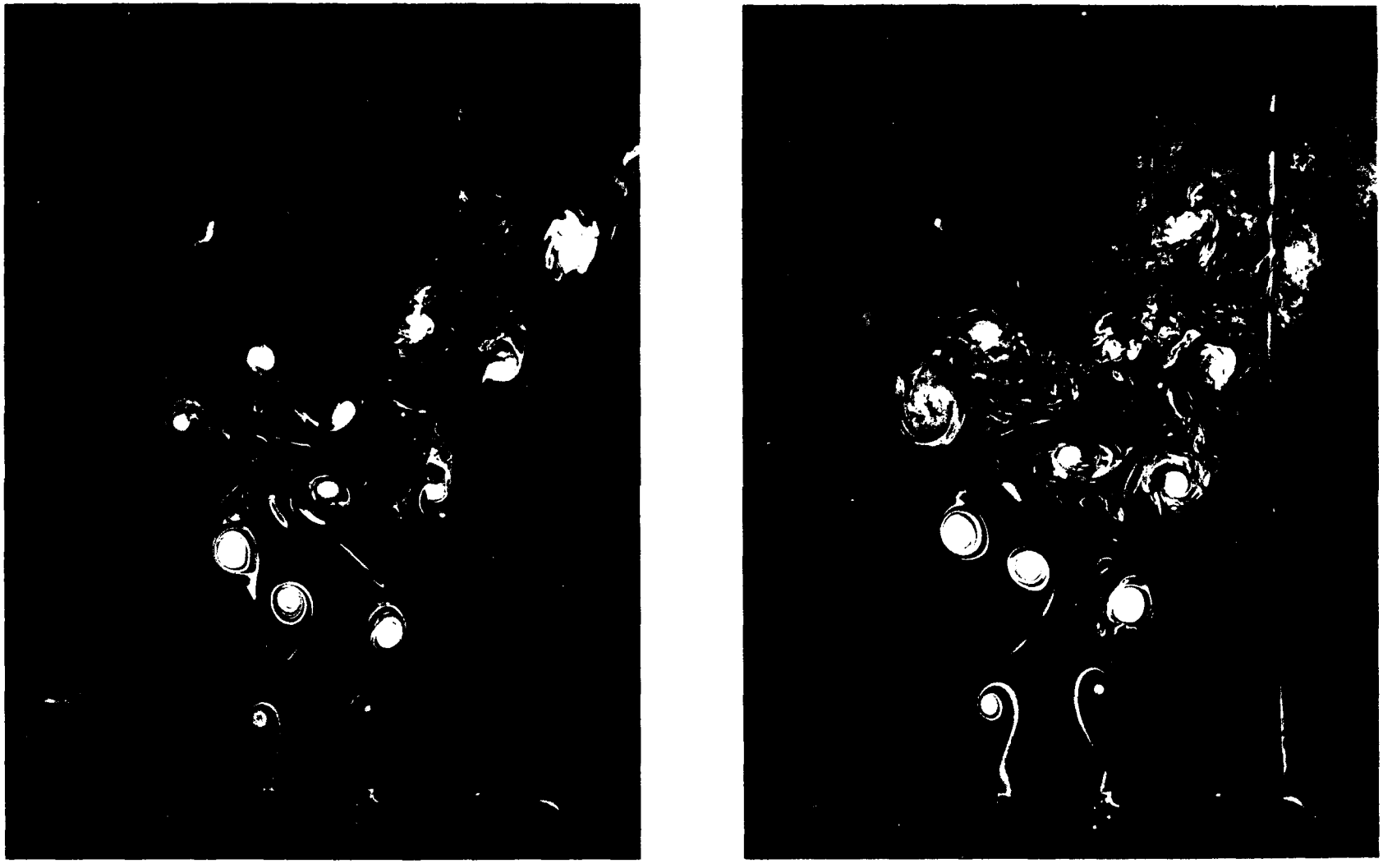

Figure 5.43. (Continued) Phase-evolution of bifurcating jet at $Re = 10,000$, $St_a = 0.55$, $\bar{p}_a = 12\%$, and $\bar{p}_h = 3.8\%$. $F = 1$.
The phase increment is 45°.

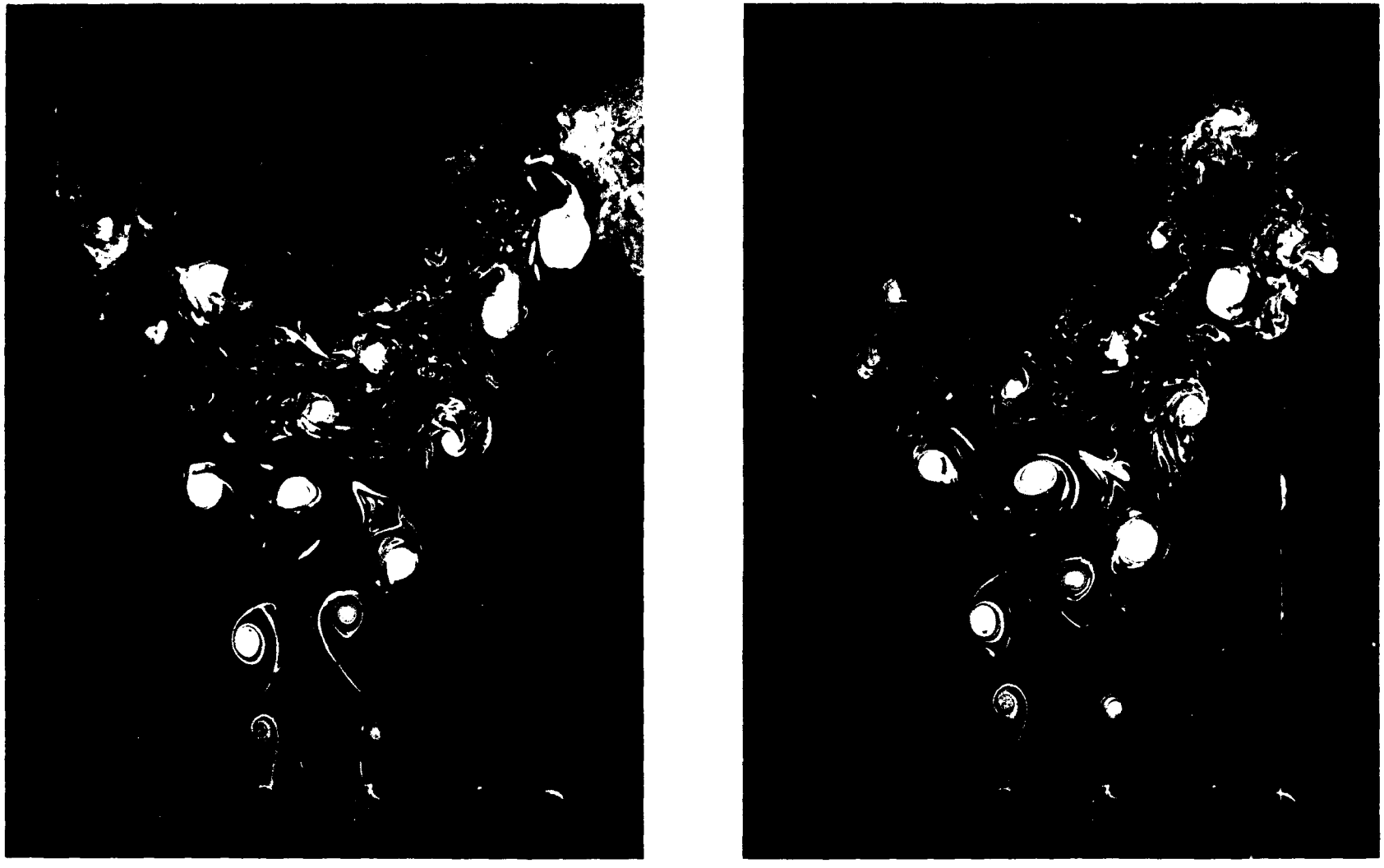

e f

Figure 5.43. (Continued) Phase-evolution of bifurcating jet at $Re = 10,000$, $St_a = 0.55$, $\bar{p}_a = 12\%$, and $\bar{p}_h = 3.8\%$. $F = 1$.
The phase increment is 45°.

Figure 5.44. Bifurcating jet at $Re = 50,000$, $St_a = 0.55$, $\bar{p}_a = 6.5\%$, and $p_h = 1.2\%$. $F = 1$.

Figure 5.45. Bifurcating jet at $Re = 100,000$, $St_a = 0.55$, $\bar{p}_a = 1.4\%$, and $\bar{p}_h = 0.71\%$. $F = 1$.

Figure 5.46: Bifurcating jet at $Re = 100,000$, $St_f = 0.55$, $p_x = 2.8\%$, and $p_z = 0.36\%$, $F = 1$.

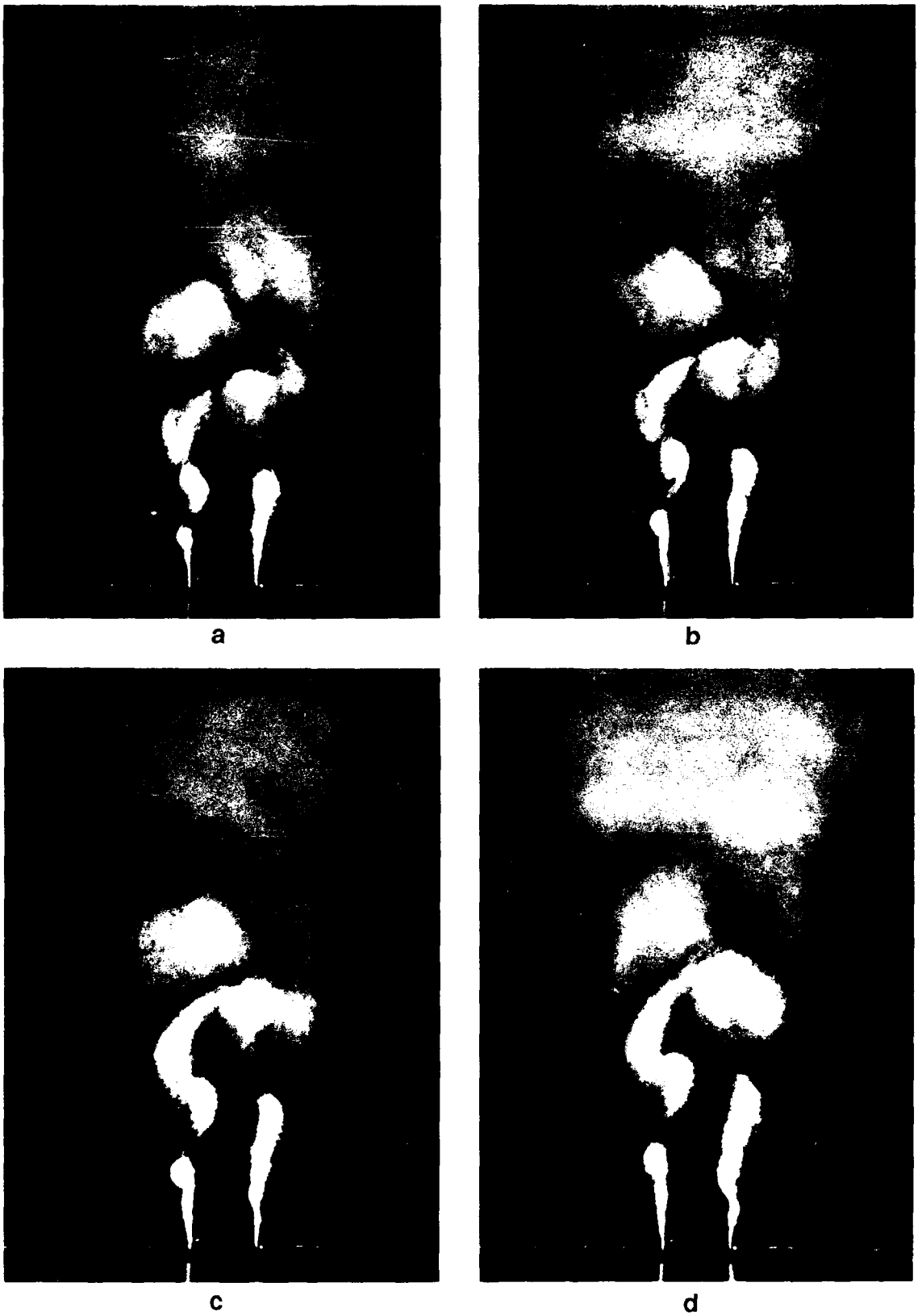

Figure 5.47. Phase-evolution of bifurcating jet at $Re = 100,000$, $St_a = 0.55$, $\bar{p}_a = 2.8\%$, and $\bar{p}_h = 0.71\%$. $F = 17$.
The phase increment is 45°.

e

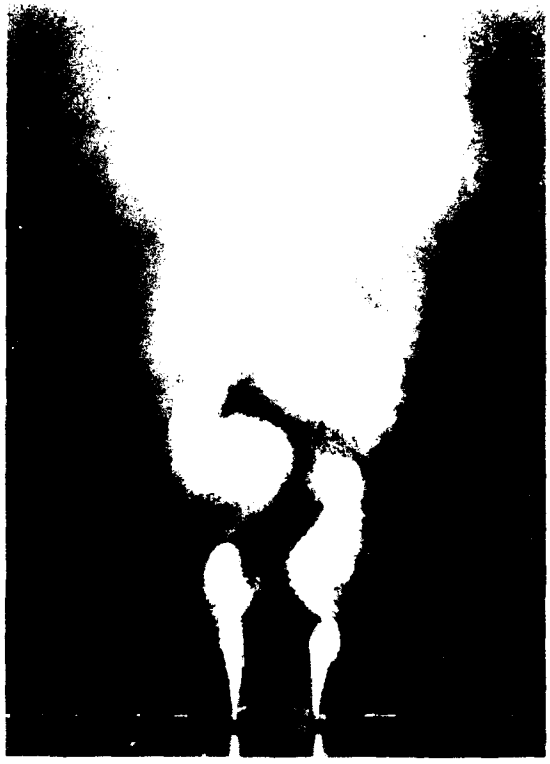

f

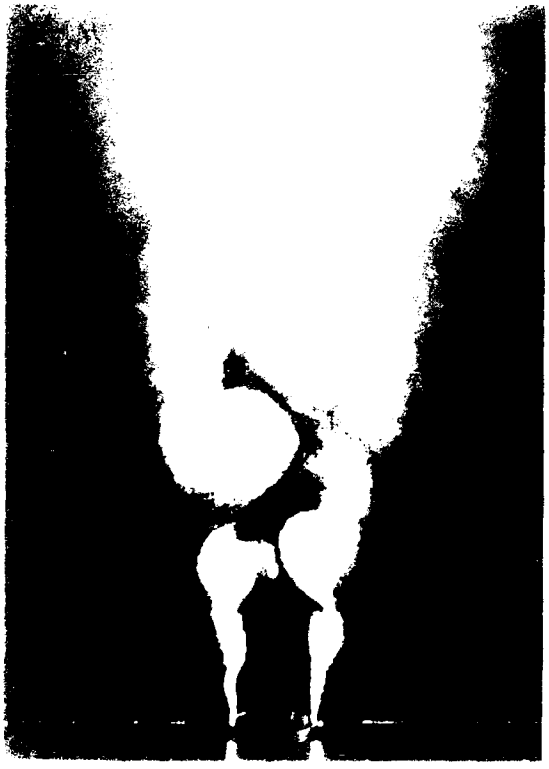

g

h

Figure 5.48. Bifurcating jet viewed in the bifurcating and transverse planes ($Re = 100,000$ and $St = 0.55$). $F = 8$. The axial excitation is produced by the driver in the plenum ($p_a = 1.8\%$ and $p_h = 1.4\%$).

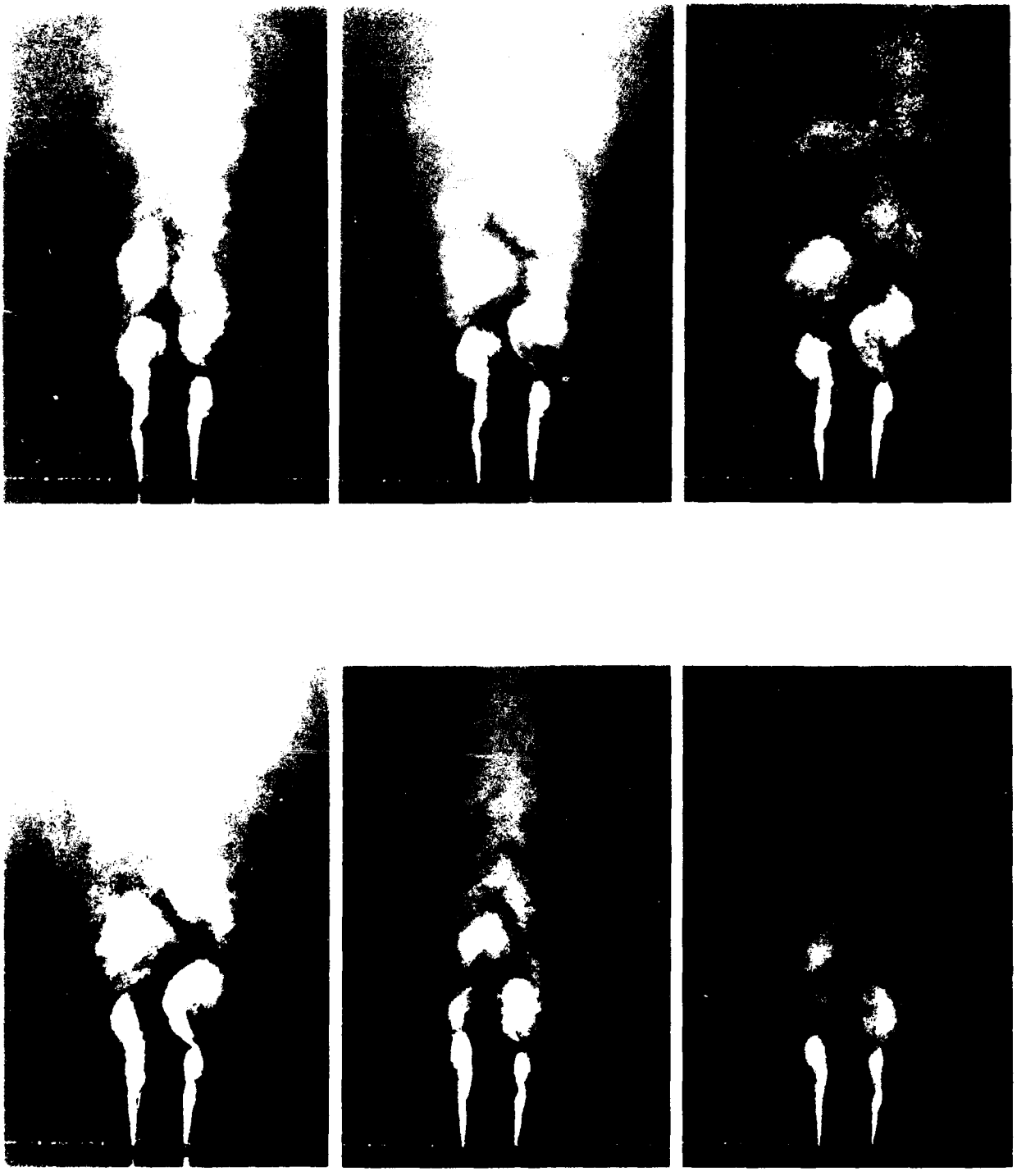

Figure 5.49. (Continued) Cross-sections of the bifurcating jet in different azimuthal planes (Re = 100,000, St_a = 0.55, p_a = 1.4%, and p_h = 0.69%). F = 17. The phase increment between successive planes is 30°.

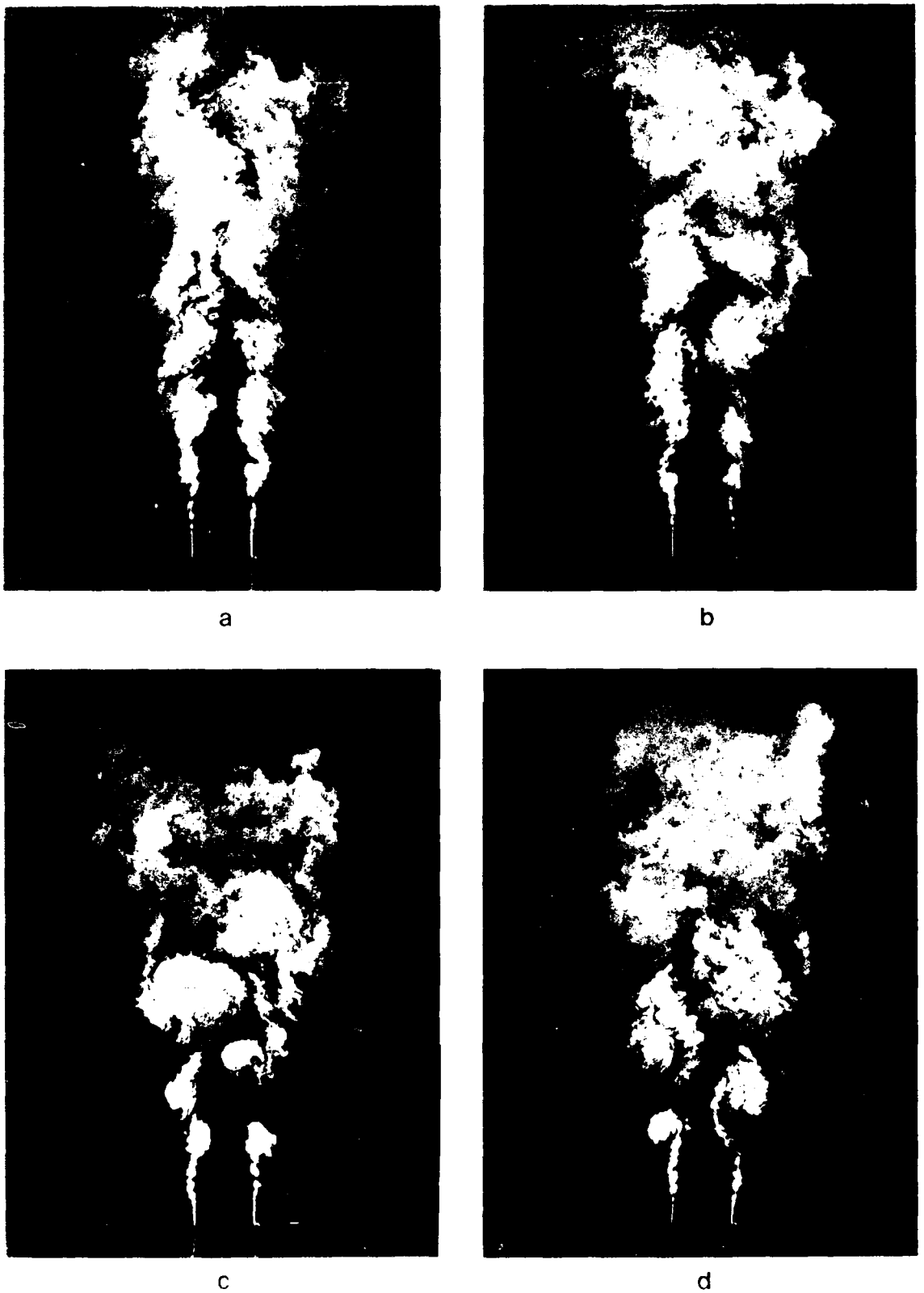
a
b
c
d

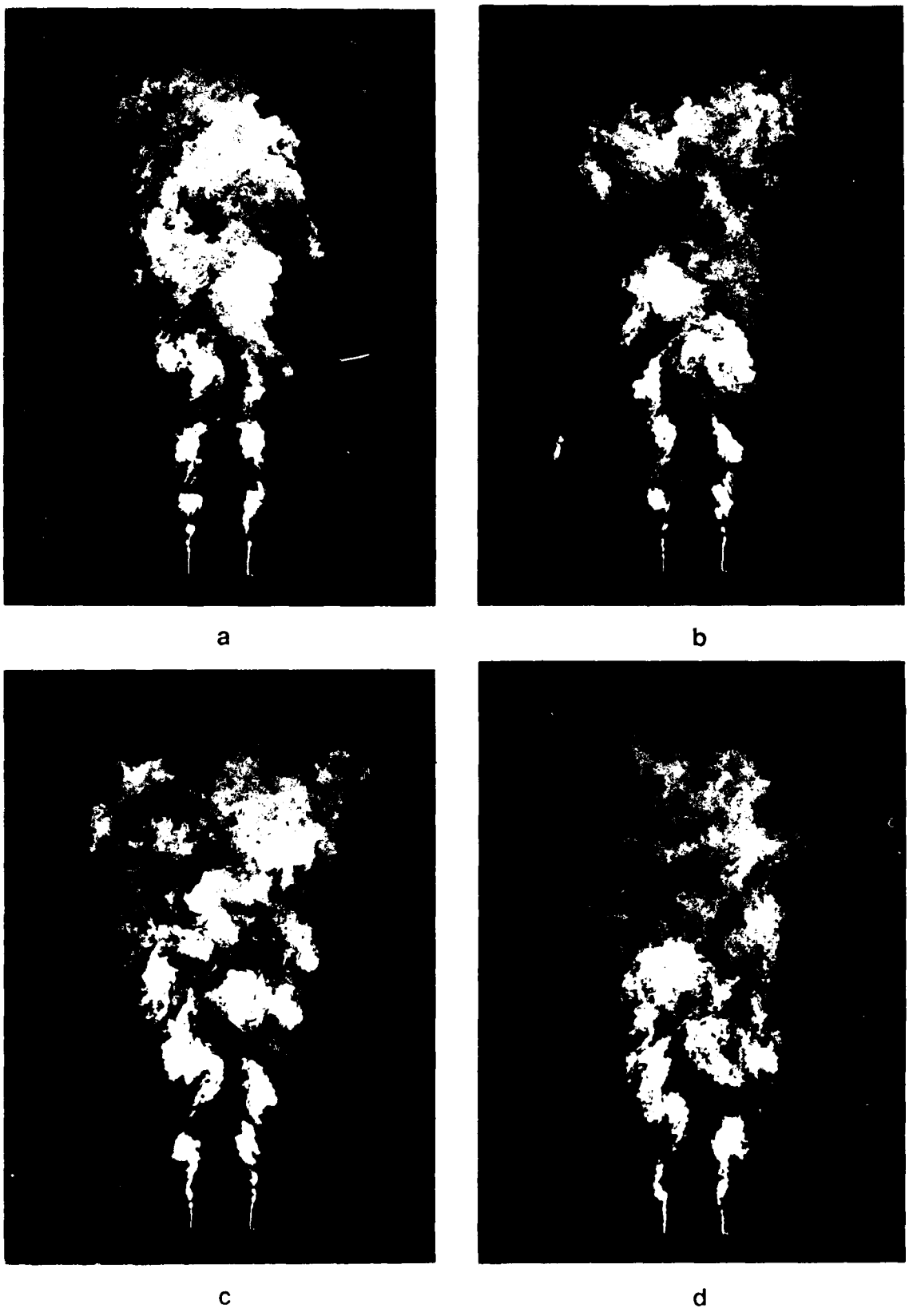

Figure 5.51 Bifurcating jet at $Re = 50{,}000$, $St_1 = 0.55$, $p_1 = 6.5\%$, and p_2 = (a) 0.30%, (b) 0.60%, (c) 1.2%, (d) 2.4%. $F = 1$.

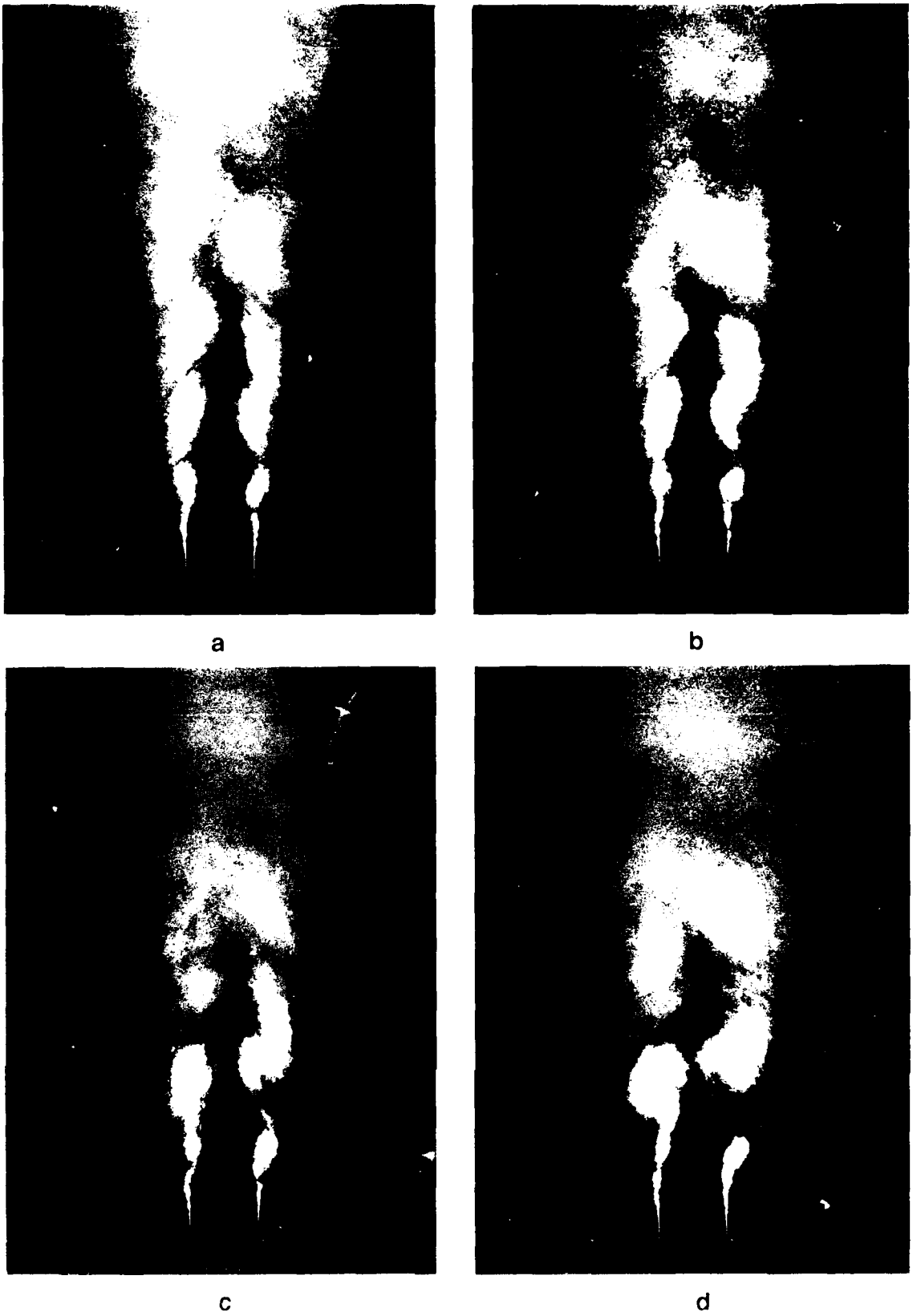

Figure 5.52. Bifurcating jet at Re = 50,000, St_a = 0.55, p_i = 1.4%, and p_b = (a) 0.30%, (b) 0.60%, (c) 1.2%, (d) 2.4%. F = 17.

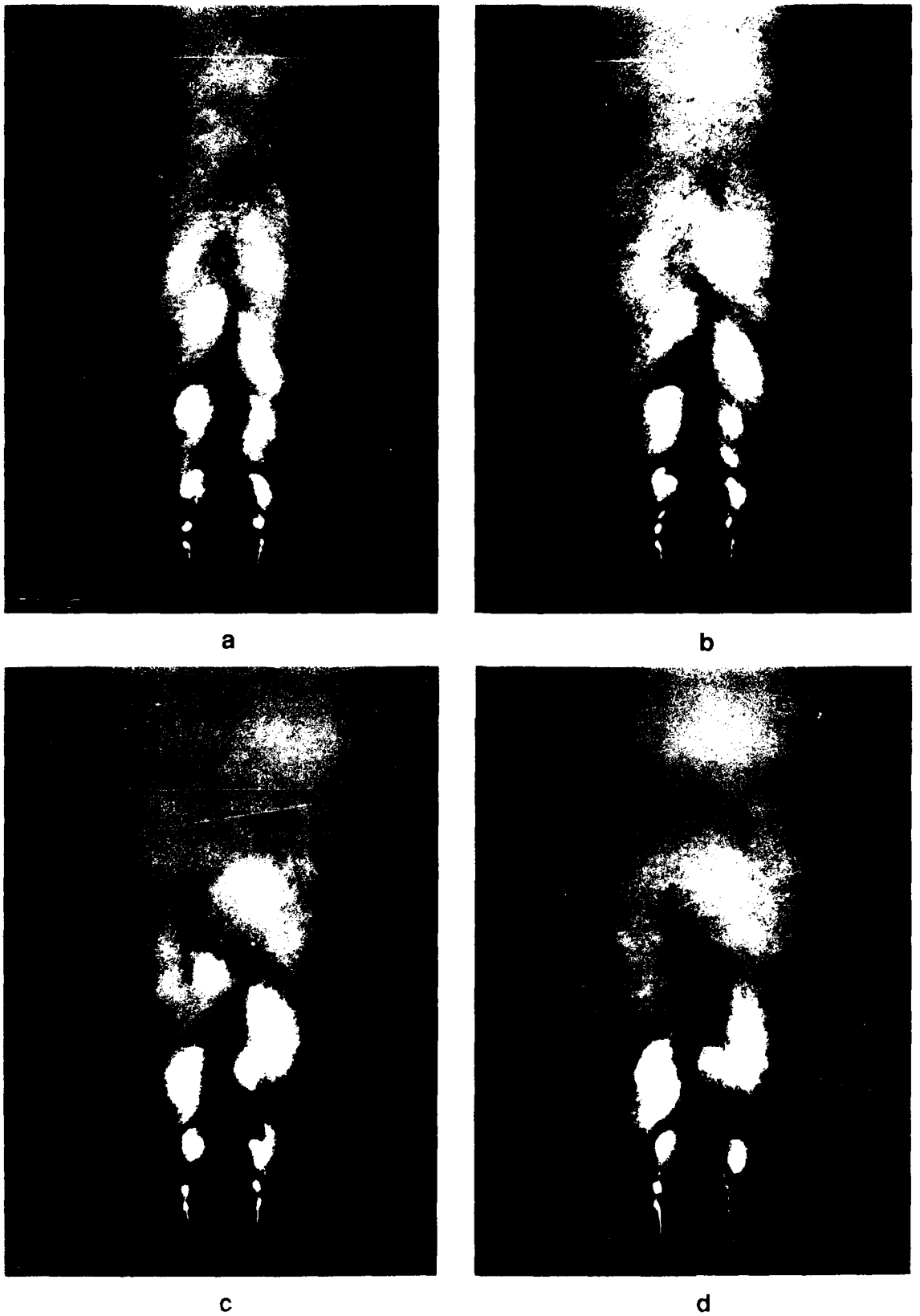

Figure 5.53. Bifurcating jet at $Re = 50{,}000$, $St_a = 0.55$, $\bar{p}_a = 6.5\%$, and p_h = (a) 0.30%, (b) 0.60%, (c) 1.2%, (d) 2.4%. $F = 17$.

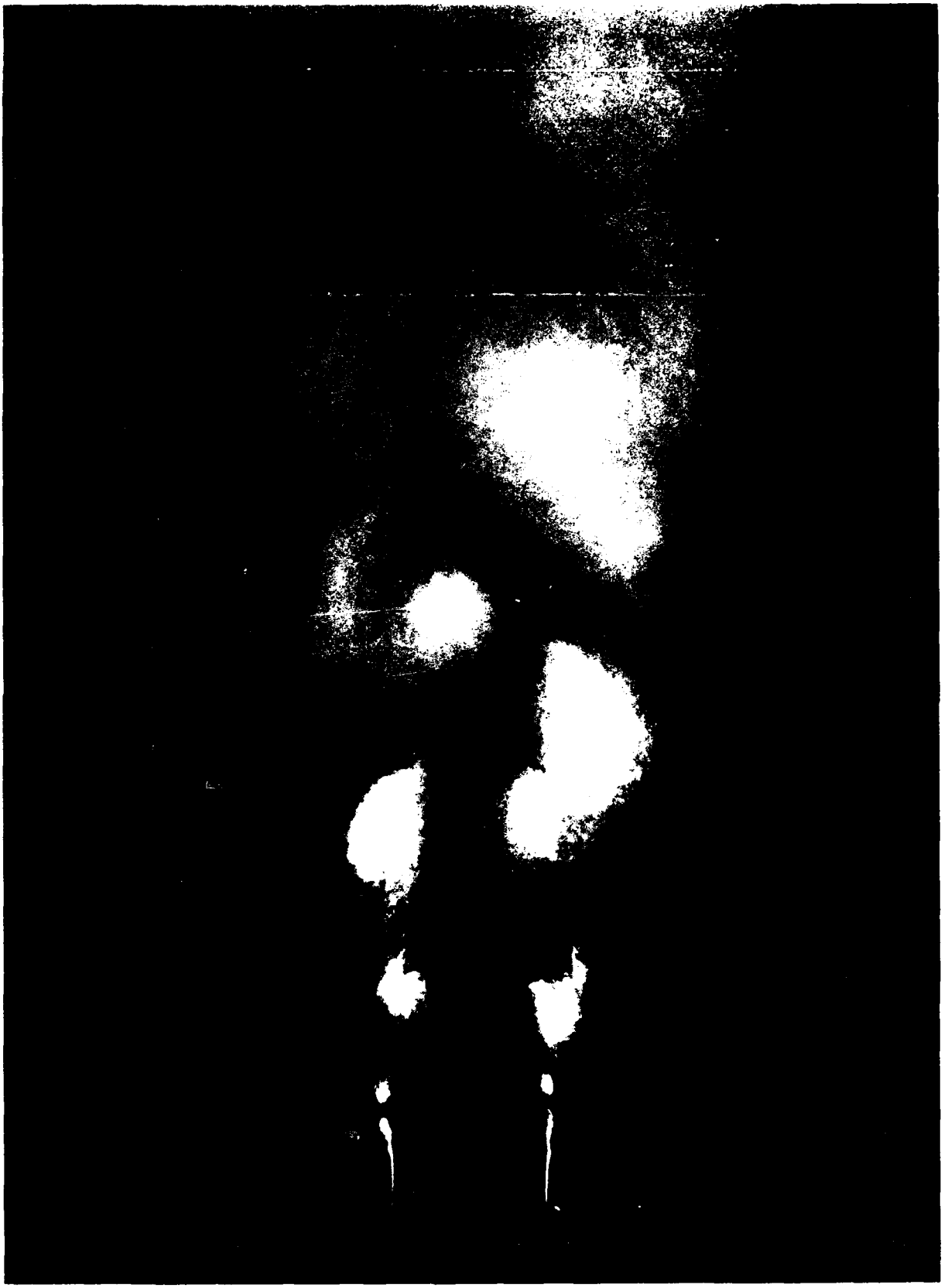

Figure 5.54. Bifurcating jet at $Re = 50{,}000$, $St_a = 0.55$, $p_a = 6.5\%$, and $p_h = 1.2\%$. $F = 17$.

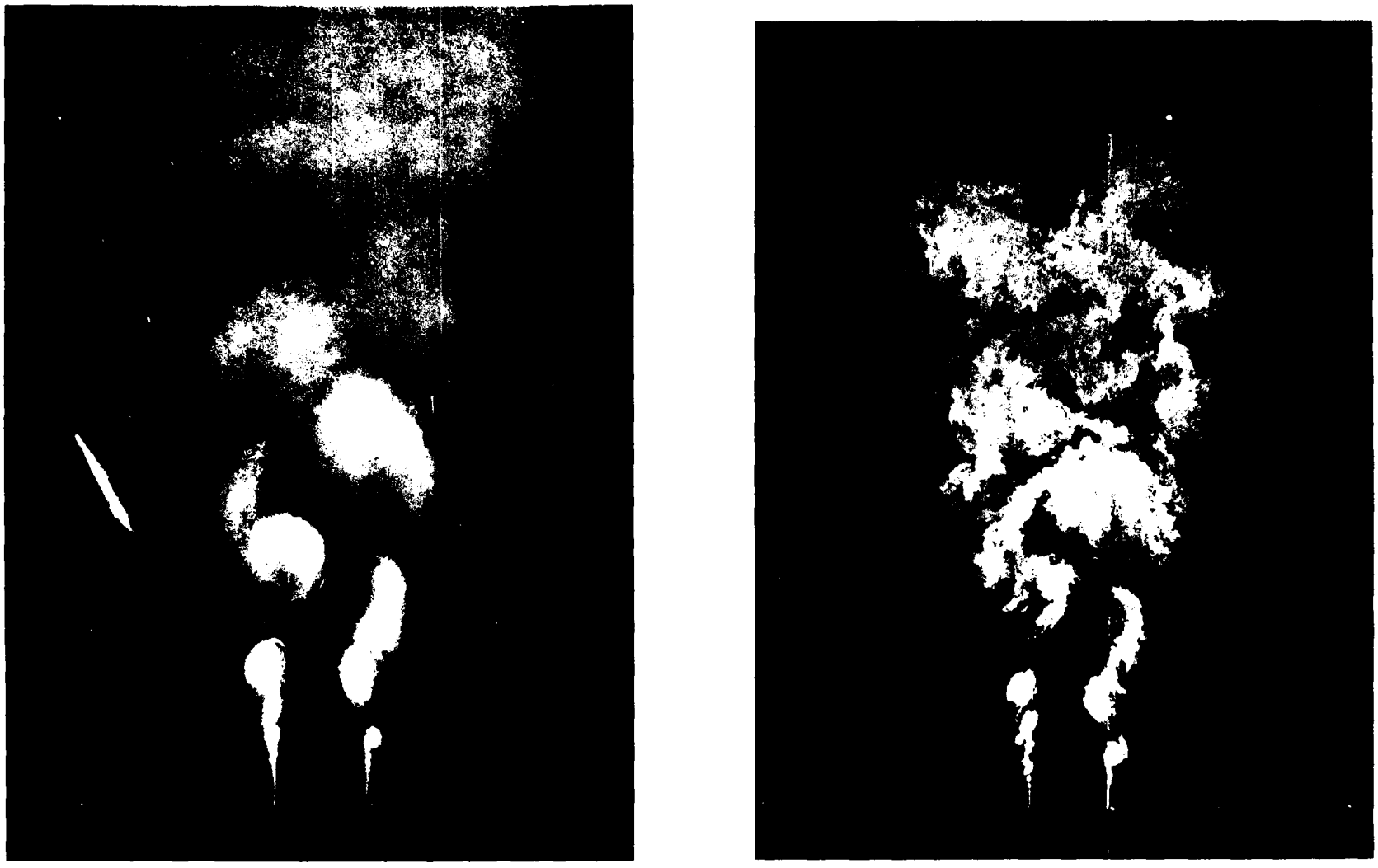

b

Figure 5.55. Comparison of (a) phase-averaged ($F = 17$) and (b) instantaneous ($F = 1$) realizations of a bifurcating jet ($Re = 100,000$, $St_a = 0.55$, $\bar{p}_a = 2.8\%$, and $\bar{p}_h = 0.71\%$).

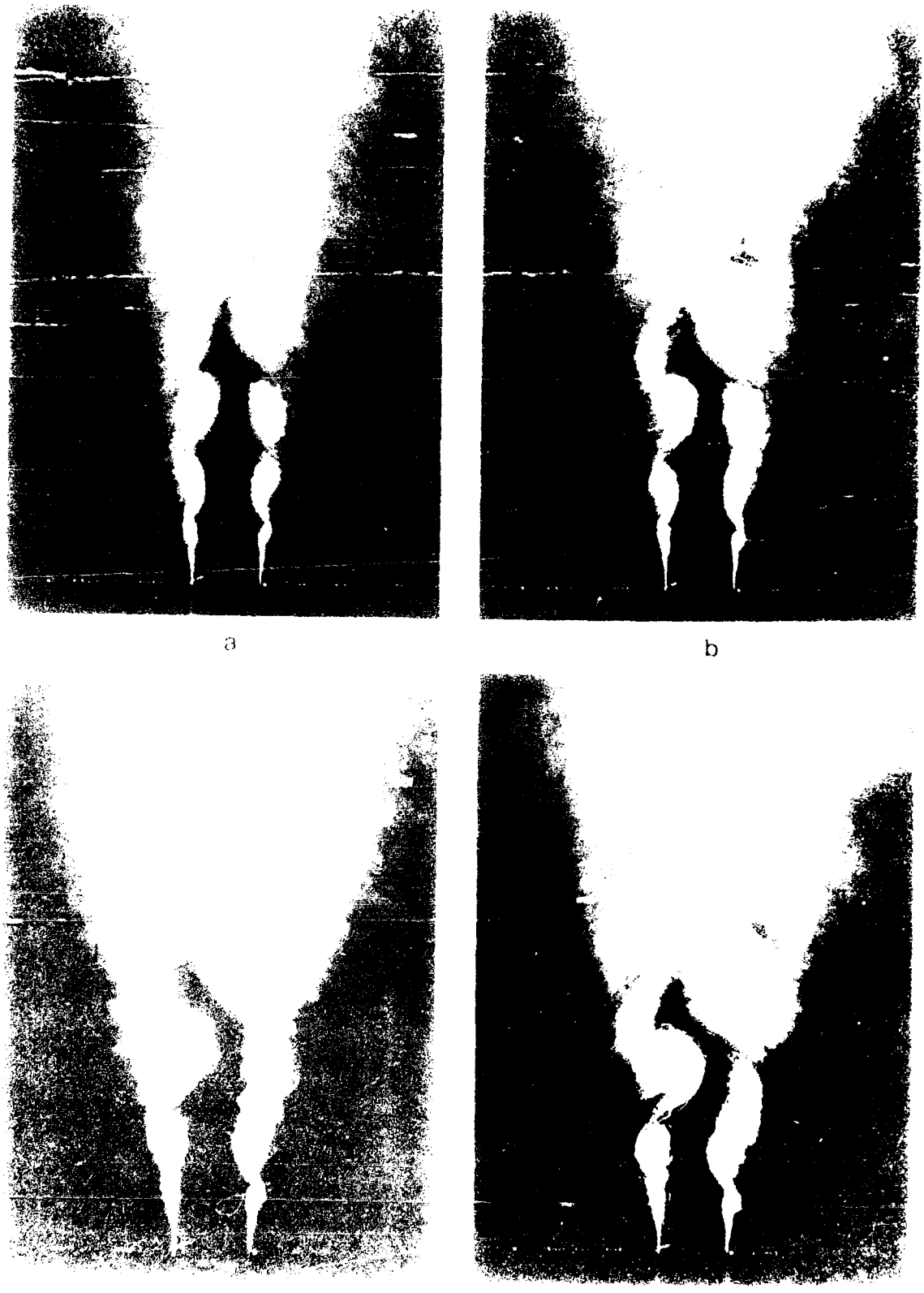
a
b

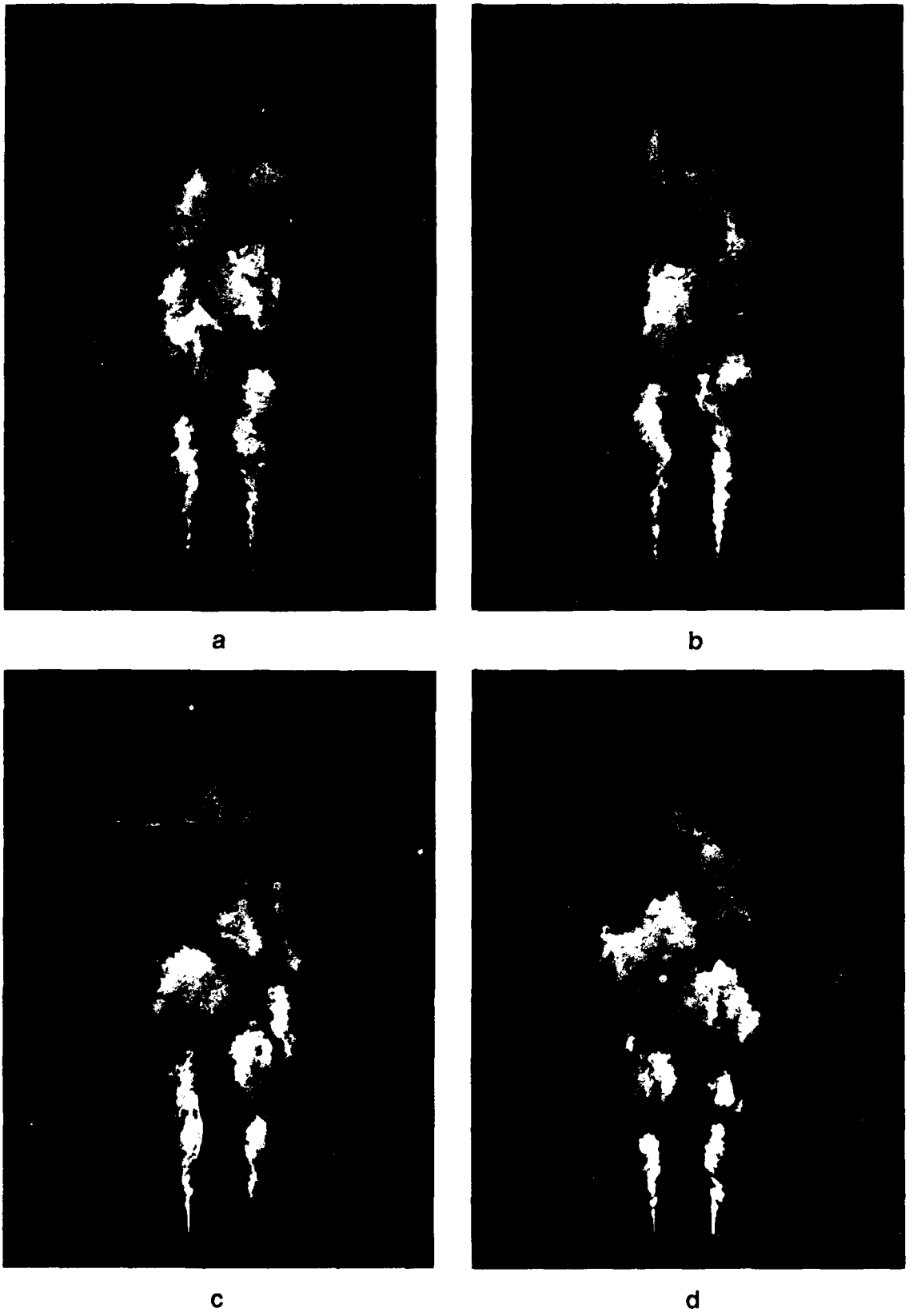

Figure 5.57. Bifurcating jet at $Re = 100{,}000$, $St_a = 0.55$, $\bar{p}_h = 0.36\%$, and $\bar{p}_a$ =(a) 0%, (b) 0.29%, (c) 1.4%, (d) 2.8%. $F = 1$.

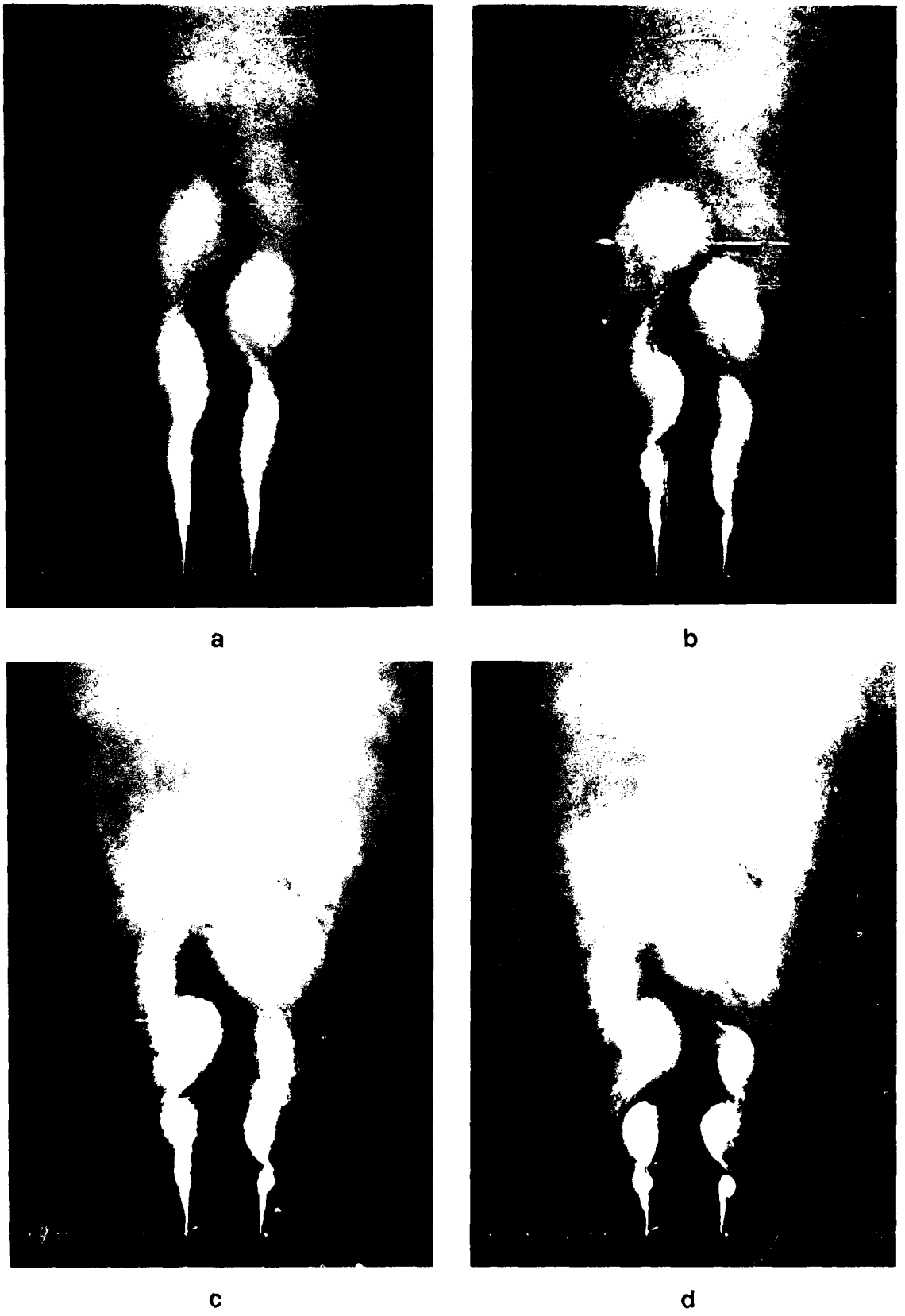

Figure 5.58. Bifurcating jet at $Re = 100,000$, $St_a = 0.55$, $\bar{p}_h = 0.36\%$, and $\bar{p}_a =$ (a) 0.29%, (b) 1.4%, (c) 2.8%, (d) 5.5%. $F = 17$.

Figure 5.59. Bifurcating jet at $Re = 100{,}000$, $St_a = 0.55$, $\bar{p}_a = 1.4\%$, and $\bar{p}_h = 0.71\%$. $F = 17$.

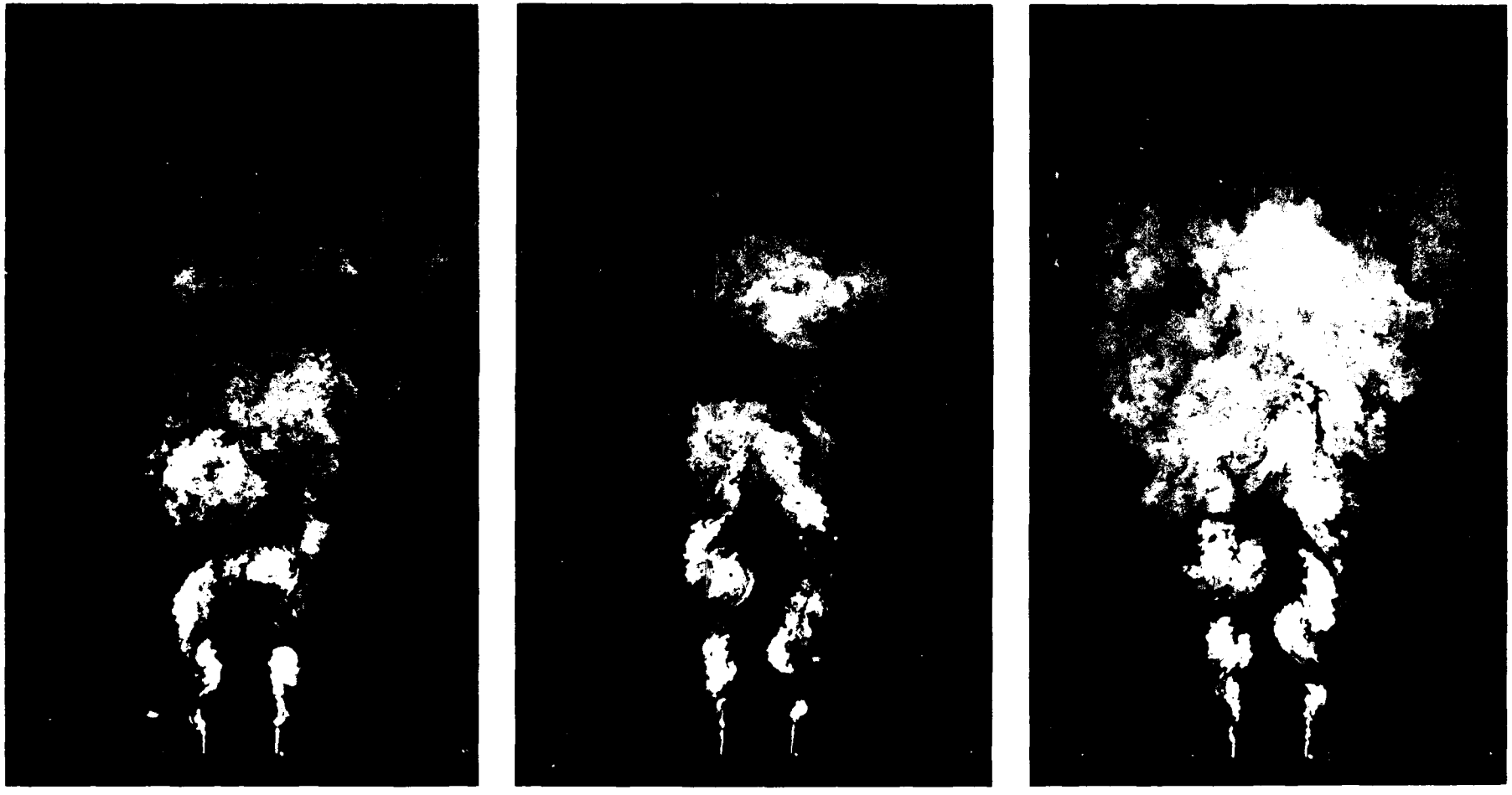

Figure 5.60. Bifurcating jet at $Re = 100,000$, $\bar{p}_a = 5.5\%$, $\bar{p}_h = 0.69\%$, and St_a =(a) 0.55, (b) 0.60, and (c) 0.65. $F = 1$.

Figure 5.61. Bifurcating jet at $Re = 100,000$, $\bar{p}_a = 5.5\%$, $\bar{p}_h = 0.69\%$, and St_a =(a) 0.55, (b) 0.60, and (c) 0.65. $F = 17$.

Figure 5.62. Bifurcating jet at $Re = 100{,}000$, $\bar{p}_a = 2.8\%$, $\bar{p}_h = 0.29\%$, and St_a =(a) 0.55, (b) 0.60, and (c) 0.65. $\Gamma = 17$.

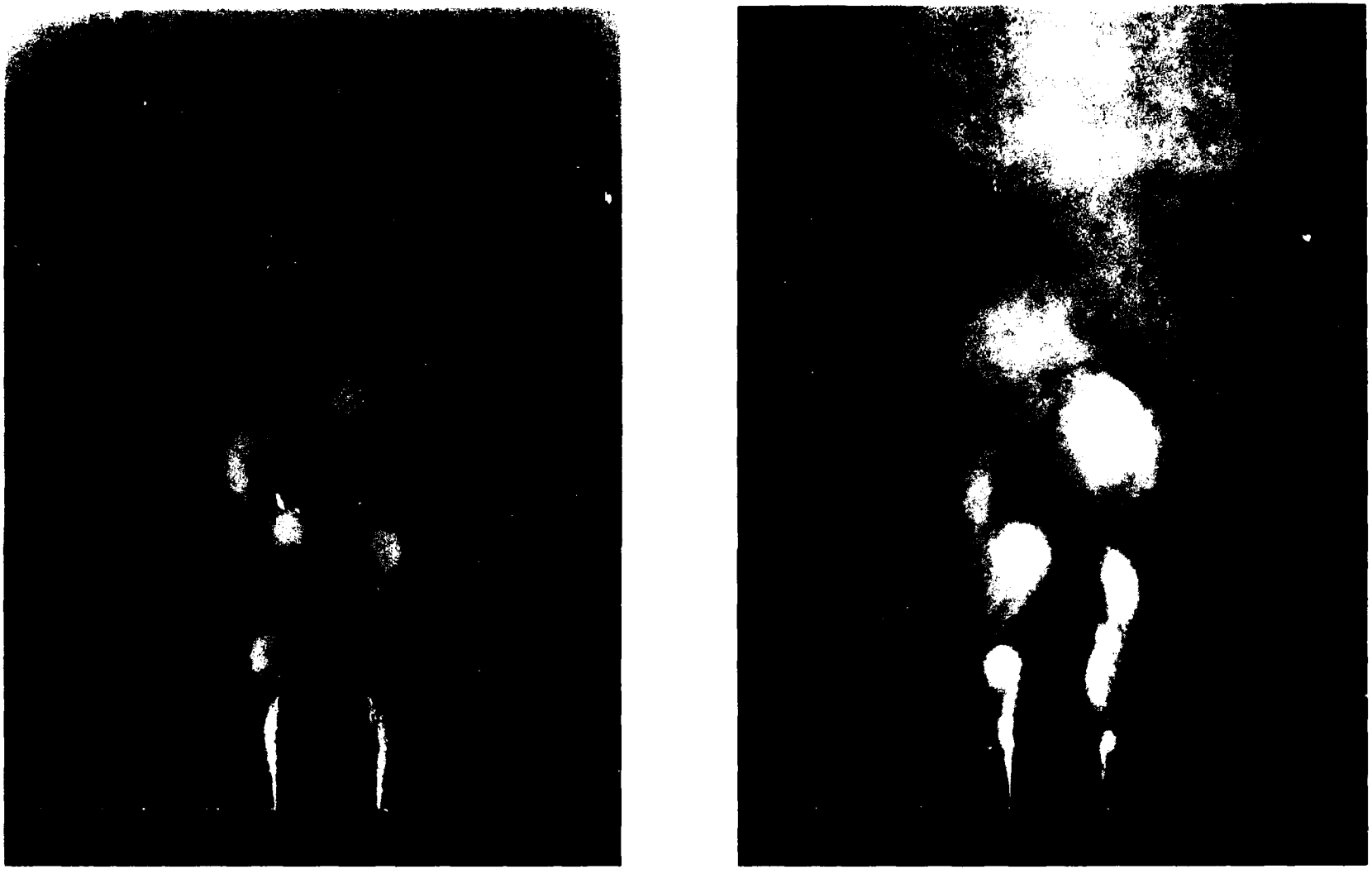

Figure 5.63. Comparison of the effects of (a) separate ($\bar{p}_a = 0.95\%$, $\bar{p}_h = 0.36\%$, and $F = 8$) and (b) combined ($\bar{p}_a = 1.4\%$, $\bar{p}_h = 0.36\%$, and $F = 17$) excitations on bifurcating jets at $Re = 100,000$ and $St_a = 0.55$.

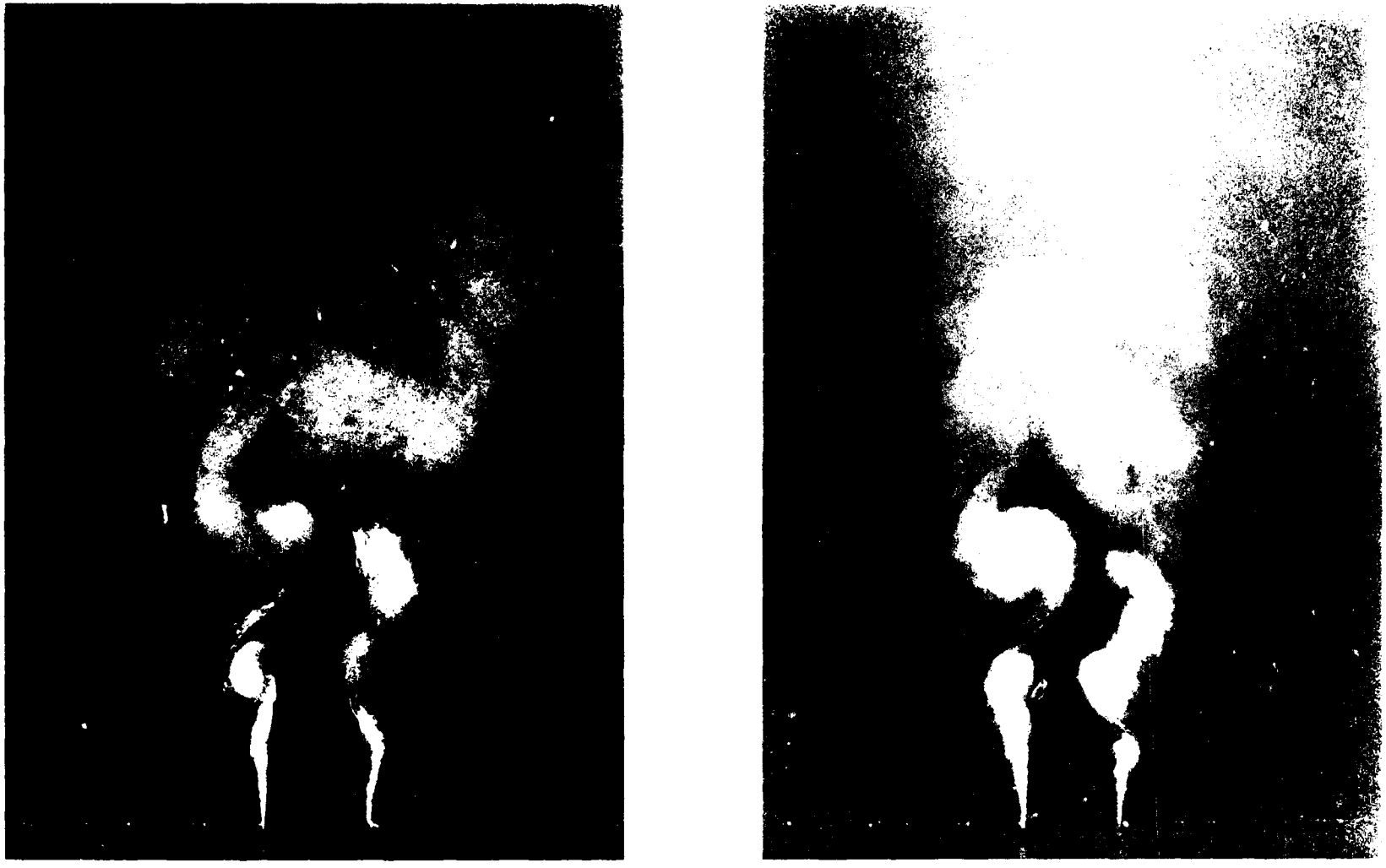

Figure 5.64. Comparison of the effects of (a) separate (p_a = 1.8%, p_h = 1.4%, and F = 8) and (b) combined (p_a = 2.8%, p_h = 1.4%, and F = 17) excitations on bifurcating jets at Re = 100,000 and St_a = 0.55.

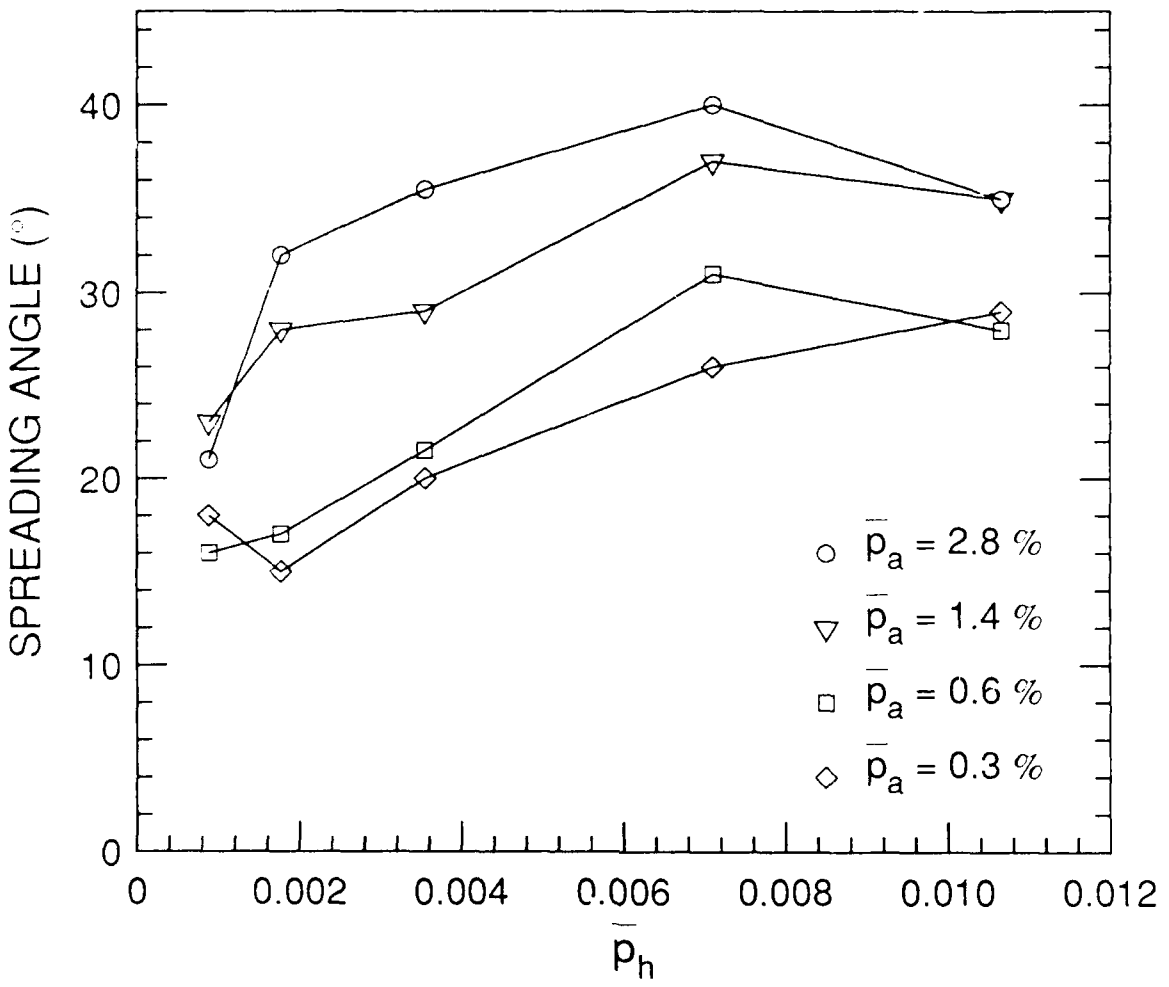

Figure 5.65a. Dependence of bifurcating jet's spreading angle on excitation amplitudes at $St_a = 0.55$ and at $Re = 100{,}000$. Axial and helical excitations are both produced by the external acoustic drivers. Measurement uncertainty is $\pm 5°$. Lines connect symbols simply to enhance readability.

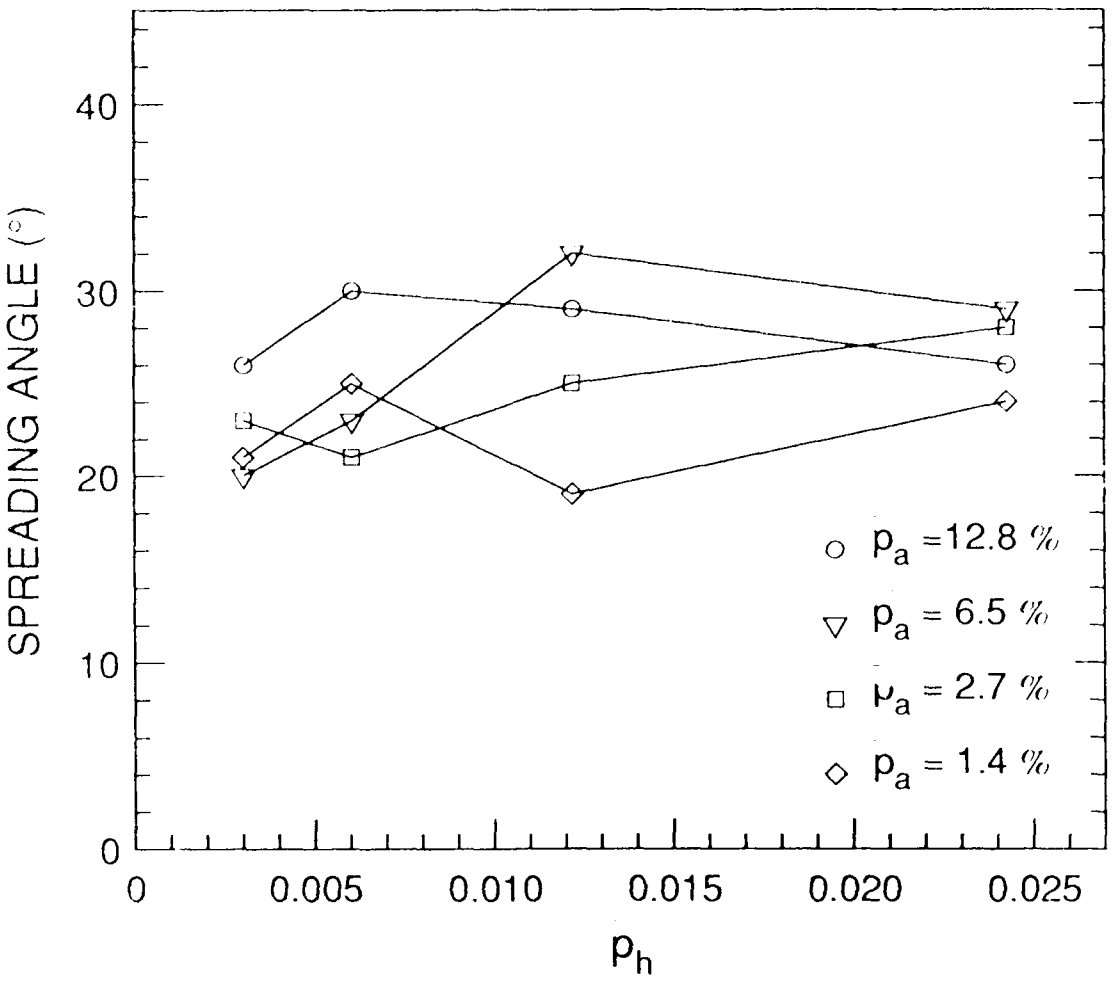

Figure 5.65b. Dependence of bifurcating jet's spreading angle on excitation amplitudes at St_a = 0.55 and at Re = 50,000. Axial and helical excitations are both produced by the external acoustic drivers. Measurement uncertainty is ±5°. Lines connect symbols simply to enhance readability.

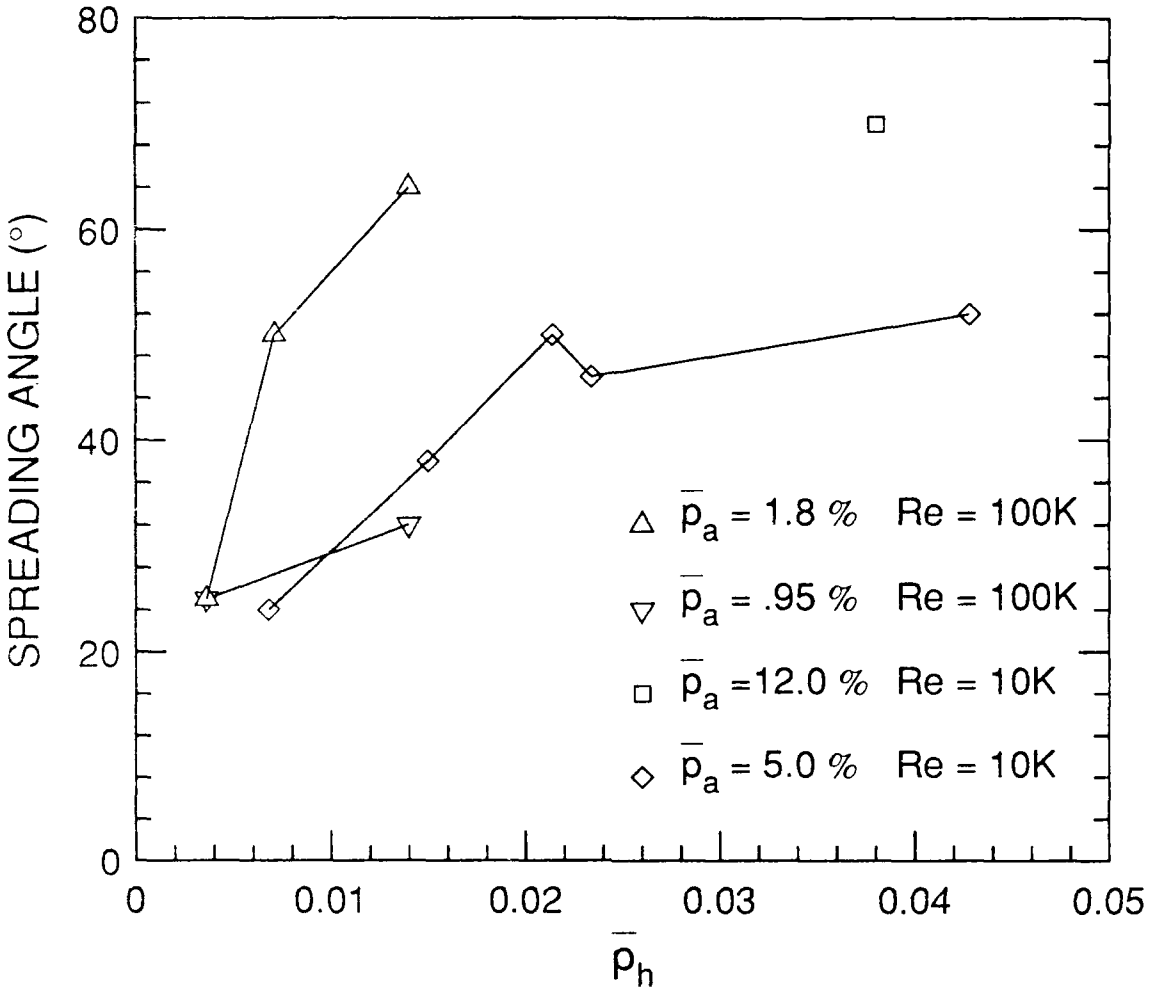

Figure 5.66. Dependence of bifurcating jet's spreading angle on excitation amplitudes at $Re = 10,000$ and 100,000 and at $St_a = 0.55$. Axial excitation is produced by internal acoustic driver. Measurement uncertainty is $\pm 5°$. Lines connect symbols simply to enhance readability.

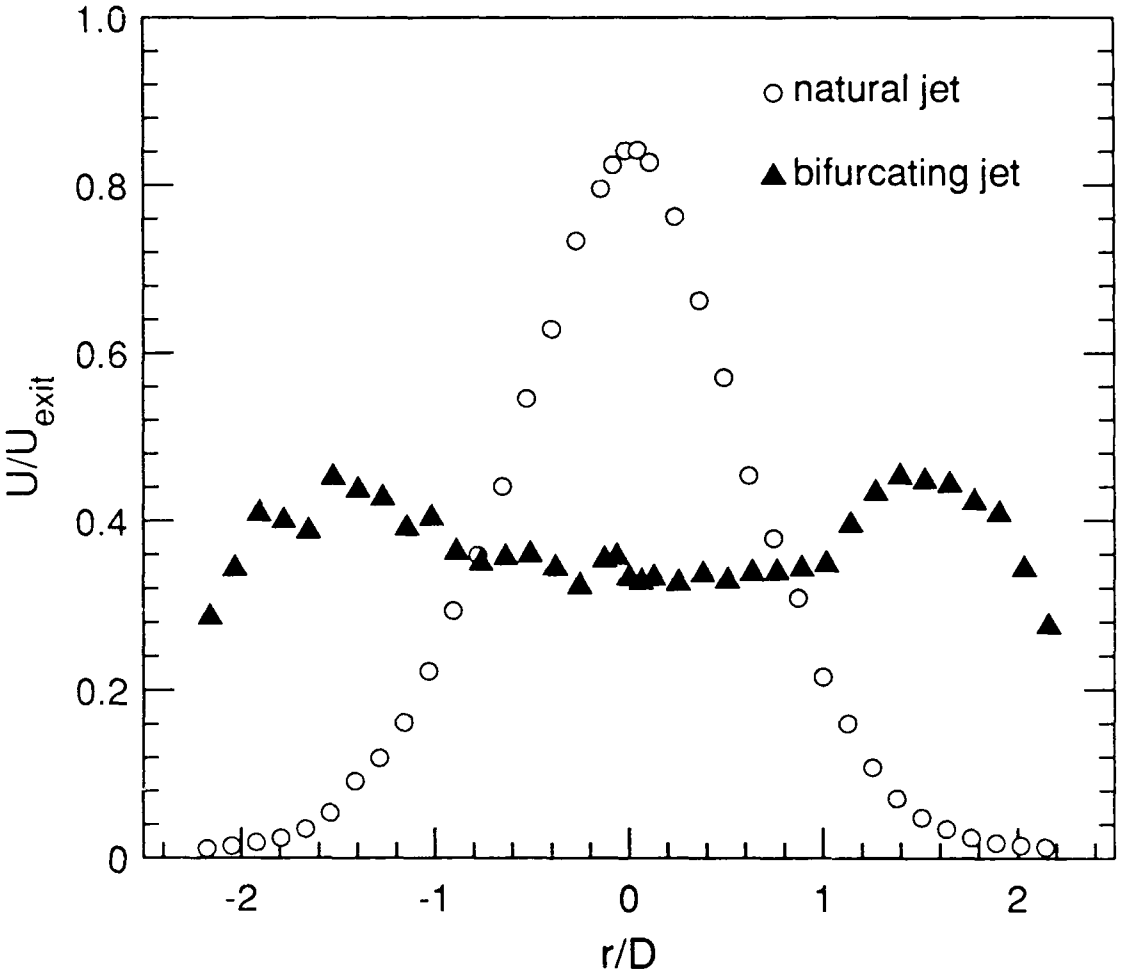

Figure 5.67. Velocity profiles of natural and bifurcating jets at $Re = 100,000$ and $z/D = 8.5$. Separate excitations are used in the bifurcating jet, with $\bar{p}_a = 1.8\%$ and $\bar{p}_h = 1.4\%$.